Forward modelling of simulated galaxies

James William Trayford

A Thesis presented for the degree of
Doctor of Philosophy

Institute for Computational Cosmology
Department of Physics
University of Durham
England

October, 2017

Dedicated to

Jessica & my family.

Forward modelling of simulated galaxies

James William Trayford

Submitted for the degree of Doctor of Philosophy
October, 2017

Abstract

I employ a *forward modelling* approach to create and study mock observables, using the *Evolution and Assembly of GaLaxies and their Environments* suite of hydrodynamical simulations (EAGLE, described in chapter 2). The majority of this analysis focuses on a subset of 30,145 simulated galaxies, selected to have stellar masses $M_\star \geq 1.81 \times 10^8$ M$_\odot$ from the largest fiducial volume at $z = 0.1$. The philosophy behind this approach is that, ultimately, our galaxy formation models should predict observables if we are to claim that they reproduce the data. The *forward modelling* approach allows us to address a number of overarching questions, in particular; i) *How well can cutting-edge simulations, such as* EAGLE*, reproduce fundamental observables over cosmic time?*, ii) *What are the systematic effects that come about when translating between the observable and physical properties of galaxies?* and iii) *What physical processes lead to the distributions of galaxy properties we observe?*

To this end, optical colours, luminosities, spectra and images are generated, where dust is modelled to either be absent, in a foreground screen or to trace the ISM using radiative transfer in chapters 3 and 5. Mock colour-mass and luminosity distributions are compared with data, revealing a broad agreement that is improved when dust is included and best for radiative transfer models. Chapter 4 shows how the $z = 0.1$ bimodal colour distribution that is found in both the data and the mock EAGLE photometry becomes established, along with the quenching mechanisms and timescales involved. In addition, chapters 5 and 6 investigate the accuracy of star formation activity proxies and mass recovery techniques, respectively. Detailed summaries are provided in each chapter, and compiled alongside conclusions in chapter 7.

Declaration

The work in this thesis is based on research carried out at the Institute for Computational Cosmology, the Department of Physics, Durham University, England. No part of this thesis has been submitted elsewhere for any other degree or qualification and it is all my own work unless referenced to the contrary in the text. Portions of this work have been published, or accepted for publication, elsewhere:

- Chapter 3 and appendix A: **Colours and luminosities of z=0.1 galaxies in the EAGLE simulation**, *James W. Trayford, Tom Theuns, Richard G. Bower, Joop Schaye, Michelle Furlong, Matthieu Schaller, Carlos S. Frenk, Robert A. Crain, Claudio Dalla Vecchia, Ian G. McCarthy*, MNRAS, Sep. 2015, vol. 452 p. 2879.

- Chapter 4: **It's not easy being green: the evolution of galaxy colour in the EAGLE simulation**, *James W. Trayford, Tom Theuns, Richard G. Bower, Robert A. Crain, Claudia del P. Lagos, Matthieu Schaller, Joop Schaye*, MNRAS, Aug. 2016, vol. 460 p. 3925.

- Chapter 5 and appendix B: **Optical colours and spectral indices of z=0.1 EAGLE galaxies with the 3D dust radiative transfer code SKIRT**, *James W. Trayford, Peter Camps, Tom Theuns, Maarten Baes, Richard G. Bower, Robert A. Crain, Madusha L. P. Gunawardhana, Matthieu Schaller, Joop Schaye and Carlos S. Frenk*, preprint available (`arXiv:1705.02331`), accepted in *MNRAS*.

Acknowledgements

Firstly, I am thankful to Prof. Tom Theuns and Prof. Richard Bower for their supervision during my PhD. Following Tom's rigorous yet far-sighted approach to research has been transformative for me, and a lesson in what it takes to truly understand something. I have benefited greatly from his trove of inspired ideas and insights. Richard's enthusiasm is contagious, with his unique perspective on science (and most other things) proving invaluable on many occasions.

I have found the EAGLE team a truly nurturing collaboration to be a part of. Particular thanks go to Matthieu and Michelle for being the best role models a fledgling eaglet could hope for. Jaime, Stuart and Stefan have been great additions, and great fun to work with, with senior members such as Rob and Joop providing much wisdom and insight, that I hope finds its way into the work presented here. I have also been very lucky to work with the Ghent group; learning greatly from Peter's masterful approach to projects, and Maarten's sage knowledge of radiative transfer. In addition, I gratefully acknowledge the CHARM project (BelSPO project P7/08) for funding my studentship.

Completing a PhD project is by no means easy, and I'm grateful for having such great company to help me through my time at Durham. Particular thanks to Alasdair, George and Peter for joining me in the mighty GLP, arguably the best prog rock combo in the department. Thanks also go to my office mates Charles, Steve, Alex and Jacob for surviving the Rochester rooftop with me, as well as Tim and Hannah providing much needed company for those final weeks in the Ogden annex. It's been great to avoid talking science at coffee or down the pub with many people, to name a few not yet mentioned: Andrew, Greg, Helen, Paddy, Sownak, Tamsyn, Violeta and Will. Steph is also someone I can always chat to,

and a great example of all the cool things you can do outside of work.

Most of all, I'm grateful to Jessica and my family for their unfailing love and support over the last 4 years and beyond. I wouldn't have made it through without you. My parents instilled a passion for learning in me from a young age, and have always encouraged me to succeed. Jessica has given me the confidence to follow my passions, and the grounding to keep perspective in the heady world of academia. Thank you for being incredible, I'm forever grateful for all you give me and only hope I can repay you in the years to come.

By day and night, fancy electronic dishes are trained on the heavens.
They are listening for smudged echoes of the moment of creation.
They are listening for the ghost of a chance.
They may help us make sense of who we are and where we came from;
And, as a compassionate side effect, teach us that nothing is ever lost.

Paddy McAloon, I Trawl the Megahertz

Contents

List of Figures

List of Tables

Chapter 1

Introduction

In the mid-18$^{\text{th}}$ century, Thomas Wright supposed that the faint nebular structures he observed could be systems of stars external to our own Milky Way, later to be termed *Island Universes* by Immanuel Kant (Wright, 1750; Kant, 1755). While provenance for the understanding that our Milky Way is merely a single instance in a greater population of '*galaxies*' can be traced back to the *Enlightenment* period, general acceptance of this concept is less than a century old. It was the detection of Cepheid stars in Andromeda (Hubble, 1926) that provided the first conclusive distance measurement of a galaxy and confirmed its extragalactic status, settling contemporary debate on the nature of the *spiral nebulae* (Shapley & Curtis, 1921). This discovery has tremendous implications for our understanding of the universe and our place within it, and founded the fields of extragalactic astronomy and modern galaxy formation theory.

Today's astronomers inherit a vast and growing repository of data on galaxies. Decades of focused observation of individual objects and the recent explosion of data from galaxy redshift surveys put strong constraints on the nature of galaxies, the prevalence of different galactic phenomena and their various evolutionary pathways. Galaxies themselves act as beacons in the distant Universe; tracing greater cosmic structures and shedding light on the unseen Universe around them. Great advancements in extragalactic observation demand a richer galaxy formation theory, and a reappraisal of how galaxies are thought about and modelled.

This thesis is concerned with using modern computational techniques to model the formation of galaxies in a cosmological context, and how we might reconcile theoretical predictions with observation. In particular, I consider the translation between the physical properties that drive galaxies and those that are observed, using *'forward modelling'* to compare simulations to observations directly. In this section I provide context for the original work presented in the thesis. In particular, I will focus on modern galaxy formation theory, the role of simulations in understanding how galaxies form and reconciling theoretical predictions with observations. As a detailed review of the field is beyond the scope of this section, I focus on the areas most relevant to this body of work, and summarise the structure of the thesis in section 1.5.

1.1 Key Observations of Galaxies

To motivate features of contemporary galaxy formation models, I first describe some of the key observations that have informed them. While a raft of diverse observations shape current theories, I focus on just a few select observables and how they may be compiled. In particular, observations from galaxy redshift surveys (e.g. SDSS, York et al. 2000; 2dF, Colless et al. 2003; GAMA, Driver et al. 2009) provide strong statistical constraints, afforded by the large number of objects they sample. Distributions of measured properties are a useful way of characterising this observed population, providing clear targets that successful formation models should aim to reproduce. The diversity of galaxy redshifts, luminosities, colours and morphologies captured observationally are exemplified by the *Hubble Ultra Deep Field* (HUDF), shown in Fig. 1.1. Conspicuous differences can be seen between the galaxies of the HUDF, and the measurement and relevance of these particular properties are detailed below.

Redshift (z) itself is a key measurement, used to infer the distances to observed galaxies and thus how long ago the light we observe was emitted (e.g. Hogg, 1999). Redshifts and angular positions from galaxy surveys have been used to map the spatial distribution of local galaxies ($z \lesssim 0.2$) in great detail, re-

vealing the characteristic filamentary structure of the *cosmic web* (see e.g. Springel et al., 2006) and yielding precise galaxy clustering statistics (e.g. Zehavi et al., 2011). Redshifts also enable us to to partition galaxies into roughly contemporaneous populations, in order to examine the evolution of galaxy properties. Redshifts are obtained using galaxy photometry (e.g. Bolzonella et al., 2000; Brammer et al., 2008) or, more reliably, spectra (see Baldry et al., 2014).

Luminosities can then be inferred with knowledge of the redshift. The number density of galaxies at a given luminosity, or luminosity function (LF), is a fundamental characteristic of the galaxy population (e.g. Blanton & Moustakas, 2009; Johnston, 2011). Rather than bolometric luminosities, which require panchromatic observations, luminosities are typically measured in wavelength bands or by integrating emission features. For optical broad-bands the LF primarily tells us about the stellar component of galaxies, with bluer bands probing younger stellar populations. The LF is commonly well-fit by a Schechter (1976) function, featuring an asymptotic slope towards dim galaxies and a sharp cut-off above a characteristic luminosity[1] that varies between bands.

Estimating luminosity functions can be tricky. Uncertainties in intrinsic UV-optical luminosities are compounded by dust in target galaxies, which may absorb $\sim 40\%$ of emitted light at these wavelengths in the local star-forming population (e.g. Viaene et al., 2016b). The complex nature of the dust-light interaction means dust corrections are often highly idealised. In addition, luminosity-dependent volume and completeness corrections are necessary to convert number counts into number densities (e.g. Baldry et al., 2012). Corrections should also be made for the fact that variations in redshift lead to different regions of the rest-frame galaxy spectral energy distributions (SEDs) being sampled by a given band ('k-corrections', e.g. Blanton & Roweis, 2007), and that galaxies evolve between their redshift of observation and the redshift that the LF is being constructed for

[1]Emission associated with the youngest stars (such as ultraviolet, Hα, far-infrared emission Kennicutt, 1998a) may be better fit by a Saunders et al. (1990) function with a shallower bright-end slope (e.g. Gunawardhana et al., 2013).

('e-corrections', e.g. Norberg et al., 2002). These two corrections can be minimised by selecting galaxies over a narrow range in redshift, but there is a trade-off with lower number counts and stronger inhomogeneity effects due to the smaller sampled volume (e.g. Blanton & Moustakas, 2009). The integration of a galaxy's light and sky subtraction also lead to uncertainties, that can introduce systematic differences at the bright end (Bernardi et al., 2013).

Despite these difficulties, LFs probing stellar emission have been well-studied locally (Blanton et al., 2001; Norberg et al., 2002; Loveday et al., 2012) and constrained out to $z \lesssim 10$, revealing evolution in how galaxy luminosities are distributed (e.g. Kauffmann & Charlot, 1998b; Zucca et al., 2009; Bouwens et al., 2015).

Colours, representing the ratio of luminosities in different bands, are a basic measure of the shape of galaxy spectra. The colour-magnitude diagram combines the LF and colour distribution, providing a key diagnostic for the observed population. Colours in the UV and optical are primarily driven by the recent star formation activity and star formation histories in galaxies (the presence of hot, massive stars in young stellar populations makes galaxies appear bluer), but can also be strongly influenced by dust content and affected by stellar metallicities. In early data sets, a narrow *'red sequence'* of galaxies was already clearly evident (e.g. Sandage & Visvanathan, 1978; Larson et al., 1980; Bower et al., 1992). The step-change in sample size afforded by the likes of the Sloan Digital Sky Survey (SDSS, York et al. 2000) revealed *'blue cloud'* population, establishing a distinct *bimodality* in local galaxy colours (Strateva et al., 2001; Bell et al., 2004; Baldry et al., 2004). Evidence for colour bimodality has been observed out to $z \lesssim 3$ (Franx et al., 2003; Faber et al., 2007; Whitaker et al., 2011). A two component model of the colour distribution[2] appears to provide a good fit for optical bands (e.g. Baldry et al., 2004; Taylor et al., 2015). However, UV-optical colours have an enhanced sensitivity to young stars and reveal a significant *'green valley'* population between the two peaks (e.g. Wyder et al., 2007; Martin et al., 2007). With luminosity and colour

[2]Fitting two Gaussian distributions to the red and blue peaks

Figure 1.1: The three colour composite image of the *Hubble Ultra Deep Field* (HUDF, Beckwith et al., 2006) illustrates the diversity of galaxy properties revealed by modern telescopes. Within this small patch of sky (2.4×2.4 arcmin), $\sim 10^4$ galaxies have been identified, spanning redshifts covering most of the history of the universe. Sizes, shapes and colours vary dramatically between galaxies, reflecting both intrinsic differences in galaxy properties as well as redshift and projection effects. Image credited to NASA, ESA, H. Teplitz and M. Rafelski (IPAC/Caltech), A. Koekemoer (STScI), R. Windhorst (Arizona State University), and Z. Levay (STScI).

indicative of a galaxy's star formation history, the evolving colour-magnitude diagram clearly encodes a great deal of information about the physical evolution of the galaxy population.

Morphology, pertaining to the surface brightness distribution in galaxies, is another important global property. While morphology has long been a conspicuous feature of galaxies, and visual classification schemes such as the *Hubble tuning fork* remain prevalent today, obtaining objective or quantitative measures of morphology is challenging. Fitting radial light profiles of galaxies with idealised functional forms[3] has proven a popular parametric approach (e.g. Peng et al., 2010), and allows us to decompose galaxy light profiles into contributing components such as centrally concentrated *spheroids* and extended *discs*. This approach can be used to provide very useful decompositions for large galaxy samples (e.g. Simard et al., 2011; Häußler et al., 2013), but the underlying assumptions about galaxy light profiles may not be representative of some galaxies and introduce systematic effects (e.g. Benson et al., 2002; Conselice, 2014). Non-parametric measures have been developed to avoid this limitation. While these do not provide direct decompositions, they quantify morphology via concentration, clumpiness and asymmetry (e.g. Conselice, 2003) and the Gini and M_{20} parameters (see Lotz et al., 2004). An alternative is to embrace human classification, and reduce subjectivity by appealing to a large number of distinct classifiers. The pioneering Galaxy Zoo project (Lintott et al., 2011) has proven a successful implementation of this, employing $\sim 10^5$ citizen scientists to obtain statistically robust classifications of $\sim 10^6$ galaxies (e.g. Willett et al., 2013). These different approaches to obtaining morphologies may be appropriate in different scenarios, or used in combination.

In addition to the colour-magnitude relation, other interrelationships between these properties have been widely explored. A strong morphology-colour relation has long been established (e.g. Larson et al., 1980), and more recently put

[3]Commonly exponentially declining, de Vaucouleurs or generalised Sérsic profiles

on a detailed, statistical footing using human classification (Schawinski et al., 2014; Smethurst et al., 2015) and numerical methods (e.g. Driver et al., 2006). Morphologies, like colours, show bimodality with luminosity locally (e.g. Kelvin et al., 2014) and evolve with redshift (e.g. Conselice et al., 2005). In addition, these intrinsic properties of galaxies correlate with the environment in which they reside, yielding a generic picture of the local galaxy population as red ellipticals in dense groups and clusters, and blue spirals in the field (e.g. Dressler, 1980; Balogh et al., 2004; Ball et al., 2008; Tempel et al., 2011; Alpaslan et al., 2015).

It seems plausible that common physical processes, arising from how galaxies form and evolve, drive the strong relationships between these observations. Indeed, these observables are widely used to estimate physical properties such as stellar mass and star formation history. For large samples of galaxies, these are derived using proxies or by fitting spectral or photometric measurements of galaxies with templates (e.g. Kennicutt, 1998a; Walcher et al., 2011), discussed further in section 1.4. The new generation of Integral Field Unit (IFU) instruments are also beginning to provide kinematic information for galaxy samples (e.g. KMOS Wisnioski et al. 2015; SAMI Allen et al. 2015; MaNGA Bundy et al. 2015). Details of the conversion between the physical and observable domains is discussed further in section 1.4. In the following section, we first review galaxy formation theory and its relation to these observations.

1.2 Galaxy formation within the ΛCDM paradigm

1.2.1 The ΛCDM Cosmology

The current concordance model of our Universe is the ΛCDM framework, the main facets of which are empirically motivated. Here, CDM references *'cold dark matter'* as the primary mass component of the cosmos, with a cosmological constant, Λ, dominating the present day energy density. Evidence for a significant 'dark' (non-emissive) matter component was first postulated in 1933 by Fritz Zwicky, who found that the large velocities of galaxies in the Coma cluster could

not be reconciled by luminous matter alone (see Zwicky, 2009, for a translation of the original article). Evidence for a significant dark matter component, favoured to comprise weakly interacting and massive particles (WIMPs e.g. Peebles, 1982), has since arrived from a number of quarters, including galaxy kinematics and gravitational lensing (e.g. Rubin et al., 1980; Brainerd et al., 1996). Measurements of clustering in large samples of galaxies (see section 1.1) can also be reconciled by invoking CDM (e.g. Springel et al., 2006).

ΛCDM incorporates a hot big bang cosmogony, where the Universe has expanded and cooled from an initial state of extreme density and temperature. When the Universe first cools to the point where hydrogen atoms form, photons that were initially coupled to baryons and leptons are able to propagate freely as the mean free path for Thomson scattering becomes large. Relic radiation from the decoupling of the photon-baryon fluid is redshifted as the Universe expands, and observable today as the cosmic microwave background (CMB, Penzias & Wilson, 1965).

Perhaps the strongest constraints on the ΛCDM model come from detailed CMB measurements. Temperature anisotropies in the CMB have been measured and mapped at increasing fidelity via the COBE (Smoot et al., 1992), WMAP (Komatsu et al., 2011), and Planck (Planck Collaboration et al., 2014) satellites. These anisotropies are indicative of density perturbations in the early Universe, consistent with inflationary models where quantum fluctuations are blown up to large scales, which appear to have sufficient amplitude to have seeded present day structure through gravitational collapse.

The angular power spectrum of temperature fluctuations also encodes information about a number of cosmological parameters. Peaks in the power spectrum correspond to acoustic modes propagating through the primordial baryon-photon fluid. The fundamental mode represents oscillations with a period twice as long as the time between their sound horizon entry and recombination, such that the fluid is maximally compressed or rarefied when photons and baryons decouple (see e.g. Hu & Dodelson, 2002). Comparing the amplitude of the first to that of the second peak (corresponding to one full oscillation before recom-

bination) constrains the cosmic baryon density at recombination. The relative amplitude of higher order modes then indicates the dark matter density at this time. Matter is found to comprise 31.5% of the present cosmic energy density in the Planck data, of which 4.5% is in baryons and the rest is in dark matter (e.g. Planck Collaboration et al., 2014). The remaining 68.5% of the cosmic energy budget is deemed to be *dark energy*, which is represented by Λ in the ΛCDM model, and observed as an acceleration term in the expansion history of the Universe today. Aside from dark energy, alternative explanations for the accelerated expansion of the Universe have also been theorised, many appealing to modifications to the behaviour of gravity from that of general relativity on large scales (see e.g. Koyama, 2016, for a review).

Once photons decouple from baryons, the pressure driving oscillations vanishes, and overdense shells of a characteristic scale are preserved about central dark matter overdensities[4]. These Baryon Acoustic Oscillations (BAO), and this resultant overdensity configuration, are a key prediction of the model. The imprint of the BAO was first detected as enhanced clustering of galaxies on these scales ($\sim$150 Mpc at $z \sim 0$), as galaxies form in these overdensities (e.g. Cole et al., 2005), and measured using galaxy redshift surveys (see section 1.1). We review the general picture of how structure collapse and galaxy formation proceeds in cosmic overdensities in the following section.

1.2.2 Galaxy Formation within Halos

The concept that galaxies form within the centre of dark matter *'halos'* has endured from the pioneering work of White & Rees (1978). In the lexicon of ΛCDM, halos form when matter overdensities become nonlinear and undergo gravitational collapse, decoupling them from the expansion of the Universe[5]. These

[4]Central overdensities are maintained as dark matter does not feel pressure forces.

[5]Peebles (1982) showed that dark matter particles must be relatively *cold* (massive with low streaming velocities) so that the anisotropies seen in the CMB collapse and are not erased by free-streaming. However, relatively *warm* dark matter (WDM) models appear feasible, where erasure of overdensities by free streaming can occur on small scales (e.g. Lovell et al., 2014).

bound structures form in a hierarchical fashion: smaller scale overdensities collapse first, and grow through mergers and accretion of material[6]. This result can be inferred from simple linear evolution of a Gaussian random density field and idealised spherical collapse models, first formalised by Press & Schechter (1974) and extended to include effects of mergers (Bond et al., 1991; White & Frenk, 1991, e.g.). These halos acquire their spin through tidal torques as they form (White & Rees, 1978; Fall & Efstathiou, 1980).

Gas is subject to the same gravitational forces as dark matter, and as such initially traces the same structure and rotation, giving halos a baryon fraction roughly equivalent to that of the Universe as a whole. As gas falls into halos, either initially or as it is accreted later, it gets shocked and its kinetic energy becomes thermalised. The thermal pressure supports this gas against further gravitational collapse and sets the gas halo into quasi-hydrostatic equilibrium. Radiation can dissipate this energy and allow the gas to condense deeper into the halo potential. While thermal emission effectively dissipates thermal energy, much of the angular momentum is conserved during the further collapse of baryons. This leads to proto-galactic gas discs forming near the potential minima of halos[7].

This gas must then form stars to be observed as a galaxy, and thus included in the galaxy statistics discussed in section 1.1. Star formation is a complex and multi-scale process, many aspects of which remain mysterious. Mercifully, strong empirical relationships between gas measurements and star formation rates have been observed. The Kennicutt-Schmidt law (Kennicutt, 1998b) shows that the inferred surface density of star formation follows a super-linear power law in inferred gas surface density. It has been suggested that this relationship is driven by the cooler molecular gas, and that refined measurement of molecular gas surface densities yield a tighter, linear relationship with star formation rate (e.g. Bigiel et al., 2011). Estimates of molecular gas content generally rely on CO emission as

[6]Note that a free streaming scale is evoked in WDM models, corresponding to the first halos that form, with halos on larger and smaller scales forming later

[7]Later-stage mergers may also augment and redistribute angular momentum in galaxies (Barnes & Efstathiou, 1987)

a tracer, but the fraction of molecules represented by CO can be ambiguous, not least due to its dependence on gas metallicity.

Metal enrichment of the gaseous inter-stellar medium (ISM) is of key importance to galaxy evolution in general. Metals are synthesised inside stars, and are typically returned to the ISM through the strong winds of AGB stars or the explosion type II and Ia supernova (SNa). These metals may be returned in a gaseous state, or as agglomerated dust grains. Metal line emission becomes an important cooling channel when the ISM is enriched, and dust grains provide vital sites for the formation of molecular gas, catalysing further star formation. The lifecycle and distribution of dust grains in the ISM is itself highly complex (see e.g. Draine 2003 for a review).

It may seem from this picture that star formation is an efficient, even runaway, process in galaxies. However, comparing the shape and normalisation of the observed NIR LF or galaxy stellar mass function (GSMF) with the halo mass function (HMF) suggest relatively low and mass-dependent star formation efficiencies in halos (e.g. White & Frenk, 1991; Benson et al., 2003). Feedback processes that disrupt star formation are invoked to explain this difference. It is thought that star formation could have been completely shut down in the smallest halos by the photoionising background after cosmic reionisation (e.g. Rees, 1986; Efstathiou, 1992; Thoul & Weinberg, 1995; Okamoto et al., 2008). It has also long been speculated that energy injected by supernovæ inhibits star formation in low mass galaxies (Larson, 1974; Dekel & Silk, 1986). Now the term *'stellar feedback'* is used generally to include photoionisation, photoheating and stellar winds as additional important feedback mechanisms associated with star formation. Combining these processes may lead to very little to no star formation in low mass halos, and naturally explain the divergence of the mass function of galaxies and of halos at the faint end (e.g. Sawala et al., 2014).

By contrast, at higher galaxy masses it is speculated to be the feedback from accreting super-massive black holes (SMBHs) that introduces a near exponential cut-off in the GSMF (Bower et al., 2006; Croton et al., 2006). Accreting black holes are identified with the observed phenomena of Active Galactic Nuclei (AGN, see

e.g. Netzer, 2015). Indirect observations provide strong evidence that most (perhaps all) galaxies contain a SMBH; nuclear velocities inferred from stars, gas and water masers are suggestive of extremely massive and compact central objects (Kormendy & Richstone, 1995). Some of the tightest galaxy scaling relations are also attributed to SMBHs (e.g. Magorrian et al., 1998; Gebhardt et al., 2000).

It is speculated that stellar and AGN feedback must drive large-scale outflows in order to be effective. These outflows move gas out of galaxies, where it might have formed stars, and into the circumgalactic environment. There is much observational evidence to suggest that outflows are prevalent in galaxies (see e.g. Veilleux et al., 2005). Outflows are observed to correlate with star-formation activity, and often the outflow rates exceed those of infall and star formation (Martin, 1999; Weiner et al., 2009; Kornei et al., 2012). This is suggestive that outflows play a crucial role in regulating star formation. Strong winds driven by AGN have also been shown to be energetically feasible, and are supported by cavities observed in the X-ray profiles of clusters (e.g. King & Pounds, 2003; Rafferty et al., 2006). In addition, galactic outflows are often observed to be dusty (e.g. Heckman et al., 2000), and its believed that radiation pressure on this dust may help to drive them (e.g. Veilleux et al., 2013).

Above I have described some of the key mechanisms of modern galaxy formation theory and how they relate to observation. Below, I review the insights we may gain from galaxy modelling. In particular; how do these complex, competing mechanisms drive the complex evolution of galaxies?

1.3 The Simulation Approach

Cosmological simulations have become instrumental to our understanding of cosmic structure formation and how competing physical processes shape galaxies. It is useful to split the simulation problem into two key questions[8];

1) *what would be the evolution of our Universe if it comprised only the dark sector*[9]*?*,

[8]This formulation is similar to Naab & Ostriker (2016).

[9]Dark matter and dark energy.

2) *how do baryonic processes alter this picture to yield the Universe we inhabit?*

The first question has largely been answered by the use of N-body simulations, that follow the growth of cosmic structure by gravity alone, which have played a crucial role in establishing the cold dark matter paradigm (e.g. Davis et al., 1985; Frenk et al., 1988). These simulations provide a coherent and convergent picture where gravity dominates, from linear large-scale structure to non-linear halo regimes (Springel et al., 2005b). They also have been used to suggest a universal profile for halos (Navarro et al., 1997), and characterise the substructures within them for CDM and alternative dark matter models.

These N-body simulations provide valuable insight into answering the second question. They place strong constraints on the growth of different environments, how halos are distributed and on accretion and merger rates of halos. However, the complex and multi scale nature of galaxy formation and baryonic physics in general means that the second question remains highly challenging. Fig. 1.2 demonstrates this complexity and dynamic range, showing a three level zoom between simulated baryon structure on cosmic and galaxy scales[10]. A number of simulation-based approaches have been developed to tackle the problem of modelling galaxy formation.

'Serial' approaches to galaxy formation take the solution to cosmic structure formation provided by N-body simulations, and afterwards model how galaxies might occupy the dark matter halos. The Halo Occupation Distribution (HOD) approach (Jing et al., 1998) assigns observed galaxies to simulated halos by some mapping between galaxy and halo properties. SubHalo Abundance Matching (SHAM) is a related approach. In its simplest form, this assumes a positive monotonic relationship between galaxy luminosity (or mass) and subhalo mass (Hearin et al., 2013). HOD, and particularly SHAM, approaches have been extensively used to produce mock catalogues for survey comparison. Despite these successes, they do not provide insight into the physical origin of these galaxies. Another serial approach is that of Semi-Analytic Models (SAMs). These gen-

[10]The EAGLE simulations shown here are introduced in detail below.

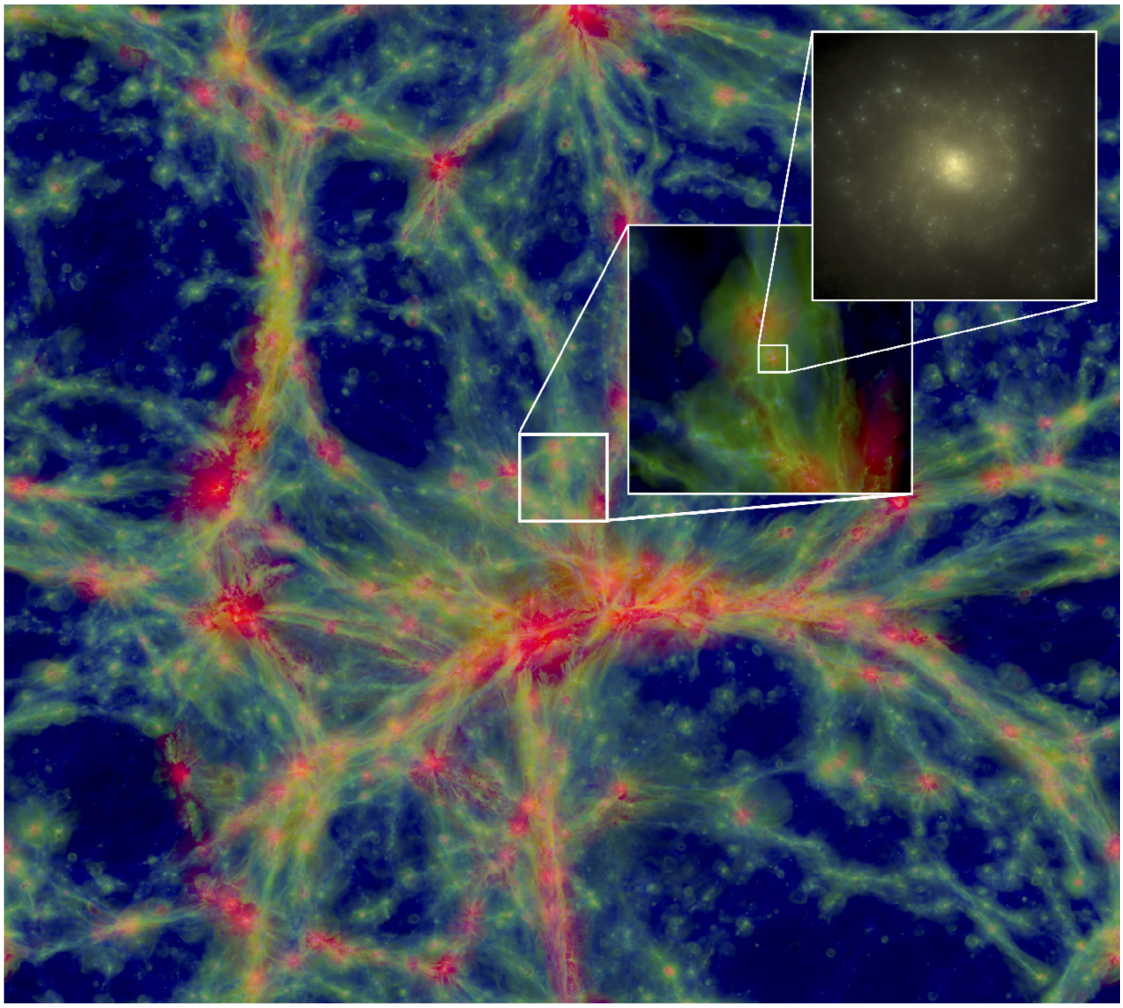

Figure 1.2: Illustration of the large range of scales needed for cosmological galaxy formation simulations, using the simulated baryon structure of the EAGLE simulations. The largest image is a 100×100 comoving Mpc projection of the simulated gas distribution, with density indicated by the brightness, and coloured from blue to red by increasing gas temperature. The smallest inset image shows a virtual 3 colour image of an EAGLE galaxy. Filamentary structures on scales of ~ 10 Mpc (the *cosmic web*) connect overdense halos, which provide the sites for galaxy formation on $\sim$ kpc scales. Simulating baryonic processes over this dynamical range has only recently become a computational reality, and resolution limitations for simulations covering these scales still remain a considerable source of uncertainty. Figure reproduced from Schaye et al. (2015).

erally aim to represent macroscopic galaxy formation and evolution processes as systems of differential equations that balance inflows, outflows, sources and sinks. Model parameters, such as those associated with feedback, are typically calibrated to reproduce a target observable or set of observables. While simple, SAMs can elucidate how important different modelled physical processes (such as feedback mechanisms) may be, by parametrising them and comparing the resultant galaxy populations with observations (e.g. Bower et al., 2006; Henriques et al., 2014; Lacey et al., 2016). SAMs have a considerable advantage in their low computational cost and flexibility; model variations and parameter space can be extensively explored using both reasoned trial-and-error and formalised MCMC methods (see Somerville & Davé, 2015, for a comprehensive review of the SAM approach). However, SAMs and other serial approaches are limited by the lack of insight they can provide into the baryon dynamics, and do not account for any back reaction by baryons on the dark component.

The 'parallel' approach, where baryons and the dark sector are modelled to evolve simultaneously, is commonly realised by hydrodynamical simulations. The more detailed physical modelling of hydro simulations may lead to processes emerging naturally that are approximated or missed by SAMs, but this advantage comes at great computational expense. Modes of gas accretion on to galaxies, ram pressure stripping of satellites falling into larger halos and the complex evolution of merging systems are among the processes that hydrodynamical simulations can aim to follow in detail.

While hydrodynamical simulations of galaxies may resolve internal galaxy structure and gas dynamics that SAMs do not, the scales at which SNæ and SMBHs inject energy remain far from reach. These simulations are thus unable to compute the net efficiency of the resulting feedback *a priori*. Simulations therefore need to rely on a phenomenological description of crucial processes occurring on unresolved ('subgrid') scales, using observations to calibrate the parameters that appear in the subgrid modules. It is then important to quantify the uniqueness and degeneracies in such modelling (Schaye et al., 2010, 2015; Crain et al., 2015), while at the same time using very high-resolution simulations (e.g. Hopkins et al.,

2011; Creasey et al., 2013, 2015; Martizzi et al., 2014; Rosdahl et al., 2015) to try and bridge the gap between numerically unresolved and resolved scales.

Hydrodynamical simulations of the cosmos have been performed for over 35 years (e.g. Efstathiou & Eastwood, 1981), and long struggled to match observables at the level of contemporary SAMs when calibrated (e.g. Katz et al., 1996; Benson et al., 2003; Crain et al., 2009). Cosmological simulations including hydrodynamics have by now matured to such an extent that they show good agreement between simulated and observed galaxies for a wide range of properties (e.g. Vogelsberger et al., 2014; Murante et al., 2015; Schaye et al., 2015; Davé et al., 2016). This maturation can be ascribed to a more nuanced understanding of the behaviour of subgrid models, particularly that feedback from forming stars and accreting black holes are implemented in such a way that they act very efficiently. Improvements in the hydrodynamics scheme have also helped to push the simulations forward (Springel, 2005, 2010; Hopkins, 2015; Schaller et al., 2015b).

With the details of the subgrid modelling proving crucial to reproduce realistic galaxy populations, their role and calibration must be carefully considered. For some subgrid models, the calibration is relatively direct; star formation rates can be related to local gas properties and calibrated to reproduce the empirical Kennicutt (1998b) relation (e.g. Schaye & Dalla Vecchia, 2008), and gas cooling rates may be parametrised for a large range of physical conditions using photoionisation codes such as CLOUDY (Ferland et al., 1998). The correct choice of subgrid modelling and parametrisation of feedback is more ambiguous, with a diversity of different approaches having developed. Feedback energy may be injected in a number of ways, and vary with local properties and redshift (see Rosdahl et al., 2017, for a comparison of implementations for SNæ). Mechanisms other than stellar and AGN feedback, such as cosmic rays and radiation pressure, may also play a role. Feedback implementations differ in philosophy; ranging from heuristic approaches that relate feedback to indirect proxies such as halo mass (e.g. Gabor & Davé, 2012) to those that aim for a more physical model despite the lack of resolution (e.g. Sijacki et al., 2007). Generally, all these feedback models have free parameters that are used to calibrate global galaxy distributions

or scaling relations (see section 1.1), and thus limit some of the predictive power of simulations. As the choice of feedback implementation can be decisive for the evolution of simulated galaxies (e.g. Scannapieco et al., 2012), subgrid modelling remains an important area of uncertainty in hydrodynamical simulations.

While hydrodynamical simulations are subject to many challenges, they can provide unique insight into galaxy evolution. How relationships between galaxy properties (and the associated scatter) emerge in simulations is particularly informative, with the caveat that certain galaxy properties are calibrated. The following section broaches the subject of exactly how we can compare simulated galaxies back to observations.

1.4 Inverse and Forward Modelling

While recent cosmological simulations claim a number of successes, comparison to data is relatively indirect due to simulations predicting physical properties (such as galaxy stellar mass or star formation rate) that are not directly observable. Any comparison between simulations and data then relies on a translation between the physical and observable domains. This may be achieved by either deriving physical properties from observations for direct comparison to theory, *inverse modelling*, or predicting observables from theory to compare directly with data, *forward modelling*.

There are common assumptions shared by both of these approaches. The stellar initial mass function (IMF) is one such assumption, representing the fraction of stars born at a given mass. As main sequence stellar temperatures are primarily determined by their masses, the form of the IMF has strong implications for the mass to light ratio in different bands. Unfortunately, the IMF cannot currently be predicted with reliability from first principles in galaxy-scale simulations, nor can it be observed directly in external galaxies. A form for the IMF was first derived empirically by Salpeter (1955) from the luminosities of Milky Way (MW) stars, and extrapolating the power law he derived for $\log_{10}(M_{\rm star}/{\rm M}_{\odot})$ in the range [-0.4,1] is often termed the *Salpeter* IMF. Subsequently, a reduction in the number of

low mass stars was favoured in MW observations, resulting in segmented power law (Kroupa IMF, Kroupa et al., 1993) or log-normal (Chabrier IMF, Chabrier, 2003) parametrisations. It is common to assume one such form for the IMF as universal when modelling or interpreting galaxy observations, but the validity of this assumption remains a topic of vigorous debate (see e.g. Bastian et al., 2010, for a contemporary review). The effects of IMF variation are not directly explored in this thesis.

It is also necessary to model how populations of stars evolve in order to relate stellar formation and enrichment histories to the light we observe. This evolution is encapsulated by *stellar population synthesis* (SPS) models which provide spectra for *simple stellar populations*; parametrised by a single starburst age, metallicity and initial stellar mass. These spectra can then be superposed to create composite populations of differing age and metallicity. Notable differences exist between SPS models in the coverage of parameter space, the evolutionary tracks of stars through temperature-luminosity diagram, and the treatment of certain stellar phases and binaries. For stellar phases in particular, representation of thermally-pulsing asymptotic giant branch (TP-AGB) stars prove a decisive difference between some SPS models, exemplified by a comparison between the Bruzual & Charlot (2003) and Maraston (2005) models. While the TP-AGB treatment is relatively unimportant for optical bands and evolved populations, it may drive differences in the NIR for intermediate-age stellar populations. Conroy et al. (2009) provide SPS models where the IMF and contribution of certain stellar phases can be varied, recognising their uncertainty. Again, SPS model variation is not directly explored in this work. The choice of SPS model is discussed further in chapter 3.

1.4.1 Inverse modelling of physical properties

'Inverse modelling' of physical properties from observed fluxes of real galaxies has lead theory for decades, constraining galaxy formation physics. This approach allows distributions of observables, such as those detailed in section 1.1, to be converted to their physical analogues. Stellar masses are often derived from

photometry given an assumed IMF and SPS model, alongside assumed templates for the star formation, enrichment histories and dust effects. This is exemplified by the analysis Li & White (2009) applied to the 7th data release (Abazajian et al., 2009a) of SDSS(York et al. 2000), or the analysis by Baldry et al. (2012) applied to the Galaxy And Mass Assembly (GAMA, Driver et al. 2009) survey. Of course, such analysis makes necessarily bold simplifications, for example assuming exponential star formation histories, uniform stellar metallicities and a screen model for dust. Mitchell et al. (2013) demonstrated how this methodology suffers from degeneracy between the star formation history, metallicity and dust properties of galaxies using SAMs.

Modelling is also needed to infer star formation rates or passive fractions. The strength of the Hα recombination line is sensitive to recent star formation, as it probes UV-continuum emission from stars that are $\lesssim$10 Myr old (Kennicutt, 1998a). However, a significant fraction of the Hα flux in star forming galaxies is emitted by dusty HII regions (e.g. Zurita et al., 2000), and therefore the conversion from flux to star formation rate requires a model to account for obscuration (e.g. James et al., 2004; Best et al., 2013; Gunawardhana et al., 2013). Similarly, the continuum strength on either side of the 4000Å break, depends on the relative contribution to the flux of old versus younger stars, and hence is a useful proxy for the specific star formation rate of a galaxy (e.g. Kauffmann et al., 2003a; Balogh et al., 1999). However, the amplitude of the break may also be affected by dust, and hence the inferred passive fraction depends on the assumed dust properties.

Full spectroscopic data may provide more power to constrain the underlying physical properties of galaxies. In particular, detailed spectroscopy can be used to infer non-parametric star formation histories with many more associated free parameters than exponential models. This *fossil record* analysis allows the fraction of stellar populations in separate bins of age and metallicity to be individually constrained. Heavens et al. (2004) used the fossil record method to determine star formation histories for $\sim 10^5$ galaxies in the SDSS sample at $z \sim 0.1$, and showed that the recovered evolution in cosmic star formation rate density is consistent with the instantaneous star formation rates measured using multiple tracers ob-

served at various redshifts. This remarkable result demonstrates the power of the technique. Despite this, the availiability of good quality spectra and degeneracies between age, metallicity and dust content still limits the insight fossil record analysis can provide for individual galaxies.

Degeneracies between the dust and stellar content of galaxies that arise in inverse modelling of optical data may be alleviated to some extent by appealing to FIR observations. Stellar light emitted at UV-optical wavelengths is absorbed by interstellar dust in galaxies and then re-emitted to dominate the IR portion of the rest-frame SED. While the FIR hump can be used to constrain the dust mass and the amount of absorption in galaxies, panchromatic data is limited to a relatively small samples of galaxies. There are also ambiguities associated with the shape of attenuation curves, dust temperatures and outstanding problems with the dust-energy balance in spiral galaxies (e.g Baes et al., 2010) that make parameter estimation difficult.

One insight that inverse modelling provides is how different the fractional contributions of mass and light appear to be for different baryonic components. Approximately half of the radiation measured from galaxies comes directly from stars, with $\sim 45\%$ coming from starlight that is absorbed by dust and re-radiated in the FIR (e.g. Finke et al., 2010). Despite their dominance of the light budget, stars contribute a mere 3.5% of the local baryon density (Li & White, 2009) and the contribution of dust mass is negligible. By comparison, atomic and molecular gas in local galaxies contribute $\sim 2\%$ of the local baryon density, and ionised gas, primarily outside of galaxies, comprises the remaining $\sim 95\%$ of baryons at the present day (Fukugita et al., 1998). Despite making a marginal contribution to the overall baryon mass budget, accreting black holes also make a non-negligible contribution to the cosmic luminosity density over the history of the universe (Hopkins et al., 2007). Appreciating the difference between the mass and light contributions of different components gives some indication of the intrinsic difficulty in comparing observations to physical models, and why we might also appeal to a *forward modelling* approach for further insight.

1.4.2 Forward modelling of observables

In addition to inverse modelling, it should be possible to apply the ingredients of the inverse models to the simulated galaxies instead, and compare mock *fluxes* to the observations. Such 'forward models' have many potential advantages. For example, the star formation histories of simulated galaxies are more detailed and diverse than the parametric models often used in inverse modelling. Similarly, the simulated - and presumably also the observed stars in any galaxy - have a considerable spread in metallicity, rather than a single uniform value. These assumed priors may introduce biases in the inferred properties of galaxies (see e.g. chapter 4). Notwithstanding any practical considerations, surely the ultimate aim of simulations should be to predict observables.

Detailed forward modelling analyses are common in large-scale SAMs (González et al., 2009; Henriques et al., 2014; Cowley et al., 2015), but appear less prevalent for hydrodynamical simulations of large cosmological volumes. This could be attributable to the more detailed and complex properties of hydrodynamically simulated galaxies, and their historical inability to reproduce salient galaxy properties simultaneously for the overall galaxy population. However, pioneering work has been carried out where hydrodynamical simulations of single isolated and merging galaxies are subject to detailed forward modelling (e.g. Wuyts et al., 2009a,b; Jonsson et al., 2009; Hayward & Smith, 2015; Feldmann et al., 2016), providing insights into the conversion between physical and observable properties. The latest generation of large-volume hydrodynamical simulations are promising from a forward modelling perspective. Model observables have been produced and analysed for the contemporary simulation suites of ILLUSTRIS (Torrey et al., 2015), MUFASA (Davé et al., 2017), and EAGLE. The primary analyses of EAGLE comprises the studies consolidated into this thesis.

In practice there are still formidable challenges associated with forward modelling, and inverse and forward modelling approaches are largely complementary. Inverse modelling is useful to assess how distinct physical quantities may contribute to observables and elucidate discrepancies between real and mock observations, while insights gained from a forward modelling approach can inform

and improve our inverse models. For instance, generating mock galaxy observations with attenuation and re-emission by dust can be used to demonstrate how numerous degeneracies in SED inversion can be lifted by incorporating FIR observations (e.g. Hayward & Smith, 2015). A forward modelling approach is adopted and explored throughout the following chapters.

1.5 Thesis outline

In this thesis I focus on the forward modelling of hydrodynamically simulated galaxies, and what can be learned from this analysis. In particular, I develop panchromatic models for galaxies taken from the EAGLE simulations (Schaye et al., 2015; Crain et al., 2015), applying different approaches for modelling dust. I then explore optical to NIR properties of EAGLE galaxies and use them to assess how well physical properties can be derived for galaxies given common assumptions.

In chapter 2 I first provide a short review of the simulations relevant to our modelling, and some of the modelling techniques I employ. The presentation of my own research begins in chapter 3, in which I focus on the optical properties of EAGLE galaxies at low redshift, particularly colour distributions and luminosity functions, and develop a simple screen model to account for dust attenuation at $z = 0.1$. Chapter 4 then looks at the evolution of intrinsic optical properties of EAGLE galaxies, particularly the colour-mass relation, and the mechanisms that drive the build up of the distinct red sequence and green valley populations. In Chapter 5, I adopt a more physical radiative transfer approach for modelling the dust and explore the effects that dust has on the optical properties of EAGLE galaxies. I use this to assess how simplistic assumptions about dust reddening may introduce systematics in SED inversion and proxies for star formation activity. In chapter 6 I then conduct a focused study of fitting EAGLE SEDs, and comparing the fitted parameters back to their input values, to investigate how well commonly adopted techniques can recover galaxy star formation rates and stellar masses. The final chapter discusses overarching conclusions from this work, and

the future projects that may emerge from it. Additional information and figures supporting the main chapters are provided in the Appendices.

Chapter 2

The EAGLE Simulations and Comparison Data

The *Evolution and Assembly of GaLaxies and their Environments* (EAGLE) project is a suite of hydrodynamical simulations that follow the formation and evolution of cosmic structure and galaxies in cosmologically representative cubic volumes, and were completed in January 2014. EAGLE is a unique resource, reproducing a number of calibrated and uncalibrated properties of the observed population to unprecedented accuracy for a large sample of hydrodynamically simulated galaxies (detailed below). EAGLE is the simulation analysed exclusively in this thesis. Full details of the EAGLE simulations can be found in Schaye et al. (2015) and Crain et al. (2015) (hereafter S15 and C15 respectively); here I provide only a brief review of the aspects of EAGLE most relevant to the collaborative and independent studies presented in this thesis. I also describe the standard analysis tools we use to identify structures in EAGLE, as well as the observational data used for comparison in chapters 3-5. The aim of this chapter is to provide a sufficient grounding on the common EAGLE simulations and datasets employed in the later chapters of this thesis.

Table 2.1: Numerical parameters of the simulations of the EAGLE suite that are used in this thesis. From left to right: simulation identifier, side length of cubic volume L in co-moving Mpc (cMpc), initial mass $m_{\rm g}$ of baryonic particles, Plummer equivalent gravitational softening $\epsilon_{\rm prop}$ at redshift $z = 0$ in pkpc, where I use 'pkpc' to denote proper kiloparsecs.

Name	L	$m_{\rm g}$	$\epsilon_{\rm prop}$
	cMpc	$\rm M_\odot$	pkpc
Ref-L025N0376 (Ref-25)	25	1.81×10^6	0.70
Ref-L025N0756 (RefHi-25)	25	2.26×10^6	0.35
Recal-L025N0752 (Recal-25)	25	2.26×10^5	0.35
Ref-L100N1504 (Ref-100)	100	1.81×10^6	0.70

2.1 The EAGLE simulations

The cubic EAGLE volumes are treated as periodic, and the evolution of structure within them is simulated using a modified version of the GADGET-3 TreeSPH code (which is an update of the GADGET-2 code last described by Springel et al. 2005a). Simulations were performed for a range of volumes and numerical resolutions. We concentrate on the 'reference' model in what follows, but also use simulations with different resolutions and model calibration to assess convergence properties. The free parameters that enter the feedback modules for the reference model were calibrated using the redshift $z = 0.1$ galaxy stellar mass function, the $z = 0.1$ stellar mass-size relation, and the $z = 0$ stellar mass - black hole mass relation (see Crain et al. 2015 for motivation and details).

In this thesis, We make use of volumes L100N1504, L025N0376 and L025N0752 from table 2, and Recal from Table 3 of S15. In Table 2.1, and throughout, I refer to these simulations as Ref-100, Ref-25, RefHi-25 and Recal-25 respectively. The EAGLE suite assumes a ΛCDM cosmology with parameters derived from the initial *Planck* (Planck Collaboration et al., 2014) satellite data release ($\Omega_{\rm b} = 0.0482$, $\Omega_{\rm dark} = 0.2588$, $\Omega_\Lambda = 0.693$ and $h = 0.6777$, where $H_0 = 100\ h$ km s^{-1} Mpc^{-1}).

Some simulation details are also listed in Table 2.1, and the $z = 0.1$ galaxy stellar mass functions that emerge in the Ref-100 and Recal-25 volumes are shown for reference in Fig. 2.1.

I focus primarily on the Ref-100 simulation volume. The 100^3 Mpc^3 volume and mass resolution of $1.2\times10^6\mathrm{M}_\odot$ in gas for Ref-100 provides a sample of ∼30,000 galaxies resolved by $>$ 1000 star particles at redshift $z = 0.1$, with ∼3000 galaxies resolved by $>$ 10,000 star particles. In addition to this primary sample of galaxies, we also use the higher-resolution RefHi-25 and Recal-25 simulations to test the level of 'strong' and 'weak' convergence. These concepts are coined by S15 and discussed fully therein; in essence, *strong convergence* refers to how well simulated properties agree when only resolution is changed and *weak convergence* refers to the level of agreement between resolutions when feedback parameters are allowed to be recalibrated. While strong convergence represents the popular definition of *convergence*, weak convergence acknowledges that the feedback modules represent processes that are far from resolved, and that the efficiency of feedback and cooling in the implemented models are explicitly tied to resolution. In this way, strong convergence tests convergence properties for a certain parametrisation of a given feedback model, whereas weak convergence is more a test of the model implementation itself.

The RefHi-25 and Recal-25 volumes have a factor 2 (2^3) superior spatial (mass) resolution than Ref-100. As RefHi-25 uses the same fiducial model at high resolution (with the same initial phases and amplitudes of the Gaussian field), it may be used to test the strong convergence of galaxy properties. The feedback efficiencies adopted by Recal-25 were recalibrated to provide better agreement with the $z = 0.1$ galaxy stellar mass function at high resolution and to test the weak convergence (see also C15). In addition, the Ref-25 simulation can be compared to Ref-100 to isolate volume effects; differences caused by the inability of smaller volumes to capture large scale power in the density distribution and to form the most massive halos.

The initial conditions of all EAGLE simulations were generated appropriately for a starting redshift of $z = 127$ using an initial perturbation field generated with

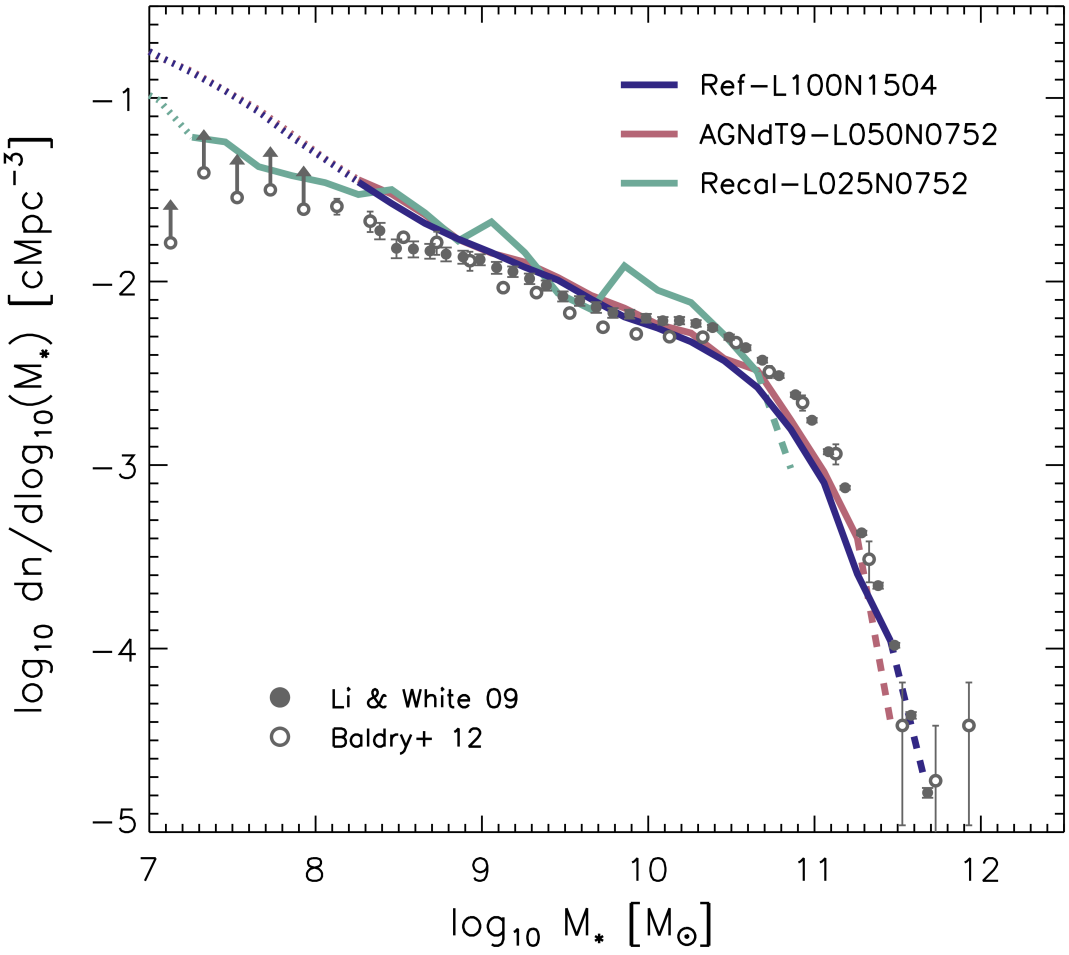

Figure 2.1: Galaxy stellar mass functions for the Ref-100 and Recal-25 EAGLE volumes at $z = 0.1$. The comoving number density of galaxies per dex in stellar mass is potted as a function of $\log_{10}(M_\star/\mathrm{M}_\odot)$, using dashed lines to indicate when the number of simulated galaxies in a bin falls below 10 and dotted lines to show the regime where resolution effects are deemed important. For comparison, the mass functions of Li & White (2009) and Baldry et al. (2012) (derived from observations) are also plotted. For galaxy stellar masses well represented (in terms of number and resolution) by EAGLE, the mass function generally reproduces the observations well. However, a consistent ~ 0.2 dex underprediction of the observed number density is noted around the 'knee'. Figure reproduced from (Schaye et al., 2015), refer to their text for details.

the PANPHASIA code described by Jenkins & Booth (2013). Smoothed particle hydrodynamics (SPH) is implemented as in Springel et al. (2005a), but using the pressure-entropy formulation of Hopkins (2013), including artificial conduction and viscosity (Dehnen & Aly, 2012), a time-step limiter (Durier & Dalla Vecchia, 2012), and the C2 kernel of Wendland (1995). These modifications to the standard GADGET-3 implementation are collectively termed as ANARCHY (Dalla-Vecchia, in prep., summarised in Appendix A of S15). Schaller et al. (2015a) show that these ANARCHY modifications are important in the largest EAGLE halos, but have minimal effect on galaxies of stellar mass $M_\star \lesssim 10^{11}\mathrm{M}_\odot$. To represent important astrophysical processes acting on scales below the resolution of EAGLE, a number of subgrid modules are also employed in the code. Relevant modules include schemes for star formation, enrichment and mass loss by stars, photo-heating, radiative cooling and thermal feedback associated with accreting black holes and the formation of stars, as described below.

A crucial aspect of EAGLE is that the parameters describing the subgrid modules have been calibrated on the observed $z \sim 0.1$ GSMF and galaxy sizes. This good agreement extends to many other observables that were not considered during the calibration, such as specific star formation rates (S15), the evolution of the GSMF (Furlong et al., 2015), molecular hydrogen fractions (Lagos et al., 2015b), and absorption by intergalactic metals and neutral hydrogen (S15, Rahmati et al., 2015).

2.1.1 Subgrid Modules

Star formation is treated stochastically in EAGLE. Star formation rates (SFRs) are calculated for individual gas particles using a pressure-dependent formulation of the empirical Kennicutt-Schmidt law (Kennicutt, 1998a; Schaye & Dalla Vecchia, 2008), with a metallicity-dependent density threshold below which star formation rates are zero (Schaye, 2004). Gas particles therefore may have some probability of being wholly converted into a star particle at each time step, inheriting the initial element abundances of their parent particle. The gravitational softening scales listed in Table 2.1 provide a practical limit on spatial resolution. Cold,

dense gas ($T < 10^4$ K, $n_H > 0.1$ cm^{-3}) with Jeans lengths below these scales is thus unresolved, and any corresponding gas would artificially fragment in the simulation. To ensure that the Jeans mass of gas is always resolved (albeit marginally), a pressure floor is enforced via a single-phase polytropic equation of state, $P_{\rm EoS} \propto \rho^{\gamma_{\rm EoS}}$, maintaining ISM gas at $T \gtrsim 10^4$ K,.

Once formed, star particles are treated as coeval simple stellar populations (SSPs), assuming a universal Chabrier (2003) stellar initial mass function (IMF) over the mass range [0.1,100] $M_\odot$. It is assumed that all the stars represented by the SSP inherit the metallicity of the converted gas particle, with a single age corresponding to the expansion factor at which the gas particle was converted. These SSPs lose mass and enrich neighbouring gas particles according to the prescription of Wiersma et al. (2009b), accounting for type Ia and type II supernovae and winds from massive and AGB stars. Eleven individual elements (H, He, C, N, O, Ne, Mg, Si, S, Ca, and Fe) are followed, as well as a 'total' metallicity (the mass fraction in elements more massive than He), Z.

Two types of abundances are tracked for the gas in EAGLE, a *particle abundance* that is changed through direct enrichment by star particles and a *smoothed abundance* that smooths particle abundances between neighbours using the SPH kernel (see Wiersma et al., 2009b). Diffusion is not implemented in the simulation, therefore no metals are exchanged between gas particles. This may occasionally lead to individual particles exhibiting extreme values as well as large variations in metallicity, even for close neighbours. Although the SPH smoothing is not strictly representative of metal diffusion, it does mitigate extreme values and reduces stochasticity in the metal distribution. For this reason we adopt the *smoothed metallicities* throughout this thesis, which were also used to compute cooling rates and nucleosynthetic yields during the simulation.

The energy that stellar populations inject into the inter-stellar medium (ISM) through supernovae, stellar winds and radiation is collectively termed *stellar feedback*. Stellar feedback is implemented per star particle (and is separate from enrichment) using the thermal feedback scheme described by Dalla Vecchia & Schaye (2012). This implementation sets a temperature change $\Delta T_{\rm SF}$, the temper-

ature by which stochastically sampled gas particle neighbours of stars are heated. The value of $\Delta T_{\rm SF} = 10^{7.5}$K is chosen for the reference model; this is high enough to mitigate catastrophic numerical losses, while low enough to prevent the probability of heating for neighbouring gas particles, $p_{\rm SF}$, from becoming small and leading to poor sampling (see S15). The p_{SF} value depends on both $\Delta T_{\rm SF}$ and the fraction of energy that couples to heat the ISM. The latter fraction is allowed to vary with local gas properties and is calibrated to reproduce observed local galaxy sizes, as detailed by C15.

Black holes are seeded in halos with mass exceeding $10^{10}h^{-1}{\rm M}_{\odot}$ following Springel et al. (2005a). The most-bound gas particle is then converted to a black hole particle with a subgrid mass of $10^{5}h^{-1}{\rm M}_{\odot}$, and is systematically moved to the position of the most bound neighbouring particle of its host halo at each timestep while its mass is below $100m_{\rm g}$. The black hole grows in mass by subgrid Eddington-limited accretion of gas, while accounting for the gas angular momentum as detailed in S15 and Rosas-Guevara et al. (2015). Black holes may also grow by merging with each other, following Springel (2005) and Booth & Schaye (2009). A fixed 1.5% of the rest-mass energy in accreted material provides the energy budget for black hole feedback. This is implemented using a similar stochastic scheme as used for injecting stellar feedback, but with a higher heating temperature ($\Delta T_{\rm BH} = 10^{8.5}$K for the reference models, and 10^{9}K for Recal-25). Note that the AGN feedback in EAGLE is single mode, as opposed to a popular approach of implementing distinct quasar and radio modes with different behaviours (e.g. Bower et al., 2006; Sijacki et al., 2007)

Photo-heating and radiative cooling are also implemented; this follows the prescription method of Wiersma et al. (2009a), based on the 11 elements traced. This model assumes that gas is optically thin and in photo-ionisation equilibrium with the cosmic UV+X-ray background as calculated by Haardt & Madau (2001).

2.1.2 Structure Finding

Dark matter halos are identified using the 'friends-of-friends' algorithm (FOF, Davis et al. 1985). A length of 0.2 times the mean inter-particle separation (Lacey

& Cole, 1994) is used to link particles in regions that are overdense by a factor of ~ 200 into FOF halos. Other particles are assigned to the same halo (if any) as the nearest dark matter particle. The mass of the halo is characterised by its $M_{200,\mathrm{crit}}$ value. This is the mass enclosed within a sphere of radius $R_{200,\mathrm{crit}}$ centred on the location of the particle with minimum gravitational potential in the halo. The radius is chosen such that the mean density within this sphere is 200 times the critical density, given the assumed cosmology. *Subhalos* are identified with the SUBFIND algorithm (Springel et al., 2001; Dolag et al., 2009).

SUBFIND identifies self-bound substructures within halos which are associated with galaxies. The 'central' galaxy is the galaxy closest to the centre of the parent FOF halo; this is nearly always also the most massive galaxy in that halo. The other galaxies in the same halo are its satellites. Particles in a halo not associated with a bound substructure (*i.e.* satellites) are assigned to the central galaxy. Central massive galaxies ($M_\star \geq 10^{11}$ $\mathrm{M}_\odot$, say) then have an extended halo of stars around them, usually referred to as intra-group or intra-cluster light. Determining the mass or indeed luminosity of such a large galaxy is ambiguous, both in simulations and in observations. For this reason an aperture is imposed on the definition of a galaxy: I follow Schaye et al. (2015) and calculate masses and luminosities for every subhalo, excluding material that is outside a 30 pkpc spherical aperture centred on the subhalo potential minima as well as material that is not bound to that subhalo. The 30 pkpc aperture has been shown to mimic an observational Petrosian aperture, and reduces intra-cluster light in massive centrals while lower mass galaxies are unaffected (Schaye et al., 2015). This aperture definition of galaxies is used throughout this thesis for consistency, and the choice of aperture is discussed further in chapters 3 and 5.

Merger trees are constructed to link halos and subhalos identified in different snapshots by Qu et al. (2017), enabling individual structures to be followed through time. This provides the basis for the EAGLE database described by McAlpine et al. (2016)[1]; the database uses an SQL interface to simplify structure selection

[1] `http://icc.dur.1ac.uk/Eagle/database.php`

and merger tree traversal, such that the evolution of integrated halo and subhalo properties (calculated from snapshot outputs) may be tracked easily. Chapter 4 exemplifies a study that uses the EAGLE database to follow the evolution of galaxies on an individual basis.

2.1.3 GAMA and SDSS survey data

Appropriate observational data sets are needed for comparison to the observable quantities modelled for EAGLE galaxies in the following chapters. Here I very briefly describe the data sets that are chosen for comparison.

The Galaxy and Mass Assembly (GAMA) survey (Driver et al., 2009; Robotham et al., 2010; Driver et al., 2011) is a spectroscopic and photometric survey of 5 independent sky fields, undertaken at the Anglo-Australian Telescope, and using the 2dF/AAOmega spectrograph system. The 3 equatorial fields we consider follow up targets from the Sloan Digital Sky Survey (SDSS) Data Release 7 (DR7) (York et al., 2000; Abazajian et al., 2009a) and the *UK Infrared Digital Sky Survey* (UKIDSS), yielding a sample of $\sim 190,000$ galaxies with SDSS $ugriz$ and UKIDSS $YJHK$ photometry (Hill et al., 2011; Taylor et al., 2011) and spectra covering the wavelength range 3700Å to 8900Å, with a resolution of 3.2Å (Sharp et al., 2006; Driver et al., 2011). Details are provided on the targeting and star-galaxy separation in Baldry et al. (2010) and on the GAMA-processed photometry, including matched aperture photometry from u to K in Hill et al. (2011).

The GAMA survey strategy provides high spectroscopic completeness (Robotham et al., 2010) and accurate redshift determination (using AUTOz; Baldry et al., 2014) for galaxies, above an extinction-corrected r-band Petrosian magnitude limit of 19.8. The galaxy stellar mass estimates and rest frame photometry for the GAMA sample used in chapters 3 and 5 are taken from Taylor et al. (2015). The high completeness and accurate redshifts of GAMA, which is volume limited and has precisely known redshifts, is well suited for comparison with EAGLE.

Emission line indices in GAMA were measured assuming single Gaussian profiles, a common redshift for adjacent lines, and a stellar continuum correction simultaneously fit to each spectrum around the measured lines, as described by

Hopkins et al. (2003) and Gunawardhana et al. (2013, 2015). Emission line fluxes are corrected for stellar absorption as described by Hopkins et al. (2003). Dust corrections are obtained using the stellar absorption corrected Balmer emission line flux ratios, also described by Hopkins et al. (2003). The uncertainties associated with correcting Balmer lines for stellar absorption are discussed in both Hopkins et al. (2003) and Gunawardhana et al. (2013).

Derived Hα luminosities and star formation rates are taken from Gunawardhana et al. (2013). Their emission line galaxies (ELGs) are initially selected to have Hα fluxes above the detection limit of 25×10^{-20} Wm^{-2} and a signal-to-noise ratio of > 3, with active galactic nuclei (AGN) identified and removed using standard [NII]λ6584Å/Hα and [OIII]λ5007Å/Hβ diagnostics (Baldwin et al., 1981). The GAMA sample is supplemented with SDSS galaxies with detected Hα emission and signal-to-noise >3 from the MPA-JHU catalogue[2], as the brightest ELGs observed by SDSS were not re-observed by GAMA.

Measurements of the 4000Å break (D4000) are also used in this thesis. For this, we compare to values measured directly from the SDSS DR7 data (Strauss et al., 2002; Abazajian et al., 2009a). We compare a stellar mass-matched sample of EAGLE galaxies to the publicly available SDSS D4000 values measured for the MPA-JHU[1] catalogue using the code of Tremonti et al. (2004), with the index defined as in Bruzual (1983). For SDSS data, we use the mass estimates of Kauffmann et al. (2003a).

[2]http://www.mpa.mpa-garching.mpg.de/SDSS/DR7/

Chapter 3

EAGLE Photometry

This chapter comprises an edited version of the article: **Colours and luminosities of z=0.1 galaxies in the EAGLE simulation**, *James W. Trayford, Tom Theuns, Richard G. Bower, Joop Schaye, Michelle Furlong, Matthieu Schaller, Carlos S. Frenk, Robert A. Crain, Claudio Dalla Vecchia, Ian G. McCarthy* published in *MNRAS* Sep. 2015, vol. 452 p. 2879, with appendices compiled in Appendix A.

3.1 Introduction

As described in chapter 2, the subgrid physics modules of the EAGLE simulation suite (Schaye et al., 2015; Crain et al., 2015) are primarily calibrated using the $z \sim 0.1$ Galaxy Stellar Mass Function (GSMF). The GSMF is not directly observable, rather it is inferred from inverse modelling of observations (see chapter 1). This requires corrections for distance, redshift and dust obscuration, and the use of stellar population synthesis (SPS) models that involve assumptions about stellar evolution, star formation histories, metallicity dependence of stellar emission, etc. With simulations such as EAGLE, we can take a converse forward modelling approach, attempting to reproduce the observational relations by inputting physical quantities tracked by the simulation. This has the advantage of allowing one to use properties modelled self-consistently such as gas content, metallicity and age to derive observable quantities, rather than treating them as free parameters in 'SED fitting' (e.g. Walcher et al., 2011) to estimate physical properties from ob-

servations. The colours of EAGLE galaxies are also an important test of the realism of the fiducial EAGLE model.

In this chapter we examine to what extent mock luminosities computed from EAGLE galaxies using SSP models and a simple correction for dust obscuration reproduce the observed luminosity functions (in a range of broad bands), as well as galaxy colours. The aim is twofold: to provide a test of the realism of EAGLE, but also to test at some level whether the procedure of going from luminosity to stellar mass is reliable, also investigated by Torrey et al. (2014) using SED fitting of galaxies from the ILLUSTRIS simulation (Vogelsberger et al., 2014). It is perfectly possible that EAGLE galaxies have the wrong colours but the right stellar masses and stellar ages if errors in dust modelling are severe. However, if masses *and* colours agree with the data, then this increases the confidence that EAGLE is useful to investigate, for example, the origin of the observed bimodality of galaxy colours, or the nature of the galaxies that lie in between the red sequence and blue cloud in a colour-magnitude diagram. These topics in particular are explored in chapter 4.

The chapter is organised as follows. In §3.2 we detail the development of our photometric model, concentrating on emission and absorption in §3.2.1 & §3.2.2 respectively. This model is applied to yield an optical colour-magnitude diagram (CMD) and multi-band luminosity functions (LFs) for galaxies, which are plotted and discussed in §3.3. We discuss our findings in §3.4 and summarise in §3.5.

3.2 Photometry

Here we compute luminosities and colours for the simulated EAGLE galaxies. We begin by modelling luminosities of star particles, taking into account their ages and metallicities using population synthesis (section 3.2.1), the photometric system used to calculate magnitudes for direct comparison to observation (section 3.2.1.3), and the effects of dust absorption (section 3.2.2). The results of this section are summarised in Fig. 3.1, in which we plot histograms of $g-r$ colours of EAGLE galaxies in narrow stellar mass bins for different models, ranging from

a simple emission model without dust, to a model including a multivariate treatment for dust.

3.2.1 Source Modelling

We compute luminosities of EAGLE galaxies from the ultraviolet (UV) to the near infrared (NIR). We limit this modelling to stellar emission, neglecting both nebular emission lines and light from AGN. Light absorbed by dust is assumed to be re-emitted in the far infrared which we do not study in this chapter. As we also neglect scattering by dust, we treat individual wavelength bands independently. This approximation is supported by observations showing that scattering is a negligible contributor to the observed attenuation curve in galaxies (eg. Fischera et al., 2003).

Population synthesis models provide spectra for a discrete range of *simple stellar populations* (SSPs) (e.g. Bruzual & Charlot, 2003; Maraston, 2005; Leitherer et al., 1999). These SSPs represent populations of stars characterised by their total initial mass, formation time, and composition while assuming some stellar IMF. By decomposing the stellar component of an observed galaxy into a superposition of SSPs, the spectral energy distribution of an entire galaxy can be approximated. In EAGLE, we treat each star particle as an SSP with given initial stellar mass, metallicity and age. These values are set and held fixed from the instant a star particle is formed, where the star particle inherits the gas particle mass and metallicity at the time of formation. The parametrisation of the SSP models are elaborated further below.

3.2.1.1 SSP Ingredients

Given the implementation of star formation, where gas particles are wholly converted into star particles, the typical mass of an EAGLE star particle is $\sim 10^6 \mathrm{M}_\odot$. Stars are assumed to form with a Chabrier (2003) IMF (for consistency with the evolutionary models used in EAGLE), and they inherit the SPH-smoothed metallicity, Z, from their parent gas particle. The mass of a newly formed star particle

is purely set by numerical resolution; the particle should not be thought of as representing a star cluster. In fact, 10^6 $\mathrm{M}_\odot$ is higher than the stellar mass formed in giant HII regions (e.g. Relaño & Kennicutt, 2009; Zaragoza-Cardiel et al., 2014). This poor sampling of star formation has the potential to adversely affect luminosities of EAGLE galaxies. Indeed, a single recently formed star particle can affect the colour of a galaxy. We try to mitigate this numerical artefact by employing a finer sampling of the star formation history of recently formed stars. We do this by assuming that the star formation rate of gas particles is constant over the past 100 Myr, and randomly spawning star particles of mass 10^4 $\mathrm{M}_\odot$, that on average represent this constant star formation rate. We do the same for recently formed star particles (age $<$ 100 Myr), using the star formation rate of the progenitor gas particle at the time of birth. We note that this typically has only a small effect for optical colours and thus for the results presented here.

The metallicity of stars affects their colours resulting in the well-known *age-metallicity* degeneracy (e.g. Worthey, 1994). In addition, Z affects stellar evolution leading to differences between models, particularly for the AGB phase (e.g Inoue, 2012; Stancliffe & Jeffery, 2007). In addition, the metallicity of stars in EAGLE galaxies is set by the intricate interaction between enrichment of the ISM, gas accretion, and the extent to which galactic winds transport metals into the galaxy's circum- and intergalactic medium. The details of such metal mixing are still poorly understood and numerically challenging to model. Hence, there is no a priori guarantee that EAGLE yields realistic stellar metallicities.

The stellar mass - metallicity ($M_\star - Z_\star$) relations provide a useful way of characterising stellar abundances as a function of galaxy mass, and as shown in S15, the Ref-100 model yields stellar and gas-phase metallicities consistent with observations (Tremonti et al., 2004; Gallazzi et al., 2005; Zahid et al., 2014) for stellar masses $M_\star \gtrsim 10^{10}\mathrm{M}_\odot$. However, lower-mass galaxies in EAGLE tend to be more metal-rich than observed, with numerical resolution playing a role: the higher-resolution Recal-25 simulation agrees with the data for $M_\star \lesssim 10^9\mathrm{M}_\odot$. It should also be noted that there are large systematics on the observed mass-metallicity relations (e.g. Kewley & Ellison, 2008). We investigate the impact of stellar metal-

licity ($Z_\star$) on EAGLE colours in more detail in Appendix A.3. In our analysis, we use the EAGLE SPH-smoothed metallicities (Wiersma et al., 2009b) for each particle, which yield less noisy estimates of $Z_\star$.

3.2.1.2 Stellar Population Synthesis (SPS) Modelling

We adopt the GALAXEV population synthesis models of Bruzual & Charlot (2003), which provide the spectral energy distribution (SED) per unit initial stellar mass of a SSP for a discrete grid of ages (ranging from $t = 10^5$ to 2×10^{10} yr) and metallicities (ranging from $Z_\star = 10^{-4}$ to 0.05). We compute the SED for each stellar particle by interpolating the GALAXEV tracks logarithmically in age and $Z_\star$, and multiplying by the initial stellar mass. The simulated stellar metallicities reach higher values than the models of Bruzual & Charlot (2003) can represent, with $\sim 1.5\%$ of star particles possessing super-enriched ($Z_\star > 0.05$) values. We extrapolate the model to predict colours for the highest metallicities[1]. We note that the more conservative approach of not extrapolating introduces a bias.

The GALAXEV spectra are based on stellar emission alone. These models are widely used, and have been shown to fit the local galaxy population in the optical bands with reasonable star formation and enrichment histories when used in conjunction with a dust model (e.g. Charlot & Fall, 2000; Cole et al., 2000). The choice of population synthesis model has been shown to be largely unimportant for low-redshift galaxy populations, especially in optical bands (e.g. Gonzalez-Perez et al., 2014b). The effect of different models (e.g. Maraston, 2005; Conroy et al., 2009), and in particular the more uncertain impact of thermally-pulsing AGB stars (TP-AGB) on the SED, should however be considered when surveying higher redshift ($z \gtrsim 1$) galaxy populations (e.g. Maraston, 2005; Gonzalez-Perez et al., 2014a).

The Bruzual & Charlot (2003) models specify $Z_\star$ values as absolute metal-mass fractions, where $Z_\star$ affects the colours of stars through its impact on stellar

[1]We find that the effect of extrapolating metallicities, as opposed to clipping metallicities to that of the highest metallicity GALAXEV spectra, has a small ($\lesssim 2\%$) effect on the optical colours.

structure and evolution - for example via the opacity, equation of state and mean molecular weight - and on stellar atmosphere models. Even so, the metallicity of the Sun ($Z_\odot$) *does* enter the population synthesis models because some parameters, such as the mixing length, are calibrated based on solar observables (Bressan et al., 1993). Recent literature determinations of $Z_\odot$ have shown significant variability, with a minimum of $Z_\odot \sim 0.0126$ (e.g. Asplund et al., 2004) from the traditional value of $Z_\odot = 0.02$ assumed in Bruzual & Charlot (2003). Although the EAGLE simulations do not make use of any particular solar abundance pattern or $Z_\odot$ value, a relatively low value of $Z_\odot = 0.0127$ (Allende Prieto et al., 2001) has been assumed in analysis for consistency with Wiersma et al. (2009b) (e.g. S15). The variation of $Z_\odot$ generally results from a different determination of the abundance of some important element, such as O, N, C or Fe which also implies a variation of the abundance partition in the Solar model. In principle one should use GALAXEV SSP models with an abundance partition consistent with the assumed value of $Z_\odot$, and take into account effects arising from the different mixing length calibration, to compute colours self-consistently. For now we neglect any such changes and use the original GALAXEV SEDs, as the effects of this change on broad-band colours are expected to be small, as long as one makes use of the absolute value of the metallicity (Bressan 2014 *private comm.*)[2].

3.2.1.3 Photometric System

Given the SED for each star particle in the simulation, and a model for attenuation due to dust as a function of wavelength, we could compute the SED for each galaxy, and calculate a broad-band magnitude by convolving with a broad-band filter. Here we use a much simpler method, namely we *first* convolve the GALAXEV spectra (for each value of age and metallicity) with broad-band filters to obtain 'un-obscured' broad-band luminosities. We use these to obtain a broad-band luminosity for an EAGLE galaxy. We only *then* take into account dust atten-

[2]We are grateful to S. Charlot and A. Bressan for their detailed explanation of the impact of $Z_\odot$ on the GALAXEV model.

uation (as described below). If, as we assume, the wavelength dependence of the dust attenuation is not very strong (*i.e.* the optical depth does not vary strongly over the wavelength extent of the filter), then these two approaches yield very similar results. For the dust models discussed below, we verified that this is indeed the case (section 3.2.2).

We use the *ugrizYJHK* photometric system for optical and near infrared photometry, to enable a direct comparison to the GAMA survey (described in Driver et al., 2011; Hill et al., 2011). The GAMA filter system is based on that of SDSS (technical description in York et al., 2000) and UKIDSS, (technical description in Lawrence, 2007). Note that when calculating photometry below, filter transmission curves include atmospheric absorption to enable a like-for-like comparison of simulation and observation. All magnitudes are calculated as rest-frame and absolute in the AB-system (Oke, 1974) in which the apparent magnitude $m_{\rm AB}$ is defined as

$$m_{\rm AB} \equiv -2.5 \log_{10}(F_\nu) - 48.6\,, \tag{3.2.1}$$

where F_ν is the isophotal flux density (in cgs units) in a particular band (e.g. Tokunaga & Vacca, 2005).

3.2.1.4 Choice of aperture

Individual EAGLE 'galaxies' are identified as described in chapter 2. We select galaxies with at least 100 star particles, whose stellar mass is reasonably well converged numerically (S15). The line of sight is chosen consistently to lie along an axis of our simulation coordinates, yielding an essentially randomised orientation for each galaxy.

Massive galaxies ($M_\star \gtrsim 10^{10.5}{\rm M}_\odot$) in EAGLE have up to $\sim 40\%$ of their stellar mass in an extended halo beyond 30 pkpc of the galaxy centre ('intra-cluster light' since most of these massive galaxies are at the centre of a group or cluster). Observationally, such galaxies also tend to have extended light distributions and, unsurprisingly, the luminosity assigned to them depends on how such light is taken into account (e.g. Bernardi et al., 2013). We apply a constant aperture of 30 pkpc centred on the minimum of the gravitational potential of each subhalo

for measuring the total luminosity, L, of a galaxy, as discussed in chapter 2. The luminosity and colour of a galaxy with a significant intra-cluster light component do depend on whether we apply a 2D aperture or a 3D aperture. This change in colour is due to colour gradients but also due to the inclusion or exclusion of small blue satellite objects below the significance of those identified by SUBFIND. This is a similar issue to that encountered when isolating galaxies in astronomical data using software such as SEXTRACTOR (Jackson et al., 2010). We choose to apply a 3D spherical aperture, consistent with our previous analysis (S15, Furlong et al. (2015)). Such an aperture is shown in S15 to yield similar stellar masses to a Petrosian aperture, often used in observational studies.

The aperture definition is not standardised in observations, and can make a difference when a considerable fraction of stellar material lies outside the aperture. This is illustrated for the Kron and Petrosian apertures in Driver (2012), where luminous galaxies with high Sérsic indices yield different magnitudes. Similarly, when analysing our simulations, the luminosities of EAGLE galaxies with $M_\star \gtrsim 10^{11}\mathrm{M}_\odot$ are sensitive to the exact choice of aperture size. However, this is not the case for lower mass galaxies, for which the fraction of light in an extended halo is much lower.

3.2.1.5 Model N

The procedure for obtaining EAGLE galaxy photometry outlined above (sections 3.2.1.1-3.2.1.4) provides a model with no consideration of dust effects. This is hereafter referred to as model N. Model N provides a basis for comparison with photometry corrected for dust attenuation, as described below (sections 3.2.2.1-3.2.2.3). Panel a) of Fig. 3.1 shows the $g-r$ colour distribution of EAGLE galaxies for this model.

3.2.2 Dust models

We develop a simple *empirically calibrated* model for dust absorption, as opposed to a more physical modelling using ray-tracing, which I will present in chapter

5. One advantage of such a model is that we can easily disentangle the effects of dust from those of the SPS modelling on galaxy colours. In addition, if we model dust attenuation using galaxy parameters that are provided by EAGLE but can also be inferred through observation, then we may calibrate the reddening of EAGLE galaxy colours empirically to reproduce observed trends. Keeping our dust model parametrisation independent of certain quantities, such as the gas distribution, also allows us more freedom to investigate the extent to which certain assumptions affect galaxy colours.

In our modelling, dust corrections are applied as a multiplicative factor that reduces a given broad-band luminosity. This factor is estimated at the effective wavelength of each filter (SDSS filter parameters taken from Doi et al. 2010, UKIRT filter parameters taken from Hewett et al. 2006), for a given dust prescription (neglecting changes in the dust opacity within a broad-band filter is a good approximation provided the dust model has a smooth wavelength dependence). In this way, dust obscuration depends on the subhalo properties of a galaxy alone, and we avoid handling entire SEDs and generating a new interpolation grid for each galaxy. This makes the analysis process very efficient. The approximation that reddening can be applied *after* the spectrum has already passed through a filter affects the $g-r$ optical colours by $\lesssim 0.02$ mag over the whole interpolation grid for the constant optical depth model discussed below.

3.2.2.1 Model GI: Galaxy-independent dust model

We begin by discussing the simplest dust model introduced by Charlot & Fall (2000), hereafter referred to as CF. This model includes two contributions to the dust optical depth in a galaxy ($\hat{\tau}_{\rm d}$): (*i*) a transient component due to dust in stellar birth clouds ($\hat{\tau}_{\rm bc}$), and (*ii*) a constant dust screen that represents dust in the ISM ($\hat{\tau}_{\rm ism}$). The transmission T of this model is

$$T(\lambda, t') = \begin{cases} \exp\left(-\left[\hat{\tau}_{\rm bc} + \hat{\tau}_{\rm ism}\right]\left(\frac{\lambda}{\lambda_v}\right)^{-0.7}\right) & \text{for } t' \leq t_{\rm disp}, \\ \exp\left(-\hat{\tau}_{\rm ism}\left(\frac{\lambda}{\lambda_v}\right)^{-0.7}\right) & \text{for } t' > t_{\rm disp}. \end{cases} \tag{3.2.2}$$

Here, t' is the stellar particle's age, $t_{\rm disp}$ is the dispersal time of the stellar birth

cloud, λ is the wavelength of light, and $\hat{\tau}_{\rm ism}$ and $\hat{\tau}_{\rm bc}$ characterise the total dust optical depth (due to ISM and birth-cloud, respectively), at wavelength λ_v. When a model SED of a galaxy is fit to an observed galaxy, $\hat{\tau}_{\rm ism}$ and $\hat{\tau}_{\rm bc}$ can be used as fitting parameters to model dust (e.g. da Cunha et al., 2008). Alternatively, these parameters can be assigned constant values to model dust for a given population of galaxies as in Bruzual & Charlot (2003), but this does then not allow for variations between galaxies.

As a first approximation we simply take $\hat{\tau}_{\rm ism}$ and $\hat{\tau}_{\rm bc}$ to be constants,

$$\begin{aligned} \hat{\tau}_{\rm bc} &= 0.67 \\ \hat{\tau}_{\rm ism} &= 0.33, \end{aligned} \tag{3.2.3}$$

with $\lambda_v = 5500$ Å and $t_{\rm disp} = 10^7$ yr, which were calibrated to fit starburst galaxies and were used for the recent analysis of the ILLUSTRIS simulations (Vogelsberger et al., 2014) by Genel et al. (2014) and Torrey et al. (2014). With the optical depths fixed, the colours of an EAGLE galaxy will only depend on the SSP modelling. Such an approximation was also used in the development of the GALAXEV model, where it was shown to work well when SED fitting a subset of the SDSS survey at $z = 0.1$ (Bruzual & Charlot, 2003). The effect of this simple dust model on $g-r$ colours can be seen by comparing panels a and b in Fig. 3.1, and is discussed in more detail below.

In this simple model (model GI), the strength of the two screen components are fixed for each galaxy (and hence do not depend on e.g. its gas mass or metallicity) and are also independent of orientation. We discuss refinements of the dust model next.

3.2.2.2 Model GD: ISM-dependent dust model

To account for variations in metal enrichment in the interstellar medium (ISM) of galaxies, we use the mass-weighted SPH-smoothed metallicity (Wiersma et al., 2009b) calculated for star-forming gas in each EAGLE subhalo, $Z_{\rm SF}$. This metallicity calculation is chosen to imitate observational measurement techniques (Tremonti et al., 2004; Zahid et al., 2014). As demonstrated in S15, the mass-metallicity rela-

tions in EAGLE are significantly affected by resolution, with the Recal-25 simulation showing better agreement with the observed $Z_g - M_\star$ relation from Tremonti et al. (2004) than Ref-100 for $M_\star \ll 10^{10}\mathrm{M}_\odot$[3]. Near the knee of the mass function, however, the EAGLE mass-metallicity relation agrees well with observation (see S15).

We take the analytic expression for the $M_\star - Z_g$ mass-metallicity relation at $z = 0.1$ of Zahid et al. (2014), $Z_{\mathrm{Z14}}(M_\star)$, evaluated at the Milky Way stellar mass, $M_{\mathrm{MW}} = 6.43 \times 10^{10}\ \mathrm{M}_\odot$ (McMillan, 2011), as the ISM metallicity represented by the optical depth values of Eq. (3.2.2). Assuming optical depth is proportional to metallicity, we then scale the optical depths $\hat{\tau}_{\mathrm{bc}}$ and $\hat{\tau}_{\mathrm{ISM}}$ that appear in Eq. (3.2.2) by the factor

$$\begin{aligned} \hat{\tau}_{\mathrm{bc}} &\rightarrow \frac{Z_{\mathrm{SF}}}{Z_{\mathrm{Z14}}(M_\star = M_{\mathrm{MW}})}\,\hat{\tau}_{\mathrm{bc}} \\ \hat{\tau}_{\mathrm{ism}} &\rightarrow \frac{Z_{\mathrm{SF}}}{Z_{\mathrm{Z14}}(M_\star = M_{\mathrm{MW}})}\,\hat{\tau}_{\mathrm{ism}}, \end{aligned} \tag{3.2.4}$$

for each EAGLE galaxy, using the optical depth values of Eq. 3.2.3.

Making the dust optical depth depend on metallicity is physically well motivated, as it is indicative of the fraction of ISM mass in dust grains. Therefore, we must also take account of the gas mass to quantify how much dust is available for obscuration. We do so by making the dust optical depth dependent on the *cold gas* mass - but still neglect how that gas is distributed.

We approximate the cold gas mass, M_{ISM}, by the mass in star-forming gas, which in EAGLE means gas above a given metallicity-dependent density threshold and below a given temperature (see S15). We then scale the birth cloud and ISM dust optical depths by the ratio of M_{ISM} for the galaxy over the value for the Milky Way (which we take to be 10 per cent of $M_\star$; Mo et al., 2010; McMillan, 2011). This scaling is derived from observations indicating that optical depths approximately scale with the overall gas surface density (Σ_g) of galaxies (e.g.

[3]Note, however, that the observed mass-metallicity relation suffers from calibration uncertainties that exceed the difference between Tremonti et al. (2004) and Ref-100 (Kewley & Ellison, 2008) and that the more recent re-analysis by Zahid et al. (2014) falls in between Ref-100 and Tremonti et al. (2004) (see figure 13 of S15).

Grootes et al., 2013; Boquien et al., 2013). By taking Σ_g as approximately $\propto M_{\rm ISM}/{R_\star}^2$, and since the $z = 0.1$ stellar mass-size relation is relatively flat for both EAGLE (S15) and observed galaxies (Shen et al., 2003), we approximate that $\tau \propto \Sigma_g \propto M_{\rm ISM}$. Neglecting the ${R_\star}^{-2}$ dependence maintains a relatively simple parametrisation, and appears to have little effect on galaxy colours, due to the limited mass range over which reddening is significant.

Such a scaling has the desired effect of reddening gas-rich spiral galaxies more than gas-poor elliptical galaxies at the same $M_\star$. The galaxy $g-r$ colour distributions for the model including metallicity and gas fraction dependent reddening (model GD) are shown in Fig. 3.1c. For comparison, we also show the $g-r$ colour distributions for EAGLE galaxies where the value of $Z_{\rm Z14}(M_\star)$ is used in Eq. (3.2.4), instead of $Z_{\rm SF}$. Because low $M_{\rm ISM}$ values provide low optical depths for the stellar mass range where EAGLE and observed mass-metallicity relations differ ($M_\star \ll 10^{10}{\rm M}_\odot$), both treatments produce similar distributions.

3.2.2.3 Model GD+O: ISM-dependent dust model with orientation effects

Finally, we represent the dependence of obscuration on orientation with a simple toy model. We assume the dust geometry to be an oblate spheroid, with major to minor axial ratio of $q = b/a = 0.2$. This q value is commonly used to represent an axial ratio typical of the intrinsic stellar distribution in disc galaxies (e.g. Tully & Fisher, 1977). We assign to each EAGLE galaxy an orientation $w = \cos(\theta)$, where θ is the angle between the galaxy's minor axis and the line of sight. To obtain a random orientation we randomly sample w from a uniform distribution over the interval $[-1, 1]$. The line-of-sight depth through the dust spheroid is then

$$l(w) = a\frac{q}{\sqrt{q^2 + (1-q^2)w^2}}. \tag{3.2.5}$$

We then scale $\hat{\tau}_{\rm ISM}$ as

$$\hat{\tau}_{\rm ism} \rightarrow \frac{l(w)}{\langle l \rangle}\,\hat{\tau}_{\rm ism}\,, \tag{3.2.6}$$

so that the mean optical depth does not change. This scaling reduces the amount of dust obscuration for most galaxies by a small amount, yet increases τ by a factor ~ 2 for a small number of 'edge-on' systems. We assume a value of q that

is appropriate for discs, but we note that elliptical galaxies - provided they have little cold gas - are not strongly reddened anyway, hence this orientation correction is not important for them. The $g-r$ colour histograms including orientation effects are shown as model GD+O in Figure 3.1d. We also show the colour distributions produced using more oblate geometries, with axial ratio values $q = 0.1$ and $q = 0.02$, for comparison.

3.3 Results

In this section we examine the effects of dust modelling on the colours, luminosities, and colour-magnitude diagrams of EAGLE galaxies taken from the Ref-100 and Recal-25 models at redshift $z = 0.1$.

3.3.1 Galaxy colours as a function of stellar mass

We contrast $g-r$ colours for EAGLE galaxies in narrow (0.3 dex) bins of $M_\star$ for different models of dust absorption in Fig. 3.1 (panels a-d). In all panels, the blue line corresponds to the observed distribution from the GAMA survey (Taylor et al., 2015). Different panels show models with no dust (model N, panel a), a dust model that is independent of galaxy type (model GI, panel b), a model in which dust opacity depends on metallicity and gas fraction (model GD, panel c), and finally a model that in addition accounts for orientation effects (model GD+O, panel d). All models are shown as histograms, normalised to have unit integral. Models including dust are plotted as solid histograms, while the dashed histograms represent model N in all panels. Ref-100 distributions for the fiducial dust models are plotted in black, whereas Recal-25 distributions are plotted (for the lowest mass bin) in red. Model variations are also plotted for Ref-100, with a model using the observed mass-metallicity relation in panel c shown in green (see section 3.2.2.2) and models with alternative q values in panel d shown in green and yellow (see section 3.2.2.3).

The observed $g-r$ colours shift from very red massive galaxies (usually termed the 'red sequence'), to a broader distribution in colours for $10^{9.8} \lesssim M_\star/\mathrm{M}_\odot \lesssim$

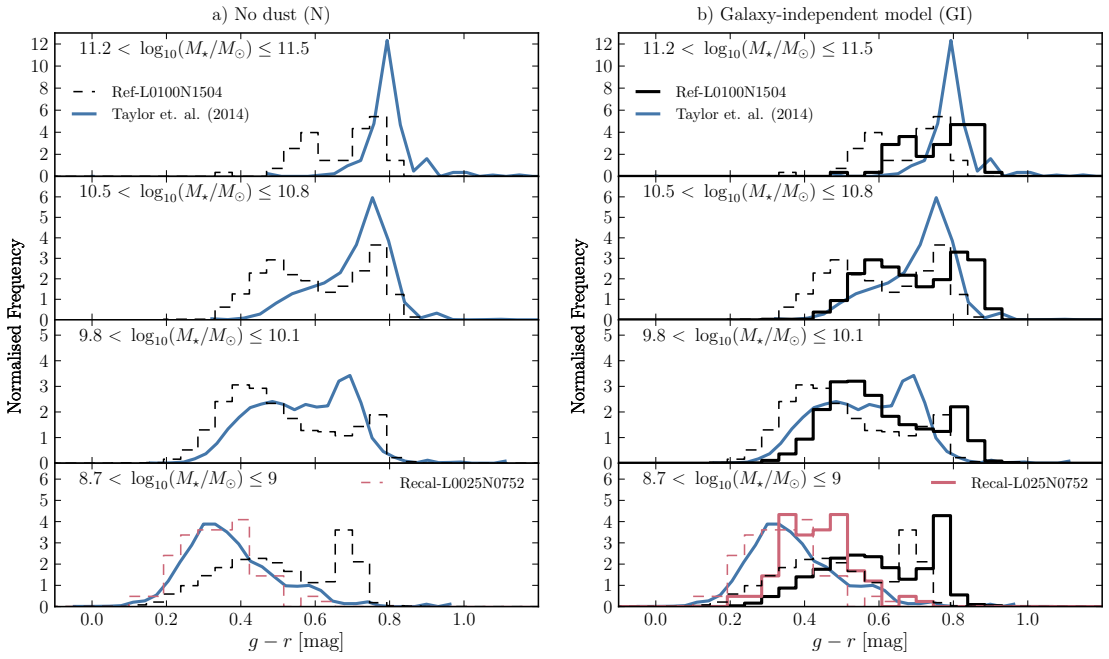

Figure 3.1: Rest-frame $g - r$ colour distributions for EAGLE galaxies at redshift $z = 0.1$, using 4 different models (*panels a-d*) for four non-contiguous ranges in stellar mass as indicated in the legend (*top to bottom*). *Black lines* indicate the fiducial Ref-100 galaxy population while *red lines* indicate the higher-resolution Recal-25 simulation. *Dashed lines* denote the unobscured SED (model N); these are repeated in each panel for comparison. *Blue lines* represent observed galaxy colours for the volume-limited sample of GAMA galaxies from Taylor et al. (2015). Models shown above are: model N without dust (panel a, see §3.2.1.5), model GI with galaxy independent dust (panel b, see § 3.2.2.1). {*continued on next page...*}

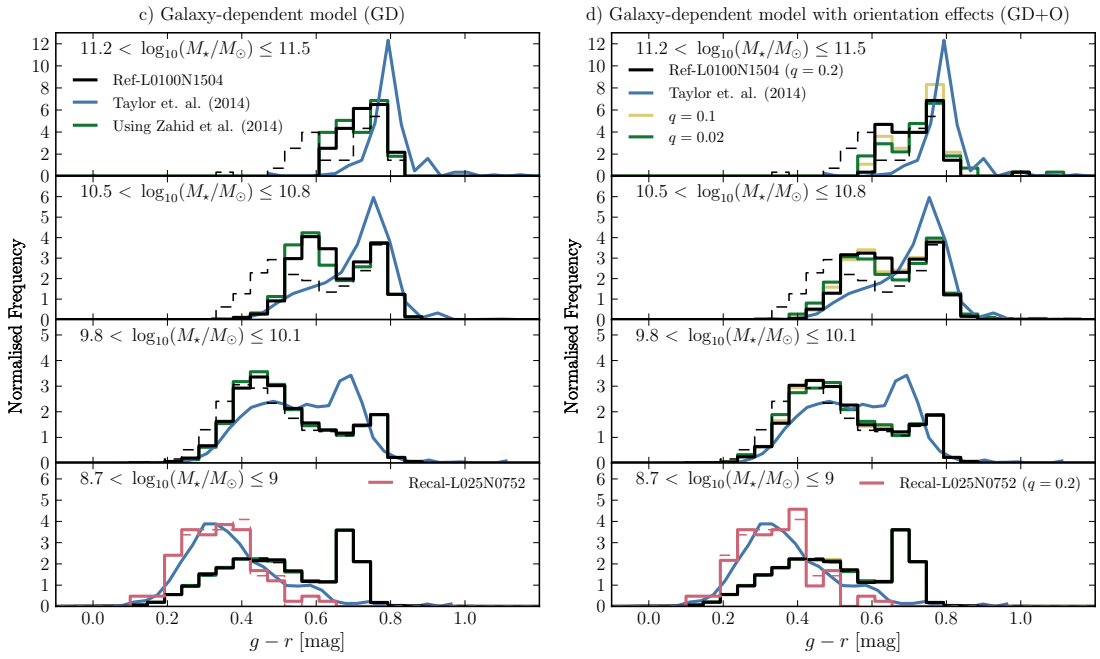

Figure 3.1: {*Continued from previous page...*} Panels show model GD where the dust obscuration depends on gas fraction and metallicity (panel c, § 3.2.2.2), and model GD+O that in addition takes into account orientation effects (panel d, § 3.2.2.3). Here, *green* and *yellow lines* also show model variations in panels c and d (see sections 3.2.2.2–3.2.2.3 for details). Overall, the figure shows the subtle quantitative effects that our different dust models have on the colour distributions of EAGLE galaxies in various $M_\star$ regimes, as is discussed further in the text.

$10^{10.8}$, and finally a blue population (usually termed 'blue cloud') at lower stellar masses. There is little evidence for a strong 'bimodality' in observed colours even though the data has often been interpreted that way (e.g. Kauffmann et al., 2003a). Such an interpretation is perhaps due to the bimodality seen at a fixed optical magnitude, where blue galaxies are pushed into higher luminosity bins.

Before comparing the models to the data, we investigate the effects of dust modelling, going from high- to low-mass galaxies (top to bottom rows in panels a-d). The most massive galaxies ($10^{11.2} \lesssim M_\star/\mathrm{M}_\odot \lesssim 10^{11.5}$, top rows) have a relatively extended intrinsic colour distribution (model N). Including a model with dust reddening independent of galaxy properties incorrectly reddens the reddest galaxies even more (model GI) but taking into account the relatively low cold-gas masses of these galaxies returns the colours to close to their intrinsic values (model GD). The tail of bluer massive galaxies is significantly affected by dust, yielding a mono-modal distribution in the highest-mass bin. Including orientation effects (model GD+O) gives a slightly broader colour distribution for the fiducial axial ratio value of $q = 0.2$.

A similar trend is noticeable for galaxies in the second most massive bin ($10^{10.5} \lesssim M_\star/\mathrm{M}_\odot \lesssim 10^{11.2}$, second row from the top). Though the fiducial value of $q = 0.2$ for GD+O produces a similar distribution to GD in this bin, varying q values appears to have the strongest effect here. Smaller q values show a more pronounced bimodality, as the majority of galaxies are subject to less reddening, while a minority of 'edge-on' galaxies are heavily reddened to $g - r$ colours $\gtrsim 0.8$.

The third bin ($10^{9.8} \lesssim M_\star/\mathrm{M}_\odot \lesssim 10^{10.1}$, third row from the top) also behaves similarly: the intrinsically bluest galaxies get reddened slightly more than the intrinsically red galaxies with scatter due to orientation having a negligible effect.

Finally, the colour distribution for galaxies in the least massive bin ($10^{8.7} \lesssim M_\star/\mathrm{M}_\odot \lesssim 10^{9}$, bottom row) is also shown for the Recal-25 simulation. There is a large difference in colours between Ref-100 and Recal-25 for the least massive galaxies, which is predominately a resolution effect: at the resolution of Ref-100 the star formation rates in these low-mass galaxies is underestimated (S15) which makes the simulated galaxies too red. This striking resolution dependence is not

surprising. In Ref-100, galaxies of mass $M_\star \sim 10^9 \mathrm{M}_\odot$ are represented by only $\sim 10^3$ star particles, and for a typical cold gas fraction of 10 per cent, by only 100 star-forming gas particles. We demonstrate in Appendix A.2 that red and blue sequence colours for galaxies across the $10^{9.8} \lesssim M_\star/\mathrm{M}_\odot \lesssim 10^{10.1}$ range[4] are quite similar in Ref-100 and Recal-25 - which gives us confidence that Recal-25 gives numerically converged answers for the bottom row of Fig. 3.1. However, the different environments probed by the Ref-100 and Recal-25 models also contribute to the difference in colours, in particular the strength of the red sequence, because the larger volume contains a population of satellite galaxies in massive halos. This is also shown in Appendix A.2 and discussed further in section 3.4. Taking into account dust obscuration and orientation effects has little effect on the colours in Recal-25 for these low-mass galaxies, with model GD+O and N yielding nearly identical colour distributions.

We now turn to comparing the colours of EAGLE galaxies to the data, going from top (most massive) to bottom (least massive) bins in stellar mass and focusing on model GD+O, Fig. 3.1d). At the massive end, the observed red sequence galaxies are about 0.05 mag redder in the data than in EAGLE. As the optical colours of old ($\gtrsim 10$ Gyr) stellar populations are dominated by metallicity effects (Bell & Rodgers, 1969), this small colour difference is attributable to SSP metallicities. The $M_\star - Z_\star$ relation for EAGLE galaxies (S15) is seen to lie slightly below (by less than 0.1 dex) observational data in galaxies with $M_\star/\mathrm{M}_\odot > 10^{11}$, resulting in a slightly bluer red sequence colour. The data also has a tail to even redder colours not present in EAGLE. In contrast, the most massive EAGLE galaxies have a tail to *bluer* colours resulting from recent star formation. It could be that such star formation is shielded more effectively in the data (*i.e.* the value of $\hat{\tau}_{\mathrm{bc}}$ used is too low), or alternatively that our AGN feedback scheme does not quite suppress star formation sufficiently. The higher than observed gas fractions for galaxy clusters in EAGLE (S15) could also contribute to the enhanced SFR of some simulated BCGs.

[4] A larger mass range is used in Appendix A.2 than in the third row of Fig. 3.1 so that Ref-25 and Recal-25 are sufficiently sampled.

The red sequence of galaxies with $10^{10.5} \lesssim M_\star/\mathrm{M}_\odot \lesssim 10^{10.8}$ is very similar in the data and the simulation, but in EAGLE there are significantly more blue galaxies. The blue cloud starts to appear in the data for galaxies with $10^{9.8} \lesssim M_\star/\mathrm{M}_\odot \lesssim 10^{10.1}$, and its colour is very similar in EAGLE. However, in EAGLE the blue peak is stronger and the red peak occurs at a slightly redder colour ($g - r = 0.75$ compared to the observed value of 0.7). Using smaller values of q in GD+O does not improve agreement with observation here. Dust reddening and orientation effects already play little role in setting the colours of EAGLE galaxies in this mass bin. Finally, in the lowest mass bin, $10^{8.7} \lesssim M_\star/\mathrm{M}_\odot \lesssim 10^{9}$, there is excellent agreement in the colour distributions of simulation and data and once more our dust reddening models are unimportant in setting EAGLE colours.

This level of agreement between galaxy colours in the simulation and the data is encouraging. By including metallicity and orientation effects in our dust treatment, we prevent the significant colour shift seen in the simple GI model. The validity of our dust model is discussed further in section 3.4. Despite the good agreement, there are some clear discrepancies between EAGLE and the GAMA colour distributions. These can be seen in the widths and relative strengths of red and blue populations. The latter discrepancy reflects the finding of S15 that the transition from actively star-forming to passive galaxies occurs at slightly (by a factor of ~ 2) too high mass in EAGLE.

The dependence of galaxy colours on stellar mass is further illustrated in Fig. 3.2, where the number density of galaxies in EAGLE with given rest-frame $g - r$ colour (computed using model GD+O) and stellar mass is compared to a volume-limited sample of GAMA galaxies taken from Taylor et al. (2015). Results are plotted down to stellar masses of $10^{8.7}\mathrm{M}_\odot$, below which volume corrections due to the influence of line-of-sight structure become increasingly uncertain in the data (Taylor et al., 2015). The colour bar shows the point density of EAGLE galaxies and how these map to the Taylor et al. (2015) contours.

The first panel shows the galaxies taken from simulation Ref-100. The simulation reproduces the trend seen in the data from galaxies being red above a stellar mass of $M_\star \sim 10^{10.5}\mathrm{M}_\odot$ to being predominantly blue below that. However, as also

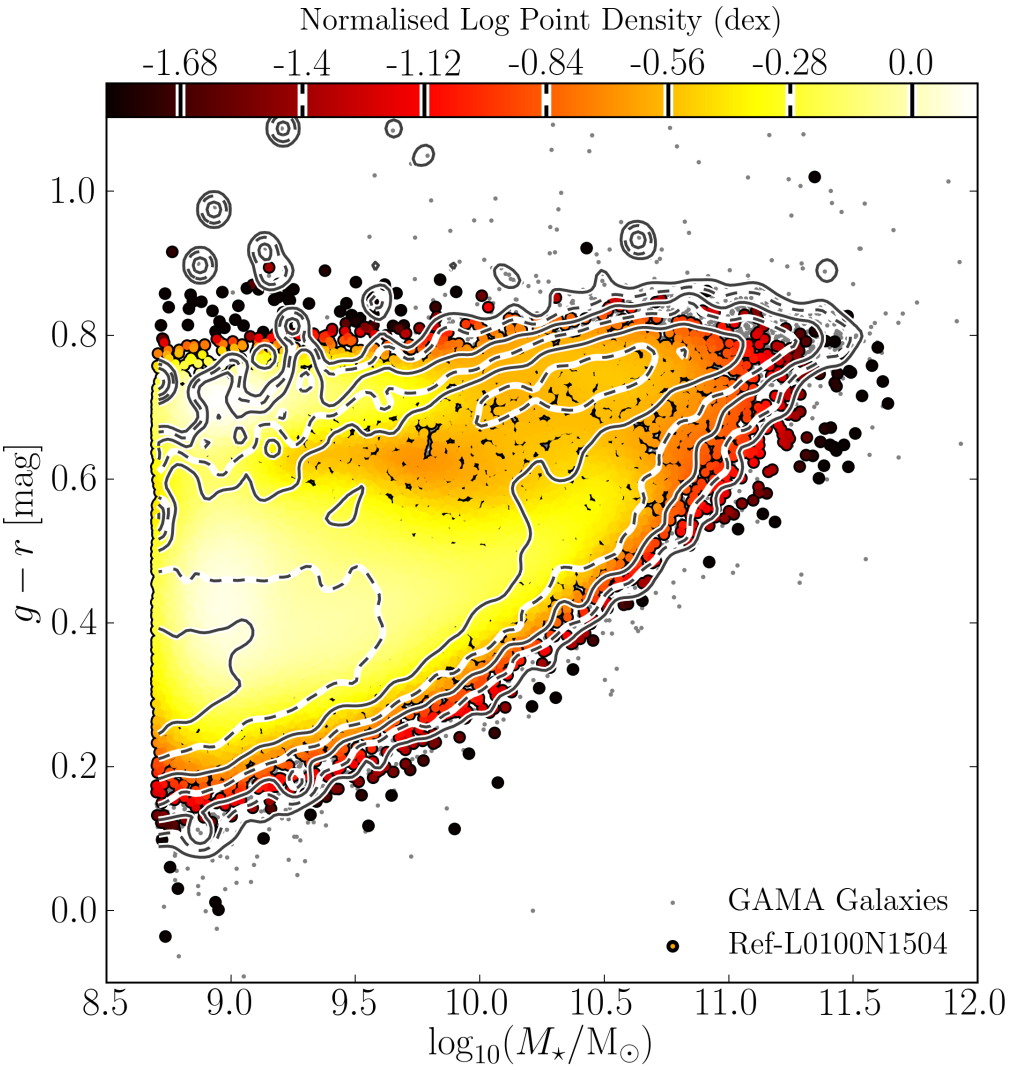

Figure 3.2: Rest-frame $g-r$ colour-stellar mass diagrams for Ref-100 EAGLE galaxies using photometry model GD+O at $z = 0.1$. *Coloured points* represent the point density of EAGLE galaxies of given $M_\star$ and $g-r$ colour (see text). *Contours* represent the colour-$M_\star$ distribution for a volume-limited set of GAMA galaxies from Taylor et al. (2015), with *grey points* representing individual galaxies. The masses of observed galaxies are obtained through SED fitting, see Taylor et al. (2015). The colour bar covers 2 dex in point density with a contour spacing of 0.28 dex, with contours mapped to equivalent densities in the colour bar. The transition of colours of observed galaxies, from the red-sequence at stellar masses above $M_\star \sim 10^{10.5}\mathrm{M}_\odot$ to the blue cloud at lower stellar masses, is reproduced in the simulation, although the blue cloud extends to slightly higher $M_\star$ and lower-mass EAGLE galaxies appear too red. {*continued on next page...*}

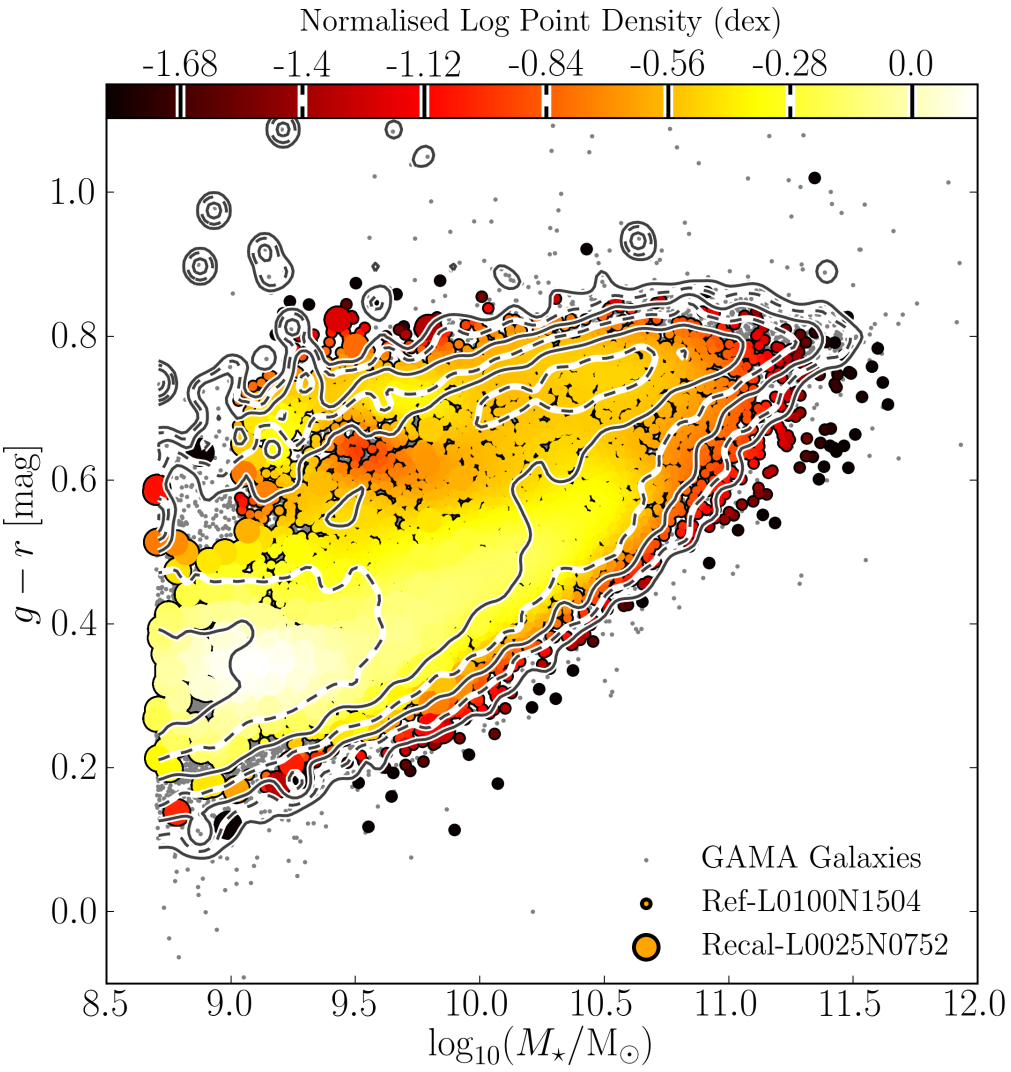

Figure 3.2: {*Continued from previous page...*}. As the previous panel, but where a composite set of EAGLE galaxies obtained by combining the higher-resolution model Recal-25 for galaxies with $M_\star \lesssim 10^9$ M$_\odot$ and Ref-100 for $M_\star > 10^9$ M$_\odot$ (*right panel*), cross-fading the sampling probability of the two galaxy populations linearly in $\log_{10}(M_\star/\mathrm{M}_\odot)$ (see text for details). The high resolution simulation better reproduces the observed colours at low mass.

seen in the previous figure, there is a population of red ($g - r \sim 0.7$) low-mass ($M_\star \sim 10^9 \mathrm{M}_\odot$) galaxies in EAGLE that is not seen in the data. These galaxies are modelled using only ~ 1000 star particles; the second panel of Fig. 3.2 therefore uses the higher resolution simulation Recal-25 for galaxies below $10^9 \mathrm{M}_\odot$ and Ref-100 above $10^9 \mathrm{M}_\odot$, cross-fading one simulation into the other. This is achieved by interpolating the frequency at which galaxies are randomly sampled from the simulations for our scatter plot linearly in $\log(M_\star)$ between two values at $10^9 \mathrm{M}_\odot$ and $10^{10} \mathrm{M}_\odot$. This is from 1 to 0 for the Ref-100 simulation and from 0 to 32 for Recal-25 simulation respectively[5]. With this we aim to show the colour-mass distribution for a larger range of well-resolved galaxies ($\gtrsim 1000$ star particles), while avoiding a discontinuity that renders the overall distribution less clear. This cross-fading is only intended to help in visualising the overall distribution of $g - r$ colours in EAGLE, taking advantage of the higher resolution at low mass end and of the larger volume run at the high mass end. A quantitative analysis of the colour distribution of EAGLE galaxies is shown in Fig. 3.1 and 3.5, and discussed below.

Combining these two resolutions, the colours of EAGLE galaxies at given $M_\star$ track the data from the GAMA galaxies (Taylor et al., 2015) well. Both display a red sequence of massive galaxies which becomes redder with increasing stellar mass, and $g-r \sim 0.7$ at $M_\star \sim 10^{10.5} \mathrm{M}_\odot$. The simulation also reproduces the width of that sequence, albeit with a shallower slope. A blue cloud of galaxies appears both in EAGLE and GAMA below $M_\star \sim 10^{10.5} \mathrm{M}_\odot$, with $g - r \sim 0.45$ at $M_\star = 10^{10.5} \mathrm{M}_\odot$. At decreasing stellar mass, the location of the blue cloud becomes bluer, reaching $g - r \sim 0.35$ at $M_\star = 10^9 \, \mathrm{M}_\odot$. Overall we find that EAGLE reproduces the mean

[5]The sampling frequency of Recal-25 galaxies in this plot are weighted a factor of 64 higher than Ref-100 galaxies to account for the smaller volume and a further factor of 2 lower to account for the boosted number counts in Recal-25 caused by poor sampling of large scale power in the smaller volume. This means that for masses $< 10^9 \mathrm{M}_\odot$ each Recal-25 galaxy contributes a factor of 32 more to the point densities in Fig. 3.2 than a Ref-100 galaxy at mass $> 10^9 \mathrm{M}_\odot$. This weighting is chosen to yield approximately the same number of galaxies plotted per unit stellar mass in the second panel of Fig. 3.2 as in the first.

trends in galaxy colours well. Though the eradication of the faint red sequence in this sample is at least partly due to improved sampling, it also comes about because these galaxies are much less abundant in the higher resolution Recal-25 simulation (further discussion of the origin of this faint red population can be found in Section 3.4 and Appendix A.2).

In addition to the mean location of galaxy colours, there are outliers in both data and simulation. The GAMA data display a scatter to extremely red colours ($g - r > 1$) at all stellar masses only seen for one high-mass outlier in EAGLE. There is also a scattering of galaxies ~ 0.1 mag bluer than the main locus in GAMA that appear in EAGLE as well. Finally, EAGLE has some very massive, relatively blue galaxies ($M_\star \sim 10^{11.5}\mathrm{M}_\odot$, $g - r \sim 0.6$); although there are such galaxies in GAMA as well, they are more numerous in EAGLE, as is more easily seen in Fig. 3.1. We suggested before that these either imply too little dust reddening in star forming regions in EAGLE, or simply that some of these massive EAGLE galaxies are undergoing too much star formation despite the inclusion of AGN feedback.

3.3.2 Luminosity functions

Luminosity functions for model GD+O in rest-frame $ugrizYJHK$ broad-band filters are plotted using absolute AB magnitudes in Fig. 3.3. The simulations Ref-100 and Recal-25 at redshift $z = 0.1$ are shown with Poisson error bars as solid black and red histograms respectively, becoming dashed when there are fewer than 10 galaxies per $\sim$0.6 mag bin. For Recal-25 the bins are correlated, as can be seen for example in the u-band for bins $M - 5\log(h) = -17.5$ to -18.5, due to poor sampling of large-scale modes in the small volume. There is generally good agreement between the two runs, with Recal-25 typically less than a factor of two (0.3 dex) higher at the faint end, and by much less for the redder bands. Note that this higher-resolution simulation does not sample the exponential cut-off at high luminosities because of its small volume. Differences in resolution are most noticeable in bluer colours, particularly in u. As discussed before, in small galaxies the stellar feedback events driving outflows are poorly sampled and the

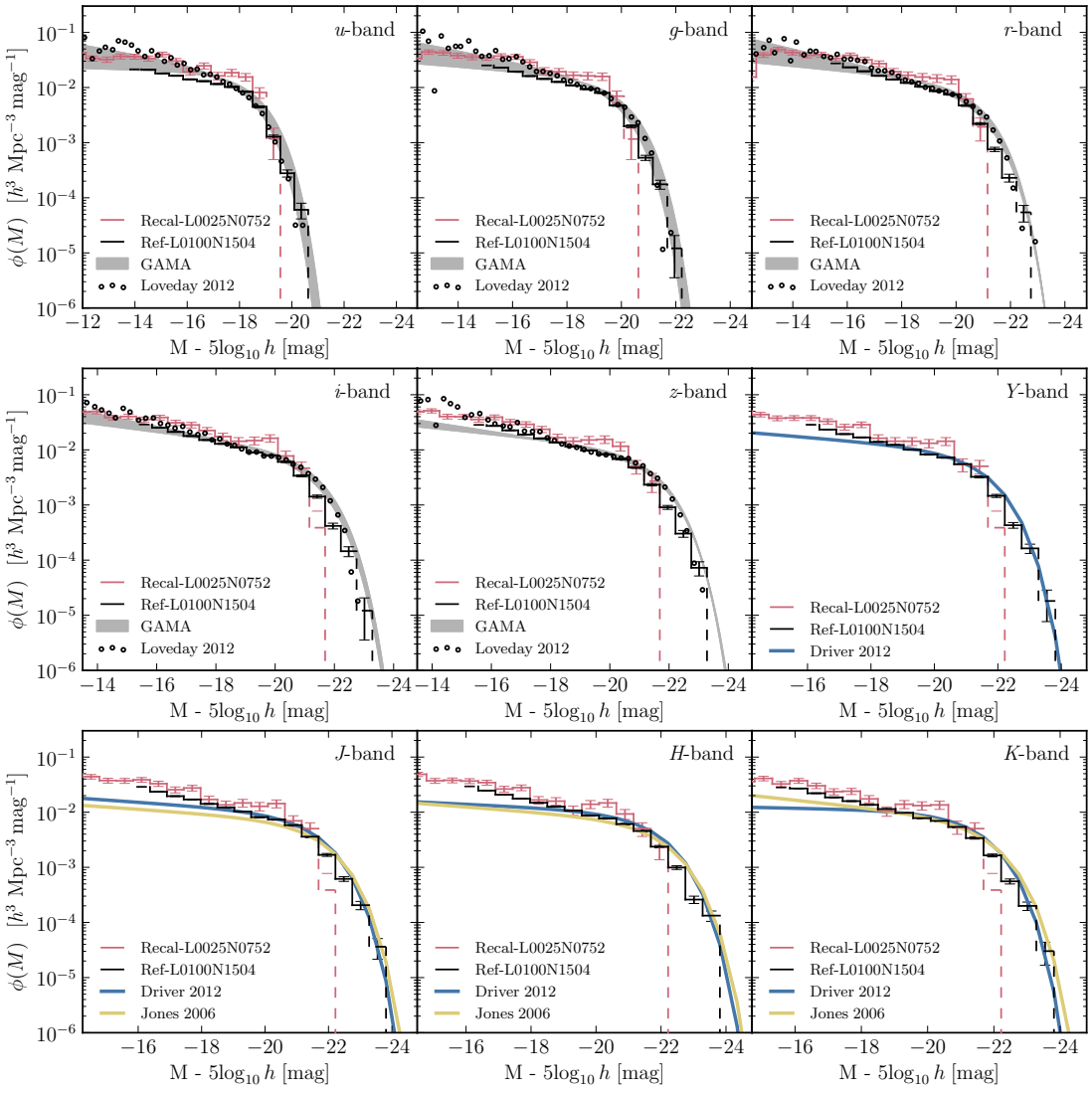

Figure 3.3: Rest-frame $ugrizYJHK$ luminosity functions in the AB system, plotted at $z = 0.1$ for the Ref-100 simulation in *black* and the Recal-25 simulation in *red* using GD+O photometry. The Ref-100 function is plotted down to the faintest magnitude bin at which most galaxies are represented by >100 star particles. $ugriz$ bands are compared to the GAMA survey luminosity functions taken from Loveday et al. (2012), k-corrected to rest-frame magnitudes and plotted as circles.

{*continued on next page...*}

Figure 3.3: {*Continued from previous page...*} The region bound by the Schechter fits to the Driver (2012) and Loveday et al. (2012) luminosity functions is shaded in grey. As these two luminosity functions are measured using Kron and Petrosian magnitudes respectively, the grey area indicates the difference due to aperture definition. Schechter fits for $YJHK$ luminosity functions are taken from GAMA (Driver et. al. 2012) and from 6DF+2MASS (Jones et al., 2006) where available Poisson error are plotted with dashed lines indicating bins containing < 10 galaxies. The EAGLE luminosity functions are similar to the observed fits across the spectral range, with some discrepancies discussed in section 3.3.

Model	Description	r-band		
		$\phi_\star$	α	$-2.5\log_{10}(\frac{L_\star}{h^2})$
		[h^3 cMpc^{-3} mag^{-1}]		[AB mag]
N	No dust	$8.1^{+1.0}_{-0.9} \times 10^{-3}$	$-1.24^{+0.03}_{-0.03}$	$-21.0^{+0.1}_{-0.1}$
GI	Galaxy-independent dust model	$7.5^{+0.9}_{-0.9} \times 10^{-3}$	$-1.25^{+0.03}_{-0.03}$	$-20.7^{+0.1}_{-0.2}$
GD	Z and $M_{\rm ISM}$ dependent	$9.3^{+1.2}_{-1.1} \times 10^{-3}$	$-1.21^{+0.03}_{-0.03}$	$-20.7^{+0.1}_{-0.2}$
GD+O	GD with orientation dependence	$9.5^{+1.5}_{-1.3} \times 10^{-3}$	$-1.21^{+0.04}_{-0.03}$	$-20.7^{+0.2}_{-0.2}$
Data	Loveday et al. (2012)	$9\pm0.7 \times 10^{-3}$	-1.26 ± 0.01	-20.7 ± 0.03

Table 3.1: Best-fitting Schechter function (Eq. 3.3.7) parameters for EAGLE AB-magnitude luminosity functions in the r-band for different dust models in simulation Ref-100 at redshift $z = 0.1$, and the observed luminosity function from Loveday et al. (2012). The EAGLE and observed luminosity functions are all fit over the magnitude range $-23.2 < r < -14.2$, 1σ errors on the best-fit parameters were computed using jackknife sampling. Best-fit parameters to $ugrizYJHK$ luminosity functions can be found in Appendix A.4.

star forming components are poorly resolved. As a result star formation rates and thus intrinsic colours are subject to considerable resolution effects. We see that the higher-resolution simulation yields higher star formation rates and hence bluer colours. We again note that this is not just a resolution issue: the Ref-100 volume contains a population of faint red quenched satellites of massive galaxies, which are simply not present in the much smaller Recal-25 volume, as discussed further in Appendix A.2. LFs in longer wavelength bands are consistent in shape between the two simulations (despite the small volume simulation being noisier).

Observed luminosity functions from Loveday et al. (2012) are plotted in each of the $ugriz$ bands, which we fit with a single Schechter (1976) function,

$$\frac{1}{L_\star}\frac{dn}{dL} = \phi_\star \left(\frac{L}{L_\star}\right)^\alpha \exp(-L/L_\star)\frac{dL}{L_\star}\,. \tag{3.3.7}$$

Single Schechter function fits are also taken from Driver (2012) and Jones et al. (2006). For the $ugriz$ bands these are shown as grey shaded regions which are bounded by the fits to the observed luminosity function of Loveday et al. (2012) and Driver (2012), both based on data from GAMA. The differences between these observed luminosity functions result from the use of Kron and Petrosian magnitudes, respectively. The thickness of the grey band is thus a measure of how these different aperture choices affect the Schechter fit. For the $YJHK$ band, we plot published Schechter fits, which are based on UKIDSS data.

There appears to be some discrepancy between Schechter fits from the observational papers and directly observed luminosity functions in the optical, as can be seen by comparing the Loveday et al. (2012) data with the Schechter fits. In particular, the data points appear systematically higher than the Schechter fit at the faint end and below the fit at the bright end. This is most visible in the z-band where the shaded region is narrowest. This could be a consequence of intermediate magnitude bins dominating the fit as this is where observational errors are minimal. It also shows that the single Schechter function is not a good fit to the observational data. In particular, it is unable to represent the observations at the faint end accurately (e.g. Loveday, 1998). The Driver (2012) and Jones et al. (2006) fits agree reasonably well, except for the faint-end slope in the K-band. The single Schechter fits are used here as simple indicators of the shape, position and

normalisation of the observed luminosity functions, but clearly their exact location depends on details of how galaxies are identified in the data, and possibly on the range and assumed errors used in the fitting procedure. We compare the parameters of Schechter fits to EAGLE luminosity functions to observational fits in Table 3.1.

From Table 3.1 we see that the dust treatment has little effect on the shape of the r-band luminosity function. The effect of including dust using the GI model makes the knee position, $-2.5\log_{10}(L_\star)$, 0.3 mag fainter and decreases the normalisation, $\phi_\star$. Scaling dust absorption by galaxy properties in GD serves to increase $\phi_\star$ for the same $L_\star$ value. The GD and GD+O model luminosity functions provide $L_\star$ and ϕ parameters that agree with the observational values within the errors. The faint-end slope, α, shows some variation between dust models, but remains within $\sim 1\sigma$ of the observational value. Information on the fitting and best-fit parameters to each $ugrizYJHK$ luminosity function for GD+O can be found in Appendix A.4.

Comparing the GD+O EAGLE luminosity functions to the data in Fig. 3.3 shows a striking overall consistency from the UV to the NIR bands. The deviations are mostly of the same order as differences in fits to the published luminosity functions of different authors. The agreement is particularly good in the optical bands $ugriz$, where EAGLE tends to fall mostly inside the grey band that represents the dependence of the luminosity function on the choice of aperture. The excellent agreement over such a wide range of colours suggests that EAGLE forms the correct number of galaxies of a given stellar mass and that those galaxies have realistic star formation histories and metallicities.

Comparing blue bands ($u-g$) to redder bands ($J-K$) at the faint end, we notice that the EAGLE Ref-100 luminosity functions tend to be slightly low in blue bands relative to the data, but high in the red bands. This is a consequence of Ref-100 producing slightly too many low-mass galaxies (S15) which have too low star formation rates (Furlong et al., 2015). Resolution also plays a role: we plot galaxies with more than 100 star particles, where we know that the stellar feedback events generating outflows and star formation rates at the faint end are poorly

resolved. In addition, even fainter galaxies with high star formation rates cannot scatter into the faint-end bins since we impose a cut in mass and not in magnitude.

The EAGLE luminosity function tends to drop below the observations at the 'knee' ($L_\star$) in the Schechter function, particularly in the bands red-ward of r. This is consistent with a slight underestimate in the masses of more massive EAGLE galaxies, as seen in the mass function plotted in S15.

The JHK bands also appear to have generally somewhat steeper faint-end slopes (parameter α in Eq.3.3.7) in EAGLE than the Schechter fits to the data. However, the data itself also shows an upturn at the faint end relative to the Schechter fits (circles in Fig. 3.3, see also Driver, 2012). Generally, the single Schechter function fit tends to underestimate the luminosity function at the faint end (Loveday, 1998). This is more pronounced in the JHK bands where the NIR sky is relatively bright (e.g. Sivanandam et al., 2012), leading to large uncertainties in the faint end data.

3.3.3 The $g-r$ colour-magnitude distribution

The colour-magnitude diagram of model GD+O for EAGLE is plotted in Fig. 3.4. As in the second panel of Fig. 3.2, we combined faint galaxies from the higher-resolution simulation Recal-25 for galaxies with $M_\star < 10^9 \mathrm{M}_\odot$ with galaxies from simulation Ref-100 at higher masses. As before, colours represent the number density of EAGLE galaxies in this plane, whereas contours show the corresponding data from the volume-limited catalogue of GAMA taken from Taylor et al. (2015). For both simulation and data, we only show galaxies with stellar mass $M_\star > 10^{8.7} \mathrm{M}_\odot$. Fig. 3.4 now contains only 'observable' quantities for GAMA galaxies[6], and in particular does not require any SED fitting. The overall agreement between EAGLE and the data is generally very good, exhibiting similar galaxy densities across the colour-magnitude plane.

[6]In practice the diagram still depends to a small extent on the applied cut in stellar mass at the faint end and on the choice of aperture to measure magnitudes.

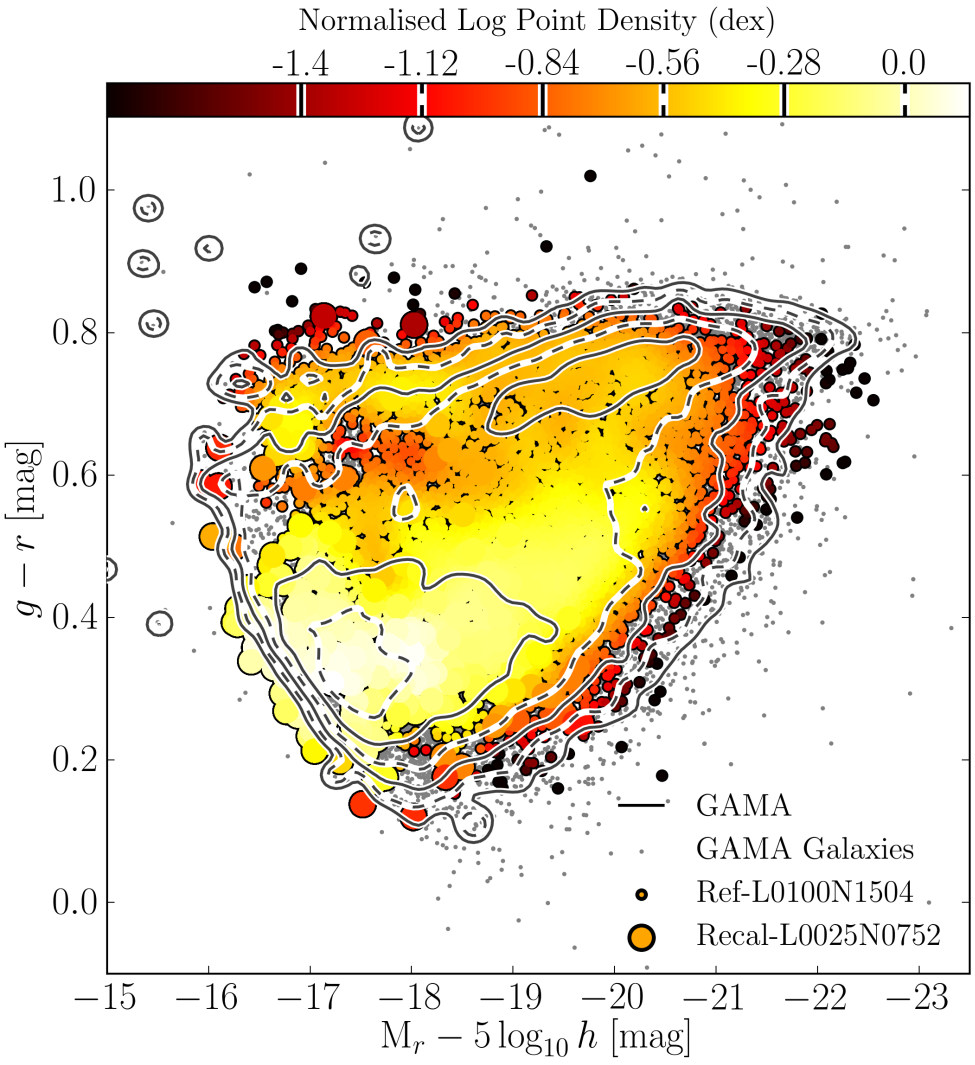

Figure 3.4: Rest-frame $g-r$ colour as a function of r-band absolute magnitude for EAGLE galaxies (colours) compared to a volume-limited sample of GAMA galaxies (Taylor et al., 2015, contour lines). Contours and point shading is the same as in Fig 3.2, with the normalised contour levels indicated on the colour bar. EAGLE photometry is obtained using the GD+O model. A composite EAGLE galaxy population is used, consisting of galaxies from Ref-100 at $M_\star > 10^9 \mathrm{M}_\odot$ and Recal-25 at $M_\star < 10^9 \mathrm{M}_\odot$ as in the second panel of Fig 3.2. There is general agreement between EAGLE and GAMA in the location and slope of the red-sequence ($g - r \approx 0.7$ at $M_r - 5\log_{10} h = -20$), the appearance of a blue cloud of galaxies with $g-r \sim 0.45$ at that magnitude, which becomes increasingly blue ($g - r \sim 0.3$) for the fainter galaxies with $M_r - 5\log h \sim -17.5$.

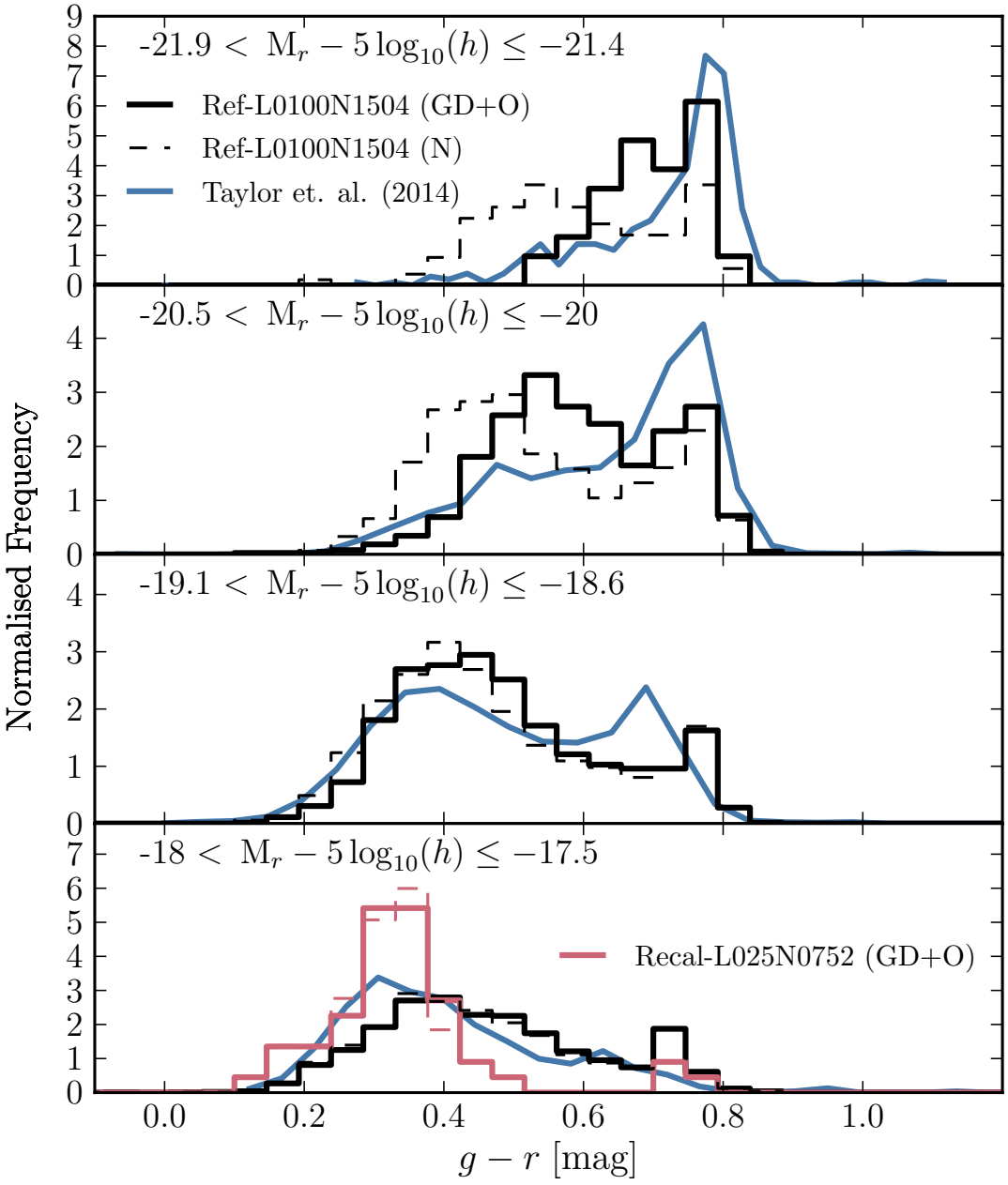

Figure 3.5: Rest-frame $g - r$ colour distributions for EAGLE galaxies at redshift $z = 0.1$ for four non-contiguous ranges in r-band magnitude as indicated in the legend (*top to bottom*). *Black lines* indicate the fiducial Ref-100 galaxy population while *red lines* indicate the higher-resolution Recal-25 simulation. *Dashed lines* denote the N photometry with *solid lines* representing the fiducial GD+O. *Blue lines* represent observed galaxy colours for the volume-limited sample of GAMA galaxies from Taylor et al. (2015).

We also plot colour distribution histograms in Fig. 3.5 for a more quantitative comparison, now in 0.5 mag bins of absolute r-band magnitude. The location of the red-sequence is within $\sim$0.1 mag of the observations in each panel. In a similar manner to Fig. 3.1d, we measure a slightly shallower red-sequence slope than observed with systematically redder colours at the faint-end. A transition between a predominately red to predominately blue distribution occurs, but at slightly brighter magnitudes than observed ($\mathrm{M}_r - 5\log(h) \sim -20.5$). In the lowest M_r bin, the colours and magnitudes of EAGLE galaxies also agree generally well with the data. To avoid the stellar mass cut affecting blue galaxies significantly, our faint end bin is chosen to have galaxies brighter than $\mathrm{M}_r = -17.5$. The Recal-25 simulation does not appear to show superior agreement with observation relative to the Ref-100 simulation in this bin. It should be noted that the number of galaxies in this bin are lower for both simulation volumes than in the lowest mass bin of Fig. 3.1d. The $g - r \sim 0.3$ colours of the faint blue galaxies appears to be well reproduced. The bright blue population in EAGLE become slightly more discrepant with data for the $-21.9 < \mathrm{M}_r < -21.4$ bin than in the high-mass bin of Fig. 3.1d, due to the fact that bluer galaxies generally possess brighter r-band magnitudes for the same $M_\star$.

The level of agreement between simulation and data in the colour-magnitude diagram shown in Fig. 3.4 and Fig. 3.5 is remarkable and suggests that these EAGLE simulations provide a relatively realistic population of galaxies at low redshift, and that the modelling of emission and dust obscuration in model GD+O works reasonably well.

3.4 Discussion

The EAGLE simulations were calibrated to reproduce the local GSMF and galaxy sizes by appropriate choice of the parameters in the subgrid model for feedback. As stellar mass is closely linked to NIR luminosity, the consistency of GSMF proxies such as the K-band luminosity function shown in Fig. 3.3 is not surprising, at least at $z \sim 0$. However, consistency with the luminosity functions in other

broad band filters is not automatic because stellar mass, star formation history, metallicity and dust obscuration all play a role.

In Section 3.3, we focused on our GD and GD+O photometric models where dust absorption is approximated by a simple two component screen, with optical depths that vary with galactic gas content, metallicity and orientation (GD+O only). The colour distributions as a function of stellar mass and r-band magnitude for model GD+O in Figs. 3.1, 3.2, 3.4 and 3.5 show a level of agreement between simulated galaxies and observations that appears unprecedented for hydrodynamical simulations, and comparable to that achieved for semi-analytical models (e.g. González et al., 2009; Henriques et al., 2014). The EAGLE luminosity functions also agree well with observations over a range in wavelengths from optical to NIR (Fig. 3.3). The relatively good agreement for number density, luminosity and colour, suggests that in EAGLE each dark matter halo forms a galaxy with stellar mass, age and metallicity close to those inferred from observation. The similar level of agreement in observed colour-magnitude space also rules out a potential circularity resulting from using the same photometric model to infer stellar mass from observational data as is used in the simulations. Even though the overall level of agreement is good between EAGLE and the data, there are discrepancies.

There is an excess of bright ($M_r - 5\log_{10} h \lesssim -20$) blue ($g - r \lesssim 0.6$) EAGLE galaxies relative to data, apparent in e.g. Fig. 3.5. Such an excess is seen in all our photometric models (see Fig. 3.1), but is least apparent for model GD+O where the recent star formation, that is the root cause of the blue colours, is most strongly obscured by dust. This parallels the findings of S15, that the fraction of passive EAGLE galaxies is too low at the high-mass end, relative to observations. It may be that massive EAGLE galaxies are too highly star forming, perhaps as a consequence of insufficient suppression of star formation by AGN. The colours of these galaxies can be sensitive to a low level of recent star formation. A 10 Gyr population requires a specific star formation rate of $\sim$0.025 Gyr^{-1} over a 0.1 Gyr period to move from $g - r \sim 0.8$ to 0.6 at a fixed metallicity of $Z = 0.02$, corresponding to $2.5\ \mathrm{M}_\odot\mathrm{yr}^{-1}$ for a galaxy of $M_\star = 10^{11}$. Whether the good agree-

ment in the colour of the blue cloud, despite the underestimate of the median star formation rates at these masses (S15), suggests underestimated reddening is discussed further below.

The EAGLE red sequence, at $g-r \sim 0.75$, is flatter than observed, both when plotted as a function of stellar mass (Fig. 3.2) and when plotted as a function of absolute magnitude (Fig. 3.4). The flatter slope may be attributable to the dependence of stellar metallicity on galaxy mass, $Z_\star(M_\star)$; although stellar metallicities of EAGLE galaxies agree well with the data at the massive end, they fall less rapidly with decreasing stellar mass compared to the observational data of Gallazzi et al. (2005), as shown in S15. Numerical resolution may play a role here, because the $Z_\star(M_\star)$ of the higher-resolution simulation Recal-25 does agree with the data; see S15.

There is an abundant population of red ($g-r \sim 0.7$), low-mass ($M_\star \sim 10^9 \mathrm{M}_\odot$) galaxies in simulation Ref-100 that is not observed (see Fig. 3.2a). The comparison of simulations Ref-25 and Recal-25 in Appendix A.2 shows that this is at least partially due to a lack of numerical resolution. Indeed, star formation and outflows driven by feedback in these galaxies are poorly resolved and poorly sampled, leading to too low values of the specific star formation rate (and correspondingly too high passive fractions) and too high metallicities (see S15). We include a re-sampling technique, described in section 3.2.1.1, in all models to try to mitigate poor sampling. Although this goes some way towards improving the modelling, it does not eliminate the discrepancy. Because the re-sampling is a post-processing step, it cannot help with the poor sampling of stellar feedback in these low-mass systems within the simulation. Related resolution problems are more intractable, and higher-resolution simulations are required to alleviate them.

Comparing simulations Ref-100 and Ref-25 that have identical numerical resolution (and the associated poor sampling of star formation in $M_\star \sim 10^9 \mathrm{M}_\odot$ galaxies), yet differ in simulated volume size, allows us to isolate the effects of environment (see Appendix A.2). Although on average the colours of galaxies agree well between these simulations, the presence of faint red galaxies is

much more pronounced in the larger volume. This is because many of these galaxies are satellites of more massive systems that are absent in the smaller volume. The fraction of satellites increases at lower stellar masses, and in the range $10^{8.7}\mathrm{M}_\odot < M_\star < 10^9\mathrm{M}_\odot$ comprises $\sim 46\%$ of the galaxy population in the Ref-100 simulation and $\sim 33\%$ in Ref-25. Evidently, satellites contribute significantly to the colour distribution at low masses. At present we cannot verify whether improved resolution will also reduce the suppression of star formation in, or decrease the metallicities of, small satellite galaxies, which would improve the colours of $M_\star \sim 10^9\mathrm{M}_\odot$ galaxies compared to data. We conclude that the redder colours of low-mass galaxies in EAGLE relative to data is at least partially a result of resolution, stemming from poor sampling of star formation and feedback. The improved agreement with the data that comes about from using a composite sample of Recal-25 and Ref-100 galaxies relative to using the Ref-100 sample alone is thus mainly due to improved numerical resolution, but also to the exclusion of red satellite galaxies that are not present in the smaller volume. The relationship between galaxy colours and environment in EAGLE is clearly an important test of the simulation, and will be explored further in future work.

The level of agreement between EAGLE colours and the data also depends on the realism of our dust reddening model. Fig. 3.1 illustrates how dust reddening depends on the assumptions made in models N (no reddening) to model GD+O (gas metallicity, gas mass, and orientation-dependent reddening). Differences between these models are typically of order $\Delta(g-r) \sim 0.1$. A dust model that is independent of galaxy properties (such as GI) incorrectly reddens red galaxies. A reddening model that takes into account the gas mass (GD) resolves this inconsistency, with most of the remaining effects of reddening affecting blue bright galaxies. Overall, we find that the details of the dust treatments make relatively little difference to galaxy colours so that differences with observations are more likely due to the ages and metallicities of the stars rather than dust obscuration. This may be due to the relatively small effect of dust at redshifts $z \sim 0.1$. We leave the investigation of evolution of colours and luminosities in EAGLE to a future work.

Taken at face value, the specific star formation rates of star-forming galaxies in EAGLE are lower than inferred from observations by ~ 0.2 dex (S15). The fact that the colours of those same galaxies nevertheless agree with the data might imply that we underestimate dust reddening. Indeed, an underestimate of the gas fraction would lead to both an underestimate of the specific star formation rate and, at fixed metallicity, the attenuation. Lagos et al. (2015b) have shown that at $M_* \sim 10^{10}\mathrm{M}_\odot$ the median H_2 fraction in EAGLE is about 0.2 dex lower than observed, and that this discrepancy goes away at higher masses and for the higher-resolution Recal-25 model.

Systematically lower attenuation for faint galaxies could thus be attributable to their low gas masses in the simulations. However, more complex models yield non-zero levels of attenuation even for very low gas surface densities (e.g. Boquien et al., 2013). The realism of mixed screen models as used here has been shown to break down when screens are optically thick (e.g. Disney et al., 1989). As dust optical depths are expected to be higher in blue bands, our dust prescription may be too crude to reproduce the data at higher levels of obscuration. This could contribute to the bluer colours of massive galaxies in EAGLE.

However, it is also possible that the levels of obscuration *are* realistic, but that star formation rates are overestimated in the data due to the absolute calibration of observed tracers of star formation. The calibration of star formation rates from tracers rely on assumptions about the intrinsic UV continuum (from population synthesis modelling) and absorption at short wavelengths, as well as an assumed form for the IMF (e.g. Kennicutt, 1998a). The cumulative build-up of stellar mass in EAGLE is lower than observed by about 0.1 dex, whereas the star formation rate is lower than that observed by 0.2-0.4 dex, depending on redshift (Furlong et al., 2015). This slight tension may suggest a small overestimate of the observationally inferred star formation rates. Estimating intrinsic properties from observables of simulated galaxies (such as star formation rates) may help to clarify these issues, see e.g. the recent study by Torrey et al. (2014).

The dust model we developed here was designed to be as simple as possible, yet to avoid unrealistic levels of reddening. The model assigns a single value of

reddening per galaxy without taking into account the non-uniform distributions of dust apart from that assigned to birth clouds. It is possible to make much more detailed estimates of reddening using 3D radiative transfer (RT) calculations (e.g. Baes et al., 2005; Jonsson et al., 2009). We postpone comparisons of the current simple model to those obtained with the radiative transfer code SKIRT (Baes et al., 2005) to chapter 5.

3.5 Summary & Conclusions

We have calculated broad band luminosities of simulated galaxies taken from the EAGLE (Evolution and Assembly of GaLaxies and their Environments) suite of hydrodynamic simulations (S15, C15), and compared them to observations of the redshift $z \sim 0.1$ galaxy population. The model uses simple stellar population modelling based on the GALAXEV population synthesis models of Bruzual & Charlot (2003). To marginally reduce sampling noise arising from single young star particles in poorly resolved galaxies, we use a re-sampling procedure for the young stellar component. In all models, galaxy luminosities are found by summing the particle luminosities within a 30 pkpc radius spherical aperture for consistency with previous analysis (S15, Furlong et al., 2015), which has been shown to mimic Petrosian apertures. Absolute magnitudes are presented in the AB system.

We compare and contrast three models of dust obscuration and to model N which neglects dust. Model GI, inspired by Charlot & Fall (2000), includes contributions to the dust optical depth from the birth clouds of young stars and from a constant dust screen, with parameters that are independent of the galaxy properties. Applying a single diffuse dust correction to all galaxies incorrectly reddens ellipticals and we avoid this with model GD in which dust reddening depends on gas phase metallicity as well as gas mass. Finally, model GD+O uses a simple geometric model to account for orientation effects, which are however small.

These simple models allow us to investigate the dependence of galaxy colours on stellar metallicities and ages, gas metallicities, and dust obscuration. Our main

conclusions are as follows:

- The GI dust prescription which applies a reddening that is independent of galaxy properties, and was used by e.g. Torrey et al. (2014), excessively reddens the red-sequence population of galaxies. As a consequence, $g-r$ colours of massive ($M_\star \gtrsim 10^{10.5}\mathrm{M}_\odot$) EAGLE galaxies are ~ 0.1 mag redder than observed, in spite of having ages and stellar metallicities that are similar to those inferred(Fig 3.1b). Scaling dust optical depths with cold gas mass and gas metallicity, as in model GD, is more realistic and improves agreement with observation (Fig 3.1c and 3.1d).

- The red sequence in EAGLE is ~ 0.1 mag bluer in $g-r$ than observed for $M_\star \gtrsim 10^{11.2}\mathrm{M}_\odot$, and has a shallower dependence on stellar mass than observed (Fig. 3.1). This is most likely a consequence of the dependence of colour on stellar metallicities.

- The appearance of a faint red sequence in the Ref-100 simulation run ($M_\star < 10^{9.75}\mathrm{M}_\odot$, $0.6 < g-r < 0.8$, see first panel of Fig 3.2) that is not observed, is largely an effect of numerical resolution. Star formation and outflows are not well resolved in galaxies of such low mass.

- A 'blue cloud' of star forming galaxies appears in EAGLE below $M_\star \lesssim 10^{10.5}\mathrm{M}_\odot$, with $g-r$ colour in agreement with the GAMA data from Taylor et al. (2015) (first panel of Fig 3.2).

- There is an excess of bright ($M_r - 5\log_{10} h \lesssim -20$) blue ($g-r \lesssim 0.6$) galaxies in EAGLE relative to the data. This may be caused by an underestimate of the reddening in star forming regions, or an overestimate of the star formation rates in these massive galaxies due to insufficient suppression of star formation by AGN.

- The $z = 0.1$ galaxies taken from EAGLE transition from mostly red ($g-r \sim 0.7$) above $M_\star \sim 10^{10.5}\mathrm{M}_\odot$ to mostly blue (ranging from $g-r \sim 0.5$ at $M_\star \sim 10^{10.5}\mathrm{M}_\odot$ becoming bluer with decreasing mass to $g-r \sim 0.35$ at $M_\star \sim 10^{9}\mathrm{M}_\odot$) at lower masses, follows the colours of GAMA galaxies from Taylor

et al. (2015) (see Fig.3.2). However the blue cloud persists to higher than observed stellar masses, consistent with a similar trend in passive fractions shown in S15.

- The $z = 0.1$ galaxy luminosity functions constructed from the EAGLE population agree well with data from UV to NIR bands, with differences of the order of the difference between using Kron and Petrosian magnitudes in the data (Fig. 3.3). This level of agreement is similar to the agreement between the EAGLE and observed stellar mass functions. In particular, there is a slight underestimate in the number density of galaxies close to the knee of the Schechter fit, and the faint-end tends to be slightly steeper than observed in most bands. We note, however, that the faint-end of the luminosity function is uncertain, especially in NIR bands, and single Schechter fits tend to underestimate the faint-end slope (Loveday, 1998). Good agreement was not surprising in the NIR where luminosities are dominated by stellar mass, whereas the good agreement in other bands suggests that the star formation histories and metal enrichment in EAGLE galaxies are relatively realistic.

- The $z = 0.1$ $g - r$ colour versus M_r magnitude diagram for galaxies with $M_\star \gtrsim 10^9 \mathrm{M}_\odot$ yields a level of agreement with data that is comparable to that of current semi-analytic models (Fig. 3.4; González et al., 2009; Henriques et al., 2014). The similar colour distributions of N and GD+O photometry (Fig. 3.1d) suggests that the dust model plays only a minor role in this agreement. This further attests to the relatively realistic evolution of the EAGLE galaxy population.

The general agreement in the colour and luminosity of EAGLE galaxies and observed galaxies suggests that the simulated galaxies have similar star formation histories, metal enrichment processes, and current star formation rates as observed galaxies. This makes the EAGLE suite well-suited to investigate the physical processes that shape galaxies through cosmic time.

Chapter 4

Colour Evolution in EAGLE

This chapter comprises an edited version of the article: **It's not easy being green: the evolution of galaxy colour in the EAGLE simulation**, *James W. Trayford, Tom Theuns, Richard G. Bower, Robert A. Crain, Claudia del P. Lagos, Matthieu Schaller, Joop Schaye* published in *MNRAS* Aug. 2016, vol. 460 p. 3925.

4.1 Introduction

In Chapter 3 we model the colour distributions of simulated EAGLE galaxies at low redshift ($z = 0.1$). We find that these distributions exhibit a bimodality comparable to what is observed, which is retained when a simple dust-screen model is applied. We also discuss the properties of blue cloud and red sequence galaxies arising in the simulations. It is difficult to determine how these sequences are established or quite how individual galaxies evolve in colour space using observations alone. This is because both star formation and galaxy destruction by mergers change the number density of galaxies of given mass across time. Faber et al. (2007) noted that the number density of blue galaxies remains approximately constant below redshift $z \sim 1$ whereas that of red galaxies increases markedly. This led them to propose a model in which one or more mechanisms operate that decrease the star formation rate of blue galaxies, with such 'quenching' making galaxies redder until they join the red sequence. Bell et al. (2012) showed that there is significant scatter in the properties of quenched galaxies.

One correlation that stood out in their sample, is that quenched galaxies usually exhibit a prominent bulge, by association suggesting a super-massive black hole.

A model in which an accreting super-massive black hole quenches star formation in its host galaxy appears very attractive. This is because black hole mass increases rapidly as a function of bulge mass (e.g. Häring & Rix, 2004; McConnell & Ma, 2013), hence such a model might explain why most massive galaxies are red - as observed. Unfortunately the evidence that star formation in galaxies hosting X-ray bright AGN is indeed suppressed appears inconclusive. Several studies have found no correlation between star formation rate and X-ray luminosity for an X-ray selected sample of AGN (e.g. Rosario et al., 2012; Harrison et al., 2012; Stanley et al., 2015). However a close to linear correlation has been observed for galaxies selected in the infrared (e.g. Delvecchio et al., 2015). The fact that the luminosity of an AGN likely *varies* on a range of time-scales (from hours to Myrs) might explain the apparent disparity (Hickox et al., 2014; Volonteri et al., 2015). Powerful radio galaxies associated with the centres of groups and clusters do appear to disrupt the inflow of cold gas (McNamara & Nulsen, 2012).

Another well-documented process that quenches star formation in a galaxy is restriction of its supply of gas by either ram-pressure stripping of disc gas (e.g. Gunn & Gott, 1972) or removal of halo gas (e.g. strangulation Larson et al., 1980), as the galaxy traverses a region of higher gas pressure associated with a group or cluster. The quenching of star-formation turns these satellites red (e.g. Knobel et al., 2013). Originally suggested by Gunn & Gott (1972), the efficiency of these mechanisms have been investigated using simulations by many groups (e.g. Quilis et al., 2000; Roediger & Brüggen, 2007), with more recently Bahé et al. (2013) pointing out that galaxies may be stripped *before* they become satellites, by the gas in the outskirts of massive systems. McCarthy et al. (2008) presented a theoretical framework that improves upon the simple analysis by Gunn & Gott (1972), and describes their simulation results well.

Observational confirmation that environmental quenching indeed operates is evidenced by the fact that red galaxies preferentially reside in regions of high galaxy number density (Dressler, 1980), or equivalently that red galaxies are more

strongly clustered than blue galaxies, even at fixed mass (e.g. Zehavi et al., 2005), and that the clustering amplitude of red galaxies depends little on mass (in contrast to that of blue galaxies, e.g. Coil et al., 2008). This is compatible with a model where red galaxies reside close to, or even inside, more massive and hence strongly clustered halos that cause the quenching. Trends between the environment and gas content of galaxies provide further evidence, with galaxies residing in clusters seen to be deficient in both HI and H_2 gas relative to the field (e.g. Cortese et al., 2011; Boselli et al., 2014). Particularly convincing is the similarity of the trails of HI gas seen to be emanating from gas rich galaxies in clusters (e.g. Chung et al., 2007; Fumagalli et al., 2014) and of the ram-pressure stripped gas behind simulated galaxies that fall onto a cluster (e.g. Roediger & Brüggen, 2008).

Even though observations suggest two empirical models of quenching (*i.e.* AGN and environmental), models of galaxy formation have struggled to reproduce simultaneously the detailed distribution of galaxies in the colour-magnitude diagram and the different clustering properties of red and blue galaxies. This is true of semi-analytical models, which use phenomenological prescriptions to describe the physical processes that lead to quenching (e.g. Font et al., 2008; Lacey et al., 2015); for example, Henriques et al. (2015) compare the Munich semi-analytical L-GALAXIES model to SDSS data. Although in many aspects this model reproduces the observations better than its predecessors, limitations remain. For example, L-GALAXIES' $u - r$ colours are considerably more bimodal than observed.

Hydrodynamical simulations can, in principle, model many physical processes self-consistently, but lack of numerical resolution and other limitations of the hydrodynamical integration may limit their realism. Fortunately, relatively small changes to the basic hydrodynamics scheme (e.g. Price, 2008; Hopkins, 2013) seem to resolve most numerical issues, such that the dominant uncertainties in hydrodynamical simulations become associated to the implementation of unresolved subgrid processes rather than the details of the hydrodynamics scheme (Scannapieco et al., 2012; Schaller et al., 2015b).

The huge dynamic range required to simulate a cosmologically representative volume with the required resolution to follow the hierarchical build-up of galaxies, presents a major challenge to numerical simulations. Until recently, such simulations did not reproduce the galaxy stellar mass function well, let alone the detailed colours/clustering of galaxies. A red/blue bimodality appears in the zoomed-simulations of Cen (2014) even though these do not include AGN. However, the $r-$band luminosity function of these simulation contains many more massive galaxies than observed. Gabor & Davé (2012) include the effects of AGN using a heuristic prescription of heating gas, where cooling is simply switched off in halos deemed massive enough to host AGN. They illustrate how this process builds-up a red sequence below redshift $z \sim 2$; initially lower-mass satellites and more massive quenched centrals appear in heated halos, with a characteristic dip in the abundance of red galaxies of stellar mass $M_\star \sim 10^{10}$ M$_\odot$ that is more prominent at higher z. While this simulation may provide valuable insight into the build up of the red sequence, the heuristic nature of the halo heating limits their practical applicability. For lower mass galaxies, Sales et al. (2015) show that the ILLUSTRIS simulation (Vogelsberger et al., 2014) broadly reproduces the colours of satellites, which they attribute to the relatively large gas fractions of satellites at infall.

The EAGLE reference model was calibrated to the $z = 0.1$ stellar mass function, black hole masses and sizes of galaxies and is currently the only hydrodynamical simulation that reproduces these observations, as detailed in chapter 2. EAGLE also reproduces many independent galaxy observations, such as the content and ionisation state of gas (Bahé et al., 2016; Lagos et al., 2015c), mass profiles (Schaller et al., 2014) and evolution in stellar mass, star formation rate and size (Furlong et al., 2015, 2017). The clustering of galaxies as a function of colour is investigated in a companion paper to this study (Artale et al., 2016). Chapter 3 showed that EAGLE reproduces the $g - r - M_r$ colour magnitude (and the $g - r - M_\star$) relation from the GAMA spectroscopic survey (Driver et al., 2011) very well. Including a model for dust-reddening computed using the SKIRT radiative transfer scheme (Baes et al., 2005; Camps & Baes, 2015) improves the quantitative agree-

ment further (see chapter 5). With low-redshift ($z \sim 0.1$) galaxy colours in EAGLE appearing to be realistic, studying how they have arisen given the physical feedback model of the simulation may provide new insight. The evolution of EAGLE galaxy colours is also afforded credibility by the reasonable evolution of the EAGLE galaxy population in terms of the stellar mass function (Furlong et al., 2015).

In section 4.1.1 I describe the photometry used in this chapter. In section 4.2 I investigate the evolution of the galaxy population across the colour-mass diagram and correlate colour changes with galaxies becoming satellites or hosting an AGN. In section 4.3 we expound these processes by analysing the behaviour of individual galaxies, using galaxy merger trees. Typical time-scales associated with colour transition are presented in section 4.3.2. We show that the colour evolution of most galaxies can be described well in terms of three generic tracks and quantify the fraction of galaxies that follow each path. Finally, our findings are summarised in section 4.4. Throughout this chapter we refer to dust-free, rest-frame colours as 'intrinsic' colours, and we take $Z_{\odot} = 0.0127$ for the metallicity of the Sun (Allende Prieto et al., 2001). Note that while the $Z_{\odot}$ value affects the normalisation of metallicities in solar units, colours are unaffected by the assumed $Z_{\odot}$ (see chapter 3).

4.1.1 Galaxy colours

The colours used throughout this chapter were obtained via the modelling described in chapter 3 applied to galaxies at multiple epochs, and summarised below. The stellar population properties (age, metallicity & assumed IMF) of an EAGLE galaxy are combined with the Bruzual & Charlot (2003) population synthesis model to construct an SED for each star particle. Summing spectra over all stars within the aperture described in Chapter 2. and convolving with a filter response function yields broad-band colours, which we compute using the *ugrizYJHK* photometric system for optical and near infrared photometry (taken from Doi et al., 2010; Hewett et al., 2006). We express these absolute magnitudes in the AB-system, see chapter 3 for more details.

It is well known that dust can alter the optical colour of a galaxy significantly,

particularly for gas-rich discs seen edge-on. We described a simple model for dust reddening in the previous chapter, and consider a model that uses ray-tracing to account for the patchy nature of dust clouds enshrouding star-forming regions described in the following chapter. However, here we use the 'intrinsic' (*i.e.* rest-frame and dust-free) colours of galaxies to examine the changes arising purely from the evolution of their stellar content. To simplify the interpretation we always quote *rest-frame* colours: there is therefore no 'k'-correction needed to compare galaxies in the same band at different redshifts. We concentrate here on $u^\star$-$r^\star$ colours (with the * referring to intrinsic colours) rather than $g^\star$-$r^\star$, because the u band is more sensitive to recent star formation, leading to more clearly separated blue/red colour sequences. Indeed, the $u^\star$-$r^\star$ index traverses the 4000Å break, often used as a proxy for star formation activity (e.g. Kauffmann et al., 2003a). The photometry is presented here without dust effects, comparison is possible with various observational data where dust corrections have been estimated (e.g. Schawinski et al., 2014).

4.2 Colour evolution of the ensemble galaxy population

Figure 4.1a shows that a scatter plot of EAGLE galaxies in a colour-stellar mass diagram, ($u^\star$-$r^\star$) vs $M_\star$, exhibits strong bimodality in colour at redshift $z \approx 0$. The well defined red sequence resides at $u^\star$-$r^\star \gtrsim 2.2$ with colours becoming redder with increasing $M_\star$. The blue cloud is at $u^\star - r^\star \approx 1.3$, with a slope similar to that of the red sequence. These two sequences are indicated by red and blue lines to guide the eye, respectively, obtained by a spline fit to the maxima in the probability distribution of $u^\star$-$r^\star$ in bins of $M_\star$. We keep the location of these lines fixed in Fig. 4.1b-d to facilitate comparison at higher z. We clearly see that:

(*i*) The red sequence becomes bluer and less populated with increasing z. It is in place at $z \approx 1$ but has mostly disappeared by $z \approx 2$. A gap in the red sequence is noticeable at $z \approx 1$ for $M_\star \sim 10^{9.7}$ M$_\odot$.

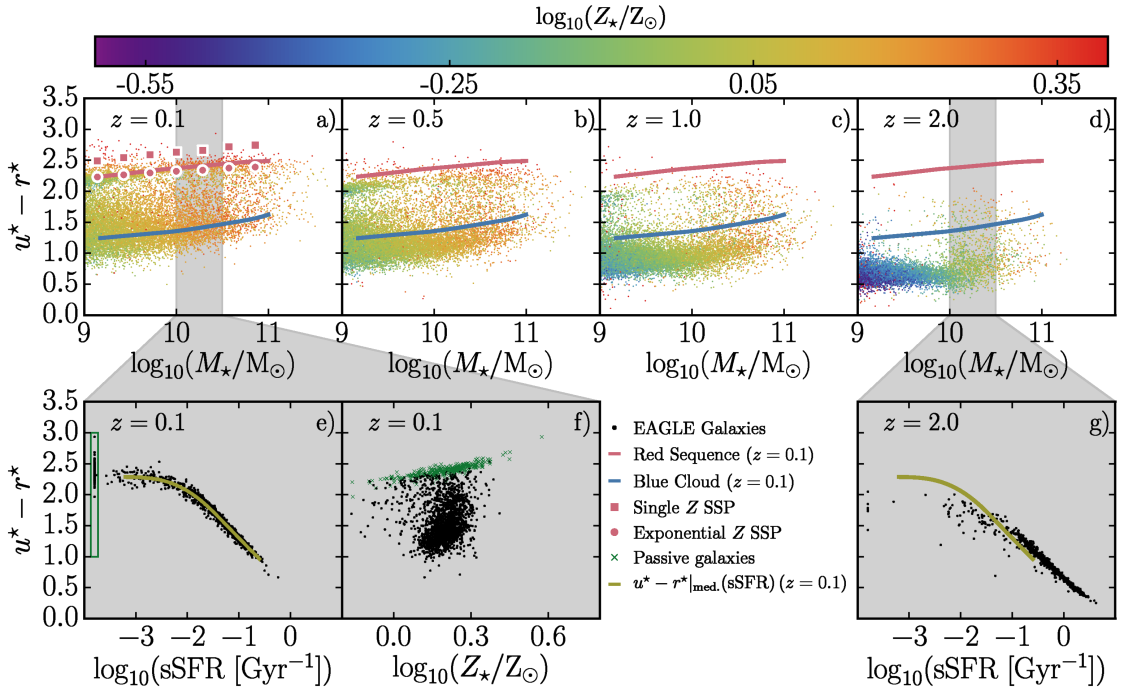

Figure 4.1: Colour evolution of EAGLE galaxies. **Top row:** $u^\star$-$r^\star$ vs $M_\star$ colour-mass diagram at four redshifts ($z = 0.1$, 0.5, 1 and 2, left to right). Individual galaxies are plotted as points, coloured by median stellar metallicity, using the colour bar in the top row. The locations of the red sequence and blue cloud at $z = 0.1$ (red and blue lines, respectively) are repeated in panels b-d to guide the eye. Filled red squares show $u^\star$-$r^\star$versus $M_\star$ for a 10 Gyr old stellar population with metallicity $Z_\star$ equal to the median metallicity at that $M_\star$; filled circles are the same, but assuming an exponential distribution of stellar metallicities with the same median. **Bottom row, panels e and g:** dependence of $u^\star$-$r^\star$colour on specific star formation rate (sSFR, $\dot{M}_\star/M_\star$) for galaxies with $10 < \log_{10}(M_\star/\mathrm{M}_\odot) < 10.5$ (the grey band in panel a, and galaxies with $M_\star$ between the two grey lines in panel d) at redshift $z = 0.1$ and $z = 2$, respectively. The olive line indicates the median $u^\star$-$r^\star$ as a function of sSFR at $z = 0.1$ for comparison at $z = 2$. **Panel f:** $u^\star$-$r^\star$ versus median stellar metallicity for the galaxies of panel e; galaxies with sSFR$< 10^{-3.5}$ Gyr^{-1}, appearing in the green box in panel e, are plotted as green dots.

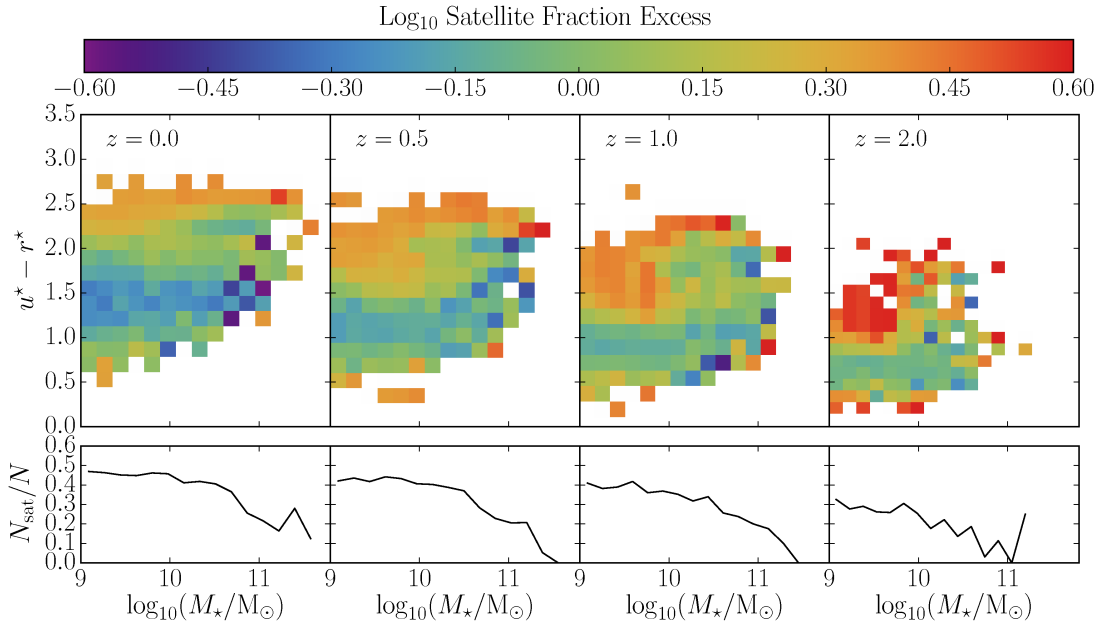

Figure 4.2: The impact of satellite fraction on the evolution of the $u^\star$-$r^\star$vs $M_\star$ colour-stellar mass relation. **Top panels:** Each square corresponds to a bin in colour and $M_\star$ and is coloured according to the median normalised satellite fraction in that bin, such that higher satellite fractions correspond to redder colours (see the colour bar). The satellite fraction is normalised to the average satellite fraction at that stellar mass (bottom panel), removing trends of satellite fraction with stellar mass and redshift. At $z = 2$, most red galaxies with $M_\star \leq 10^{10}\,\mathrm{M}_\odot$ are satellites (red colour in satellite fraction). This trend persists to $z = 0$, although it becomes weaker as galaxies classified as centrals also get quenched. **Bottom panels:** Fraction of galaxies classified as satellites as a function of $M_\star$. At redshift $z = 0$, the satellite fraction is nearly constant at just below 50 per cent below $M_\star = 10^{10}\mathrm{M}_\odot$, and decreases above that mass. At higher z the satellite fraction decreases for all $M_\star$.

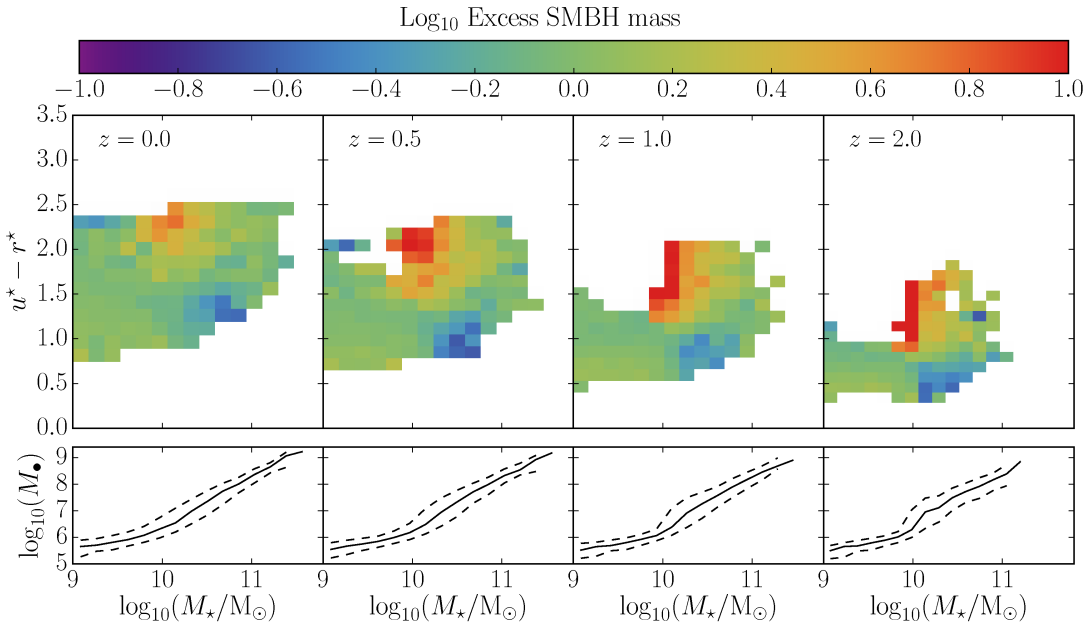

Figure 4.3: The impact of black hole mass on the evolution of the $u^\star$-$r^\star$ vs $M_\star$ colour-stellar mass relation for central galaxies. **Top panels:** Each square corresponds to a bin in $u^\star$-$r^\star$ and $M_\star$, and is coloured according to the median black hole mass, $M_\bullet$, in that bin, such that larger values of $M_\bullet$ correspond to redder colours (see the colour bar). The median black hole mass in each square is normalised to the median black hole at that stellar mass (bottom panel), removing trends of $M_\bullet$ with $M_\star$ and redshift. At $z = 2$ there is a trend for redder galaxies to have more massive black holes. This trend is particularly striking for galaxies with $M_\star \sim 10^{10}\mathrm{M}_\odot$ and becomes less pronounced at higher masses. There is no obvious correlation at lower stellar mass. These trends persist to lower z but become weaker. **Lower panels:** The median black hole mass, $M_\bullet$, as a function of stellar mass is plotted in solid black. Dashed black lines represent the 16th and 84th percentiles. $M_\bullet$ is nearly independent of $M_\star$ below $M_\star \sim 10^{10}\mathrm{M}_\odot$, and increases with $M_\star$ above this characteristic mass. This trend is almost independent of redshift.

(*ii*) The blue sequence becomes bluer with increasing z, and exhibits decreasing scatter.

The main features of the galaxy population that drive these trends are illustrated in the bottom panels of the figure. Figs. 4.1e & g show that for a narrow stellar mass range around $M_\star = 10^{10.25}$ M$_\odot$ that $u^\star$-$r^\star$ is strongly anti-correlated with the specific star formation rate, $\mathrm{sSFR} \equiv \dot{M}_\star/M_\star$, provided the galaxy is star-forming ($\log_{10}(\mathrm{sSFR/Gyr}) \gtrsim -2$). This is not surprising since the light in the $u^\star$ filter is dominated by emission from massive and hence young stars, while $r^\star$ is dominated by the older population. Galaxies in this plot follow a very tight relation at a given z, sliding along a narrow locus in colour that becomes bluer at higher z. At $z = 2$, the galaxies follow almost the same relation in $u^\star$-$r^\star$ versus sSFR as at $z = 0$, with just a small but noticeable offset towards redder colours (≈ 0.1 mag) for $\log_{10}(\mathrm{sSFR/Gyr}) \gtrsim -1.25$. This is a result of the redder population being younger on average and hence brighter for a $z = 2$ star-forming galaxy, compared to a star-forming galaxy at $z = 0$. For lower star formation rates ($\log_{10}(\mathrm{sSFR/Gyr}) \lesssim -1.25$) the old population has more influence on $u^\star$-$r^\star$, and the younger average stellar age of $z = 2$ galaxies causes an offset to blue colours.

With $u^\star$-$r^\star$ colour so strongly correlated with sSFR, the colour vs $M_\star$ diagram of Fig. 4.1 is one view of the 'fundamental plane of star-forming galaxies', discussed recently by Lagos et al. (2015a). These authors showed that EAGLE galaxies from different redshifts fall onto a single 2D surface when plotted in the 3D space of $\dot{M}_\star - M_\star$ and gas fraction (or metallicity), which they attributed to self-regulation of star formation. Lagos et al. (2015a) also showed that observed galaxies follow very similar trends. The increasingly bluer colours of the blue cloud towards higher z is a consequence of the increased star formation activity at fixed $M_\star$.

The scatter in colour at fixed $M_\star$ on the red sequence is mostly due to metallicity, Z, as is clear from examination of the $u^\star$-$r^\star$ distribution of galaxies at a given $M_\star$ with low sSFR $< 10^{-3}$ Gyr^{-2}, plotted as green points in Fig. 4.1f. The colour of star-forming galaxies with sSFR $> 10^{-3}$ Gyr^{-1} (black points) also depends on

Z, but from comparison of these panels it is clear that this effect is much smaller than the dependence of colour on sSFR itself - it induces the small scatter in $u^\star$-$r^\star$ in panel e, on top of the main trend with sSFR.

As discussed by many others, the *slope* of the red sequence demonstrates the dependence of colour on Z for galaxies: more massive galaxies are more metal rich and hence redder (see chapter 3). Because the mass- and light-weighted metallicities are not equivalent, the internal metallicity distribution for stellar populations in a galaxy may also affect the normalisation of the red sequence. To illustrate this, we calculated the median metallicity, $Z_{\rm med}(M_\star)$, in bins of stellar mass. We then calculated $u^\star$-$r^\star$ colours for a 10 Gyr old population with that dependence of Z on $M_\star$, and plot the resulting $u^\star$-$r^\star$ colour as a function of $M_\star$ in Fig. 4.1a as red squares. Although this sequence has the same slope as the red sequence in EAGLE, it is systematically redder by ≈ 0.25 magnitudes. This is not an age effect, but a consequence of stellar populations exhibiting a spread in metallicity within an EAGLE galaxy. In fact, the metallicity distribution function of stars in an EAGLE galaxy is fairly well described by an exponential distribution. We therefore generated another comparison toy model for the red sequence colour, in which we impose an exponential metallicity distribution and again assume a coeval 10 Gyr old population. The exponential metallicity distribution is defined by a mean value at fixed mass, given by the $Z_{\rm med}(M_\star)$ dependence of EAGLE galaxies. This model is plotted as filled red circles and it reproduces the EAGLE red sequence very well. This simple exercise shows that the assumption that all stars have the *same* metallicity results in systematic errors in the metallicity from broad-band colours.

The consistent red sequence slope between the toy model and EAGLE suggests that any changes in the internal stellar Z distribution of EAGLE galaxies with mass are not strong enough to bias the median colours of red galaxies. We note that the slope of $u^\star - r^\star$ relation as a function of $M_\star$ in the blue cloud is set by the sSFR-$M_\star$ relation and not by metallicity effects. Therefore, the similarity between the slopes of the blue and red lines is coincidental.

4.2.1 Satellite colours

The extent to which satellite galaxies are preferentially red relative to the general population is illustrated in Fig. 4.2. We divide colour vs mass diagrams at different redshifts into equal bins of $u^\star$-$r^\star$ and $\log_{10}(M_\star/\mathrm{M}_\odot)$. The satellite fraction in each bin is computed and normalised by the total satellite fraction for all galaxies in the same stellar mass range. Bins containing > 10 galaxies are shaded by the $\log_{10}$ normalised satellite fraction, such that positive values indicate a higher than average satellite fraction for that mass, while negative values indicate a lower than average value. The satellite fraction as a function of stellar mass in EAGLE is plotted for each redshift in the bottom panels.

Galaxies with $M_\star \leq 10^{10}\mathrm{M}_\odot$ that are red are predominately satellites, seen most strikingly at $z \approx 2$. At lower z there is still a trend for low-mass red galaxies to be satellites, but the trend is less pronounced because some galaxies classified as centrals are also red. To some extent this may be a consequence of galaxies being quenched by ram-pressure stripping in the outskirts of more massive halos, *before* they are classified as being a satellite (e.g. Bahé et al., 2013). Indeed, they may not be part of the FOF halo (yet). Another possibility is that some of these galaxies were stripped as satellites when they fell inside a massive halo but have travelled out again, the so-called backsplash population (Balogh et al., 2000).

At redshift $z \approx 0$, the fraction of satellites is ≈ 50 per cent at $M_\star \sim 10^9\mathrm{M}_\odot$, decreasing slowly to 30 per cent by $M_\star \sim 10^{10.5}\mathrm{M}_\odot$, and then dropping rapidly towards higher $M_\star$. Satellite fractions decrease slowly at all $M_\star$ with increasing z to $z \approx 1$, and then drop much faster to below 30 per cent at all masses by $z = 2$. This rapid drop in the satellite fraction with increasing z is the reason that the red sequence disappears at low $M_\star \lessapprox 10^{10}\mathrm{M}_\odot$ for $z \gtrsim 2$.

4.2.2 AGN host colours

The effect of feedback from accreting black holes on galaxy colours is illustrated in Fig. 4.3. We only plot *central* galaxies to disentangle satellite quenching from effects induced by AGN. The figure is analogous to Fig. 4.2, with median black hole

mass replacing satellite fraction. The median black hole mass ($M_\bullet$) as a function of $M_\star$ is plotted for each redshift as the bottom panels in Fig. 4.3.

At redshift $z = 2$, there is a very strong trend for red galaxies with $M_\star \approx 10^{10}$ M$_\odot$ to exhibit unusually high black hole masses, more than 4 times the median black hole mass at that stellar mass. This trend persists but becomes weaker at higher $M_\star$, and is completely absent at lower masses. This correlation between the residuals of the $M_\bullet - M_\star$ relation and the colour of the galaxy is still mostly present at $z = 1$, but begins to be washed out at later times.

The trend for galaxies with high black hole masses to be predominantly red when $M_\star \gtrapprox 10^{10}$ M$_\odot$ is likely related to the largely redshift independent characteristic *halo* mass, $M_\mathrm{h} \sim 10^{12}$ M$_\odot$, above which black holes start to grow rapidly in EAGLE, fed by the growing hot halos around them (Bower et al., 2017). The accreting black hole then quenches star formation in its host galaxy, turning it red. A corollary of the existence of this characteristic halo mass, is that black holes only start to grow significantly when the galaxy's stellar mass is $\sim 10^{10}$ M$_\odot$ (Fig. 4.3, bottom panels). The scatter in the $M_\star - M_\mathrm{h}$ relation results in the transition between dormant and rapidly growing black holes being less well-defined in the $M_\bullet - M_\star$ relation in comparison to a $M_\bullet - M_\mathrm{h}$ plot.

4.2.3 Colour transformation mechanisms

Combining the results of Figs. 4.2 and 4.3 enables us to understand the origin of the evolution in the $u^\star$-$r^\star$ vs $M_\star$ diagram of Fig. 4.1: galaxies with $M_\star < 10^{10}$ M$_\odot$ tend to become red when they become satellites, whereas galaxies above this characteristic mass are quenched by their AGN. This reasoning also explains why the red sequence starts to build-up from both the low-mass and the high-mass ends, leaving initially a noticeable scarcity of red galaxies at $M_\star \approx 10^{9.7}$M$_\odot$ at $z \approx 1$. Such galaxies are too low mass to host a vigorously accreting black hole, yet too massive to be satellites in the typically lower-mass groups at that higher z. It is not until redshifts $z < 1$ that the more massive halos that host $M_\star \approx 10^{10}$ M$_\odot$ satellites appear.

The extent to which EAGLE predicts the characteristic stellar mass above which

AGN quenching occurs, and the evolution of the under-abundance of intermediate-mass red galaxies, not only depends on the details of the subgrid physics but also on the volume that is simulated. This is because massive clusters are under-represented or simply absent due to missing large-scale power in the density field, and poor sampling of rare objects in the relatively small, periodic EAGLE volume of 100^3 cMpc^3. However we believe that the relevant physics described here is robust, and corroborates the similar conclusions of Gabor & Davé (2012) who used an *ad-hoc* model for quenching in massive galaxies, as opposed to our physically motivated subgrid scheme for the EAGLE simulations that are implemented on smaller (sub-kpc) scales.

A corollary of satellite quenching for lower-mass galaxies, and AGN quenching for more massive galaxies, is that these low- and high-mass red galaxies tend to inhabit the *same* dark matter halos. The more massive red galaxy is the central galaxy of this halo and is quenched by its AGN. Conversely, the lower-mass red galaxies are the satellites of a massive central red galaxy. As a consequence, the low- and high-mass red galaxies have similar clustering strengths, with both clustering more strongly than blue galaxies. EAGLE reproduces the observed clustering as a function of colour and luminosity well, as is discussed by Artale et al. (2016). We next investigate how, and at what rate, individual galaxies move through the $u^\star$-$r^\star$ vs $M_\star$ diagram.

4.3 Colour evolution of individual galaxies

4.3.1 The flow of galaxies in the colour-$M_\star$ plane

Fig. 4.4 illustrates how galaxies move through the ($u^\star$-$r^\star$, $M_\star$) plane. Selecting galaxies in equal bins of $u^\star$-$r^\star$ and $\log_{10}(M_\star)$ at one redshift, we measure the median difference in $u^\star$-$r^\star$ and $\log_{10}(M_\star)$ for their descendant galaxies at a second redshift. We plot these differences for galaxies over an equal time period at high ($z \approx 1$) and low ($z \approx 0$) redshift. This is achieved by using two consecutive snapshots ($z = 1.3$ and $z = 1$) for the right panel, corresponding to a time interval

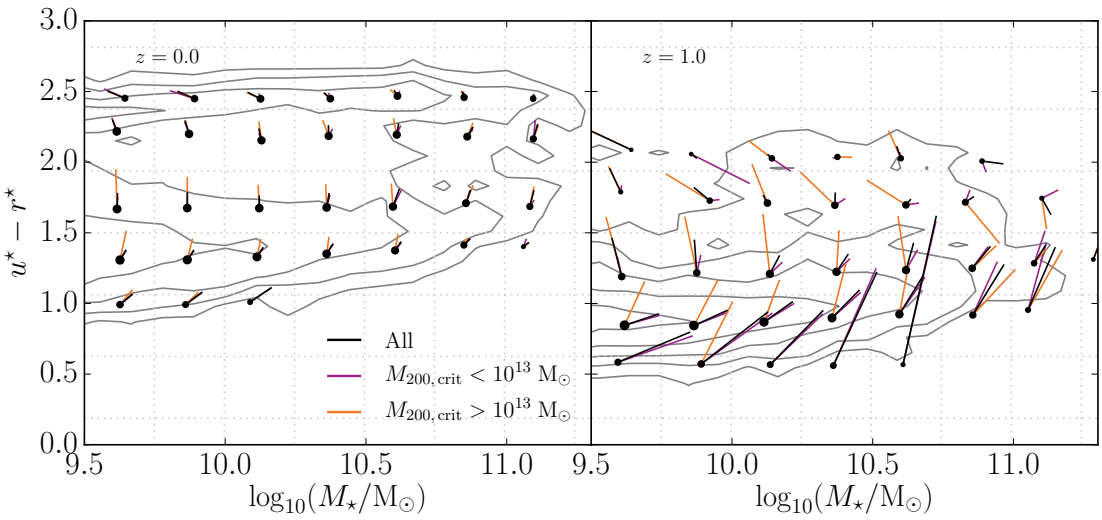

Figure 4.4: The flow of galaxies in ($u^\star$-$r^\star$, $M_\star$) space between two redshifts, z_1 to z_2. *Right panel* shows the galaxy flow between $z_1 = 1.3$ and $z_2 = 1$ snapshots, a period of ≈ 0.9 Gyr. The *left panel* shows the galaxy flow interpolated between the $z = 0.1$ and $z = 0$ snapshots to yield the same time period, with $z_1 = 0.07$ and $z_2 = 0$. *Black circles* represent the mean location of galaxies at z_1, selected in a bin of $u^\star$-$r^\star$- $M_\star$; the size of the circle is proportional to the logarithm of the total stellar mass in galaxies in that bin. *Black vectors* represent the mean motion of the galaxies in that bin between z_1 and z_2. *Orange vectors* (purple vectors) are for those galaxies that at redshift z_2 belong to halos with virial mass $M_{200,\mathrm{crit}} > 10^{13}\mathrm{M}_\odot$ ($M_{200,\mathrm{crit}} < 10^{13}\mathrm{M}_\odot$). Centre coordinates and vectors sampling fewer than 10 galaxies are not plotted. The overall distribution at the later redshift is plotted as *grey contours* for comparison. We do not take into account galaxies merging into hosts that are more than four times their mass, illustrating such mergers in more detail in Fig. 4.8.

of ≈ 0.9 Gyr, and interpolating the galaxy vectors between the lowest redshift snapshots ($z = 0.1$ and $z = 0$) to match the same time period. Descendants that grow in $M_\star$ by a factor > 4 through merging into a more massive host galaxy are eliminated from the measurement, to prevent them contributing extreme vectors to their bin.

For both redshift ranges, it is clear that the colours of galaxies generally become redder, with vectors pointing in the positive $u^\star$-$r^\star$ direction. Exceptions can be seen on the red sequence, in which some red galaxies become star-forming following a gas-rich merger - we discuss the fraction of such 'rejuvenated' galaxies below. Red sequence galaxies show little change in $u^\star$-$r^\star$, but in general those with $M_\star \lesssim 10^{10.75}\mathrm{M}_\odot$ lose mass, with only the most massive red sequence galaxies showing mass growth. Considering that we do not count mergers into hosts of factor > 4 higher $M_\star$, this suggests that red sequence galaxies are being stripped prior to a dry merger with a massive central. We also see evidence of 'mass quenching', with the vectors for blue-cloud selected galaxies becoming steeper with increasing stellar mass. For $M_\star > 10^{10}\mathrm{M}_\odot$ this is attributable to the presence of AGN (Fig. 4.3).

Another notable behaviour seen in Fig. 4.4 is that the bluest galaxies ($u^\star$-$r^\star$ ≈ 0.5, right panel) tend to change their $u^\star$-$r^\star$colour *more* than the average blue galaxy, to the extent that they end-up on the *red* side of the blue sequence at the later redshift. The strong reddening and mass increase of these galaxies suggests that they are starbursts triggered just prior to a merger. Such a scenario is consistent with the fact that a higher proportion of satellites are found at these colours than at the centre of the blue peak (see Fig. 4.2). Note that this effect is only observed for the high redshift panel, partially due to the bluest bins failing to meet the minimum galaxy count criterion of 10. These extreme starbursts are clearly rarer at low redshift.

For each redshift range, we see that galaxies in more massive halos (orange vectors) have a stronger median shift in $u^\star$-$r^\star$ than their low-mass halo counterparts (purple vectors), suggesting that they have a higher likelihood of quenching.Galaxies in massive halos also generally exhibit more mass loss than the over-

all population, showing the role of environment in how galaxies evolve in the ($u^\star$-$r^\star$, $M_\star$) plane.

4.3.2 Evolution of colour populations in EAGLE

To track the evolution of galaxies selected to be *red*, *blue* or *green*, we must first define these populations. To do this we apply cuts that evolve with redshift z for red and blue galaxies.

$$\begin{aligned}(u^\star - r^\star)_{\rm red} &> 0.2\log_{10}(M_\star/{\rm M}_\odot) - 0.25\,z^{0.6} + 0.24 \\ (u^\star - r^\star)_{\rm blue} &< 0.2\log_{10}(M_\star/{\rm M}_\odot) - 0.25\,z^{0.6} - 0.3 \end{aligned} \tag{4.3.1}$$

The green galaxies are taken to be those that are not included in either set. These cuts are defined in an *ad-hoc* way to divide the galaxies into three populations at each redshift. This is a similar procedure to that used by many observational studies, with authors adopting differing functional forms and normalisations (see e.g. the discussion in Taylor et al. 2015). The exact form of the colour cuts is unimportant for our qualitative analysis, but is considered when we discuss our quantitative results.

The evolution of the $u^\star$-$r^\star$ colours of galaxies, selected by colour either at high redshift ($z = 0.5$) or low redshift ($z = 0.1$), is illustrated in Fig. 4.5. We bin galaxies in the three colour bins described above and plot the colour distribution of the descendants and main progenitors (odd and even rows, respectively) of galaxies selected to be red, green or blue (top two, middle two, and bottom two rows, respectively). We use the galaxy merger trees to identify descendants and main progenitors via the EAGLE database (McAlpine et al. 2016, see chapter 2). For each panel, the $u^\star$-$r^\star$ colour distribution of all galaxies at the indicated redshift, with $M_\star > 10^{10}{\rm M}_\odot$, is plotted in grey.

From the top two rows it becomes clear that most galaxies that are red at $z = 0.5$ stay red to $z = 0$, whereas a substantial fraction of galaxies that are red at $z = 0$ were green at $z = 0.1$ or even blue at $z = 0.5$. Galaxies that are green at $z = 0.5$ predominantly become red at $z = 0$, but a fraction of green galaxies becomes blue (third row). Galaxies that are green at $z = 0$ had a range of colours

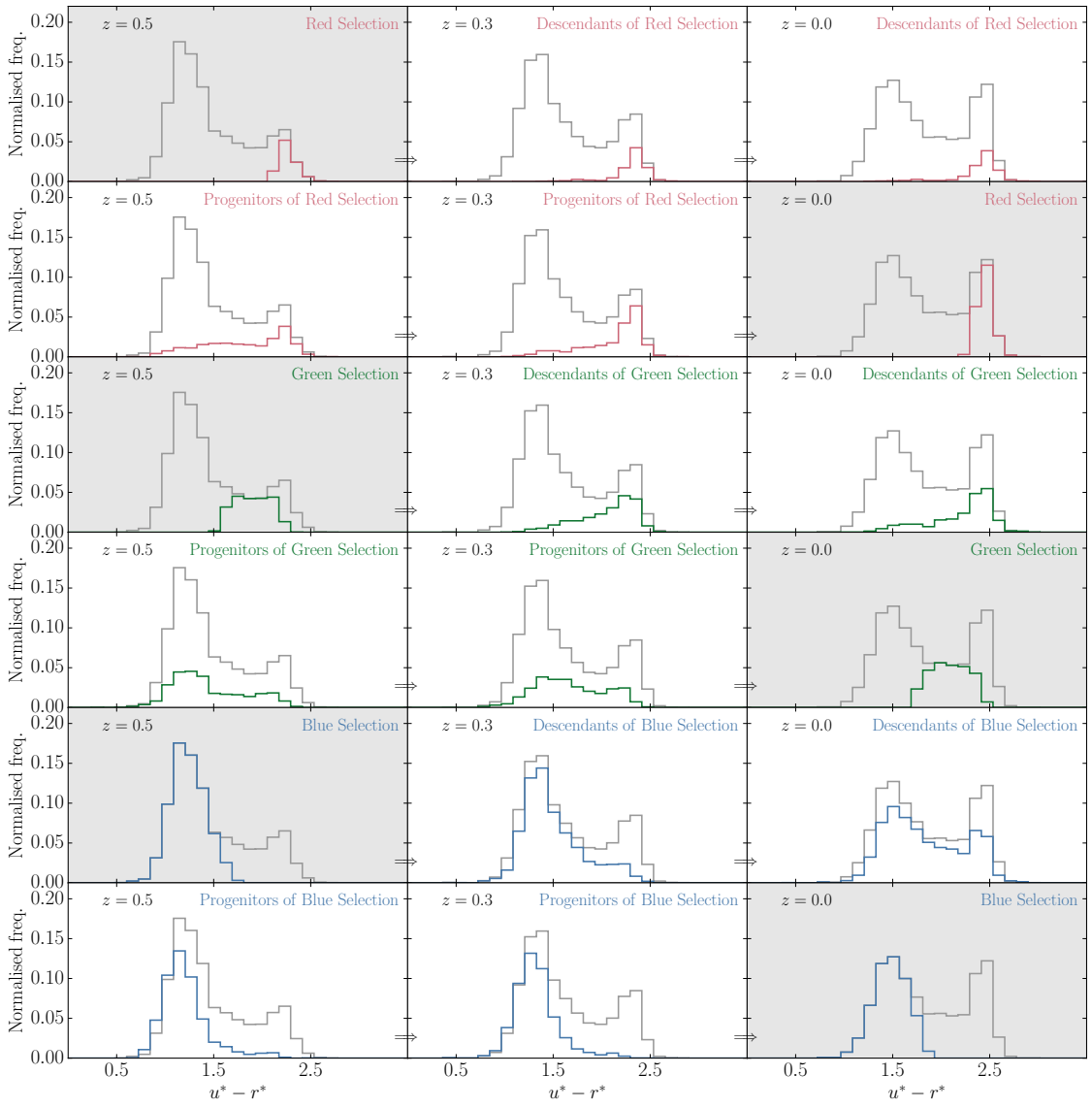

Figure 4.5: *Grey histograms:* $u^\star$-$r^\star$ colour evolution of all galaxies from redshift $z = 0.5$ to $z = 0$, with redshift decreasing from *left* to *right* in each row; each panel is labelled with the corresponding redshift. Only galaxies with $M_\star > 10^{10}\mathrm{M}_\odot$ are included. Colour selections are made using Eq. 4.3.1 and are as follows: *top row:* we select red galaxies at $z = 0.5$ (red histogram) and plot the colour distribution of their descendants at low z as a red histogram. *Second row from top:* we select red galaxies at $z = 0$ (red histogram), and plot the colour distribution of their main progenitors as a red histogram at higher z. *Rows 3 and four from the top:* as above, but for green galaxies. *Bottom two rows:* as above, but for blue galaxies. The background colour of the panel in which galaxies were selected is coloured grey for ease of reference.

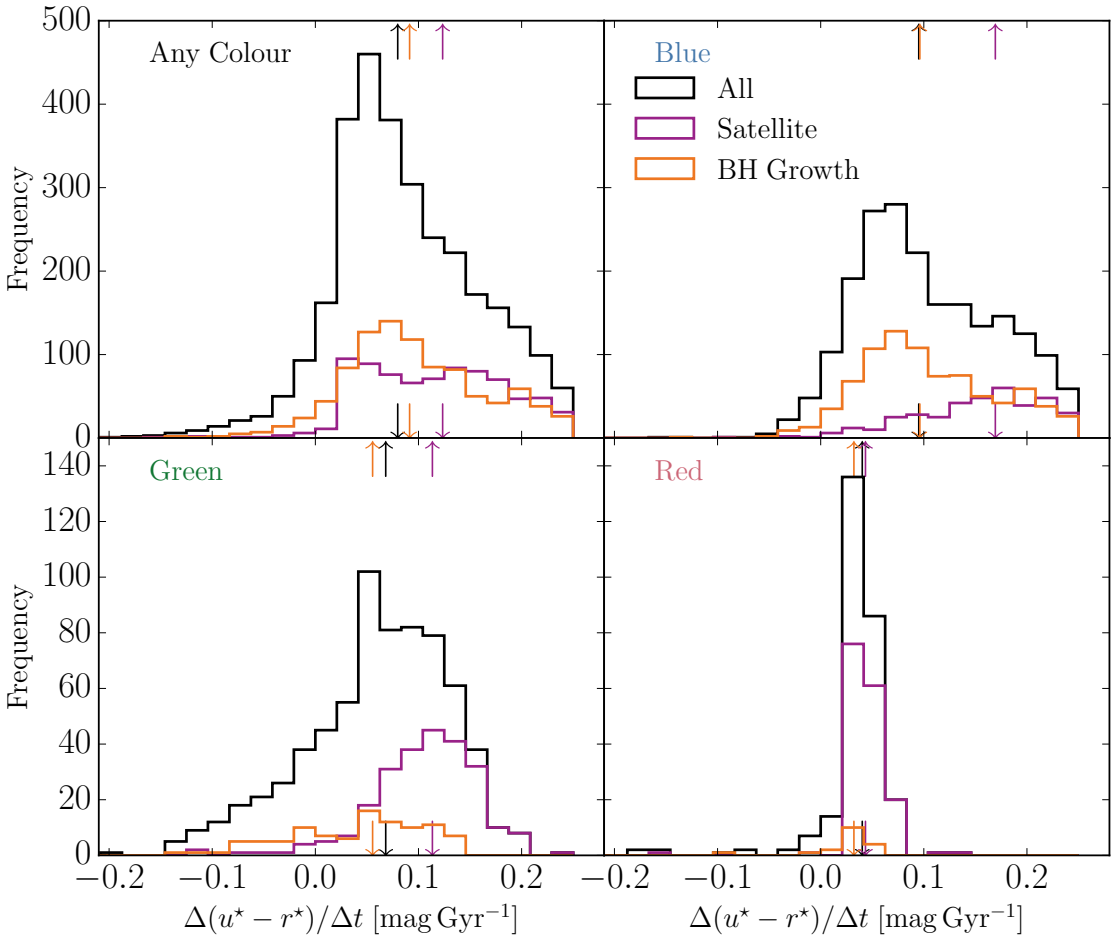

Figure 4.6: **Top left panel:** Distribution of the average rate of colour change over the redshift interval $z = 0.5 \rightarrow 0$, $\Delta(u^\star\text{-}r^\star)/\Delta t$, for galaxies with mass $M_\star > 10^{10}\mathrm{M}_\odot$; vertical arrows (top and bottom) denote the median rate. **Other panels:** As the top left panel, but for galaxies selected at $z = 0.5$ to be blue, red, and green (clock wise from top right). In each panel, *black lines* refer to all selected galaxies, *purple lines* to the fraction that at $z = 0.5$ are satellites, *orange lines* to the fraction whose central black hole has grown by at least a factor of 1.5 between $z = 0.5$ and $z = 0$. The rate of change of the median colour is typically small, but individual galaxies can change colour more dramatically over this period, $-0.2 < \Delta(u^\star\text{-}r^\star) < 0.25$ up to $|\Delta(u^\star - r^\star)/\Delta t| = 0.25$ Gyr^{-1}, particularly for green and blue galaxies.

at $z = 0.5$, although they were bluer than average (fourth row). The similar and dominant blue (red) fractions in the two green progenitor (descendant) panels suggests that the typical time to transition through the green valley is shorter than the redshift intervals used here. Finally, galaxies that are blue at $z = 0.5$ have a large range of colours at $z = 0$ with a distribution that is similar to that of the population as a whole (fifth row), whereas galaxies that are blue at $z = 0$ were mostly blue at $z = 0.5$ as well (bottom row).

The rate at which galaxies with stellar mass $M_\star > 10^{10}\mathrm{M}_\odot$ at $z = 0.5$ change $u^\star$-$r^\star$ colour over the redshift range $z = 0.5$ to $z = 0$ (elapsed time $\Delta t \approx 5$ Gyr) is quantified in Fig. 4.6. We identify the $z = 0$ descendant for all galaxies with $M_\star > 10^{10}\mathrm{M}_\odot$ at $z = 0.5$, compute the change in colour, $\Delta(u^\star$-$r^\star)$, and plot a histogram of rates, $\Delta(u^\star$-$r^\star)/\Delta t$. We also identify if a galaxy is a satellite at $z = 0.5$, or if the mass of its central black hole increases by a factor ≥ 1.5. This threshold is chosen to represent an above average black hole growth, while still providing a significant sample of galaxies.

The rate of change of the *median* colour of galaxies is small, $\Delta(u^\star$-$r^\star)/\Delta t \approx 0.08$ mag Gyr^{-1} to the red, but is larger for galaxies whose black hole grows more than average ($\Delta(u^\star$-$r^\star)/\Delta t \approx 0.09$ mag Gyr^{-1}) or those that are satellites ($\Delta(u^\star$-$r^\star)/\Delta t \approx 0.12$ mag Gyr^{-1}). Galaxies that are red at $z = 0.5$ typically change little in colour to $z = 0$, ($\Delta(u^\star$-$r^\star)/\Delta t \approx 0.03$ mag Gyr^{-1}), except for the occasional outlier that becomes blue. The rate of change of the median colour is larger for galaxies that are green or blue at $z = 0.5$, with individual galaxies changing colour more rapidly, both to the red and to the blue. Galaxies that are satellites can undergo rapid changes to the red, $\Delta(u^\star$-$r^\star)/\Delta t \gtrsim 0.2$ mag Gyr^{-1}, whether blue or green at $z = 0.5$. Note that this rate is averaged over a considerable period (≈ 5 Gyr), and instantaneous rates of colour change for galaxies can be much higher, as explored below.

4.3.3 Colour-mass tracks of individual galaxies

We have examined a large number of tracks of individual galaxies in ($u^\star$-$r^\star$, $M_\star$) space and have identified three generic tracks of central galaxies that we illustrate

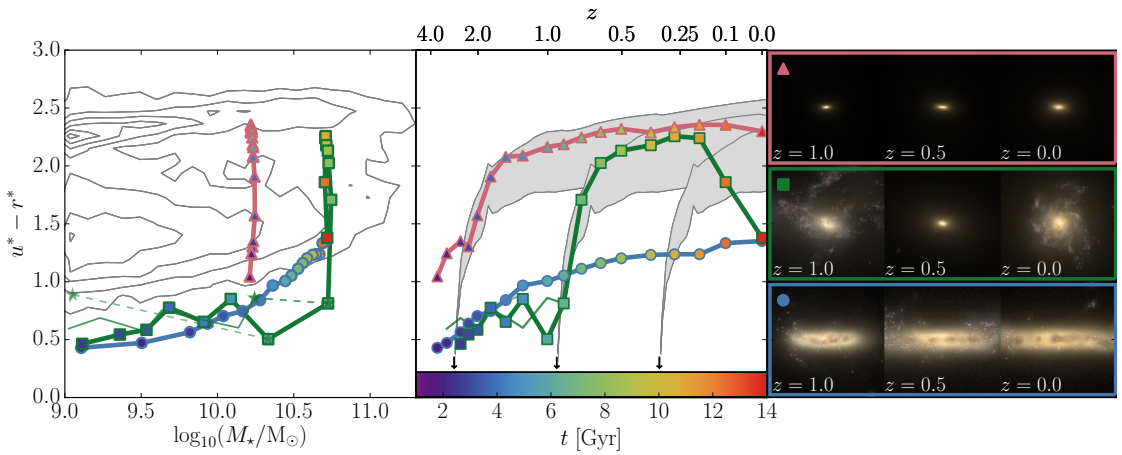

Figure 4.7: Tracks illustrating the change in mass, colour and morphology, of a quiescently star-forming galaxy (thick blue curve & filled circles), a rapidly quenched galaxy (thick red curve & filled triangles), and a rejuvenated galaxy (thick green curve & filled squares). Thin tracks show merging satellites (see caption of Fig. 4.8). *Left and middle panels:* tracks in the ($u^\star$-$r^\star$, $M_\star$) plane (left panel) and colour as function of time and redshift (middle panel), from redshift $z = 4$ to $z = 0$. Symbol colour corresponds to cosmic time as per the colour bar. Background contours in the left panel correspond to the $z = 0$ colour-$M_\star$ distribution. Grey tracks in the middle panel depict the colour evolution of a passively-evolving coeval starburst (indicated with an arrow). Each burst is assumed to be composed of stars with an exponential distribution of metallicities with given mean. The width of the grey region corresponds to varying this mean metallicity over the range of [1/3,3] times solar ($Z_\odot = 0.0127$). *Right panel:* edge-on gri-composite image of side length 40 pkpc, calculated using ray-tracing to account for dust (described in chapter 5), for the $z = 0$ galaxy and its $z = 0.5$ and $z = 1$ main progenitor. The corresponding symbol for each track is indicated on galaxy images.

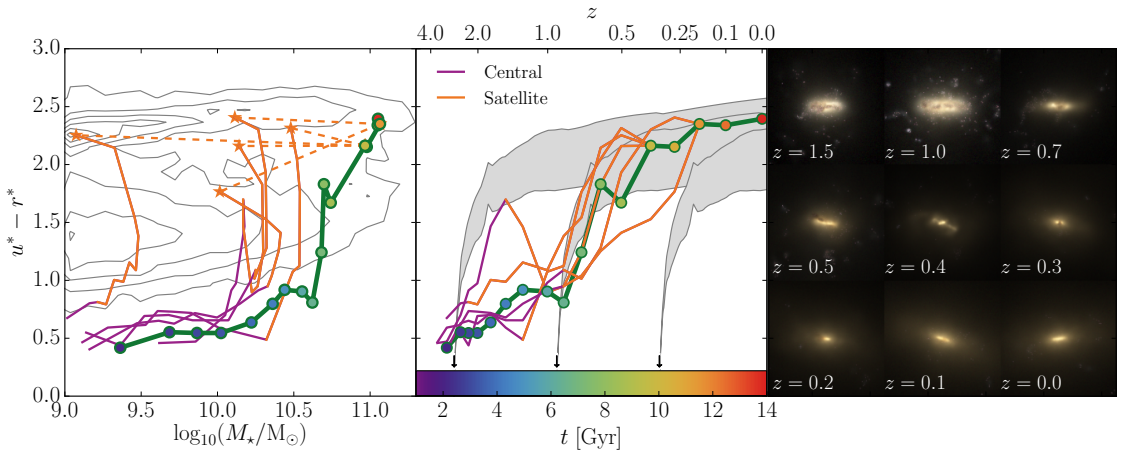

Figure 4.8: Same as Fig. 4.7, but for a massive galaxy (green track & filled circles) and galaxies that merge with it (thin tracks). Tracks for merging galaxies (merging with $M_\star > 10^9$ M$_\odot$) are coloured *purple* when they are centrals, and *orange* when they are satellites as indicated in the legend; a star identifies the last snapshot before the satellite merges with the massive galaxy, and the track is linked to that of the massive galaxy at the following snapshot by a dashed line. The right panel shows edge-on gri-composite images of the central galaxy of side length 40 pkpc, at various redshifts labelled in each separate panel.

Table 4.1: Properties of the galaxies plotted as main tracks in Figs. 4.7-4.8. The Symbol/Figure is given to identify the galaxies on the figures. For each galaxy we quote the unique galaxy identifier (GalaxyID) taken from the EAGLE public database (McAlpine et al., 2016), the $z = 0$ black hole mass ($M_\bullet$), and indicate whether a galaxy was ever classified as a satellite (y) or not (n).

Sym./Fig.	GalaxyID	$M_\bullet/\mathrm{M}_\odot$	Satellite
Circle/4.7	18169630	7.09×10^6	n
Square/4.7	15829793	1.03×10^8	n
Triangle/4.7	14096270	6.00×10^7	n
Circle/4.8	15197399	1.84×10^8	y

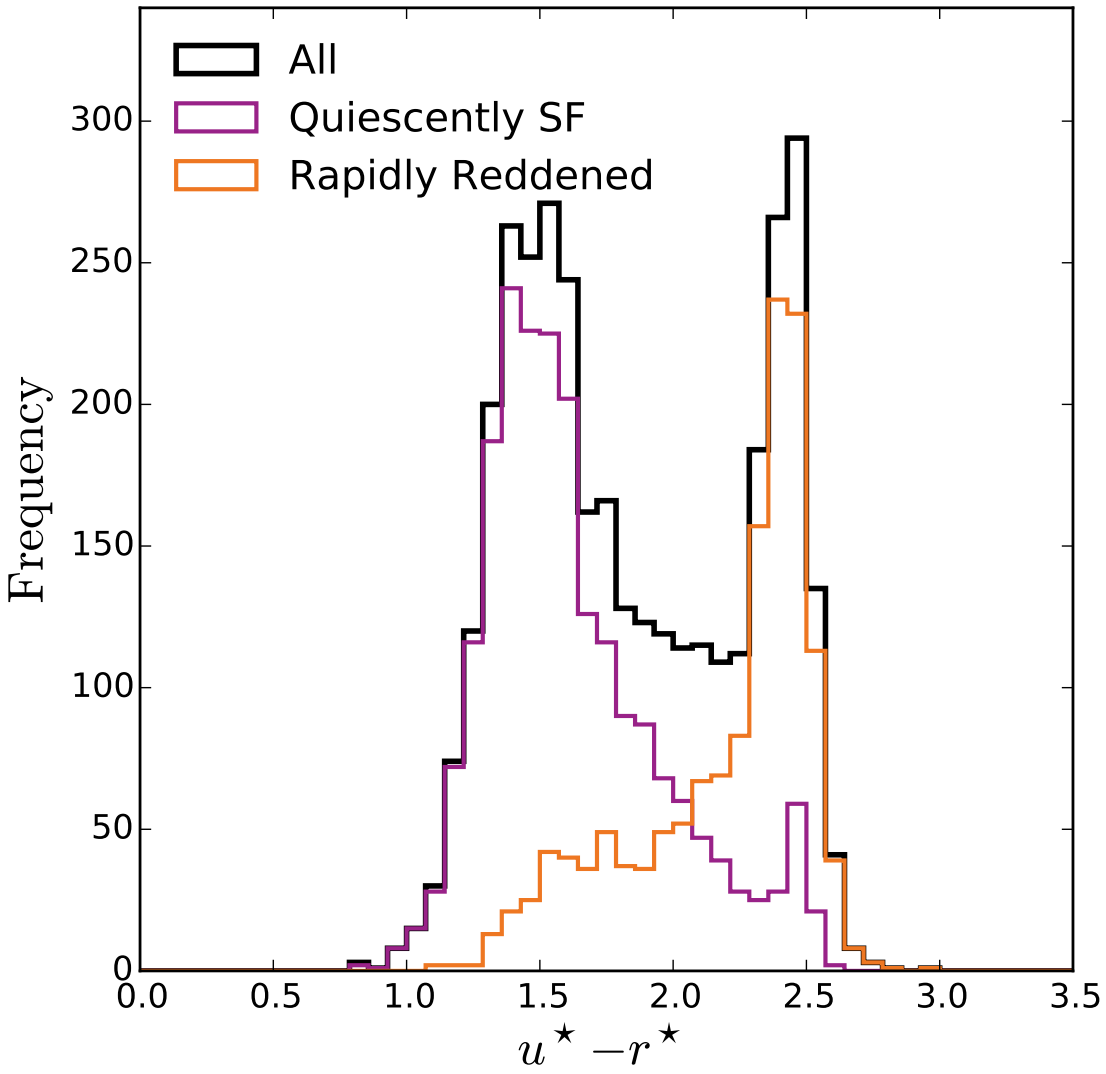

Figure 4.9: $u^\star$-$r^\star$ colour distribution for $M_\star > 10^{10}\mathrm{M}_\odot$ galaxies at $z = 0$. Galaxies identified as 'quiescently star-forming 'are plotted in *purple*, while those that underwent a rapid colour transition to the red are plotted in *orange*. The combined distribution is plotted in black. We see that the quiescently star-forming galaxies predominately inhabit the present-day blue cloud, but with a tail to red colours. Galaxies that underwent a rapid reddening ($\Delta(u^\star\text{-}r^\star) > 0.8$ in 2 Gyr) are predominately red at $z = 0$, but the distribution has a blue tail resulting from recent star formation.

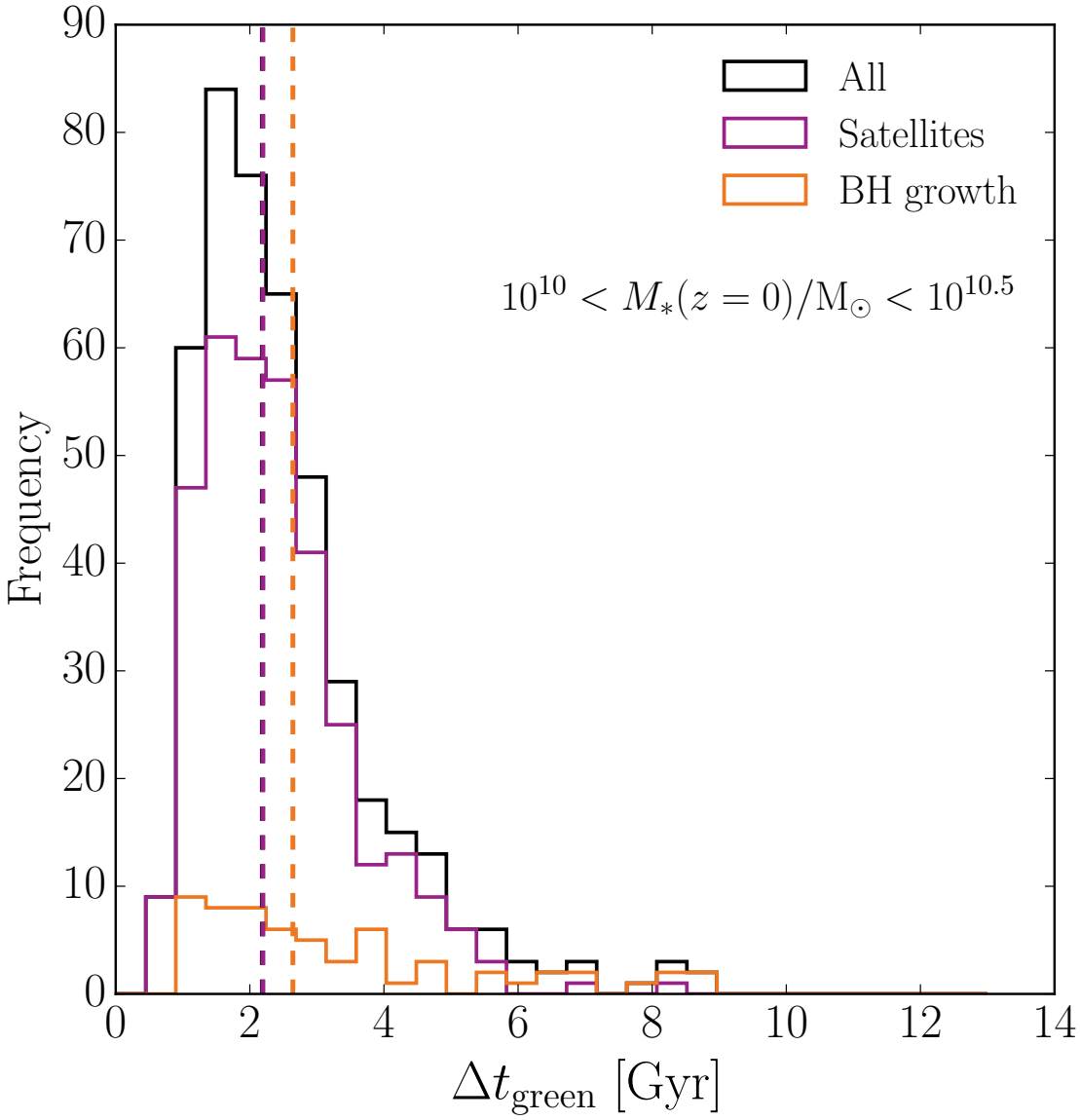

Figure 4.10: Histograms of the time interval galaxies spent crossing the green valley from being blue to becoming red, $\Delta t_{\mathrm{green}}$ (see text). The black histogram is for all galaxies in the current mass selection, *purple* histogram for galaxies that are satellites at $z = 0$, *orange* histogram for galaxies whose black holes grew by more than a factor of 1.5 while crossing the green valley. Median values for the selections are plotted as dashed lines with the corresponding colour. This panel shows galaxies selected in the $z = 0$ mass range $10^{10} < M_\star/\mathrm{M}_\odot < 10^{10.5}$. Satellite galaxies dominate in both mass ranges. The transition time-scale for a blue galaxy to turn red is typically $\lesssim 2$ Gyr, which corresponds to the time a blue population of stars reddens passively, as seen in Fig.4.7. {*Continued on next page*}

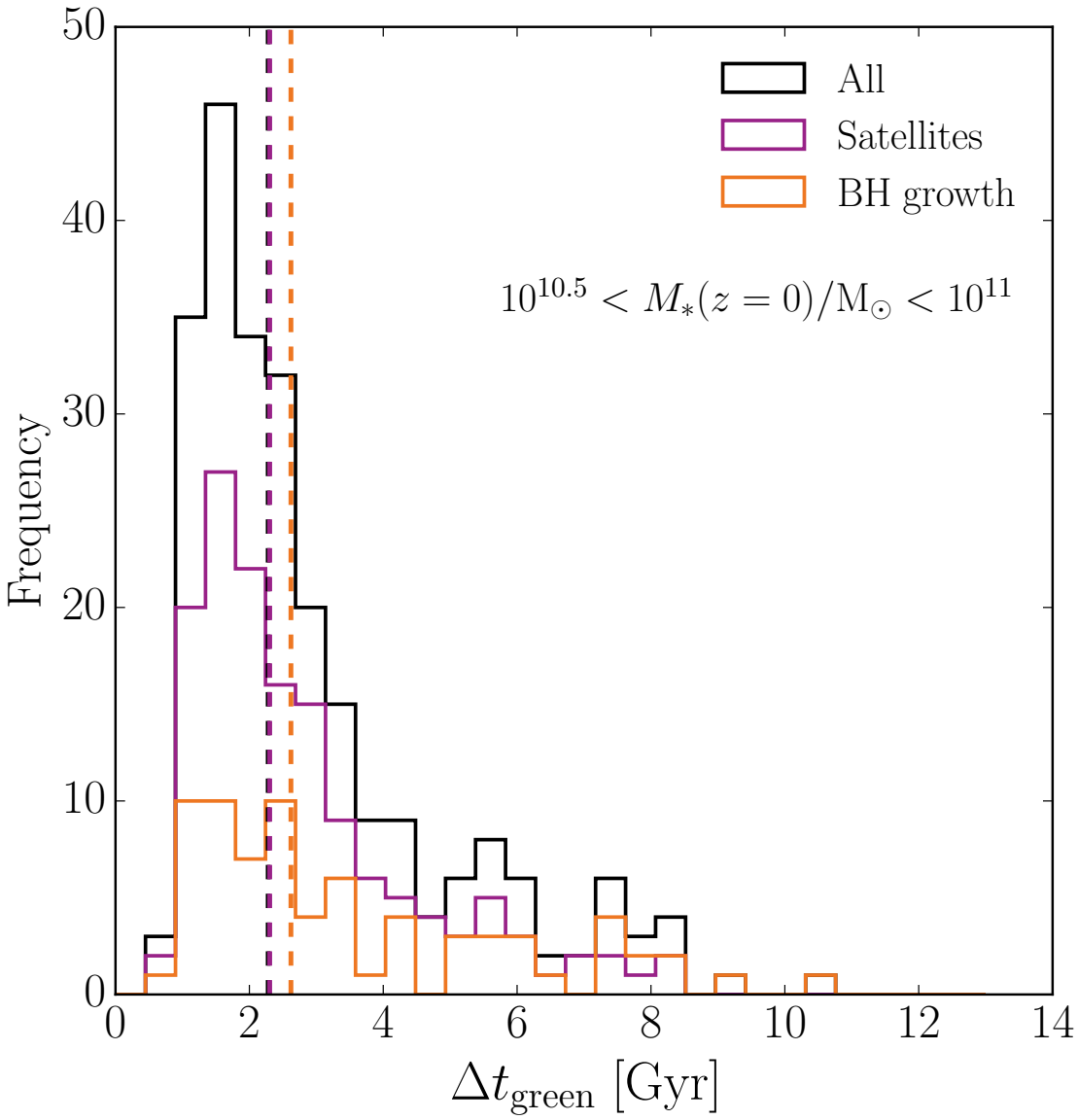

Figure 4.10: {*Continued from previous page*} As the previous panel, now corresponding to the $10^{10.5} < M_\star/\mathrm{M}_\odot < 10^{11}$. The typical timescales are very similar for both mass ranges.

in Fig. 4.7. In Fig. 4.8 we also show the track of a central galaxy that is very massive at $z = 0$ ($M_\star \sim 10^{11}\mathrm{M}_\odot$), to illustrate individual tracks of satellites that merge with it. More details of the four galaxies tracked in these panels are given in Table 4.1. The time-scale over which galaxies transition to the red sequence is compared to that of a passively evolving population, by plotting (single) starburst tracks initiated at different times (grey curves in middle panels).

The blue track in Fig. 4.7 is for a galaxy that remains in the blue cloud down to $z = 0$, forming stars in a blue disc that grows in time. As its sSFR decreases with time, and the contribution of an older population of stars becomes more important, it slowly reddens, with $\Delta(u^\star\text{-}r^\star) \approx 0.2$ from $z = 1$ to $z = 0$ (elapsed time ≈ 8 Gyr). We see from Table 4.1 and Fig. 4.3 that the black hole mass is ≈ 0.6 dex lower than the median value for its stellar mass (at approximately the 3rd percentile of galaxies for that $M_\star$), suggesting low levels of black hole feedback in the galaxy's history.

The red track in Fig. 4.7 corresponds to a galaxy that becomes red more rapidly, reddening by $\Delta(u^\star\text{-}r^\star) \approx 1$ in ≈ 2 Gyr, joining the red sequence at $z = 2$. From then on, its colour or stellar mass hardly changes; it has been a very compact elliptical galaxy since at least $z = 1$, maintaining a stellar half-mass radius of < 2.3 pkpc. The similar rate of colour transition for this galaxy to that of an instantaneous starburst suggests rapid quenching of star formation. Considering the black hole mass in Table 4.1 and the bottom-left panel Fig. 4.3 shows that the galaxy has a central black hole mass ≈ 0.6 dex higher than the median black-hole stellar mass relation (at approximately the 99th percentile of galaxies for that $M_\star$), suggestive of black hole quenching.

The thick green track shows a galaxy that reddens at a similar rate ($\Delta(u^\star\text{-}r^\star) \approx 1.5$ in ≈ 2 Gyr) at $z \approx 1$, after undergoing a near-equal mass merger (thin green line indicates the track of the other galaxy) leading to significant AGN growth. It then changes morphology from being a disturbed disc to a compact elliptical at $z = 0.5$. At redshift $z = 0.25$, it starts forming stars again, turning blue ($\Delta(u^\star\text{-}r^\star) \approx -1$) over ≈ 2 Gyr. By $z = 0$,it has grown significantly in size, with a prominent bulge and an extended distribution of stars around it. The value of

$M_\bullet$ in Table 4.1 puts the black hole mass at approximately the 75th percentile of galaxies for that stellar mass.

Note that the black hole masses for galaxies selected in Fig. 4.7 (and listed in Table 4.1) are all in the upper or lower quartiles for their stellar mass. While galaxies with average black hole masses have diverse histories, more extreme $M_\bullet$ values can be indicative of the certain types of track represented here. The quiescently star forming and quenched galaxies are both associated with particularly low and high levels of black hole growth respectively. The rejuvenated galaxy has a high black hole mass, though less extreme. The black hole growth is associated with a quenching event at $z \approx 1$, but the galaxy re-accretes gas and is able to recommence prolonged (> 2 Gyr) star formation in spite of its high black hole mass. We saw in Fig. 4.3 that for $z = 0$ and at these masses the overall correlation between galaxy colour and the residuals of the $M_\bullet$-$M_\star$ relation is rather weak.

The massive $z = 0$ galaxy in Fig. 4.8 is a blue star-forming disc until just below $z = 1$, after which it becomes red and evolves into an elongated elliptical. Thin lines show the tracks of five galaxies that merge with it, with the line colour changing from purple to orange while these galaxies become satellites. Examination of these tracks reveals that while some galaxies become red when they are still centrals, most galaxies quench after being identified as satellites. This suggests that satellite identification is a good predictor of colour change in EAGLE, particularly for galaxies falling into a more massive halo. The satellite tracks exhibit a characteristic shape of rapid quenching followed by stellar mass loss, as the galaxy is stripped and eventually merges. We also see that the central galaxy exhibits quite a stochastic colour evolution compared to those in Fig. 4.7. This is perhaps due to the higher frequency of satellite interactions and mergers for the higher mass halo represented in Fig. 4.8, with only the rejuvenated track of Fig. 4.7 showing (two) mergers with satellites of $M_\star > 10^9 \mathrm{M}_\odot$.

The heterogeneous colour evolution of galaxies illustrated in Fig. 4.7 and 4.8 are consistent with observations that the green valley population is diverse (e.g. Cortese & Hughes, 2009; Schawinski et al., 2014). In particular, Cortese & Hughes (2009) also find examples of galaxies moving off the red sequence through re-

accretion of gas reminiscent of the green track in Fig. 4.7.

To quantify the fraction of galaxies that undergo a rapid colour transformation, we trace the main progenitors of all galaxies with mass $M_\star > 10^{10}\mathrm{M}_\odot$ at $z = 0$ back in time (a sample of ≈ 3000 galaxies). We find that the fraction of galaxies with at least one $\Delta(u^\star\text{-}r^\star) > 0.8$ change over any 2 Gyr period in their history is ≈ 40 per cent. We will refer to such galaxies as rapidly reddening galaxies; they tend to follow a track similar to the red track in Fig.4.7. Of the galaxies that redden quickly, ≈ 1.6 per cent undergo a colour change to the *blue* of $\Delta(u^\star\text{-}r^\star) < -0.8$ over a 2 Gyr period. We will refer to this small fraction of galaxies as 'rejuvenated'; they follow a track similar to the green track in Fig. 4.7[1]. Galaxies that do not ever undergo such a rapid reddening event make-up 60 per cent of the sample. We will refer to these as 'quiescently star-forming' galaxies; they follow a track similar to the blue track in Fig.4.7.

Fig. 4.9 shows the distribution of $z = 0$ colours for $10^{10} < M_\star/\mathrm{M}_\odot < 10^{10.5}$ galaxies classified as having undergone a rapid transformation to redder colour (orange histogram), and those that never underwent such a rapid reddening (quiescently star-forming galaxies, purple histogram). A small fraction of galaxies become red without ever experiencing a rapid reddening event: this is the tail of the purple histogram towards red $u^\star$-$r^\star$ colour. Similarly, there is a tail to blue $u^\star$-$r^\star$ colour in the orange histogram, representing galaxies that underwent a rapid colour transition to the red, followed by more recent star formation turning them blue once more. The fraction of these galaxies is much higher than the 1.6 per cent of galaxies we classified as 'rejuvenated': the majority of galaxies that are blue now but were red in the past ($\approx 10\%$ of total), became blue more gradually than the $\Delta(u^\star\text{-}r^\star) = -0.8$ over 2 Gyr that we used to define 'rejuvenated galaxies'.

Galaxies must become blue rapidly or traverse the entire green valley to meet these criteria. However, it is also interesting to note the probability that a galaxy

[1]Galaxies may also undergo slower colour transitions due to secular evolution, and the number density of galaxies does not remain constant because of mergers. These quoted fractions therefore inevitably depend on how galaxies are selected. *i.e.* the colour choice we made in Eq. 4.3.1.

identified in the green valley is on a bluer trajectory in the colour-$M_\star$ plane. We identify this for green valley galaxies at $z < 2$, enforcing that a galaxy must undergo a monotonic colour change of $\Delta(u^\star\text{-}r^\star) < -0.05$ to be deemed significant (above the level of photometric error, e.g. Padmanabhan et al., 2008). We find that the EAGLE green valley galaxies have a 17% chance of being on a significantly blue trajectory. Conversely, we find the probability of a green galaxy being on a significantly red trajectory to be 75%, taking $\Delta(u^\star\text{-}r^\star) > 0.05$ as the criteria for being significant.

The tracks of individual galaxies enable us to characterise the colour transition time-scale of a galaxy by the time interval, $\Delta t_{\rm green}$, it spent in the green valley on its way from the blue cloud to the red sequence. We calculate $\Delta t_{\rm green}$ as follows: using Eq. (4.3.1) we select red galaxies at $z = 0$ and trace their main progenitors back in time to identify the earliest time they became red (t_1) and the last time prior to t_1 that they were blue (t_2). Histograms of colour transition times, $\Delta t_{\rm green} \equiv t_1 - t_2$, for galaxies that at $z = 0$ have $10^{10} < M_\star/{\rm M}_\odot < 10^{10.5}$ and $10^{10.5} < M_\star/{\rm M}_\odot < 10^{11}$ are plotted in Fig. 4.10 (top and bottom panels, respectively).

The mode of the colour transition time distribution is ≈ 1.5 Gyr, with a median of ≈ 2 Gyr, mostly independent of whether quenching is likely due to becoming a satellite or AGN activity (purple and orange histograms, respectively). This is the time-scale for a passively evolving blue population of stars to turn red, as can be seen from Fig.4.7. Strikingly, there is a very long tail to high values in the distribution of $\Delta t_{\rm green}$ as inefficient quenching allows a small fraction of galaxies to spend a long time in the green valley before eventually turning red, whether due to becoming a satellite or hosting an AGN. Though quenched galaxies are more prevalent in high-mass halos, the colour transition time-scales show little dependence on halo mass. Despite this, the longest time-scales we measure are for halo masses $< 10^{13}$ ${\rm M}_\odot$.

The time-scales for colour transition and the quenching of star formation are clearly linked, however colour transition times are longer due to the passive evolution of stellar populations. This is illustrated by the grey curves in Fig. 4.7 and

4.8, showing that the colour transition time for an SSP is ≈ 2 Gyr. The quenching time-scales of observed satellites presented by e.g. Muzzin et al. (2014) and Wetzel et al. (2013) are significantly shorter, typically $\lesssim 0.5$ Gyr and $\lesssim 0.8$ Gyr respectively. Although the $u^\star$-$r^\star$ colour index alone is not sensitive enough to resolve these quenching times, the typical colour transition times of EAGLE galaxies are consistent with such rapid quenching.

However, there are cluster studies in the $0 < z < 0.5$ redshift range that infer longer timescales ($\gtrapprox 1$ Gyr, e.g. von der Linden et al., 2010; Vulcani et al., 2010; Haines et al., 2013). Fig. 4.10 does show a tail to longer quenching times for both AGN and satellites, though they are not typical at low redshift. Ultimately, the different observational tracers and modelling used to infer quenching times are still subject to significant systematics that may explain the different measurements (McGee et al., 2014). In particular, colour transition and quenching timescales are not equivalent, and galaxies may move between the red and blue populations when observed in optical and UV colour (e.g. Cortese, 2012). As UV-optical colours are more sensitive to the very youngest stellar populations (e.g. Wyder et al., 2007), these provide a more sensitive probe of the physical quenching timescale than $u^\star$-$r^\star$. Remaining at optical-NIR wavelengths, 'super-colours' may also prove a more sensitive probe to the quenching timescale; these are linear combinations of photometric bands optimised through principle component analysis, and have been used to effectively separate post-starburst galaxies (Wild et al., 2014). An analysis of the physical quenching timescale and its evolution, using both simulated values and observable proxies, is left to a future study.

4.4 Conclusions

We have investigated the evolution and origin of the colours of galaxies in the EAGLE cosmological hydrodynamical simulation (Schaye et al., 2015; Crain et al., 2015). We apply the single population synthesis models from Bruzual & Charlot (2003) to model galaxy colours in the absence of dust, as described in chapter 3. We also use galaxy merger trees to trace descendants as well as main progenitors

through time.

The $u^\star$-$r^\star$ vs $M_\star$ diagram is bimodal at redshift $z = 0$, with a clearly defined red sequence of quenched galaxies, and a blue cloud of star-forming galaxies. The scatter and slope of the red sequence are both determined mainly by stellar metallicity, while the normalisation additionally depends on stellar age (Fig. 4.1). The scatter in the blue cloud, in contrast, is mostly due to scatter in the specific star formation rate at fixed stellar mass ($\mathrm{sSFR} = \dot{M}_\star/M_\star$). The slope of blue cloud colours versus $M_\star$ is similar to that of the red sequence, but as their origins are different, this is coincidental. At higher z, both colour sequences become bluer, and the red sequence becomes less populated until it has mostly disappeared by $z = 2$.

From studying the evolution of EAGLE galaxies in $u^\star$-$r^\star$ and $M_\star$, we note that in general:

- Galaxies in EAGLE turn red either because they become satellites (mainly at lower masses, see Fig. 4.2) or because of feedback from their central supermassive black hole (mainly for more massive galaxies, see Fig. 4.3). As a consequence, the red sequence builds-up from both the low-mass and high-mass sides simultaneously, with the low-mass red galaxies being satellites of the massive red centrals that are quenched by their AGN. This results in a dearth of red galaxies at intermediate mass, $M_\star \sim 10^{10}$ M$_\odot$, at $z \approx 1$ - such galaxies are too low mass to host a massive black hole, but too massive for a large fraction of them to be satellites in the EAGLE volume. While we believe the existence of such a deficit is unlikely to change with increased simulation volume, it should be noted that the limited volume and lack of large scale power in the EAGLE 100^3 Mpc^3 simulation may affect the depth of the deficit.

- The colour evolution in the blue cloud is driven by the decrease in the sSFR rates of star-forming galaxies with cosmic time.

- The characteristic time scale for galaxies to cross the green valley, from the blue cloud to the red sequence (Fig. 4.10), is $\Delta t_{\mathrm{green}} \approx 2$ Gyr, mostly inde-

pendent of galaxy mass and cause of the quenching. It is determined by the rate of evolution of a passive population of blue stars to the red. This timescale is consistent with rapid or instantaneous quenching of star formation, as inferred from observations of satellite galaxies by Muzzin et al. (2014). The distribution of $\Delta t_{\rm green}$ has an extended tail to ~ 10 Gyr: a small fraction of galaxies remain green for a long time. However, most galaxies spend only a short time, $\Delta t_{\rm green} \lesssim 2$ Gyr, in the green valley - it is not easy being green.

We identified three characteristic tracks that galaxies follow in the $u^\star$-$r^\star$vs $M_\star$ diagram (Figs. 4.7 and 4.8). *Quiescently star-forming galaxies* remain in the blue cloud at all times, without sudden reddening episodes of $\Delta(u^\star\text{-}r^\star) > 0.8$ in any 2 Gyr interval. Nearly 60 per cent of galaxies with stellar mass at $z = 0$ greater than $M_\star = 10^{10}$ M$_\odot$ fall into this category (see Fig. 4.9). The remaining 40 per cent of galaxies do undergo such sudden episodes of star formation suppression. The majority of these *rapidly reddened galaxies* move onto the red sequence permanently as per the evolutionary picture of Faber et al. (2007), however we find that 1.6 per cent undergo an episode in which star formation causes the galaxy to change colour to the blue again, having $\Delta(u^\star\text{-}r^\star) < -0.8$ over a 2 Gyr period (e.g. Fig 4.7). The fraction of such *rejuvenated galaxies* is thus very small. Nevertheless, a much larger fraction of the galaxies that at $z = 0$ are blue were red in the past: the rate of colour transition of galaxies to the blue is generally significantly slower than the quenching timescale. We also find that the fraction of green valley galaxies on blue trajectories (where $\Delta(u^\star\text{-}r^\star) < -0.05$) at a given instance from $z < 2$ is larger still at 17%, implying that only a subset transition completely from red to blue and remain there.

Chapter 5

Dust Radiative Transfer with SKIRT

This chapter comprises an edited version of the article: **Optical colours and spectral indices of z=0.1 EAGLE galaxies with the 3D dust radiative transfer code SKIRT**, *James W. Trayford, Peter Camps, Tom Theuns, Maarten Baes, Richard G. Bower, Robert A. Crain, Madusha L. P. Gunawardhana, Matthieu Schaller, Joop Schaye and Carlos S. Frenk*, preprint available (`arXiv:1705.02331`), accepted for publication in *MNRAS*, with appendices compiled in Appendix B.

5.1 Introduction

The treatment of dust exemplifies a major area of uncertainty in forward modelling. While dust represents a marginal fraction of the mass in galaxies and simulations do not typically model an explicit dust phase (with exceptions, e.g. Bekki, 2015; Aoyama et al., 2016; McKinnon et al., 2016), interstellar dust can play an important role in processing the light we observe from galaxies.

On average, about a third of the UV plus optical starlight emitted in local star-forming galaxies is absorbed by dust and re-radiated at longer wavelengths (e.g. Popescu & Tuffs, 2002; Viaene et al., 2016b). The effect of dust attenuation introduces various systematics, particularly for young stellar populations: the cross-sections for absorption and scattering generally increase with the frequency of incident light, such that the relatively blue emission from young stars is more affected. But the impact of dust also depends on the morphology and orienta-

tion of the galaxy: young stellar populations are typically found in a thin disc and near the dense, dusty ISM regions from which they formed. These regions are therefore likely to have relatively high dust obscuration, and, if this is not accounted for, may affect inferred structural measures of galaxies such as scale lengths/heights and bulge-to-disc ratios. Because young stars may be more obscured than old stars, the *attenuation curve* (the ratio of observed over emitted radiation as function of wavelength for the observed galaxy) of a galaxy differs in general from the *extinction curve* that describes the wavelength dependence of the photon-dust interaction. The modelling of dust is clearly an important aspect of comparing models to observations, and is the subject of this chapter.

An idealised dust model is that of an intervening dust screen with a wavelength-dependent optical depth, the attenuation of which can be computed analytically. The geometry of the dust distribution and some effects of scattering, can be accounted for to some extent by making the attenuation curve 'greyer' (i.e. less wavelength dependent) than the extinction curve (e.g. Calzetti, 2001), and/or by using multiple screen components. Chapter 3 adopted the two component screen model of Charlot & Fall (2000) to represent dust absorption in the EAGLE simulations (Schaye et al., 2015) when generating broad-band luminosities and colours. Absorption is boosted by a fixed factor for young (< 30 Myr) stars in this model, and the overall optical depths depend on the gas properties of each simulated galaxy with additional scatter to account for orientation dependence[1].

Chapter 3 showed that optical colours and luminosities generated for EAGLE galaxies are broadly compatible with the GAMA measurements, while exhibiting some notable discrepancies. In particular, the modelling resulted in a *more* pronounced bimodal distribution of colours at a given stellar mass than observed. In particular, model colours exhibited bimodality amongst even the most massive galaxies for which bimodality is absent in the data. A related discrepancy was that the red and blue fractions were also somewhat inconsistent between model and data, with the model yielding an excess of blue galaxies at high $M_\star$. The

[1]The GD+O photometry developed in chapter 3 is compared to the radiative transfer solution, and referred to throughout this chapter.

cause of these discrepancies was attributed to both differences between the intrinsic properties of the simulated and observed galaxy populations (higher specific star formation rates in EAGLE), as well as uncertainties in the modelling of the photometry (especially dust effects). Of particular concern was that lower than observed average star formation rates in EAGLE galaxies (Furlong et al., 2015) and underestimated reddening could have a compensatory effect, potentially yielding a fortuitous agreement with GAMA colours.

The dust screen model applied in chapter 3 may not represent attenuation in EAGLE galaxies well. Indeed, the effects of complex geometries cannot be captured by a screen (e.g. Witt et al., 1992): there are degeneracies between dust geometry and dust content. Colours of galaxies where dust and stars are well mixed can be confused with dimmer dust-free galaxies if a screen is assumed (e.g. Calzetti, 2001; Disney et al., 1989). Screens also neglect scattering into the line of sight, or attempt to account for it with approximative absorption. With scattering being as important as geometry at optical wavelengths, and often producing effects entirely dissimilar to absorption, a screen-based approximation is often insufficient (Baes & Dejonghe, 2001; Byun et al., 1994)

While screen model parameters have been calibrated to yield average optical attenuations that are reasonable at low redshift (Charlot & Fall, 2000), how this parametrisation should evolve and the model's general applicability over cosmic time is ambiguous. This is exacerbated by significant changes in galaxy morphologies with redshift, away from the mature discs prevalent locally. As a result, only the evolution of intrinsic colour was considered in chapter 4.

Fully accounting for dust in arbitrary geometries requires three-dimensional radiative transfer calculations (e.g. Steinacker et al., 2013), and, given the lack of symmetry, Monte Carlo radiative transfer (MCRT) (e.g Whitney, 2011) techniques appear to be well suited. These follow the path of photons from sources through the dusty ISM to a camera. A variety of MCRT codes are publicly available, such as SUNRISE (Jonsson, 2006) and SKIRT (Baes et al., 2003, 2011; Camps & Baes, 2015). SUNRISE has been applied to zoomed galaxy simulations (e.g. Wuyts et al., 2009a,b; Jonsson et al., 2010; Guidi et al., 2015), and by Torrey et al. (2015) to

compute images of galaxies from the ILLUSTRIS simulation (Vogelsberger et al., 2014). Note, however, that Torrey et al. (2015) did not actually include dust in the SUNRISE models. SKIRT has been applied to galaxy models (e.g. Gadotti et al., 2010; Saftly et al., 2015) but also to dust around AGN (Stalevski et al., 2012, 2016). Full MCRT dust models of simulated galaxies in a cosmologically representative volume are yet to be published.

Previous studies that apply MCRT dust modelling to galaxy zoom simulations can provide insight into this approach. Scannapieco et al. (2010) use MCRT to produce representative optical images and decompose them into bulge and disc contributions, but find that dust effects are negligible due to low gas fractions and metallicities in the simulations themselves. Simulations with more realistic gas phase metallicities have also been processed with MCRT to produce mock observables across the UV to sub-mm wavelength range (e.g. Jonsson et al., 2009; Guidi et al., 2015; Hayward & Smith, 2015). The influence of galaxy orientation and geometry on attenuation properties and recovered physical quantities are explored by Hayward & Smith (2015), showing how the effective attenuation curves vary with orientation and morphological transformation for idealised merger zooms.

In this chapter, we generate optical broad-band fluxes and spectra for EAGLE galaxies using SKIRT, comparing mock fluxes to GAMA observations and to the GD+O dust-screen model of chapter 3.

The simulation does not trace dust explicitly: we describe dust associated with star forming regions using the MAPPINGS models by Groves et al. (2008), and assume that the ISM dust/gas ratio depends on metallicity. This procedure was developed for this work and for the companion study of Camps et al. (2016), who looked at the FIR properties of present-day EAGLE galaxies. This chapter compared SKIRT models to FIR observations of local galaxies to calibrate dust models, showing that observed dust scaling relations can be reproduced. Camps et al. (2016) uses dust parameters identical to those used in this chapter. The influence of these parameters is discussed in section 5.2 and the Appendix.

Chapter 2 provides a summary of the EAGLE simulations used in this chapter,

how we define galaxies in our simulated sample and the datasets we compare to. This chapter is organised as follows: In section 5.1.1 we first give a brief appraisal of the modelling and galaxy selection that produces the chapter 3 photometry, which is taken for comparison in this chapter. Section 5.2 details the procedure used to produce observables with SKIRT. We investigate the predicted photometric colours in section 5.4 and compare the effects of dust to the GD+O screen model. In section 5.5.1 we present novel measurements of spectral indices for EAGLE galaxies, and again quantify dust effects. We focus in particular on the star formation proxies of Hα and the extent to which EAGLE reproduces the statistics of, and the correlation in, the D4000 break. We summarise our findings and conclude in section 5.6. Those only concerned with our main results may want to read from section 5.4 onwards; outputs of the model are described in section 5.2.3.

The mock EAGLE observables used in this work, and additional data products listed in section 5.2.3, are to be made available via the public data-base (McAlpine et al., 2016). The modelling, described and tested at low redshift ($z \leq 0.1$), is also used to provide these mock observables for galaxies taken from EAGLE simulations and redshifts that are not considered in this work.

5.1.1 Previous photometric modelling and galaxy selection

Chapter 3 presented model photometry for EAGLE galaxies at $z = 0.1$. The model adopted here is based on that implementation with some differences as described below. In chapter 3, photometric fluxes were calculated in standard $ugrizYJHK$ broad-bands (Doi et al., 2010; Hewett et al., 2006). We use a similar approach here, with full details provided in section 5.2.1.2. The GD+O screen model employed in chapter 3 was based on the two component dust screen of Charlot & Fall (2000), with the optical depth additionally depending on the gas properties and including a prescription to account for orientation-dependent dust obscuration.

In this chapter we adopt many of the same surveying and modelling procedures: individual subhalos are considered potential galaxy hosts, with the 'galaxy' comprising the bound material within a 30 pkpc spherical aperture centred on the

subhalo's baryonic centre of mass. This choice was initially made in S15 to reasonably approximate a Petrosian aperture, and we adopt this galaxy definition for consistency with prior measurements of various galaxy properties. In all but the most massive galaxies, the bound mass excluded by the aperture is negligible (see S15 for details). We find that in $\lesssim 3\%$ of cases more than 10% of the bound baryons lie outside our aperture. While bound material outside of the aperture could modify observable in some galaxies, this effect is insignificant in the majority of galaxies. Primarily, a consistent choice of aperture allows us to isolate aperture effects from other influences. Each galaxy is processed in isolation, therefore there is no contribution from other structures along the line of sight. The same selection of EAGLE galaxies is used as in chapter 3, processing galaxies with stellar masses of $M_\star \geq 1.81 \times 10^8$ M$_\odot$ (~ 100 star particles at standard resolution).

5.2 Dust Modelling with SKIRT

Given a set of sources and a dust distribution, the SKIRT Monte Carlo code (Baes et al., 2003, 2011; Camps & Baes, 2015) follows the dust absorption and scattering of monochromatic 'photon packets' until they hit a user-specified detector, optionally calculating the heating and re-radiation of the dust grains including non-equilibrium stochastic heating. The position on the detector and wavelength of each arriving photon is registered, allowing a full integral field image of the galaxy to be constructed. Convolving this data cube with a filter yields mock fluxes.

The modular nature of SKIRT makes it straightforward to implement multiple source components and absorbing media using arbitrary spectral libraries and geometries. The choices and assumptions we make to represent the emissive and absorbing components of EAGLE galaxies in SKIRT are detailed in sections 5.2.1 and 5.2.2. To represent the particle-discretised galaxies of EAGLE as continuous matter distributions for radiative transfer, particles are smoothed over some scale. For gas particles the SPH smoothing is used, while stellar smoothings are recalculated via a nearest neighbour search of star particles, as explained in Appendix

B.1. While SKIRT is capable of very efficient processing, Monte Carlo radiative transfer is fundamentally computationally expensive. We examine the issues of spectral resolution and convergence in Appendix B.2.

5.2.1 SKIRT modelling: input SEDs

The spectrum of a star particle in the simulation is assigned using spectral energy distribution (SED) libraries. Each particle is treated as a simple stellar population (SSP) with a truncated Gaussian emissivity profile, parametrised by a position, smoothing length and SED. SKIRT then builds a 3D emissivity profile through the interpolation of these individual kernels. The point of emission of individual photon packets are sampled from these kernels at user-specified wavelengths, and photon packets are launched assuming isotropic emission. For the optical wavelengths considered here, we neglect emission from dust and other non-stellar sources. Our representation of the source component for EAGLE galaxies, including sub-grid absorption for the youngest stars, is detailed in sections 5.2.1.1 and 5.2.1.2 below, and an example spectrum showing the different SED components is plotted in Fig. 5.1. Input SEDs and broad band luminosities are stored for EAGLE galaxies, as described in section 5.2.3.

5.2.1.1 Old stellar populations

Stellar populations with age greater than 100 Myr are assigned GALAXEV (Bruzual & Charlot, 2003) SEDs, as described in chapter 3. Briefly, initial masses, (smoothed) metallicities and particle ages are extracted directly from the simulation snapshot. Absolute metallicity values, as opposed to those in solar units, are used to assign SEDs for the reasons given in section 3.1.2 of chapter 3. Stars are assumed to form with a Chabrier (2003) IMF covering the stellar mass range of [0.1,100] $M_{\odot}$, consistent with what is assumed in EAGLE. Star particle coordinates are also taken directly from the simulation output. Smoothing lengths specifying the width of the truncated Gaussian profile are determined using a nearest neighbour search, as detailed in Appendix B.1. Note that we do not explore alternative population

synthesis models (e.g. Leitherer et al., 1999; Maraston, 2005; Conroy et al., 2009) in this chapter; differences are expected to be small for the $z = 0.1$ galaxies at optical wavelengths studied here (e.g. Gonzalez-Perez et al., 2014a).

5.2.1.2 Young stellar populations

The treatment of the young stellar component is more involved due to two limitations of the simulation: (*i*) the relatively coarse sampling of star formation due to the limited mass resolution (see Table 2.1), and (*ii*) the inability of resolving birth cloud absorption associated with recent star formation. Though the diffuse ISM dust can be traced by enriched cold gas, the birth clouds of stellar clusters exhibit structure on sub-kpc scales (e.g. Jonsson et al., 2010), below the resolution limit of EAGLE. Such birth clouds are thought to disperse on timescales of ~ 10 Myr (e.g. Charlot & Fall, 2000). To treat birth cloud absorption, we use the MAPPINGS-III spectral models of Groves et al. (2008), which track stars younger than 10 Myr, and include dust absorption within the photo-dissociation region (PDR) of the star-forming cloud, following the methodology of Jonsson et al. (2010). We therefore have two sources of dust: that associated with birth clouds which is modelled using MAPPINGS-III, and ISM dust whose effects we model using SKIRT.

We use an extended version of the re-sampling procedure of chapter 3 to mitigate the effects of coarse sampling. Recent star formation is re-sampled in time over the past 100 Myr, from both star-forming gas particles and existing star particles younger than 100 Myr, as follows. The stellar particle stores the gas density of its parent particle, which is used to compute a star formation rate. We use this rate for young stars, and the star formation rate of star-forming gas particles, to compute how much stellar mass these particles formed on average over the past 100 Myr (assuming a constant star formation rate). We then randomly sample this stellar mass in terms of individual star-forming regions, with masses that follow the empirical mass function of molecular clouds in the Milky Way (Heyer et al., 2001),

$$\frac{\mathrm{d}N}{\mathrm{d}M} \propto M^{-1.8} \quad \text{with } M \in \left[700, 10^6\right] \mathrm{M}_\odot \,. \tag{5.2.1}$$

For each particle resampled, sub-particle masses are drawn from this distribu-

tion until the mass of the parent particle is exceeded. Rejecting the last drawn sub-particle, the masses of sub-particles are rescaled such that the sum of their masses, $\Sigma m_{\rm r}$, exactly matches that of the parent. Sub-particles are then stochastically assigned formation times using the star formation rate of the star-forming particle. In this way, we replace star-forming gas particles, and young star particles, by a distribution of star-forming molecular clouds with the same total mass and spatial distribution as the original set of particles.

Stellar populations resampled with ages in the range 10 Myr $\leq t_{\rm age} <$ 100 Myr are assigned GALAXEV spectra, parametrised in the same way as in section 5.2.1.1. They inherit the position and smoothing length of the particle from which they are sampled. These smoothing lengths are assigned to parent star and gas particles differently, as described in Appendix B.1.

Those resampled to have ages in the age range $t_{\rm age} \leq 10$ Myr are assigned the MAPPINGS-III spectra of Groves et al. (2008). One caveat with using these spectral models is that the intrinsic spectra of stars used to model the spectra are specified by the Leitherer et al. (1999) (SB99) population synthesis models. This leads to some inconsistency in the modelling of the intrinsic stellar spectra, which come from GALAXEV for older populations. However, these differences are small in the optical ranges considered here (e.g. see Gonzalez-Perez et al., 2014a). Another caveat is that a Kroupa (2001) IMF is assumed for these spectral models rather than that of Chabrier (2003), though again the differences in optical properties are minimal.

The MAPPINGS-III spectral libraries represent HII regions, and their emerging spectrum therefore already treats the reprocessing of star light by dust in the star-forming region. In other words, birth cloud dust absorption and nebular emission are included in the SKIRT input spectra before any SKIRT radiative transfer is performed. We describe below how we avoid double counting dust in HII regions.

The MAPPINGS-III SEDs are parametrised as follows:

- **Star Formation Rate ($\dot{M}_\star$):** The MAPPINGS-III spectra assume a given (constant) star formation rate between 0 and 10 Myr, the star formation rate assigned to a particle of initial mass $m_{\rm r}$ is given by $\dot{M}_\star = 10^{-7} m_{\rm r}$ yr^{-1}, in

order to conserve the mass in stars.

- **Metallicity (Z):** The metallicities are specified by the SPH-smoothed absolute values of the simulation snapshot.

- **Pressure (P_0):** The ambient ISM pressure, P_0, is calculated from the density of the gas particle from which the sub-particle is sampled. This is not directly accessible in EAGLE, but can be estimated using the polytropic equation of state that limits the pressure for star-forming gas (Dalla Vecchia & Schaye, 2012). Because the simulation snapshot contains the density at which each star particle formed, this estimator can be used for re-sampling both star-forming gas and young stellar particles.

- **Compactness ($\log_{10} C$):** The compactness, C, is a measure of the density of an HII region. This is calculated using the following equation from Groves et al. (2008),

$$\log_{10} C = \frac{3}{5} \log_{10} \frac{M_{\rm cl}}{\mathrm{M}_\odot} + \frac{2}{5} \log_{10} \frac{P_0/k_{\rm B}}{\mathrm{cm}^{-3}\mathrm{K}} \,, \tag{5.2.2}$$

  where $M_{\rm cl}$ is the star cluster mass, taken to be the re-sampling mass $m_{\rm r}$, P_0 is the HII region pressure taken to be the particle pressure above, and $k_{\rm B}$ is Boltzmann's constant. The parameter C predominately affects the dust temperature and thus the FIR part of the SED, and therefore has little effect on the results presented here, see Camps et al. (2016) for a thorough discussion on how C affects FIR colours of EAGLE galaxies.

- **PDR Covering Fraction ($f_{\rm PDR}$):** The photo-dissociation regions (PDRs) associated with HII regions are influenced by processes well below the resolution of EAGLE. PDRs disperse over time as O, B and A stars die out. We assume a fiducial value of $f_{\rm PDR} = 0.1$ for the PDR covering factor, which can be compared to the 'typical' value of $f_{\rm PDR} = 0.2$ used by Groves et al. (2008) and Jonsson et al. (2010), following the calibration presented by Camps et al. (2016).

With the parameters of the STARBURST SEDs determined, the SKIRT source emissivity profile is then set. As explained by Jonsson et al. (2010), the scale of

the HII region emissivity profile should be set so as to enclose a similar mass of ISM to that required to be consistent with the subgrid absorption. Doing so avoids double-counting the dust in the subgrid absorption (which already affects the source spectra) and dust absorption in the diffuse ISM modelled by SKIRT. To approximate this, we assume a fixed mass for the re-sampled particles of $M_{\rm PDR} = 10 M_{\rm cl}$ (e.g. Jonsson et al., 2010), and set the corresponding size of the region to be $r_{\rm HII} = \sqrt[3]{8 M_{\rm PDR}/\pi \rho_g}$ (for a cubic spline kernel), with ρ_g the local gas density, taken from the parent particle. This is taken to be the smoothing length of MAPPINGS-III sources. As noted previously, the MAPPINGS-III model assumes the presence of birth cloud dust and that needs to be accounted for to ensure that the total dust mass is conserved. We budget for this additional dust using the ISM dust distribution, as described in section 5.2.2.2. HII region positions are sampled within a kernel of size $r_{\rm s} = \sqrt{r_{\rm p}^2 - r_{\rm HII}^2}$, with $r_{\rm p}^2$ being the parent kernel smoothing length, and about the parent particle position. This is such that in the infinite sample limit the net kernel of the HII regions is equivalent to that of the parent. Again, the smoothing lengths of gas and star parent particles are obtained differently, as explained in Appendix B.1. Finally, those sub-particles that are not converted to either a stellar or HII region source over the re-sampling period are reserved for the absorbing component to ensure mass conservation. Absorption in the (diffuse) ISM is modelled as described in section 5.2.2 below.

5.2.2 SKIRT modelling: observed properties

Having detailed the parametrisation of the source components, we proceed to describe the modelling of dust in the diffuse ISM. This dust component is mapped to an adaptively refined (AMR) grid, for which the optical depth of each cell is calculated at a given reference wavelength. Neglecting Doppler shifts, this enables the computation of the dust optical depth at any other wavelength once the wavelength-dependence of the dust attenuation is specified. Details of the modelling of the dust and gas contents are given in sections 5.2.2.2 and 5.2.2.1, respectively.

5.2.2.1 Discretisation of the ISM

Dust in galaxies exhibits structure on a range of scales, from galaxy-wide dust lanes to sub-kpc 'dark clouds', with significant absorption across the range, down to the scale of molecular clouds (e.g. Hunt & Hirashita, 2009). We cannot resolve sub-kpc dust structures in EAGLE, which is why we include such small-scale dust via the source model of HII regions, as described in Section 5.2.1.2. We use the gas particles in EAGLE galaxies to estimate how dust is distributed in the diffuse ISM, and use SKIRT to calculate obscuration by this dust, as follows.

We discretise the gas density on the AMR grid using the octree algorithm (Saftly et al., 2013). A cubic root cell of size 60 pkpc is created, centred on the galactic centre of mass, to capture all galactic material (see section 5.1.1), and is refined based on the interpolated dust density derived from the gas particles, between a specified minimum and maximum refinement level. We increase the refinement level until the photometry is converged. Clearly, the minimum cell size should be smaller than the approximate spatial resolution of EAGLE to best capture ISM structure in the simulated galaxies. We find that a maximum refinement level of 9 (corresponding to a finest cell of extent $60\ \mathrm{kpc}/2^9 = 0.11\ \mathrm{kpc}$ or $\approx 1/6$ of the $z = 0$ gravitational softening), provides a grid structure that yields converged results when combined with a cell splitting criterion[2] of 2×10^{-6}. We therefore adopt a maximum refinement level of 9 for our analysis, together with a minimum refinement level of 4. While we use a minimum cell size twice as large as that of Camps et al. (2016), we have verified that this has a negligible effect on our results in the optical and NIR, while increasing the speed of our SKIRT simulations.

[2]This is the maximum fraction of the total dust mass that can be contained within a single dust cell. If the cell contains a larger fraction and is below the maximum refinement level, the cell is subdivided.

5.2.2.2 Dust model

Dust traces the cold metal-rich gas in observed galaxies (e.g. Bourne et al., 2013). Here we assume that the dust-to-metal mass ratio is a constant,

$$f_{\rm dust} \equiv \frac{\rho_{\rm dust}}{Z\rho_{\rm g}} = 0.3\,, \tag{5.2.3}$$

where Z is the (SPH-smoothed) metallicity, and $\rho_{\rm dust}$ and $\rho_{\rm g}$ are the dust and gas density, respectively. The numerical value was determined by calibrating FIR properties of EAGLE galaxies by Camps et al. (2016), and is consistent within the uncertainties of observationally inferred values (e.g. Dwek, 1998; Draine et al., 2007). The assumption of a constant value of $f_{\rm dust}$ is common and is observed to apply to a wide variety of environments (e.g. Zafar & Watson, 2013; Mattsson et al., 2014), though there are indications it can vary in some cases (e.g. De Cia et al., 2013; Feldmann, 2015). We implement this constant ratio by assigning a dust mass of $m_{\rm dust} = f_{\rm dust} m_g$, where m_g is the particle mass. We use the dust model described by Zubko et al. (2004); a multi-component dust mix tuned to reproduce the abundance, extinction and emission constraints on the Milky Way. Following Camps et al. (2016), gas must be either *star-forming* (i.e. assigned a non-zero star formation rate by the simulation or in the re-sampling procedure) or sufficiently cold (with temperature $T < 8000$ K) to contribute to the dust budget.

To account for the dust mass already associated with birth clouds when using the MAPPINGS-III source SEDs, we introduce 'ghost' particles that contribute *negatively* to the local dust density. These ghost particles are placed at the location of each HII region, have a mass of $M_{\rm PDR} = 10 m_{\rm r}$, where m_r is the stellar mass formed in the star-forming region, and a smoothing length equal to three times that of the HII region. The assumption that the PDR mass, $M_{\rm PDR}$, is ten times that of the stellar mass formed follows the recommendation of Groves et al. (2008), the greater smoothing of the ghost contribution avoids negative dust densities. The creation of 'holes' in the dust distribution around HII regions may seem unphysical, as observed HII regions are typically embedded in the densest (and dustiest) ISM. However, we have tested an alternative implementation where the dust mass of all contributing particles are downscaled to balance the additional dust invoked

by the MAPPINGS-III SEDs, and find little perceptible difference in the results presented here. We will see that ISM dust obscuration is still higher around young stars, even in the presence of these ghost particles.

5.2.3 Data products

This section describes the data products that are generated by SKIRT. We reiterate that we do not consider kinematics when using SKIRT, *i.e.* no Doppler shifts are yet accounted for beyond any line broadening present in the input SEDs. We perform a convergence test in Appendix B.2 to determine how to best sample the SED, both in terms of wavelength sampling and photon-packet sampling. We construct integrated spectra for all simulated galaxies in three orientations; edge on, face on and randomly orientated with respect to the galactic plane. The calculation of orientations for EAGLE galaxies is described in section 5.3 below. The data products produced include the following:

- **Integrated spectra** capture all the photon packets emanating from the mock galaxy for the fixed list of specified wavelengths, and in a given direction. The standard resolution spectra consist of 333 wavelengths in the range 0.28−2.5 μm, chosen to sample the rest-frame $ugrizYJHK$ photometric bands (see Appendix B.2 for details). Spectra are produced with and without ISM dust at redshifts $z = 0$ and redshift $z = 0.1$ (the snapshot redshift from which the galaxies were selected). An example integrated rest-frame SED of a star-forming galaxy and including dust attenuation is plotted in Figure 5.1.

- **Data cubes**, or mock IFU data, consist of 256x256 spatial pixels, each with a spectrum at standard spectral resolution. Given that the field of view corresponds to 60 pkpc on a side, this corresponds to $234\ \mathrm{pc/pixel}$. Images are produced in both the rest and observed frames, but only for dust attenuated galaxies with $M^\star > 10^{10}\mathrm{M}_\odot$. Again, these do not include kinematic effects, which will be the focus of future work.

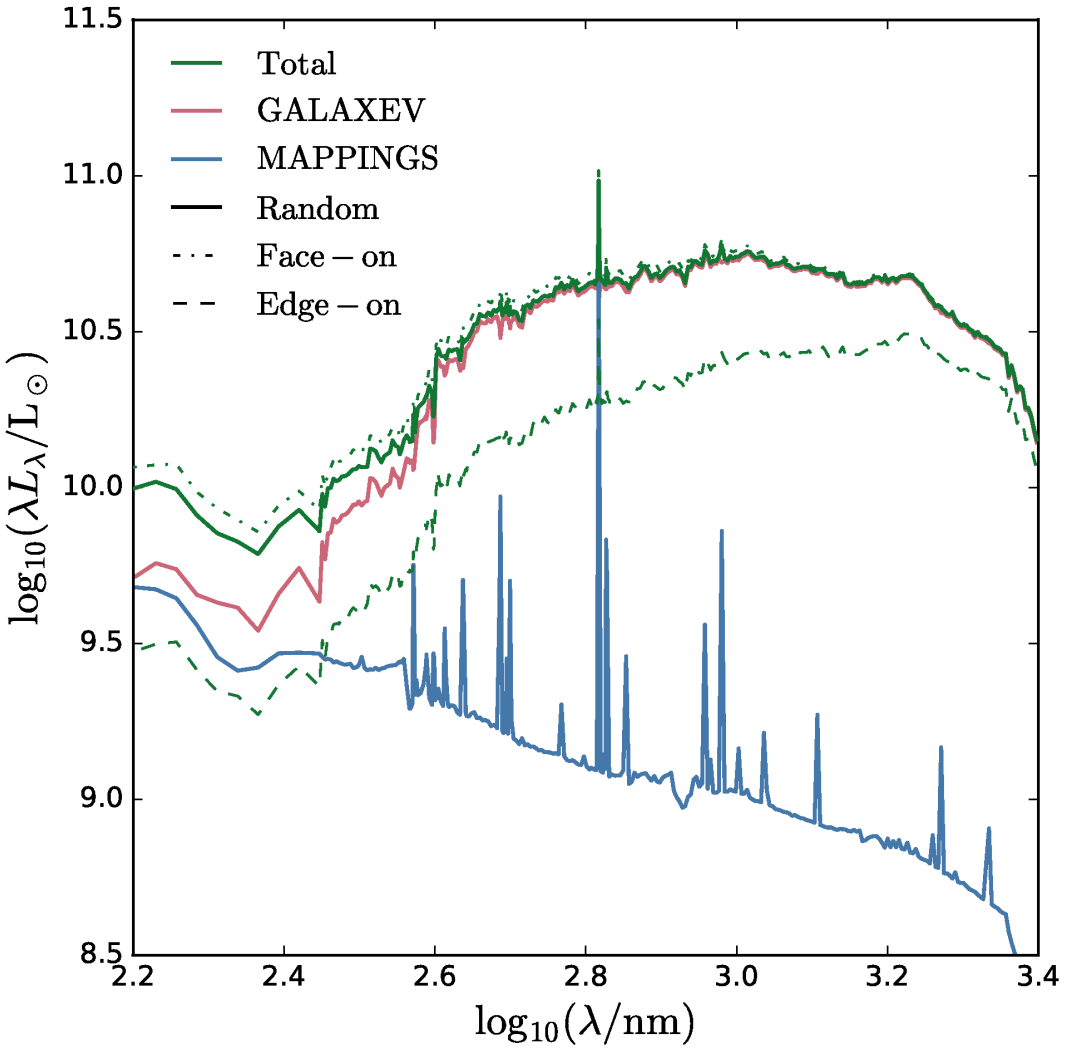

Figure 5.1: Example integrated rest-frame galaxy SED including ISM dust effects, generated for a late type (S) EAGLE galaxy taken from simulation Ref-100 (galaxy ID=15814162 in the EAGLE database described by McAlpine et al. 2016). The *green line* indicates the total SED in the presence of dust. *Solid lines* show the integrated SED when the galaxy is observed along the z-direction of the simulation volume (an inclination angle of 50.2°), while *dashed* and *dot-dashed* lines denote edge and face-on views, respectively. The *red* and *blue lines* are the ISM dust-free contributions from the old stellar population ($t > 10$ Myr) modelled using GALAXEV (Bruzual & Charlot, 2003), and the young population ($t < 10$ Myr) modelled using MAPPINGS-III (Groves et al., 2008), respectively. Properties and images of this galaxy can be found in Table 5.1 and Fig. 5.2 respectively. We see from the solid lines that the MAPPINGS-III SED contributes relatively more flux in the UV, and for some strong emission lines.

Table 5.1: Properties of galaxies shown in Fig 5.2. All properties are extracted from the EAGLE database (McAlpine et al., 2016), for a 30 pkpc aperture.

Type	Galaxy ID.	$M_\star$ [$M_\odot$]	SFR [$M_\odot$ yr^{-1}]
Late (S)	15814162	9.94×10^{10}	3.96
Irregular (Irr)	14318126	1.34×10^{11}	4.60
Early (E)	19099219	2.05×10^{10}	0.00

- **Broad-band photometry** The fluxes through the $ugrizYJHK$ filters and are obtained by convolving the integrated spectra with the filter transmission curves (transmission curves were taken from Doi et al., 2010; Hewett et al., 2006). We compute both rest-frame and observed-frame photometry for the entire galaxy sample both with and without ISM dust attenuation.

- **Broad-band images** are produced by integrating along the wavelength axis of the data cubes. These are generated including dust for the $ugriz$ SDSS bands, and provided in 3 colour PNG (portable network graphic) format[3] via the approach of Lupton et al. (2004). Figure 5.2 shows three-colour gri images at $z = 0.1$ for three different galaxies and three orientations. We picked a late-type, an irregular and an early-type galaxy. Some properties of these galaxies are listed in Table 5.1. Structural features resembling spiral arms and tidal tails are distinguishable for the late and irregular types, respectively, while the early type exhibits a smooth, featureless light distribution. Star-forming HII regions appear pink due to Hα emission in the MAPPINGS-III SEDs for these $z = 0.1$ galaxies. We also observe scattering and absorption by dust for the late and irregular types.

[3]Note that these images are initially intended for illustrative purposes only, as the detailed light distributions are dependent on the somewhat *ad-hoc* choice of stellar smoothing (similarly demonstrated by Torrey et al., 2014). While we find the influence of smoothing to be small for the results presented in this chapter (see Appendix B.1), analysing the influence smoothing has on morphologies is left to a future work.

Data products are to be made available via the EAGLE public database (McAlpine et al., 2016), with the exception of data cubes, which are available through collaboration with the authors[4]. We will below compare the output from the SKIRT simulations to those with the same source model but without obscuration by ISM dust. Note, however, that the MAPPINGS-III source model always includes dust associated with the birth cloud. We will refer to the these models as 'ISM dust-free' in what follows.

5.3 Attenuation Properties of SKIRT galaxies

In this section we focus on how attenuation depends on galaxy orientation at low redshift ($z = 0.1$). This helps us to separate the effects of geometry and dust content, and facilitates the interpretation of a comparison with observations.

5.3.1 Broad-band attenuation

The orientation of a galaxy can profoundly affect its measured colours, particularly in the case of thin spiral galaxies where the edge-on view is much more affected by dust than the face-on view. Indeed, the reddest galaxies observed in the local Universe are often edge-on spirals (e.g. Sodre et al., 2013). The SKIRT modelling naturally accounts for this effect, as opposed to the two component screen models presented in chapter 3 which relies on simple geometrical arguments to account for this. To quantify orientation effects in disc galaxies, we use 3 lines of sight: parallel, perpendicular and randomly oriented with respect to the galactic plane. This helps constrain orientation effects on dust extinction for each galaxy individually, as well as providing a set of photometry with random orientations used when comparing to data.

We assume that the disc of a galaxy is perpendicular to the spin vector, $\mathbf{S}$, of its stars. We calculate $\mathbf{S}$ by summing the spin vectors of all star particles within

[4]To access the database and receive updates on its content, register at `http://icc.dur.ac.uk/Eagle/database.php`

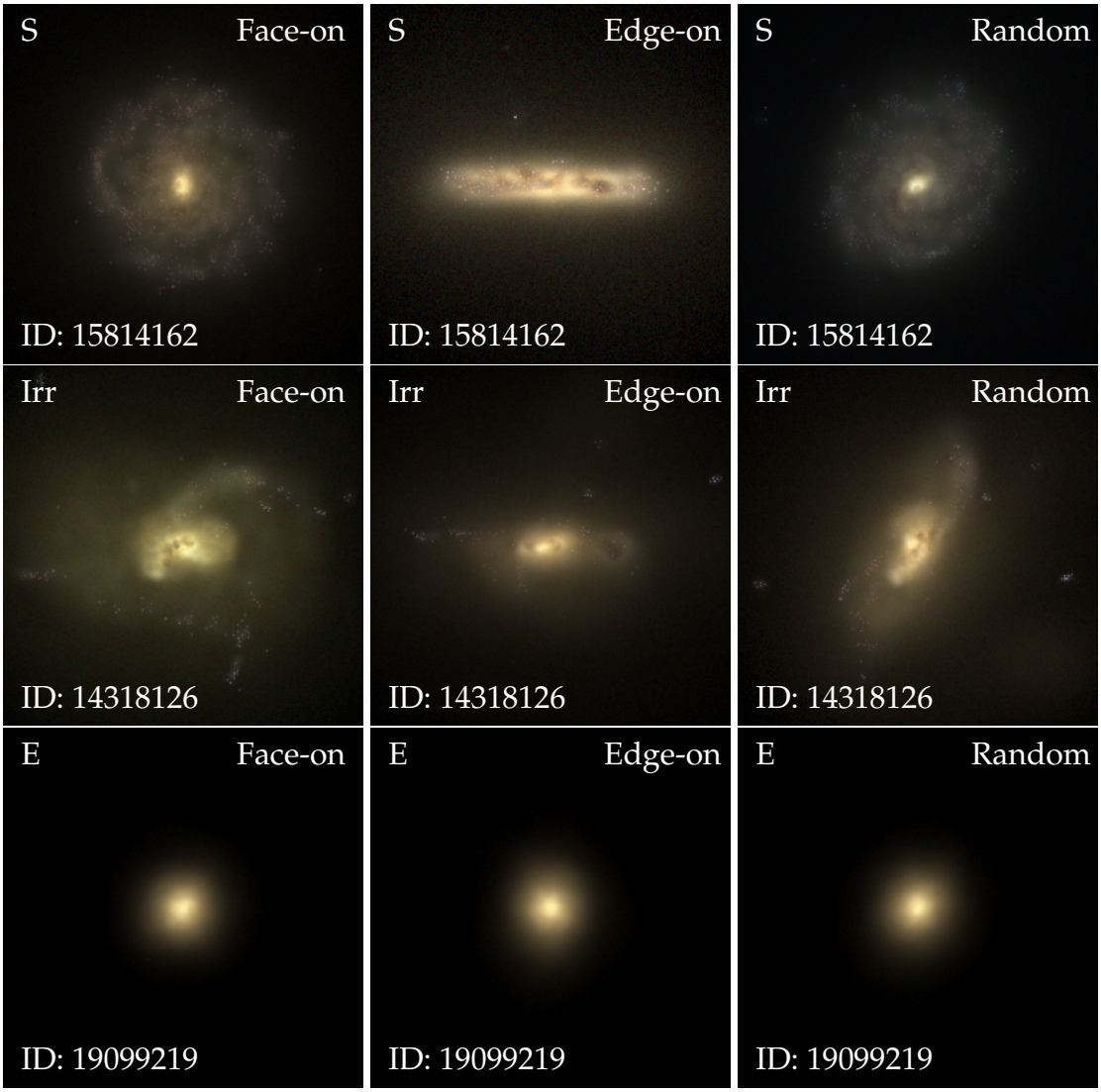

Figure 5.2: Observer frame true colour gri images of selected EAGLE galaxies from Ref-100 at $z = 0.1$, including dust obscuration. The galaxy ID can be used to identify each galaxy on the EAGLE database (McAlpine et al., 2016), see also Table 5.1. Rows from top to bottom show a late type spiral (Hubble type S), an irregular type (Irr) and an early type (E) galaxy, with columns from left to right showing face-on view (parallel to the stellar angular momentum axis), edge-on view, and the view along the z-axis of the simulation volume ('random').

{*continued on next page...*}

Figure 5.2: {*Continued from previous page*} Images are produced using 4×10^6 photon packages at each of 333 wavelengths, spaced as described in Appendix B.2. HII regions appear pink in the colour scheme, due to strong Hα emission at $\sim$6700 Å red-shifted into the i-band, dust lanes are clearly visible in the S and Irr images. The kinematic orientation works well for the spiral galaxy, but the disordered gas distribution caused by an ongoing merger event in the Irr case yields more absorption in the face-one view than in the edge-on view. Images are 60 pkpc on a side.

a shell with inner and outer radii of 2.5 pkpc and 30 pkpc, respectively, in the centre-of-mass rest-frame of the galaxy. The outer radius corresponds to the aperture radius of a galaxy assumed in chapter 2, the inner radius was chosen to avoid a significant contribution from a bulge or regions strongly affected by gravitational softening. We found that with this selection, **S** is generally dominated by the dynamically cold rotating disc component, if present. We characterise the orientation of a galaxy by its inclination angle θ, such that face-on galaxies have $\cos(\theta) = 1$.

In Fig. 5.3 we plot the attenuation in the B-band, A_B, as function of orientation, for all EAGLE galaxies from simulation Ref-100 with stellar mass $M_\star > 10^{10}\mathrm{M}_\odot$; points represent individual galaxies coloured by intrinsic $u^\star - r^\star$ (* denotes intrinsic photometry). Two sequences are observed: (*i*) a broad sequence of intrinsically blue (star-forming) galaxies where A_B increases with decreasing $\cos(\theta)$ and (*ii*) a very tight sequence of intrinsically red (passive) galaxies showing no orientation dependence. Such a dichotomy is of course unsurprising: red galaxies typically have low cold gas fractions and therefore negligible dust attenuation, whereas star forming (intrinsically blue) galaxies have relatively high cold gas fractions, with gas distributed in a disc, hence dust obscuration is higher and depends on orientation.

The median A_B of intrinsically blue galaxies with $A_B \geq 0.05$ in bins of $\cos(\theta)$ is plotted as black squares in Fig. 5.3), with the grey region enclosing the 16th-84th percentiles. The median attenuation A_B of EAGLE galaxies increases from

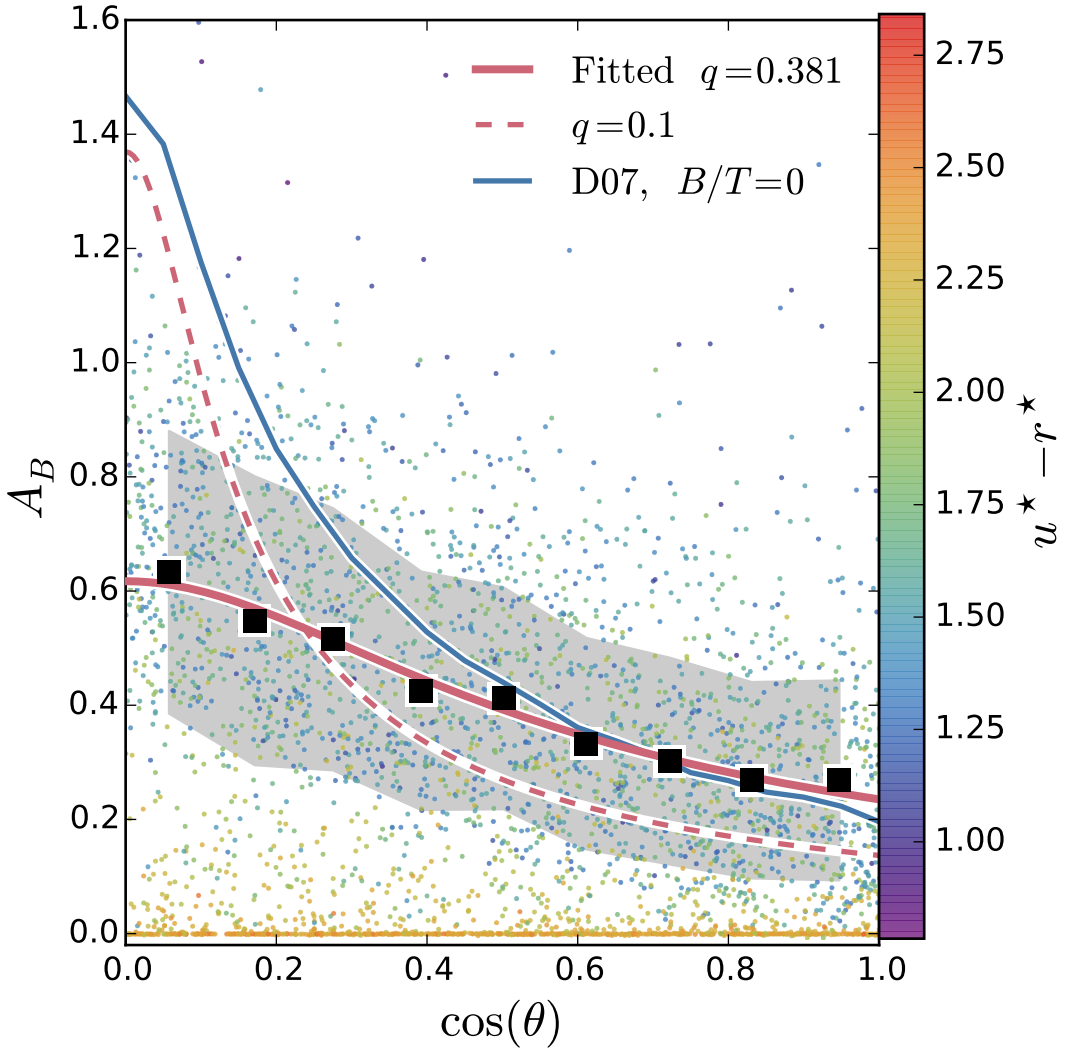

Figure 5.3: The Johnson rest-frame B-band attenuation, A_B, as a function of inclination angle; $\cos\theta = 1$ corresponds to face-on. *Points* are individual EAGLE galaxies from simulation Ref-100 at $z = 0.1$, with $M_\star > 10^{10}\mathrm{M}_\odot$, coloured by ISM dust-free $u^\star - r^\star$ colour. *Black squares* indicate the median relation for galaxies with $A_B \geq 0.05$, binned by $\cos(\theta)$. The *grey, shaded* region indicates the 16th-84th percentile range in each bin. The *red, solid line* shows the best fit of the form Eq. (5.3.4), which has $q = 0.396$. The *red, dashed line* shows the same fit, except with $q = 0.1$ to represent a thinner discs, which follows the trend of the intrinsically blue galaxies better. Galaxies with $A_B < 0.05$ are typically red in $u^\star - r^\star$ and occupy a tight distribution in $A_B \approx 0$, independent of orientation. For comparison we also overlay the observed relation from Driver et al. (2007) (D07 in the legend) for the median attenuation curve of the disc component only, of galaxies with bulge/total ratio smaller than 0.8.

0.3 to ≥ 0.6 from face-on to edge-on orientation but the scatter around the trend is large (≈ 0.5 mag). We fit the angular dependence of the median relation using the ellipsoidal dust model discussed in chapter 3,

$$A_B(\cos\theta) = a\frac{q}{\sqrt{q^2 + (1-q^2)\cos^2\theta}}\,, \tag{5.3.4}$$

where a is the edge-on obscuration and q represents the axial ratio of the galaxy; lower q corresponds to thinner galaxies. We treat a and q as free parameters in the fit, and plot the fitted curve in red. The functional form fits the trend well for an axial ratio of $q = 0.381$. The scatter around the median likely originates from both diversity in the ISM distribution in different galaxies, i.e. deviation from an idealised disc, but also from errors in identifying the correct orientation of the disc plane. Indeed, we showed in Figure 5.2 that the galactic plane is not always easily defined, as evidenced by the irregular galaxy shown in the middle row.

Driver et al. (2007) use a sample of galaxies from the Millenium Galaxy Catalogue (MGC) with estimated bulge-to-total (B/T) light ratios of $B/T < 0.8$ to measure the extent to which the location of the 'knee' in the B-band luminosity function (Schechter, 1976) depends on inclination. They fit their results with the model of Tuffs et al. (2004) to obtain the typical attenuation separately for bulge and disc components. We plot the relation of Driver et al. (2007) for a typical disc ($B/T = 0$) in Fig. 5.3 as a solid blue line.

The median EAGLE A_B values (black squares) and the fitted form of Eq. (5.3.4) (red line), are consistent with those obtained by Driver et al. (2007) for nearly face-on discs ($\cos(\theta) \geq 0.5$), but are significantly lower for highly inclined discs. While there is uncertainty in the absolute values measured for A_B, as discussed by Driver et al. (2007), the difference between typical face- and edge-on A_B values is better constrained[5] and clearly significantly larger in the data compared to EAGLE. Note that the Driver et al. (2007) data is represented by a pure disc (blue line) for simplicity. While EAGLE spirals clearly possess bulges (see e.g. Fig. 5.2), the *difference* between face-on and edge-on attenuation found by Driver et al.

[5]Driver et al. (2007) derive the relative attenuation directly by measuring how the knee position of the luminosity function differs for edge-on and face-on galaxies.

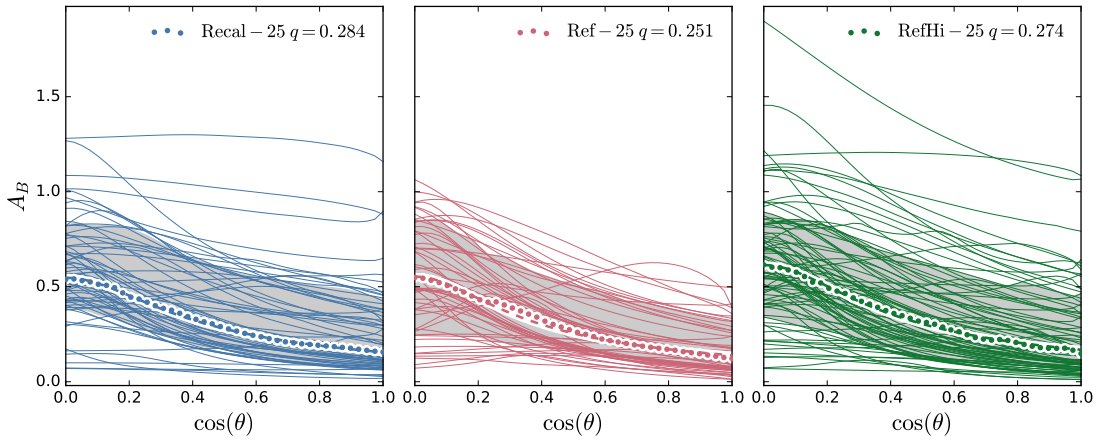

Figure 5.4: Johnson rest-frame B-band attenuation as function of orientation for EAGLE galaxies, taken from simulations Recal-25, Ref-25 and RefHi-25 at $z = 0.1$ (left to right panels, see Table 2.1 for details). Thin curves show A_B for individual galaxies as a function of inclination, the shaded circle represent the median trend, and the grey region includes the 16th-84th percentiles. The dashed line approximately overlying the circles represents the fit of Eq. (5.3.4); the best-fit value of q is indicated in each panel. We see significant galaxy-to-galaxy variation in the shape of the attenuation-inclination relation, with the highest attenuation values in the higher-resolution galaxies, but little difference between the trend of the median inclination as a function of $\cos(\theta)$.

(2007) varies little with B/T. The blue line provides a guide curve to highlight the smaller range in A_B with inclination for EAGLE. Decomposition of SKIRT light profiles into bulge and disc contributions is left to a future study.

The $q = 0.1$ curve, which models thinner discs for the same dust content as the fitted curve, demonstrates much better agreement with Driver et al. (2007) than the median EAGLE relation. This suggests that the discrepancy is likely due to EAGLE galaxies not being as thin as observed galaxies. The fact that EAGLE galaxies are thicker than observed is not only due to numerical resolution. Indeed, we compare the $A_B(\cos\theta)$ relation for galaxies taken from the three $(25\ \mathrm{Mpc})^3$ simulations listed in Table 2.1. These simulate the same volume, but at different resolutions. The number of galaxies with $M_\star > 10^{10}\mathrm{M}_\odot$ in this smaller volume is $\lesssim 100$, therefore the two-sequences in the $A_B(\cos\theta)$ relation are not well constrained if we simply use the mock photometry of randomly oriented galaxies as we did in Fig. 5.3. We therefore calculate $A_B(\cos\theta)$ for all sufficiently massive galaxies ($M_\star > 10^{10}\mathrm{M}_\odot$) at 40 inclinations for each galaxy, equally spaced in $\cos(\theta)$, and plot the resulting curves in Fig. 5.4. Equation (5.3.4) is fit to the median relation and plotted as a dashed coloured line. While higher values of A_B are seen in the higher resolution RefHi-25 and Recal-25 samples, the difference with respect to the median values of Ref-25 is small. Neither the plotted curves for individual galaxies nor the fits using Eq. (5.3.4) to the median trend, show strong evidence for A_B being more sharply peaked at improved numerical resolution.

The weaker inclination dependence and lower edge-on values of A_B in EAGLE are instead likely a consequence of EAGLE's subgrid physics, in particular the use of an imposed Jeans-limiting, polytropic relation for star forming gas (chapter 2). This relation yields a Jeans length at the star formation threshold of the $\sim$1.5 kpc, and EAGLE discs are unable to be much thinner than this. This relation is imposed to avoid numerical fragmentation below the resolution of the simulation, as explained by S15. Dust discs in observed galaxies, on the other hand, are much thinner, $\sim$100-200 pc (e.g. Xilouris et al., 1999; De Geyter et al., 2014; Hughes et al., 2015). In a thin disc seen edge-on, the dust optical depth to young stars will be much higher than if the disc where thick, and this seems to be the main difference

between observed and simulated galaxies.

This comparison demonstrates that the $A_B(\cos\theta)$ dependence displays both strong and weak convergence behaviour, with increased numerical resolution not changing the relation significantly - and not improving the agreement with the data. We show in Appendix B.1 that reducing all star particles to point sources only boosts the edge-on value of A_B by $\lesssim 0.1$ mag. We conclude from this that the lower values for A_B for edge-on EAGLE galaxies are likely a result of the the simulations being unable to represent cold gas; the high column densities and clumpy structure of molecular gas observed in real disc galaxies is not reproducible in the EAGLE simulations without realistic modelling of gas with $T \lesssim 10^4$K. The influence that thicker discs (and thus lower edge-on attenuation) has on our results is discussed further below.

5.3.2 Broad-band colour effects

The extent to which inclination affects the optical colour distribution of EAGLE galaxies with $10^{10}\mathrm{M}_\odot \leq M_\star < 10^{11}\mathrm{M}_\odot$ is illustrated in Fig. 5.5, where we plot intrinsic (ISM dust-free) $g^\star - r^\star$ colour against $g - r$ in the presence of dust. In the left panel we shade regularly spaced colour-colour bins by the median value of $\cos\theta$ of galaxies in that bin (provided the bin contains more than 10 galaxies). We see a clear trend in attenuation with inclination, especially for intrinsically blue galaxies of $g^\star - r^\star \lesssim 0.6$, with galaxies possessing median $\cos(\theta)$ values of ≈ 0.25 and ≈ 0.65 for maximal and minimal offsets from the 1:1 relation, respectively. For galaxies with redder intrinsic colours, the trend is less pronounced and the maximal offset is lower, as expected for less dusty galaxies.

In the right panel of Fig. 5.5 we plot logarithmically spaced contours representing the number of galaxies per colour-colour bin. Intrinsically red ($g^\star - r^\star \approx 0.75$) galaxies follow the 1:1 relation closely with little offset, whereas intrinsically blue ($g^\star - r^\star \approx 0.4$) galaxies are offset to redder colours and show a large scatter. Worth noting is the approximately constant median offset to the red of ≈ 0.1 mag for galaxies with $g^\star - r^\star \lessapprox 0.6$, implying that a similar average reddening is experienced by star forming galaxies regardless of star formation rate.

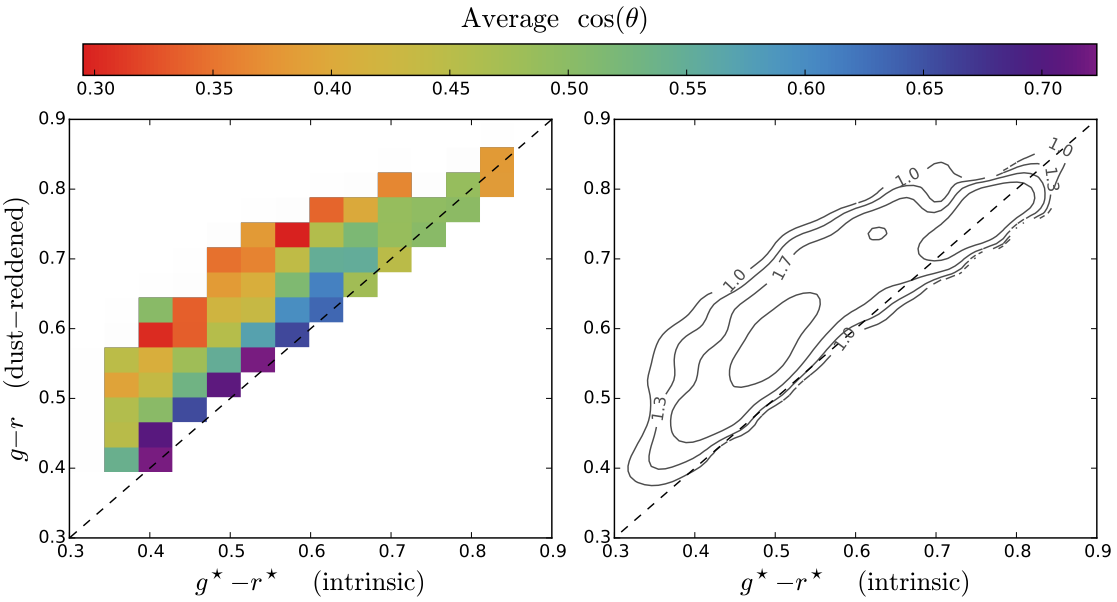

Figure 5.5: Comparison of ISM dust-free SDSS $g-r$ colour to $g-r$ including ISM dust for EAGLE galaxies in the mass range $10 \leq \log(M_*/\mathrm{M}_\odot) < 11$ at $z = 0.1$; the *black dashed line* indicates the 1:1 relation in both panels. In the *left panel*, the median value $\cos(\theta)$ is plotted in regularly spaced bins in colour (only bins with more than 10 galaxies are shown). The *right panel* shows the number density n of galaxies per colour-colour bin as grey contours labelled by $\log(n)$. There is a clear trend of increased reddening at higher $\cos(\theta)$ as expected. Some galaxies lie marginally below the 1:1 line, the reasons for which are discussed in the text.

Some galaxies lie marginally *below* the 1:1 relation. In most cases this is due to uncertainty in the photometry (see appendix B.2), particularly in dust-free galaxies where the attenuation is small anyway, and these negative reddening measurements are ~ 0.001 mag. However in rare instances, measured for higher redshift EAGLE galaxies, significant negative reddening is observed. This can be attributed to those galaxies demonstrating heavy obscuration in their central regions, leading to higher contribution of young stars in the outskirts, conspiring to produce bluer colours overall.

5.3.3 Attenuation curves

The *extinction curve* is an intrinsic property of a given dust grain population; combining the wavelength dependent cross-sections of absorption and scattering. Our choice of dust mix thus sets the optical depth of dust cells modelled by SKIRT. However, the extinction does not provide a direct mapping between the intrinsic and observed SEDs, which additionally depends on the relative distribution of stars and dust and the orientation of the galaxy along the line of sight. This galaxy and line-of-sight specific mapping is referred to as the *attenuation curve*. One example of why the curves may differ significantly is that the young stars that dominate emission at short wavelengths are in general embedded in dusty regions and hence their blue light is more strongly dust-attenuated.

As a result, the attenuation curves may differ systematically in shape from the extinction curve of the individual dust cells. The shape of the curve is also likely orientation dependent, for example stars in a central bulge may be obscured in edge-on but not face-on projections. As a result, the normalisation, shape and orientation dependence of the attenuation curve are to some extent degenerate in observed integrated spectra when an attenuation proxy such as the Balmer decrement is used.

It is typical to assume a fixed shape of the attenuation curve to de-redden observed SEDs. Using the SEDs we generate for EAGLE galaxies, we can explore the typical attenuation curves that arise from our MCRT treatment, and how these may vary systematically with orientation. While EAGLE galaxies appear to have

thicker discs than observed (see section 5.3.1), we hope to provide an indication of the ways in which real galaxy attenuation curves can vary from basic screen models using the comparatively realistic and diverse morphologies that arise in EAGLE galaxies. Studies of variation in galaxy attenuation curves have been performed for observed galaxies assuming idealised geometries by (e.g. Byun et al., 1994; Baes & Dejonghe, 2001; Wild et al., 2011; Kriek & Conroy, 2013) and for small samples of zoomed galaxy simulations by Wuyts et al. (e.g. 2009a); Natale et al. (e.g. 2015).

We plot the r-band luminosity-weighted average attenuation curves of intrinsically blue ($u^\star - r^\star < 2.0$) EAGLE galaxies, normalised by the attenuation in the V-band, in Fig. 5.6. Face-on, edge-on and random projections are plotted as blue, red and green curves, respectively. Recall that dust in birth clouds is accounted for in our models by the MAPPINGS-III SEDs of Groves et al. (2008) for which we do not have the analytical description of the intrinsic attenuation curve. Therefore, we approximate the attenuation given the modelled dust content assuming a foreground screen. Fortunately, the proportion of optical light attenuated in the HII regions or associated PDR is small relative to the diffuse component, except at some specific atomic transitions. Nevertheless, we find that the increased attenuation visible in Fig. 5.6 at the Hα and Hβ wavelengths is still clearly present even when only the diffuse contribution is taken into account: this is because the PDR are preferentially embedded in denser regions of the ISM, and it is this diffuse ISM dust that causes the high attenuation. We emphasise that preferential attenuation of young stars due to dust in a birth cloud screen is explicitly built in to both the SKIRT and the Charlot & Fall (2000) model employed in chapter 3. The difference is due to additional preferential attenuation of the diffuse ISM represented as a single screen in Charlot & Fall (2000).

In all cases, attenuation increases rapidly towards shorter wavelengths with significantly higher attenuation at certain discrete wavelengths and a broad absorption feature at ≈ 220 nm. For face-on galaxies, the slope is much steeper than the intrinsic dust extinction law. The discrete wavelengths correspond to atomic transitions at which star forming regions dominate emission, their boosted atten-

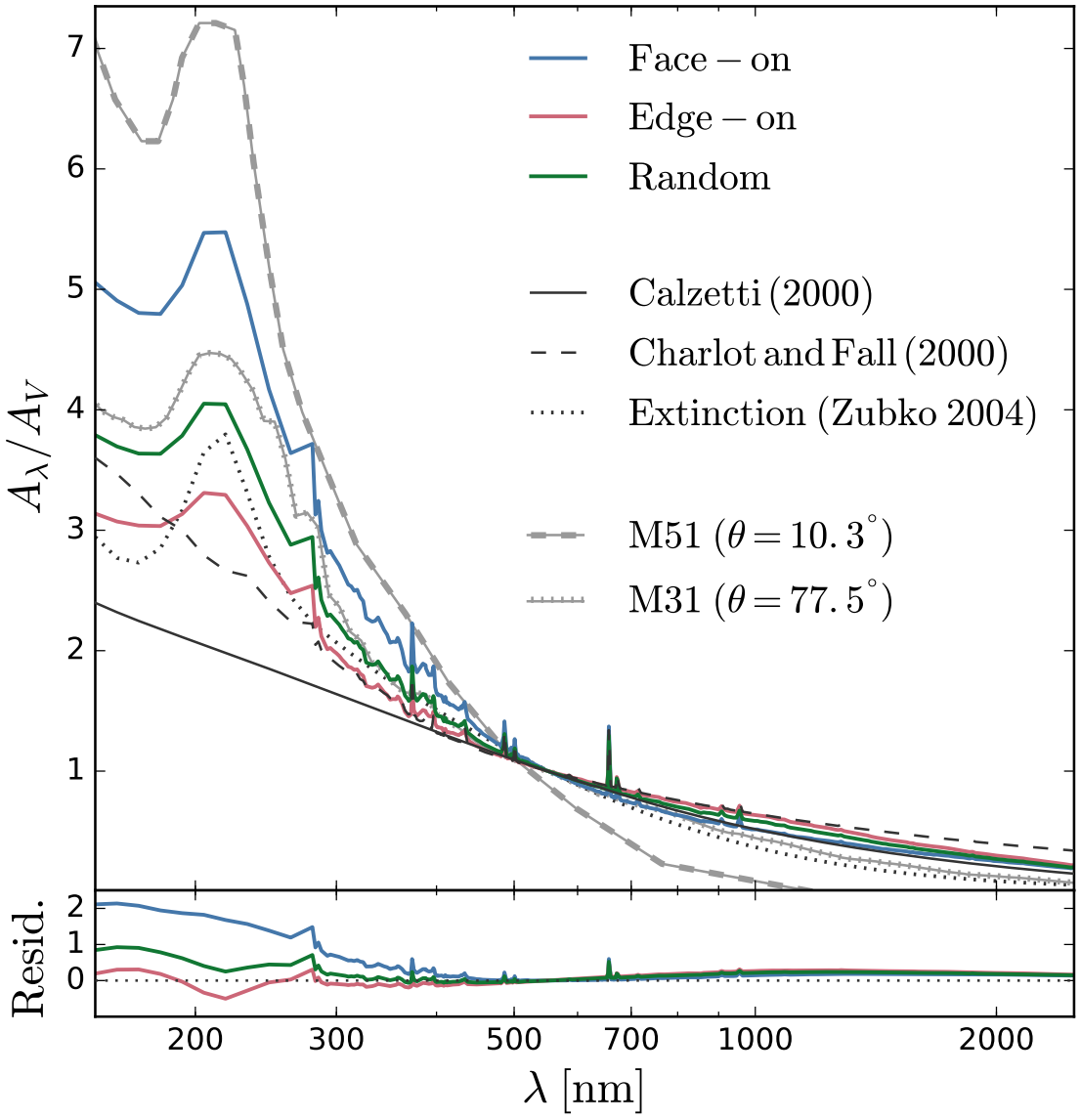

Figure 5.6: Attenuation as a function of wavelength, normalised to attenuation in the V-band at 550 nm. The luminosity-weighted average attenuation curves of intrinsically blue ($u^\star - r^\star < 2.0$) EAGLE galaxies for face-on, edge-on and random orientations are plotted as blue, red and green curves, respectively. {*continued on next page...*}

Figure 5.6: {*Continued from previous page...*} The attenuation laws of Calzetti et al. 2000 and Charlot & Fall 2000 are plotted as solid and dashed black lines, respectively, and the attenuation curve inferred for the galaxy M51 by De Looze et al. (2014) and for M31 by Viaene et al. (2016a), are plotted as dashed and dotted grey lines, respectively. The inclination of these galaxies is plotted in the legend. We also plot the intrinsic extinction curve used by SKIRT, Zubko et al. (2004). The bottom panel shows the residuals between the three EAGLE curves and the dust extinction curve of Zubko et al. (2004), assumed by SKIRT. The shape of the attenuation curve for EAGLE galaxies varies with orientation, with face-on galaxies exhibiting a stronger wavelength dependence.

uation is due predominately to the increased diffuse dust around these regions[6]. The feature at ≈ 220 nm is intrinsic to the assumed dust extinction law.

The average edge-on attenuation curve is less steep, or 'greyer', than that of face-on galaxies. This appears to be because the dust in EAGLE galaxies is spatially correlated with star forming gas, therefore intrinsically blue stars are preferentially obscured in the face-on view, while in the edge-on view that dust also acts as a screen for older stars. The A_λ curve for the randomly oriented values exhibits an intermediate steepness between the face-on and edge-on curves.

The extinction curve assumed by SKIRT when processing EAGLE galaxies is that of Zubko et al. (2004). The extinction curve is plotted as a black dotted line in the top panel (again normalised to 1 for the V-band), while in the bottom panel we plot the residuals of the EAGLE attenuation curves once the V-band normalised extinction is subtracted, to isolate the influence of geometry and orientation. We see that the EAGLE curves are steeper than the intrinsic extinction curve, again a manifestation of the preferential obscuration of young stars, most exaggerated for the face-on projection. We also see that the EAGLE curves lie

[6]Constructing ISM attenuation curves for the HII regions alone (see appendix B.5) yields curves similar to the Calzetti et al. (2000) and Charlot & Fall (2000), with the Hα feature reduced by ≈ 90 %.

above the extinction curve at NIR wavelengths. This can be ascribed to absorption overtaking scattering as the primary photon-dust interaction at wavelengths longer than optical, leading to a smaller fraction of attenuated light being scattered into the line of sight than at optical wavelengths. As a result, when curves are normalised at optical wavelengths, the NIR attenuation appears boosted relative to the pure extinction curve.

For comparison, we plot the attenuation curves of the Calzetti et al. (2000) and Charlot & Fall (2000) screen models. Comparing to the screen-model curves we see that the attenuation curves for EAGLE are generally steeper at all orientations. The screen models are closest to the edge-on curve at short wavelengths, due to dust behaving as a screen for many stars in an edge-on view. The Charlot & Fall (2000) curve represents a two component screen model, accounting for additional attenuation of young stars associated with stellar birth clouds. This age-dependent attenuation model provides better agreement with the EAGLE curves than the single screen Calzetti et al. (2000) model, laying closest to the edge-on EAGLE curve. The fact that young stars are also preferentially attenuated by diffuse ISM in our SKIRT modelling may explain why the EAGLE attenuation curves are steeper still. It seems that the preferential attenuation of young stars may be decisive to the sense of this result too; while we find geometric effects generally steepen attenuation curves relative to the input extinction, indiscriminate mixed attenuation models can lead to significantly flatter attenuation than the input model (e.g. Wuyts et al., 2009a). For simplicity, and consistency with our previous work, the attenuation profile is kept the same for both ISM and birth cloud attenuation in the Charlot & Fall (2000) model as described in Equation 3.2.2. However, some empirical studies advocate for steeper attenuation profiles associated with the birth clouds about star forming regions, based on line-of-sight measurements in the Milky Way (Wild et al., 2007; da Cunha et al., 2008). Adopting such a parametrisation could further steepen the effective attenuation and modify the boosted emission line absorption represented by the Charlot & Fall (2000) model.

We also plot attenuation curves derived for local galaxies M31 and M51 (from

Viaene et al. 2016a and De Looze et al. 2014, respectively) M31 is a relatively edge-on galaxy, with an inclination angle of $\theta = 77°$ (Brinks & Burton, 1984), whereas M51 is practically face-on at $\theta = 10°$ (De Looze et al., 2014). The M31 attenuation curve lies between the face-on and edge-on curves at wavelengths short-ward of the V-band, residing closest to the random projection curve. The M51 curve is steeper than any of EAGLE or screen-model curves. The M31 and M51 curves are both steeper than the EAGLE curves for comparable galaxy orientations. They also show more difference in slope than between the face-on and edge-on curves. We suggest that this is because EAGLE galaxy discs are thicker, and smoother than observed discs, both a consequence of limitations in the sub-grid physics. This could indicate that the orientation dependence we identify in EAGLE galaxies may become stronger if EAGLE galaxies possessed more realistic, thinner discs.

Observational studies have explored attenuation curve variation through SED fitting of low and high redshift galaxy samples and assuming screen-like attenuation (e.g. Wild et al., 2011; Kriek & Conroy, 2013, respectively). Wild et al. (2011) find a similar trend between attenuation curve slope and inclination for nearby galaxies as we observe here. However, both Wild et al. (2011) and Kriek & Conroy (2013) find a slight weakening of the 2175Å bump feature for face-on galaxies, which is not apparent in EAGLE. As this feature and its variation is attributed to poorly understood dust grain species that inhabit certain regions of galaxies, and given our modelling does not include spatial variation of the dust mix, this is perhaps unsurprising. A better understanding of the nature of these enigmatic dust grains, and their location in galaxies, would allow us to incorporate this into our modelling.

5.4 SKIRT colours of EAGLE galaxies

In this section we compare colours of EAGLE galaxies to GAMA data, as well as to the fiducial GD+O model of chapter 3 (which we will refer to simply as the GD+O model below). We recall that our modelling, described in section 5.2, represents dust attenuation in two distinct ways; attenuation effects associated with

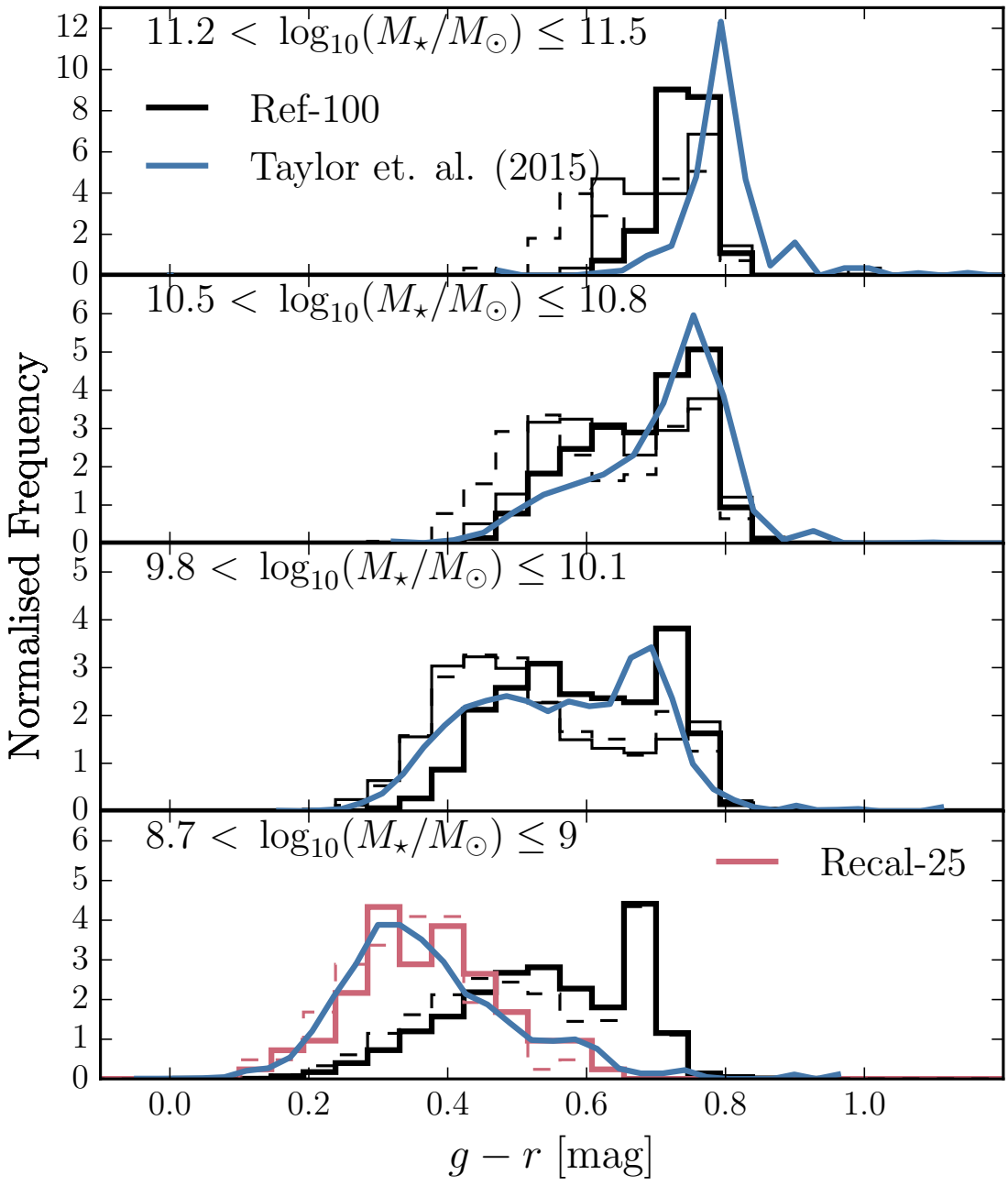

Figure 5.7: Rest-frame $z = 0.1$ SDSS $g - r$ colour distributions of galaxies in four non-contiguous bins of stellar mass, labelled in each panel. EAGLE galaxies of simulation Ref-100 are shown in black, where dashed lines neglect ISM dust, thin solid lines indicate the GD+O colours of chapter 3, thick solid lines include ISM dust modelled using SKIRT. Red lines (bottom panel only) are galaxies from the higher resolution simulation Recal-25, processed with SKIRT. *Blue* lines show the observed distributions of Taylor et al. (2015).

HII regions are built into the MAPPINGS-III spectra, while dust in the diffuse ISM is accounted for by the SKIRT radiative transfer calculation. We will sometimes refer to models without ISM dust as 'intrinsic' colours and to these galaxies as 'dust free' but note that this only refers to ISM dust, not the dust associated with the MAPPINGS-III source model.

5.4.1 Comparison with observations

5.4.1.1 Colour distribution at a given stellar mass

The distribution of rest-frame galaxy $g-r$ colours at $z=0.1$, in narrow (0.3 dex) non-contiguous stellar mass bins, showing both $z=0.1$ EAGLE galaxies and GAMA data, is plotted in Fig. 5.7 (which can be compared to the simpler GD+O dust-screen model, thin solid lines). Stepped lines represent the EAGLE colour histograms, using black to denote simulation Ref-100 and red to denote simulation Recal-25. These are either thin dashed to indicate colours without ISM dust, thin solid to represent the GD+O model, or thick solid representing those obtained using radiative transfer with SKIRT. Continuous blue lines correspond to rest-frame (volume-limited) GAMA galaxy colours without dust correction from Taylor et al. (2015). Stellar masses for the GAMA galaxies, inferred through SED fitting, are taken from Taylor et al. (2011). All distributions are normalised to unit area. Here we compare the SKIRT to observed distributions, additionally comparing to the GD+O model in sections 5.4.1.2-5.4.2.2.

Comparing dashed to solid lines in the top panel demonstrates that dust reddening in massive ($10^{11.2} < M_\star/\mathrm{M}_\odot < 10^{11.5}$) blue galaxies is significant, with blue galaxies redder in SKIRT compared to intrinsic colours by 0.1-0.2 mag in $g-r$, changing the bi-modal ISM dust-free colour distribution to a single red peak at $g-r \approx 0.75$. The intrinsically blue colours of massive EAGLE galaxies are caused by relatively low levels of residual star formation, not completely suppressed by the AGN feedback. The dust content of these star forming regions is high, however, leading to significant dust-reddening when processed with SKIRT. At these masses, about half of the galaxies on the SKIRT red sequence are dust reddened

from an intrinsically bluer colour[7].

Dust reddening also affects the $g-r$ colour of galaxies with masses $10^{10.5} < M_\star/\mathrm{M}_\odot < 10^{10.8}$ strongly (second panel from top), shifting blue galaxies to higher $g-r$ by ≈ 0.1 mag, to $g-r \approx 0.6$, and changing the bi-modal colour distribution into a single red peak with a tail to bluer colours. This blue tail, due to galaxies with more moderate reddening, hints that the intrinsic colour distribution is in fact bi-modal. At these masses, about a third of the *'green valley'* population with $g-r \approx 0.65$ comprises dust-reddened galaxies. The remaining galaxies have intrinsic colours that puts them in the green valley, and are typically transitioning between the blue and red populations, as discussed in detail in chapter 4.

The second-lowest mass bin ($10^{9.8} < M_\star/\mathrm{M}_\odot < 10^{10.1}$) again contains a population of strongly-reddened galaxies. A distinct bi-modality remains after reddening, with the red peak stronger than the blue peak, opposite to the case of intrinsic colours. Intrinsically blue galaxies appear less attenuated on average, with the blue peak shifted by only ≈ 0.05 mag relative to the ISM dust-free photometry, to $g-r \approx 0.5$. The *'green valley'* population is also boosted relative to the ISM dust-free photometry. Recalling Fig. 5.5, we see that the dust-boosted red and green galaxy populations produced by SKIRT have a tail to significantly bluer colours. The tail consists of galaxies that have little or no ISM dust as well as dusty galaxies seen nearly face-on with ISM dust-free colours typical of the star-forming population.

At the lowest stellar masses, $10^{8.7} < M_\star/\mathrm{M}_\odot < 10^{9}$ (bottom panel), EAGLE galaxies show very little reddening when processed with SKIRT. Indeed, comparing the ISM dust-free and SKIRT $g-r$ distributions separately for the Ref-100 and

[7]Note that while the dust attenuation in EAGLE appears to be systematically lower than observed for edge-on galaxies (see section 5.3.1), increasing attenuation would not necessarily lead to the EAGLE red sequence position shifting to even redder colours. Unlike in a screen model where extreme reddening is possible, in our SKIRT modelling galaxies with high dust content have colours that saturate to that of old stellar populations, as these populations are preferentially unobscured by dust. If the dust clouds are made optically thick, the galaxy photometry is essentially that of the unobscured population. More realistic attenuation values might, however, lead to more galaxies appearing as members of the red sequence.

Recal-25 simulations shows that dust effects are minimal.

In the most massive bin, observed colours from GAMA conform to a tight red sequence centred at $g - r \approx 0.7$. The SKIRT distribution is similar but shifted by ≈ 0.05 mag to the blue. The median stellar metallicity of EAGLE galaxies agrees well with the observationally inferred values (S15), and the stars in these galaxies are generally old. It is therefore somewhat surprising that the simulated and observed colours do not agree better, since reddening is not important for these galaxies anyway (either in our model, or in the GAMA data). In chapter 4 I show that the metallicity distribution of star particles in EAGLE galaxies is nearly exponential, and it is the lower Z particles that make EAGLE galaxies bluer than observed. A possible reason for the discrepant colours is thus that massive EAGLE galaxies have too low metallicities, even though the mass-weighted simulation metallicity agrees well with the luminosity-weighted observed metallicity, see chapter 4 for more discussion.

The second most massive bin shows striking consistency between SKIRT and observed colours. The agreement with the data is in fact superior to that obtained with the GD+O dust-screen model. In particular, the relative fraction of red and blue galaxies is much closer to the observed ratio when using the SKIRT. The reason for this is explored further below.

The second lowest mass bin shows similarly good agreement with the observed distribution, with SKIRT colours systematically shifted to somewhat redder values ($\lesssim 0.05$ mag). Again, the colours conform better to observation than those of chapter 3, with the latter's dust-reddened colours in fact close to the intrinsic EAGLE colours.

Finally, in the lowest mass bin, the Ref-100 colours show poor agreement with observation. Furlong et al. (2015) showed that at these lower galaxy masses, numerical effects and poor sampling in EAGLE cause the star formation rates to be too low and too many galaxies to be quiescent. We therefore also show the colours for the higher-resolution Recal-25 simulation (red). These agree well with GAMA. The SKIRT colours of each of the simulations are very similar to those of GD+O, which is understandable as both are very close to the intrinsic colours (i.e. are

subject to minimal reddening) in this mass range.

5.4.1.2 Colour-mass diagram

The $g-r$ colour versus stellar mass distribution of EAGLE galaxies is compared to that obtained from GAMA in Fig. 5.8. As explained above, the star-formation rate and hence colour of low-mass galaxies in Ref-100 is not well-resolved numerically (Furlong et al., 2015). We therefore combine the more massive EAGLE galaxies from Ref-100 with the low mass galaxies from the higher-resolution Recal-25 simulation, cross-fading between the two in the mass range $10^{10}\mathrm{M}_\odot$ to $10^{9}\mathrm{M}_\odot$ as in chapter 3. The observed GAMA contours are based on the analysis of Taylor et al. (2015). Note that the cross-fading between two simulations (performed as described in chapter 3) extends the mass range over which galaxies are well resolved, but also introduces some inconsistencies, for example the different simulation volumes probe different environments. As such, this is intended only to provide a qualitative comparison with the observations, with quantitative comparison facilitated by Fig. 5.7.

Similar to Fig. 5.7, we see that the EAGLE colours obtained with SKIRT generally show good agreement with the observed distribution. The blue cloud and red sequence populations in EAGLE appear to be in approximately the observed position and contain a roughly similar share of the galaxy population across the mass range. The green valley population is enhanced relative to the GD+O photometry, in better agreement with GAMA data. The inconsistent surplus of blue galaxies at the high-mass end, $M_\star \gtrapprox 10^{10.5}\mathrm{M}_\odot$, is also largely suppressed with respect to GD+O. This is attributable to the more representative treatment of the spatial distribution of the dust in SKIRT, with the ISM dust enshrouding young stars, rather than being distributed in a diffuse galaxy-sized disc as assumed in chapter 3.

However, there are still some notable discrepancies between EAGLE and GAMA. Across all masses the red sequence in EAGLE is flatter than observed, with slightly bluer colours at high mass and redder colours at low mass. This is consistent with the findings of chapter 3, and is symptomatic of the fact that the metallicity of EA-

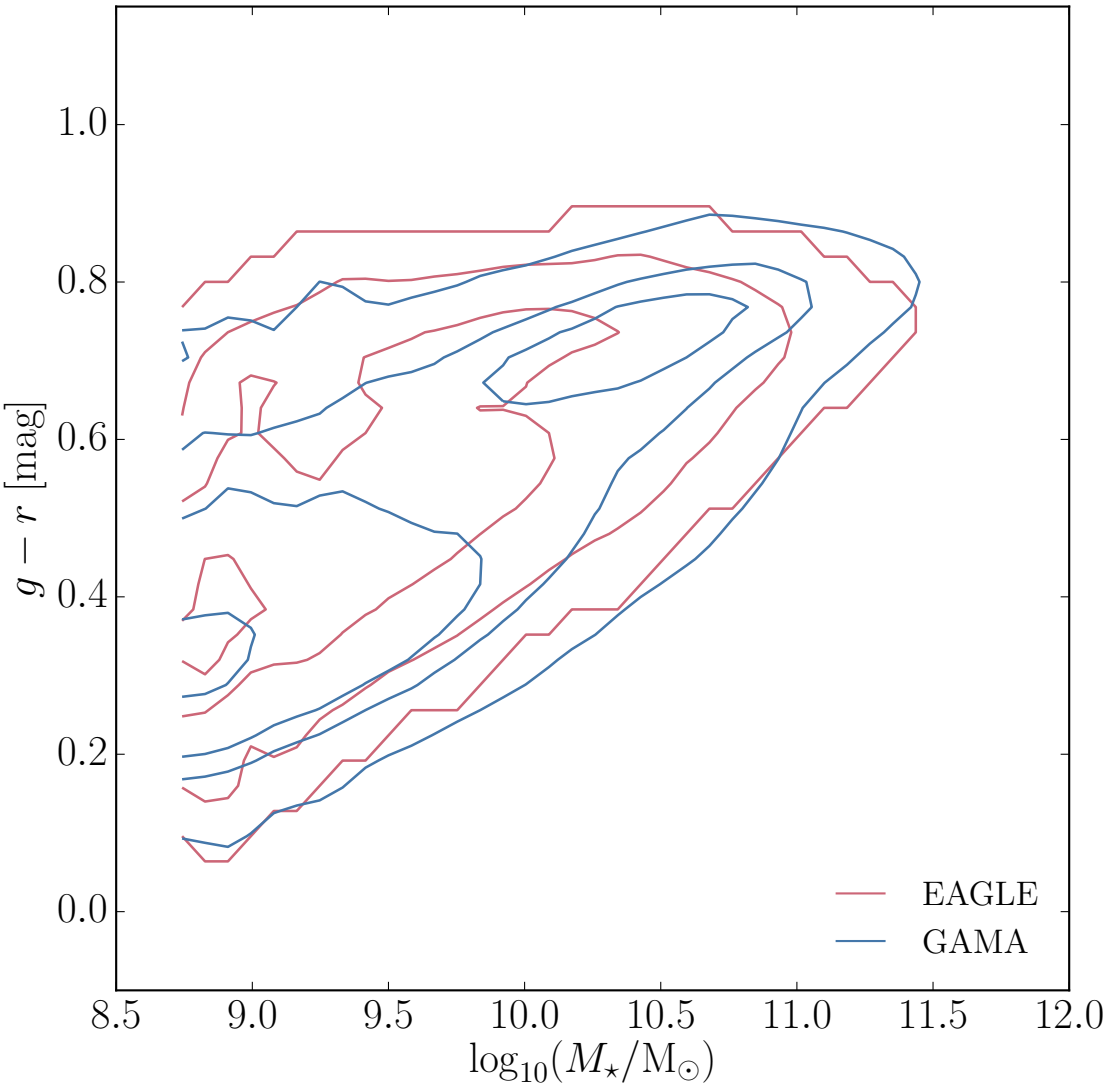

Figure 5.8: Rest-frame $z = 0.1$ SDSS $g - r$ colour as a function of galaxy stellar mass, for qualitative comparison of EAGLE and GAMA. *Red Contours* are for randomly-oriented EAGLE galaxies, processed using SKIRT. The EAGLE sample combines galaxies taken from simulation Ref-100 at high mass with galaxies from simulation Recal-25 at lower stellar mass, to mitigate the poorer resolution of Ref-100 (see text). *Blue contours* show the observed distribution taken from Taylor et al. (2015). The contour levels from low to high exclude 3, 18, 48, and 93 percent of the galaxies in each sample.

GLE galaxies does not increase with $M_\star$ as steeply as observed. This is at least in part due to insufficient numerical resolution, as shown by S15 (their Fig. 12). A moderate surplus of blue galaxies relative to the observations can also still be seen between $\sim 10^{10}\mathrm{M}_\odot$ and $\sim 10^{10.5}\mathrm{M}_\odot$, likely due to a combination of lower passive fractions and lower typical dust attenuation in the EAGLE galaxies relative to those observed. Differences between the observed and simulated stellar mass functions also contribute to this discrepancy: the EAGLE simulation has a deficiency of galaxies at the knee of the mass function ($M_\star \sim 10^{10.5}\mathrm{M}_\odot$, S15), such that the contours are skewed to lower masses than in the GAMA distribution.

5.4.2 Comparison of SKIRT colours to dust-screen models

We now turn to comparing the GD+O photometry with that generated using SKIRT. The screen modelling of chapter 3 employs several parameters, notably τ_{BC}, the dust optical-depth in the birth-clouds of stars, τ_{ISM}, the dust optical depth in the ISM, and $q = b/a$, the axial ratio of the oblate spheroid within which the ISM dust is assumed to be distributed. The fiducial values of these parameters were informed by observational studies, but they do not necessarily reflect the ISM distribution in EAGLE. To test whether the radiative transfer photometry is better reproduced with a different parametrisation of the GD+O model, we fit the GD+O parameters to the SKIRT results. The parameter fits are obtained using Bayesian inference, where a Markov-chain Monte Carlo (MCMC) method is used to find the maximum-likelihood parametrisation. We simultaneously find the maximum-likelihood (ML) values of τ_{ISM} and q, enforcing the constraint that $\tau_{\mathrm{BC}} = 2\tau_{\mathrm{ISM}}$ as in the fiducial model of Charlot & Fall (2000). The application of this constraint and full details of the MCMC procedure are given in Appendix B.3.

The ML parameters from fitting the fiducial SKIRT model using the free parameters of GD+O are given in Table 5.2. We find that the ML τ_{ISM} and τ_{BC} values needed to describe the SKIRT results for Ref-100 are $\approx 10\%$ lower than the fiducial values of GD+O. This offset is small, implying similar typical attenuation values in both models. Because the values of τ_{ISM} and τ_{BC} used in chapter 3 come

Table 5.2: Maximum likelihood parameters for the GD+O model of chapter 3 that best describes the fiducial SKIRT photometry. These values are derived using an MCMC approach, as detailed in Appendix B.3.

Model	$\tau_{\rm ISM}$	$\tau_{\rm BC}$	q
Fiducial GD+O values	0.33	0.67	0.2
Ref-100 ML	0.301	0.602	0.556

from the original fitting by Charlot & Fall (2000) of the SDSS observations, it is encouraging that they are recovered independently by fitting the SKIRT results: this suggests that our SKIRT model yields realistic average optical dust attenuations for galaxies of a given metallicity and gas fraction, and also that the relative stellar and ISM geometries and our dust mapping are reasonable.

However, the q parameter is significantly higher for the SKIRT model, implying less inclination dependence and lower edge-on attenuation in the model, as is indeed seen in Fig. 5.3. This most likely reflects the artificially 'puffed-up' ISM in simulated galaxies. We repeat that this higher disc thickness is partly set by numerical resolution, but is mostly due to the assumed temperature-density relation for star-forming (disc) gas in the EAGLE sub-grid model.

Overall, we find that the fiducial SKIRT model, which is based on physical modelling of the EAGLE galaxies, produces typical dust attenuations at optical to NIR wavelengths similar to the GD+O model. Although the $f_{\rm dust}$ and $f_{\rm PDR}$ parameters of the model were chosen to reproduce FIR observables by Camps et al. (2016), this result is in fact independent of that calibration. To demonstrate this, we apply our ML fitting procedure to an 'uncalibrated' SKIRT model; produced using the default literature values of $f_{\rm dust}$ and $f_{\rm PDR}$. Similar levels of agreement between the fiducial $\tau_{\rm ISM}$, $\tau_{\rm BC}$ and q values of GD+O are recovered, as shown in Appendix B.4. Given these findings, when comparing models we do not modify the parameters of the SKIRT and screen model from the published values of Camps et al. (2016) and GD+O. The fiducial SKIRT model photometry and that of the GD+O model are compared below.

5.4.2.1 Colour-colour distributions

To further explore the effects of dust-reddening, we compare colour-colour distributions for dust-free photometry of EAGLE galaxies from chapter 3, the GD+O dust-screen model of chapter 3 and the full SKIRT modelling in Fig. 5.9. We plot rest-frame $u-g$ against $g-J$ colours, analogous to the UVJ diagram used by Williams et al. (2009), to separate actively star forming but dust reddened galaxies from intrinsically red and passive galaxies. Data points are shaded from red to yellow by point density, to indicate how galaxies are distributed. Thin green lines indicate the mean reddening vectors for the two dust models relative to the intrinsic photometry of chapter 3, in regular bins of ugJ intrinsic colour. These are only plotted for bins with > 10 galaxies. The colour-colour bin centres from which the vectors emanate are highlighted by green points. We over-plot the ugJ cut used to separate active from passive galaxies by Schawinski et al. (2014) in bold green. The passive fractions of EAGLE galaxies, as inferred from applying this cut, are indicated in each panel.

The three photometric models produce qualitatively similar distributions, but with some important differences. The dust-free model in the left panel exhibits two well-defined peaks, a 'blue peak' at $(u-g,\, g-J) \approx (1.2, 1.0)$ and a 'red peak' at $\approx (1.6, 1.6)$. The intrinsic distribution is relatively tight for galaxies with $M_\star > 10^{10}\mathrm{M}_\odot$, with $\lesssim 0.2$ mag scatter in $u-g$ for a given $g-J$ colour. The passive fraction is $f_{\mathrm{passive}} = 0.23$ for galaxies with $M_\star > 10^{10} M_\odot$.

The middle panel, showing galaxy colours produced by the GD+O dust screen model, exhibits a similar distribution in the passive region. From the lack of visible lines at $u-g > 1.4$, we see that there is minimal reddening of galaxies into or within this region. The recovered passive fraction of $f_{\mathrm{passive}} = 0.24$ reveals that indeed the passive region is $< 5\%$ polluted by the galaxies defined as active in the dust-free (left) panel. The active region galaxies, however, exhibit more variation. While the blue peak is similarly well defined relative to the dust-free colours, the position of the peak is shifted to slightly redder colours by ~ 0.1 mag and is broadened by scatter to redder colours, with many more star-forming galaxies having $g-J > 1.5$. The mean reddening vectors are small relative to the distance

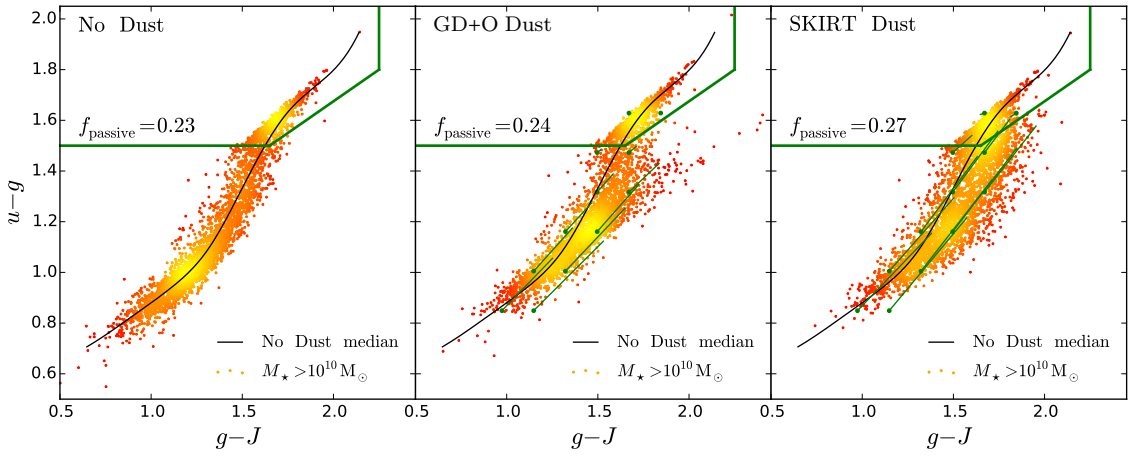

Figure 5.9: Rest-frame $z = 0.1$ ugJ colour-colour diagrams for different photometric models. *Points* are EAGLE galaxies from simulation Ref-100 with stellar masses $> 10^{10}{\rm M}_\odot$, shaded from red to yellow to indicate local point density. The dust-free photometry of chapter 3, the ML parametrisation of the GD+O dust-screen model, and the SKIRT photometry including ISM dust and HII regions are shown in the left, middle and right panels respectively. *Thick, green lines* show the passive galaxy cut advocated by Schawinski et al. (2014), the corresponding passive fraction of EAGLE galaxies using this cut is indicated in each panel. *Black curves* indicate the median $u - g$ values as a function of $g - J$ for the dust-free photometry, these are repeated in each panel to guide the eye. *Thin, green lines* indicate the mean reddening vectors of EAGLE galaxies in the dusty models relative to the dust-free model. These emanate from green points, specifying the centre of each bin from which a vector is computed. Note that vectors point from bottom-left to top-right. The SKIRT model gives higher passive fractions than the intrinsic and GD+O dust photometry, indicating significant pollution of the passive region by star forming galaxies.

between the peak and the most extremely attenuated active galaxies, which have colours $g - J \gtrsim 2$.

The right panel, showing the SKIRT model colours, reveals some consistent features. The passive region galaxies reveal a similar distribution as in the left and middle panels, with a red peak in a very similar position. The active region galaxies also occupy a similar region of the ugJ plane to the GD+O (middle) panel, with a blue peak shifted to slightly redder colours relative to the dust-free model in the left panel. However, in detail there are some notable differences. The blue peak is significantly depleted relative to the other panels, with the red peak exhibiting a tail to bluer colours. Though the SKIRT model does not possess the extremely reddened galaxies of the GD+O (middle) panel, the magnitude of the mean reddening vectors are generally larger across the intrinsic distribution and show less reduction with redder intrinsic $u - g$ colour relative to GD+O. We also see an enhanced 'green' population of galaxies with intermediate colours $1.25 < u - g \lesssim 1.5$ in the active region. The enhanced average reddening across the distribution also results in a higher recovered passive fraction of $f_{\rm passive} = 0.27$. This indicates that the passive region has a $\approx 15\%$ pollution by galaxies defined as active in the dust-free (left) panel. The reddening of galaxies from the blue peak to the red peak in the ugJ diagram corresponds to the significant boost (depletion) of the red (blue) sequence population for the SKIRT photometry relative to the dust-free colours seen in Fig. 5.7.

The differences between the GD+O and SKIRT panels in Fig. 5.9 can be attributed to the nature of the dust modelling. The GD+O reddening vector is close to parallel with the sloped boundary of the passive region, as illustrated by a tail of extremely reddened active galaxies with $g - J > 2$. This is unsurprising, as the screen model of Calzetti et al. (2000) is used by Schawinski et al. (2014) to define the boundary between active and passive galaxies. This may explain why few dusty galaxies move into the passive region when applying the GD+O screen model. The SKIRT model, which exploits the 3D distribution of dust around stars, yields generally steeper reddening vectors of higher magnitude, both of which contribute to moving dusty star forming galaxies into the region where galaxies

are deemed to be passive when using the Schawinski et al. (2014) colour-colour cut. This is because nascent stellar populations embedded in dense ISM are effectively shielded in the SKIRT model, leading to more active galaxies masquerading as passive. Again, the fraction of galaxies misclassified as passive could be underestimated due to the lack of highly attenuated edge-on EAGLE galaxies, attributable to the artificially 'puffed-up' ISM in the simulation.

5.4.2.2 Passive fractions

We use the colour-colour cut of Schawinski et al. (2014) from Fig. 5.9 to calculate passive fractions as a function of mass for both SKIRT and ISM dust-free photometry. The results are shown in Fig. 5.10, where we compare to the passive fractions calculated directly from the aperture star formation rates (see S15, Furlong et al., 2015). The value of the specific star formation rate $\mathrm{sSFR} \equiv \dot{M}_\star / M_\star$ below which a galaxy is deemed passive is somewhat arbitrary. As we are using the Schawinski et al. (2014) cut in ugJ for the colour cut, we use a value of $10^{-2.5}$ Gyr^{-1} which yields good agreement with the dust-free photometric estimates for numerically well-resolved galaxies ($M_\star \gtrapprox 10^{10}\mathrm{M}_\odot$). Note that S15 and Furlong et al. (2015) used a higher value of 10^{-2} Gyr^{-1}.

The differences between the photometric passive fraction estimates with and without ISM dust become apparent at masses $M_\star > 10^{9.5}\mathrm{M}_\odot$. For better-resolved galaxies, $M_\star > 10^{10}\mathrm{M}_\odot$, the passive fraction obtained when including dust reddening lies ≈ 0.1 dex above the value estimated using intrinsic colours or calculated using the sSFR cut. This offset suggests that, using colours alone, $\approx 15\%$ of the apparently passive population may be misclassified active galaxies for stellar masses $M_\star > 10^{10}\mathrm{M}_\odot$. This fraction could be higher still if our mock photometry had levels of attenuation closer to observation (see Fig. 5.3). It is important to note that the ugJ selection used here also represents a particularly stringent passive cut, hence why we compare to a specific star formation rate cut of $10^{-2.5}$ Gyr^{-1} rather than one at 10^{-2} Gyr^{-1}. We find that by relaxing the ugJ cut (a -0.1 shift in $u-g$ to approximate a 10^{-2} Gyr^{-1} selection) leads to a higher proportion of active galaxies being misclassified as passive due to dust effects ($\approx 38\%$). It seems

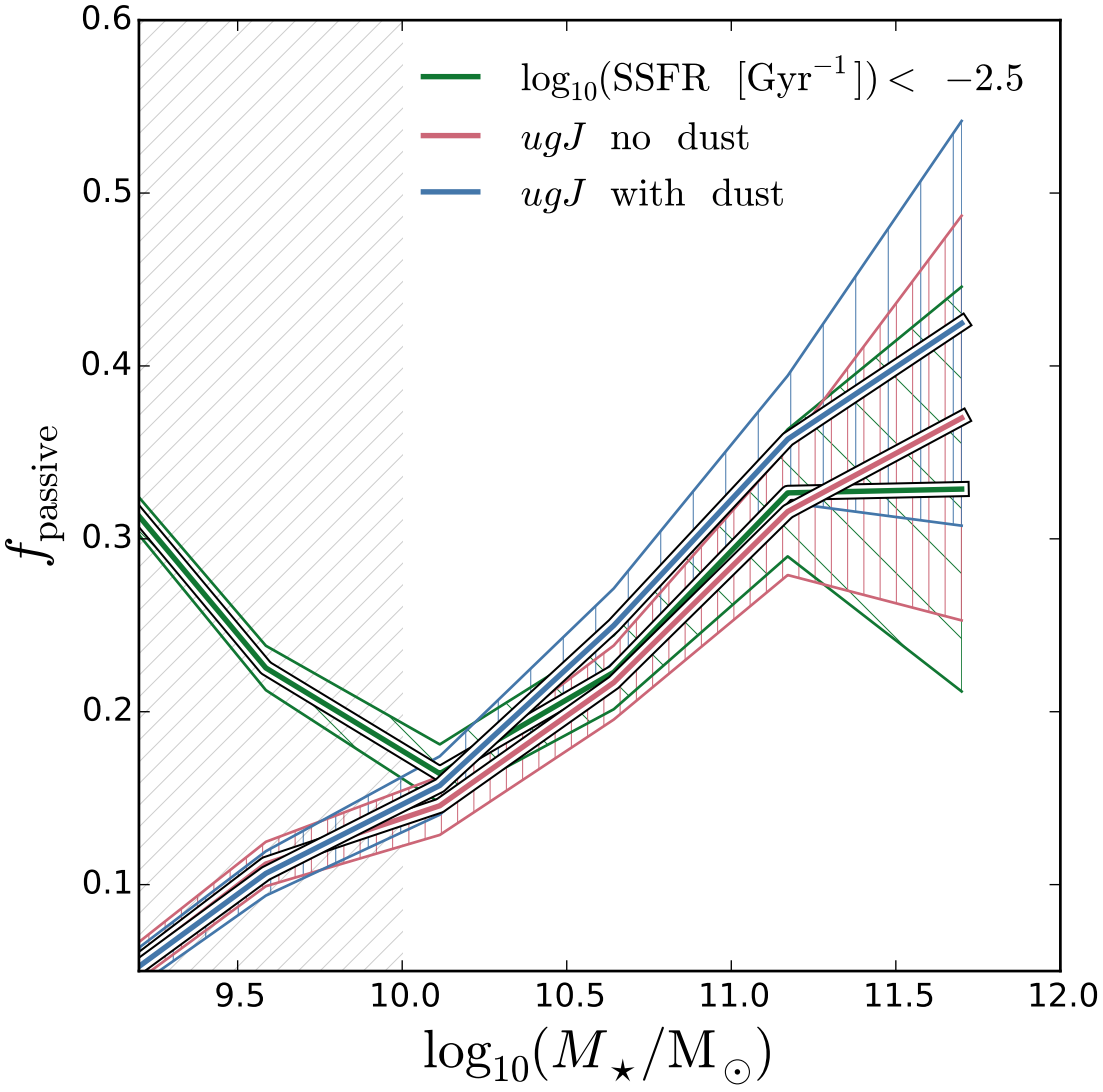

Figure 5.10: Passive galaxy fractions for the Ref-100 EAGLE simulation in bins of $M_\star$, equally spaced in $\log_{10} M_\star/\mathrm{M}_\odot$. The *green* line shows the values obtained using a $\dot{M}_\star/M_\star$ cut at $10^{-2.5}$ Gyr^{-1}. *Red* and *blue* lines show the fractions obtained using the photometry without and with ISM dust, respectively. *Coloured, hatched regions* indicate the uncertainty for each line, corresponding to the fractional Poisson error on the number of galaxies in each bin. The diagonally hatched region $M_\star < 10^{10}\mathrm{M}_\odot$ indicates where the true passive fraction (green line) decreases with stellar mass, due to resolution and volume effects. We see that the discrepancy between the passive fractions obtained using intrinsic and dust attenuated photometry increases with stellar mass above $10^{10}\mathrm{M}_\odot$.

that the use of a stringent cut minimises misclassification of passive galaxies to the 15% level.

There is a striking divergence between the sSFR and photometrically defined passive fractions for galaxies with $M_\star < 10^{10}\mathrm{M}_\odot$ apparent in Fig. 5.10. This occurs in a region where star formation rates are subject to resolution and volume effects, however it is the metallicities of these galaxies that is likely driving this discrepancy. Indeed, a (passive) 10 Gyr old stellar population with a metallicity of $Z = 0.4Z_\odot$ will lie *below* the $u - g = 1.5$ threshold of Schawinski et al. (2014) in the Bruzual & Charlot (2003) model - and hence is too blue to be classified as passive. As the SDSS sample of Schawinski et al. (2014) is dominated by galaxies of mass $\gtrsim 10^{10}$ M$_\odot$, it is likely that only a few of the observed galaxies would be affected by this.

5.5 Spectral Indices

We apply SKIRT modelling to compute two spectral indices that are often used as proxies for star formation activity, the Hα luminosity, $L_{\mathrm{H}\alpha}$ (e.g. Kennicutt, 1998a), and the strength of the 4000 Å break, D4000 (e.g. Kauffmann et al., 2003a). We compare the indices for EAGLE galaxies to both theoretical and observed values below, concentrating on the effects of dust, and test the correlation of these indices with the intrinsic star formation rate of EAGLE galaxies.

5.5.1 Dust effects on the Hα flux

The Hα luminosity of a galaxy is thought to be a reliable proxy for its star formation rate, basically because the recombining gas that emits the Hα photons is thought to be photo-ionised by massive ($> 10\mathrm{M}_\odot$) and hence recently (< 20 Myr) formed stars (e.g. Kennicutt, 1998a). However, as we have seen, such star-forming regions are typically dust obscured (not just by the dust in HII birth-clouds, but by ISM dust as well), and the measured flux therefore needs to be corrected for dust. Here we compare the intrinsic $L_{\mathrm{H}\alpha}$ values, emanating only from HII regions in our model, to those obtained using empirical corrections to observed spectra.

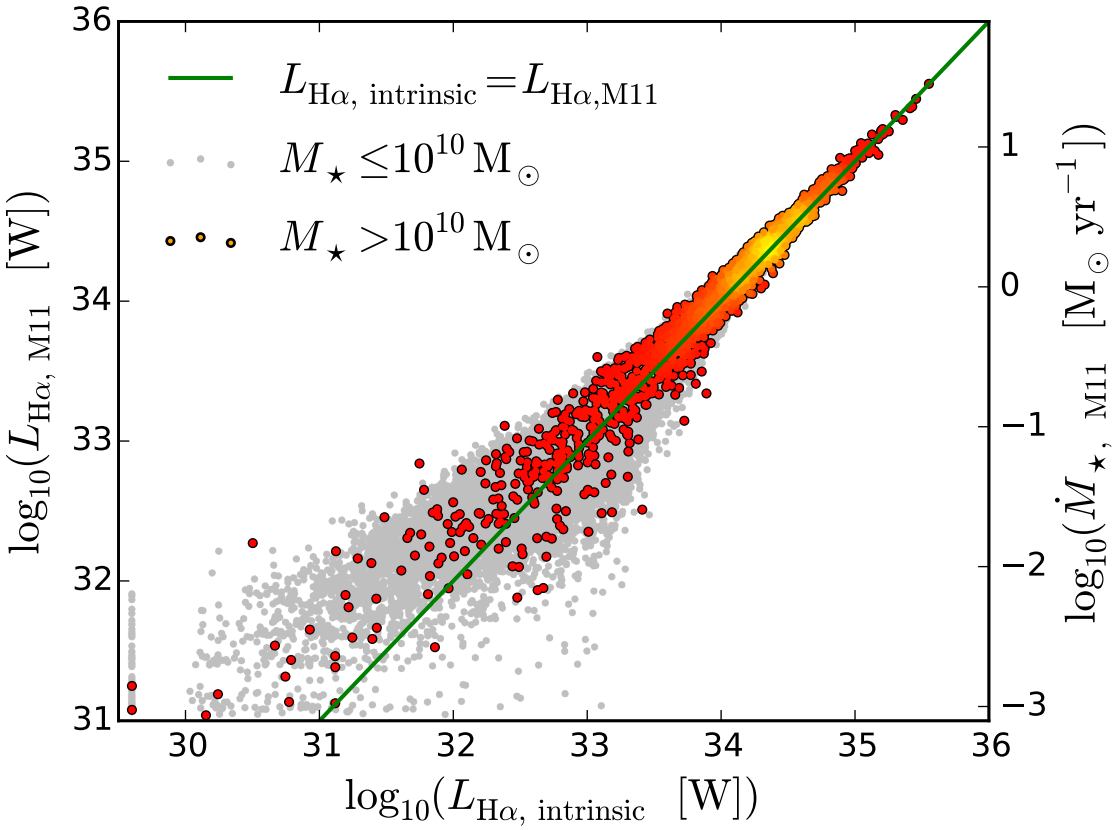

Figure 5.11: Hα fluxes of EAGLE galaxies. In this panel, ISM dust-free Hα flux from the MAPPINGS-III model compared to Hα flux computed from Eq. (5.5.5), where $\dot{M}_\star$ is the instantaneous star formation rate within a 30 kpc aperture; the value of $\dot{M}_\star$ is indicated on the right y-axis. Coloured dots are individual EAGLE galaxies with $M_\star > 10^{10}$ M$_\odot$ with colour a measure of the point density of galaxies in the plot; *grey points* represent galaxies of lower stellar mass. Galaxies where Hα is not detected are clipped to $\log_{10}(L_{\mathrm{H}\alpha}\ [\mathrm{W}]) = 29.8$; the *green line* indicates the 1:1 relation to guide the eye. {*continued on next page...*}

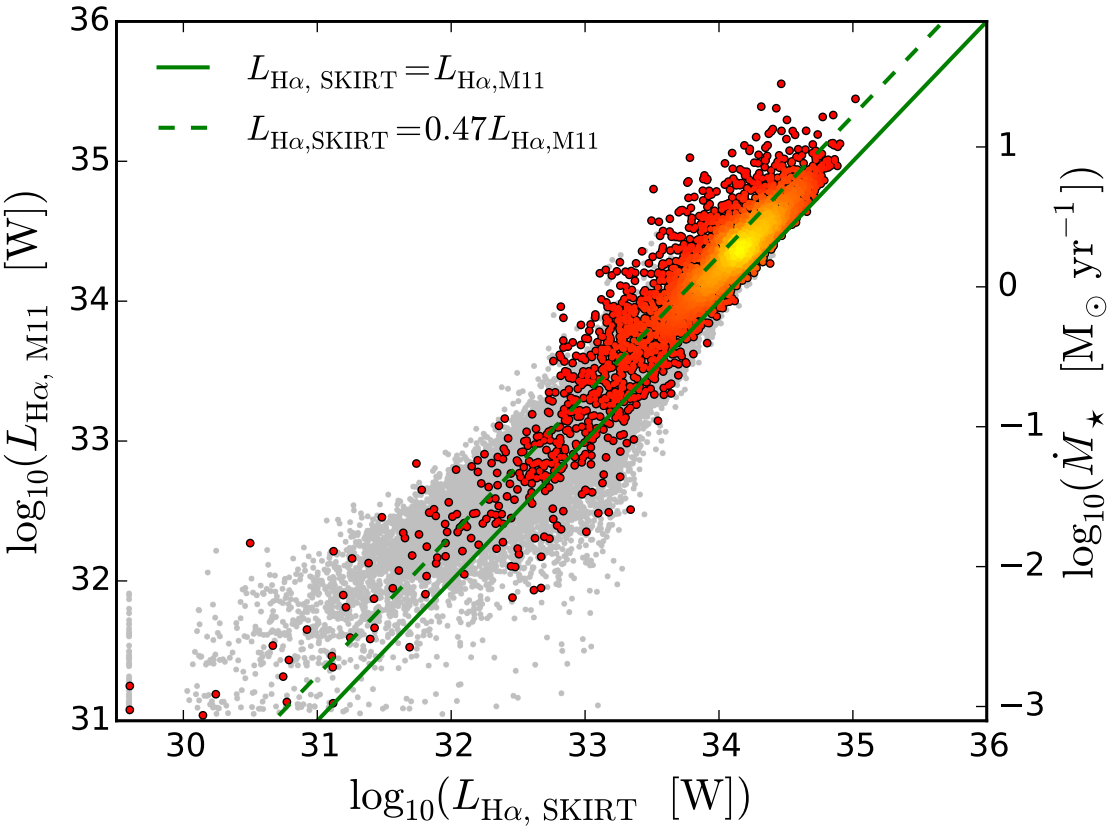

Figure 5.11: *Continued from previous page* Same as first panel, but showing the Hα fluxes computed using SKIRT *i.e.* including ISM dust; the *dashed* line is the best linear fit to the coloured points (excluding undetected galaxies), and represents the average dust attenuation factor. $L_{\mathrm{H}\alpha}$ values measured from ISM dust-free spectra generally recover those given by equation 5.5.5 very well, as expected, with a relatively large scatter at low values ascribed to shot noise in the sampling of HII regions. The dust attenuated values show an offset and large ($\sim$ 1 dex) scatter.

When measuring emission lines, we only use the HII region component of the source spectra (the blue line in Fig. 5.1) to minimise the contribution (either in emission or more likely in absorption) from the stellar continuum (a correction that needs to be applied to observational data). This enables us to isolate the effects of dust on inferred line fluxes, which we can investigate with SKIRT, from those caused by continuum fitting.

The relation between Hα line flux and star formation rate advocated by Murphy et al. (2011) is

$$L_{\mathrm{H}\alpha,\,\mathrm{M11}} = \left(\frac{\dot{M}_\star}{5.37 \times 10^{-42}\ \mathrm{M}_\odot\ \mathrm{yr}^{-1}} \right)\ \mathrm{erg\ s}^{-1}\,, \tag{5.5.5}$$

and is a recalibration of the relation from Kennicutt (1998a). The recalibration accounts for the different IMFs assumed by Kennicutt (1998a) (Salpeter) compared to Murphy et al. (2011) (Kroupa), and is thus consistent with the (Kroupa) IMF of the MAPPINGS-III models that we use for young stars. For a like-for-like comparison with $L_{\mathrm{H}\alpha}$ values obtained with SKIRT, we use the instantaneous $\dot{M}_\star$ within a 30 pkpc aperture from the EAGLE database (McAlpine et al., 2016). This is calculated by summing over the $\dot{M}_\star$ values of gas particles within that aperture.

As a first test of our HII region prescription and subsequent measurement procedure for calculating $L_{\mathrm{H}\alpha}$, we compare the values obtained using the ISM dust-free spectra, $L_{\mathrm{H}\alpha,\,\mathrm{intrinsic}}$, to $L_{\mathrm{H}\alpha,\,\mathrm{M11}}$ in the first panel of Figure 5.11. For this comparison we over-plot galaxies with $\log_{10}(M_\star/\mathrm{M}_\odot) > 10$ coloured by the local point density, with lower-mass galaxies under-plotted in grey. The green line indicates the 1:1 relation to guide the eye.

The tight 1:1 correlation between the two values for high SFR, $\dot{M}_\star \gtrsim 0.1\ \mathrm{M}_\odot\ \mathrm{yr}^{-1}$ ($L_{\mathrm{H}\alpha} \gtrsim 10^{33}$W), is reassuring, implying that the re-sampling technique used to parameterise HII regions (see section 5.2.1.2) reproduces the expected Hα measurements. This good agreement is expected: the same population synthesis models and a similar treatment of nebular components are employed in both the MAPPINGS-III model that we use, and the model used by Murphy et al. (2011) that yields the conversion factor given in Eq. 5.5.5.

At low SFR, the $L_{\mathrm{H}\alpha,\,\mathrm{intrinsic}}/L_{\mathrm{H}\alpha,\,\mathrm{M11}}$ ratio exhibits large scatter. This is due to

HII regions being sampled stochastically from the mass function of Eq. (5.2.1), yielding increased sampling noise for lower star formation rates. Galaxies without HII regions, and thus without Hα in our modelling, are plotted at $L_{\mathrm{H}\alpha,\,\mathrm{intrinsic}} = 10^{29.5}$ W in the figure. The right hand panel shows the corresponding plot for the ISM dust attenuated spectra (without attempting to correct the Hα flux for dust correction). We over-plot the 1:1 relation with a constant dust attenuation factor of $A = 0.47$ (dashed green line, this corresponds to 0.82 mag extinction). This factor is the mean offset between the measured (dust attenuated) and intrinsic Hα luminosities, as determined using a least-squares fit for Ref-100 galaxies of $\log_{10}(M_\star/\mathrm{M}_\odot) > 10$. The convergence of H$\alpha$ luminosities and A values are tested for the other simulations listed in Table 2.1 in Appendix B.2.2. The observed average attenuation in local galaxies is ≈ 0.4 (Kennicutt, 1992) (1 mag of extinction), a factor of ≈ 1.2 lower, but our value is still within the systematic uncertainty of the average extinction inferred from Balmer decrement measurements at $z \lesssim 0.5$ (e.g. Ly et al., 2012).

5.5.2 The Hα luminosity function

Having shown that our implementation of mock Hα emission lines yields line luminosities consistent with the underlying assumed SSP model, we now proceed to compute the Hα luminosity function and compare it to data. It is common practise to apply a constant dust correction to observed Hα fluxes obtained from narrow-band surveys to infer 'intrinsic', ISM dust-free, luminosities (e.g. Sobral et al., 2013). This yields an (intrinsic) Hα line luminosity function with a Schechter form. However, the bright-end slope of the best-fit function that results from applying a constant dust correction is steeper than when the dust correction is performed using Balmer decrements (e.g. Gilbank et al., 2010; Gunawardhana et al., 2013). This systematic difference is partially attributable to the star formation rate dependence of attenuation[8] (Brinchmann et al., 2004; Zahid et al., 2013).

[8]Poor sampling of the strongest Hα emitters, due to the small volume of narrow-band surveys, may also contribute to a steeper bright-end.

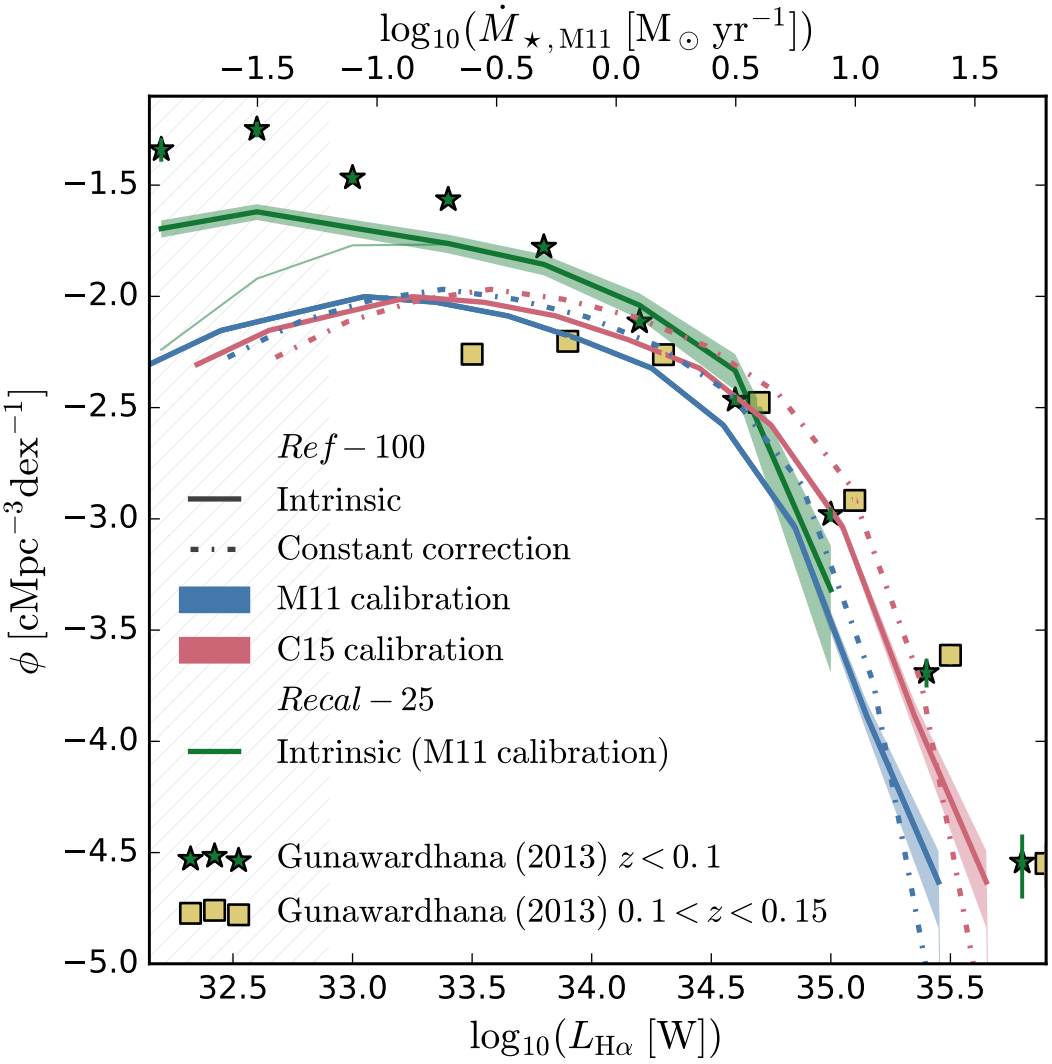

Figure 5.12: Redshift $z = 0.1$ dust corrected Hα luminosity functions of EAGLE galaxies compared to observations. *Solid coloured lines* are the ISM dust-free EAGLE LFs for simulation Ref-100 for randomly oriented EAGLE galaxies with $M_\star \geq 1.81 \times 10^8\ \mathrm{M}_\odot$ using the Murphy et al. 2011 and Chang et al. 2015 (M11 and C15 respectively, see text) ratio of $\dot{M}_\star/L_{\mathrm{H}\alpha}$, respectively, with the shading showing the Poisson error range. The *dot-dashed* curves are the corresponding LFs computed using SKIRT, dust corrected using the best-fit constant dust correction to the attenuated spectra (A, see Fig. 5.11). {*continued on next page...*}

Figure 5.12: {*Continued from previous page...*} The *green curves* are the ISM dust free LF for simulation Recal-25 using the Murphy et al. 2011 ratio of $\dot{M}_\star/L_{\mathrm{H}\alpha}$, for galaxies with $M_\star \geq 1.81 \times 10^8$ M$_\odot$ and $M_\star \geq 2.26 \times 10^7$ M$_\odot$ shown as *thin* and *thick green lines*, respectively. The *hatched region* marks where these deviate by $> 10\%$, indicating luminosities for which incompleteness is important for the $M_\star \geq 1.81 \times 10^8$ mass limit. Observational data is taken from Gunawardhana et al. (2013), who use the Balmer decrement dust-corrected GAMA sample, for redshift ranges $z < 0.1$ (star symbols) and $0.1 < z < 0.15$ (squares). Error bars indicate the statistical uncertainty on observed data points, but are too small to be seen for all but the highest luminosities. The simulated LF using the Chang et al. 2015 calibration is closer to the observed measurements; the intrinsic LFs possess a broader knee than when a constant dust correction is applied.

Because SKIRT provides both the ISM dust-free and dust-attenuated SEDs, we can compare with the 'true' dust correction for our simulated galaxies at different orientations and investigate this effect further.

A potential caveat for the realism of Hα luminosities computed for EAGLE galaxies is that the simulated specific star formation rates may be low compared to observations, both locally and at higher redshifts (Furlong et al., 2015). This is in fact somewhat puzzling since the stellar mass functions do agree relatively well. The observed SFRs are inferred from various proxies, including emission lines, FIR and radio data. However, the calibration may rely on assumptions about the UV continuum, which depends on the assumed IMF and population synthesis model (see Kennicutt, 1998a). Some recent studies suggest that stellar rotation and binary stars may contribute more to the UV continuum than previously thought, affecting this calibration (e.g. Hernández-Pérez & Bruzual, 2013; Horiuchi et al., 2013). When instead considering the Hα fluxes (including dust effects) the realism of galaxy attenuation and ISM also becomes important. Discrepancies in star formation rates and ISM attenuation can have degenerate effects on the Hα measurements. It is therefore important to consider the intrinsic Hα and dust attenuated Hα measurements separately to isolate reasons for discrepancy

or agreement.

Recently, Chang et al. (2015) performed SED fitting of galaxies with SDSS and WISE photometry and obtained star formation rates for $z \approx 0.1$ star-forming galaxies. Their values are systematically lower by ≈ 0.2 dex compared to previous work such as that of Kennicutt (1998a), and in better agreement with those predicted by EAGLE. If the lower $\dot{M}_\star$ values of Chang et al. (2015) point to a previous miscalibration of star formation rate indicators, then the $L_{\mathrm{H}\alpha}$ values predicted by Eq. (5.5.5), and thus present in the intrinsic EAGLE SEDs (see Fig. 5.11), may be too low. To test the effect of such a change in normalisation when comparing to the Hα luminosity function, we plot $L_{\mathrm{H}\alpha}$ both with and without a $+0.2$ dex shift, referring to this as the Chang et al. (2015) conversion[9].

Figure 5.12 compares mock Hα luminosity functions to data. Comparing thick and thin green lines, which use the same $\dot{M}_\star$ to Hα flux conversion, but correspond to imposing a mass limit of $M_\star \geq 2.26 \times 10^7$ M$_\odot$ (100 star particles at high resolution) and $M_\star \geq 1.81 \times 10^8$ M$_\odot$, respectively, enables us to estimate the level of numerical convergence. A hatched region marks where these differ by more than 10%, ie. where incompleteness effects become important for the higher mass cut. We therefore focus on the model Hα luminosities above 10^{33} W.

Up to luminosities of $\sim 10^{34}$ W, the solid green and solid blue curves (that both use Eq. 5.5.5) differ by ≈ 0.5 dex (a factor of three), indicating that the Recal-25 simulation predicts significantly higher values of ϕ than Ref-100, such that Recal-25 is in better agreement with the data. As seen in Fig 5.11, below $L_{\mathrm{H}\alpha} \sim 10^{34}$W the poor sampling of HII regions contributes to this resolution effect. For the hatched region, $L_{\mathrm{H}\alpha} \lesssim 10^{32.9}$ W, the discrepancy is driven by incompleteness due the imposed mass limit for the Ref-100 simulation. However, at intermediate luminosities this is due to real differences between the properties of the galaxies in the high- and standard-resolution runs. Indeed, we recall from Fig. 5.7 that these two simulations differ substantially in the lowest mass bin: Recal-25 galax-

[9]Note that Chang et al. (2015) do not explicitly advocate such a correction, rather, this conversion represents the case that the discrepancy they find exists due to previous miscalibration of absolute SFR.

ies tend to be intrinsically blue and star forming, whereas a significant fraction of Ref-100 galaxies are intrinsically red and passive. This contributes to the boost in the Recal-25 luminosity function at intermediate $L_{\mathrm{H}\alpha}$ ($10^{32.9} \lesssim L_{\mathrm{H}\alpha} \lesssim 10^{34}$ W), yielding better agreement with the observed luminosity functions. The higher number density of galaxies at these intermediate Hα luminosities is due to the similar contribution of volume and resolution effects. Volume effects and convergence are discussed further in Appendix B.2.2. The offset between the blue and green curves at lower luminosities is therefore, in part, a measure of numerical convergence.

We next compare solid lines (intrinsic luminosities) to dot-dashed lines (SKIRT dust-attenuated luminosities corrected using a constant dust correction), for either blue or red lines. These agree well at the faint end ($L_{\mathrm{H}\alpha} \lessapprox 10^{34}$ W) where the luminosity functions are close to flat, but significant differences can be seen for brighter galaxies, with the number of bright sources higher at the knee of the constant dust correction luminosity function. A constant dust correction tends to overestimate the true level of dust attenuation around the knee, and underpredict it for the most Hα bright galaxies, resulting in a steeper bright end slope. Note that the constant dust correction we use is essentially indistinguishable from the common observational assumption of 1 mag in this plot.

Finally, we compare the intrinsic Hα luminosity function (solid lines) to the observed result corrected for dust using the Balmer decrement (symbols). Although similar at faint fluxes, $L_{\mathrm{H}\alpha} \lessapprox 10^{35}$ W, the simulated luminosity function is significantly below the observations at the bright-end when using Eq. 5.5.5 (blue), with the difference much reduced when using the Chang et al. (2015) conversion (red curve). The shape at the bright-end is so steep that even a small error in the observed luminosity determination can make EAGLE and GAMA consistent. In addition, the EAGLE stellar mass function is lower than observed around the knee (S15), which will also contribute to the deficit at brighter luminosities.

In summary: the EAGLE Hα luminosity function is in relatively good agreement with observations when applying the Chang et al. (2015) inspired[7] conversion between $\dot{M}_\star$ and Hα luminosity. The effects of insufficient numerical reso-

lution are apparent at lower luminosities ($L_{\mathrm{H}\alpha} \lesssim 10^{34}$ W). Applying a constant correction to the EAGLE dust-attenuated Hα values does not reproduce the shape of the underlying 'true' EAGLE Hα luminosity function well, over-estimating the star formation rates at higher Hα luminosities ($L_{\mathrm{H}\alpha} \gtrsim 10^{34}$ W). This comes about due to the higher attenuation in more Hα luminous galaxies, shown directly in Appendix B.2.2.

5.5.3 D4000 Index

The 4000 Å break (D4000) was used by Kauffmann et al. (2003a) to analyse a large sample of galaxies from the SDSS. In older stellar populations, the opacity due to several ions in stellar atmospheres combines to induce a noticeable discontinuity in the flux around 4000 Å, which is mostly absent in hot stars. The size of the discontinuity is hence a measure of the relative contribution of young hot stars to the flux - and hence of the specific star formation rate of the galaxy (e.g. Bruzual, 1983). The D4000 index is the logarithm of the ratio of the red and the blue continuum, measured using narrow-band top-hat filters. We use $[4050, 4250]$ Å and $[3750, 3950]$ Å to sample the red and blue continuum respectively, as defined by Bruzual (1983). The D4000 index is commonly used to distinguish between active (star forming) and passive populations, similar to the colour-colour plots of Fig. 5.9. Indeed, D4000 can be thought of as a colour index (analogous to e.g. $u-r$), but is generally considered robust against dust effects due to it being a differential measure with a relatively small wavelength separation between bands.

The D4000 distribution used by Kauffmann et al. (2003a) and Kauffmann et al. (2003b) are from a flux-limited selection of SDSS galaxies, and shows strong bimodality where massive galaxies have a high value of D4000, low-mass galaxies have low values, with the transition mass around $M_\star \sim 3 \times 10^{10}\mathrm{M}_\odot$, see Fig. 1 of Kauffmann et al. (2003b). Even the largest, 100^3 Mpc^3, EAGLE volume does not have enough massive galaxies to allow for a direct comparison with these measurements.

To make a comparison to data meaningful, we therefore create a sample of SDSS galaxies mass-matched to the EAGLE population over the range $10^{10}\mathrm{M}_\odot <$

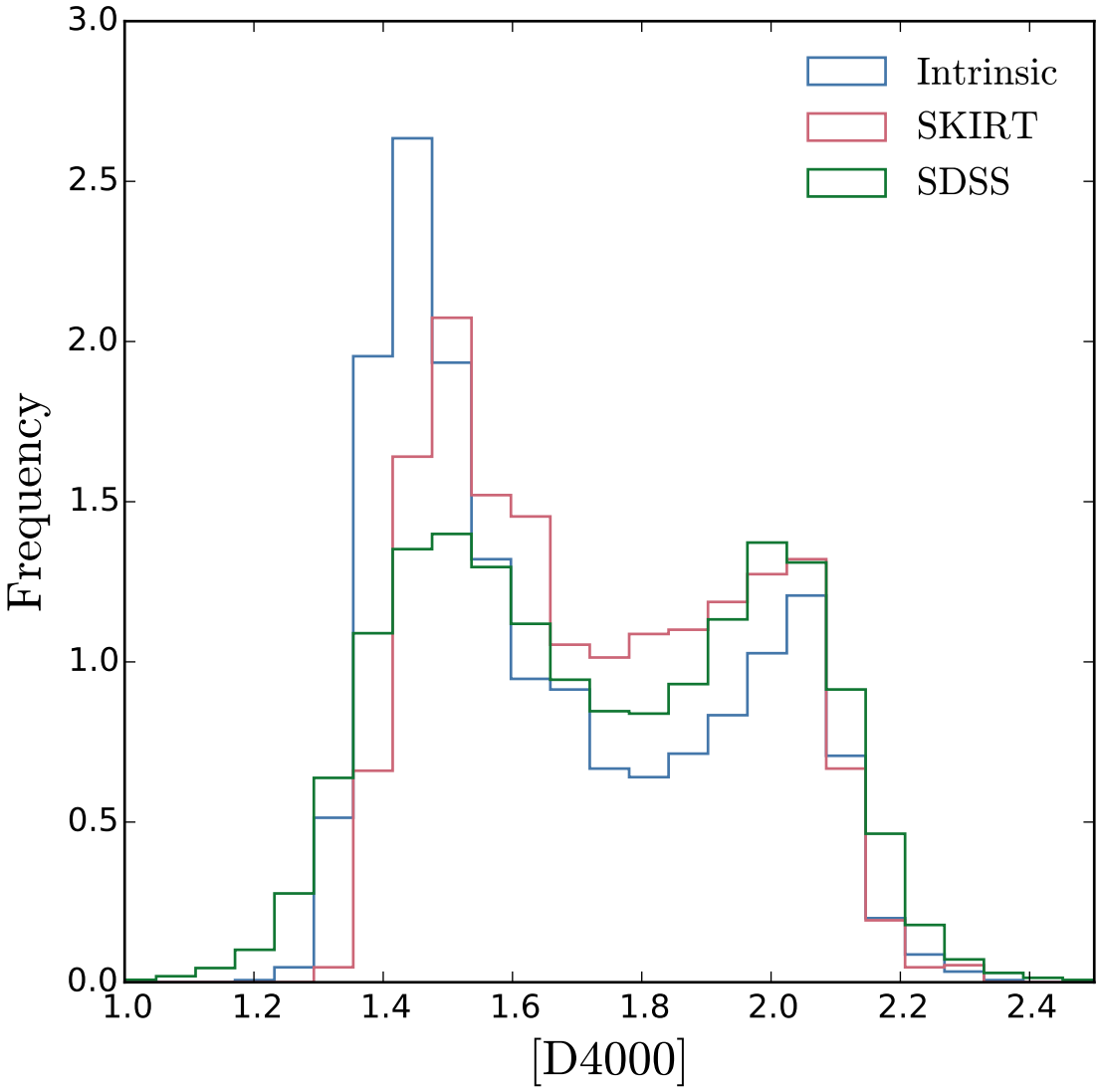

Figure 5.13: Histogram of D4000 values for intrinsic and radiative transfer (SKIRT) photometry of $z = 0.1$ galaxies with $10^{10}\mathrm{M}_{\odot} < M_{\star} < 10^{11}\mathrm{M}_{\odot}$. The low and high D4000 peaks are taken to represent active and passive populations respectively. *Blue* indicates the intrinsic values, *red* after dust is applied. Values of D4000 measured for a mass-matched sample of SDSS galaxies are plotted in green. A considerable difference in the active and passive peaks recovered with this technique is observed when dust is applied.

$M_\star < 10^{11}\mathrm{M}_\odot$, using the observed masses from Kauffmann et al. (2003a). The corresponding broad-band (Bruzual, 1983) D4000 values are taken from the MPA-JHU catalogue, released for SDSS DR7 (Abazajian et al., 2009a). We then compare the D4000 distribution to that of EAGLE for both the intrinsic and dust-reddened spectra in Fig. 5.13. Each distribution is normalised to integrate to unity. We employ a cut at D4000=1.8 to separate the active and passive population, which is near the minima of each histogram. We recover passive fractions of 32% and 41% for EAGLE galaxies using intrinsic and SKIRT spectra, as compared to 55% for the SDSS sample.

We first compare the 'intrinsic', ISM dust-free, EAGLE distribution (blue) to that produced using SKIRT (red). Both distributions exhibit a clear bi-modality, with low and high D4000 peaks at ≈ 1.5 and ≈ 2 respectively. A stark difference between the two distributions is that the population with low D4000, a common proxy for the star formation, is significantly depleted when ISM dust is included with SKIRT. There is also a shift of the low D4000 peak to higher values. The relative depletion of the low D4000 population in the SKIRT distribution corresponds to a relative boost at intermediate and high D4000. This boost reduces in significance for higher D4000 values, falling below 10% near the high D4000 peak of ≈ 2. Although there is little difference in overall attenuation between the two D4000 bands, including the preferential obscuration of light from young stars by dust attributed both stellar birth clouds and the diffuse ISM via SKIRT leads to some star-forming galaxies registering higher D4000 values, and even appearing completely passive in this proxy. This is the same effect seen for broad-band colours in Fig. 5.7 and 5.9. We find that $\approx 20\%$ of EAGLE galaxies deemed to be passive according to the D4000>1.8 criterion, are star forming.

We next compare the EAGLE distributions to the SDSS distribution (green). A clear bi-modality can be seen in the SDSS distribution, exhibiting similar peak positions to EAGLE at D4000 ≈ 1.5 and ≈ 2. The SDSS peak positions agree more closely with the SKIRT model distribution, which should be a fairer comparison. The fraction of galaxies in the low D4000 (active) population for the SDSS sample is smaller than for either EAGLE distributions, but agrees better with the SKIRT

histogram. The high D4000 (passive) fraction is larger for SDSS than EAGLE, and also closer to the dust reddened values of SKIRT. The inferred passive fraction for SDSS galaxies is 70% higher than inferred for the intrinsic EAGLE spectra, and 35% higher than for SKIRT. While the frequency of SDSS galaxies at intermediate D4000 values (≈ 1.8) is under-predicted by the intrinsic EAGLE distribution, the boost in the population seen for the SKIRT distribution over-predicts the number density of galaxies by a similar factor. Generally the agreement with observation is improved by the inclusion of SKIRT ISM dust modelling, but remains slightly discrepant. While modelled dust effects can improve the inferred passive fractions, an excess of high-mass active galaxies persists relative to observation. This could reflect a genuine overproduction of active galaxies in EAGLE, as suggested by Furlong et al. (2015).

Additionally we see that the SDSS distribution is broader than for EAGLE, with tails extending to more extreme high and low values. These tails might be due to outliers with unusually large photometric errors. The limited parameter coverage of the populations synthesis models could also prevent the occurrence of the most extreme values in the simulation.

We used the D4000 continuum band definitions of Bruzual (1983) rather than the narrower band definition of Balogh et al. (1999) employed by Kauffmann et al. (2003a). The reason for this choice is that D4000 is better converged at our standard spectral resolution for SKIRT. A caveat is that the broad band definition is observed to be significantly more susceptible to dust effects than narrow bands (Balogh et al., 1999; Kauffmann et al., 2003a; Wild et al., 2007), potentially leading to larger dust uncertainties.

To test how well the measured D4000 predicts star formation activity for the EAGLE spectra, we plot D4000 against specific star formation rate (sSFR) for $z = 0.1$ 'active' ($\dot{M}_\star > 0$) EAGLE galaxies in Fig. 5.14. At $\log_{10}(\mathrm{sSFR}/\mathrm{yr}^{-1}) > -12$, and despite a clear negative trend of D4000 with sSFR, we see that the median D4000 is higher for the SKIRT spectra (red circles) than for the spectra without ISM dust (blue circles). The distribution of active galaxies in this plane also shows a significant tail to high D4000 when ISM dust is included (shaded squares), a significant

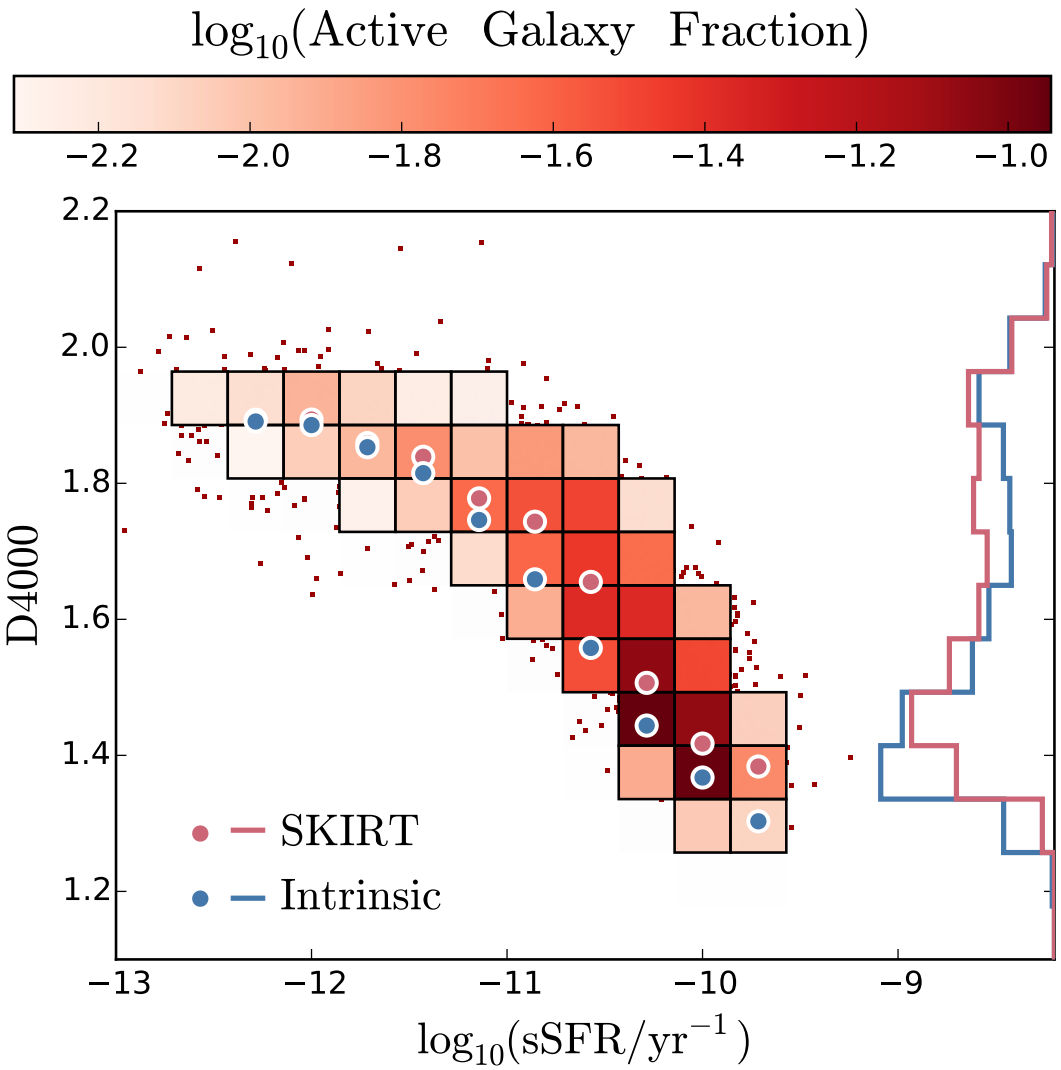

Figure 5.14: D4000 index as a function of specific star formation rate (sSFR) for $z = 0.1$ EAGLE galaxies with $M_\star > 10^{10}\mathrm{M}_\odot$. *Circles* indicate the median D4000 value in bins of $\log_{10}$sSFR, with *blue* representing the intrinsic values and *red* including dust (SKIRT). *Shaded squares* represent evenly-spaced bins in D4000 and log sSFR. These are shaded by the fraction of active galaxies (SFR> 0) they contain for the SKIRT values of D4000, and are only displayed within the 95% contour of the active galaxy distribution. Galaxies outlying the 95% contour are represented individually as *red points*. D4000 histograms are also displayed as in 5.13, again *blue* represents intrinsic values and *red* SKIRT values. We see that, despite the trend of D4000 with sSFR for $\log_{10}(\mathrm{sSFR/yr^{-1}}) > -12$, a significant number of galaxies are scattered toward the high D4000 population when dust is included. A few galaxies also exhibit relatively low D4000 despite low sSFRs ($\log_{10}(\mathrm{sSFR/yr^{-1}}) < -12$)

number of galaxies with $\log_{10}(\mathrm{sSFR}/\mathrm{yr}^{-1}) > -11.5$ have D4000 consistent with the passive population. This suggests that dust effects are significant for this index when applied to the SKIRT spectra, and can be ascribed to star formation being hidden by the dense, dusty ISM of some galaxies. Conversely, a few outlying galaxies (red points) show relatively low D4000 at $\log_{10}(\mathrm{sSFR}/\mathrm{yr}^{-1}) < -12$. This is due to these galaxies being relatively metal poor, analogous to the anomalously blue passive galaxies identified in chapter 4 using $u - r$ colour (their Fig. 1d).

5.6 Summary and Conclusion

We have made mock optical observations of galaxies simulated within the EAGLE suite of cosmological, hydrodynamical simulations, including the effects of dust, utilising the public SKIRT[10] code. SKIRT calculates three-dimensional radiative transfer on each galaxy, and we used the cool, enriched gas as a tracer of dust in the diffuse interstellar medium (ISM). To ameliorate limitations resulting from limited numerical resolution, we apply a subgrid model to represent unresolved HII regions and the associated dust attenuation by using the MAPPINGS-III model of Groves et al. (2008). The full procedure is presented in section 5.2, and was developed in this work and in the companion work of Camps et al. (2016) (C16). The dust modelling introduces extra parameters, such as the dust-to-gas ratio in the ISM, and parameters of the MAPPINGS-III model such as the covering factor and compactness of HII regions. These were chosen by comparing far-infrared mock observations of EAGLE galaxies with observations of local galaxies, as described by Camps et al. (2016). We apply no additional calibration in the optical regime.

To enable a detailed comparison of numerically resolved EAGLE galaxies to observations from the GAMA survey (Driver et al., 2011), we selected galaxies at redshift $z = 0.1$ above a stellar mass cut of $M_\star \geq 1.81 \times 10^8\ \mathrm{M}_\odot$ (~ 100 star particles at standard resolution). We focus on the largest fiducial EAGLE simulation, a 100^3

[10] www.skirt.ugent.be

Mpc^3 volume, which provides a sample of 30145 galaxies that satisfy this selection criterion. Galaxies are defined and selected in the same way as in chapter 3, to enable direct comparison with their dust-screen model. Integrated spectra, broad-band magnitudes, broad-band images and mock IFU data were produced for each galaxy for three orientations (face-on, edge-on and along the z-axis of the simulation volume), with properties detailed in section 5.2.3. These will be made available through the public EAGLE database (McAlpine et al., 2016).

In section 5.3 we studied the attenuation in the B-band as a function of inclination, comparing to the observationally inferred relation of Driver et al. (2007). We found that:

- The B-band attenuation-inclination relation for EAGLE galaxies, Fig. 5.3, exhibits large galaxy-to-galaxy scatter, on top of a smooth trend of increasing median attenuation for galaxies seen more edge-on. This trend is weaker than observed, as is the level of the edge-on attenuation. We attribute this to the fact that the stellar and gas disc in EAGLE galaxies is thicker than in observed galaxies, a consequence of the artificial pressure floor imposed on the simulated ISM (as opposed to being purely limited by numerical resolution, see Fig. 5.4).

- Stacked attenuation curves of EAGLE galaxies at different orientations, Fig. 5.6, reveal different profiles. Face-on galaxies show the steepest frequency dependence as the youngest stars are preferentially dust obscured by the diffuse ISM component. Conversely, the curve for edge-on galaxies shows a weaker (or 'greyer') frequency dependence as both young and old stellar populations are obscured by the diffuse dust disc, closer to a screen model. We also see that nebular emission features (such as Hα) suffer from strongly increased *ISM attenuation* (over and above the attenuation of the stellar birth clouds), due to star-forming regions being embedded in denser and dusty gas.

Comparing optical SKIRT photometry to ISM dust-free models, the GD+O dust-screen model, and colours from the GAMA survey, we find that

- Optical SKIRT galaxy colours match the data remarkably well, Fig. 5.7. In fact, they match significantly better than the GD+O dust-screen model photometry of chapter 3. The SKIRT colours exhibit a mass-dependent boost of the *'green valley'* and red populations compared to either intrinsic or dust-screen colours.

- The improved agreement with observation demonstrated by SKIRT, relative to the GD+O screen model, is attributable to the spatial distribution of dust compared to that of young stars, and the better capturing of orientation effects as compared to a screen model. Fig. 5.5 shows how highly-inclined galaxies with intrinsically blue colours may scatter to the reddest colours.

- Dusty galaxies can confound simple star-formation activity proxies, such as colour-colour cuts. Fig. 5.9 shows that a ugJ colour-colour cut can recover passive fractions well when dust is modelled as a screen, but with the more realistic SKIRT dust modelling a significant fraction of active galaxies masquerade as passive. For the $M_\star > 10^{10}\mathrm{M}_\odot$ range, we find that approximately 15% of galaxies with SKIRT colours that place them in the passive region are classified as star forming when dust is neglected. We note that the ugJ cut used in this chapter is relatively stringent, and more relaxed cuts may yield significantly higher misclassification rates (see section 5.4.2.2 for details).

Finally, we investigated spectral indices often used as proxies for star formation activity, such as the Hα line flux and the 4000Å break (D4000). We plotted the Hα luminosity functions (ϕ) and compared directly to the function computed for the GAMA sample by Gunawardhana et al. (2013) in Fig. 5.12. Given that the star formation rates of EAGLE galaxies are typically 0.2 dex lower than reported for observations using the Kennicutt (1998a) calibration (Furlong et al., 2015), and that the conversion from $\dot{M}_\star$ to Hα follows the standard Kennicutt (1998a) relation (see Fig. 5.11), it is unsurprising that the EAGLE luminosity function is systematically low at the bright end. However, the recent study of Chang et al. (2015) argued that absolute $\dot{M}_\star$ values should be normalised ≈ 0.2 dex lower, so we also plotted ϕ using Hα boosted by this factor. The D4000 distributions were compared to

a mass-matched sample of SDSS galaxies in the range $10^{10}\mathrm{M}_{\odot} < M_{\star} < 10^{11}\mathrm{M}_{\odot}$. From studying these indices, we found that:

- The bright end of the recalibrated, intrinsic Hα luminosity function ($L_{\mathrm{H}\alpha} > 10^{34.5}\mathrm{W}$) agrees reasonably with observations, particularly when using the Chang et al. (2015) calibration. Applying a constant dust correction to the SKIRT Hα predictions distorts the shape of the luminosity function, appearing more Schechter-like with a steeper bright end than seen in either the intrinsic or observed LFs.

- D4000 values produced by SKIRT show similar distributions to a mass-matched SDSS sample over the range $10^{10}\mathrm{M}_{\odot} < M_{\star} < 10^{11}\mathrm{M}_{\odot}$, Fig. 5.13, but with somewhat fewer galaxies at high D4000. Dust reddening significantly boosts the high D4000 population relative to the intrinsic distribution, analogous to the red sequence boosting observed in Fig.5.7. This leads to higher inferred passive fractions, with the light from young stars preferentially extinguished by dust. The scattering of galaxies to high D4000 by dust, for a given specific star formation rate, is characterised in Fig. 5.14.

Including dust radiative transfer effects with SKIRT allows us to model the inhomogeneous dust distribution and how that is correlated with regions of recent star formation, while improving the level of agreement of mock fluxes with observations compared to the GD+O dust screen model. However, there are clear limitations. In particular, the edge-on attenuation of disc galaxies is lower than observed. Improving this would likely require higher-resolution simulations with an explicit cold phase, allowing us to resolve thin molecular gas discs on scales $\lesssim 100$ pc

It is perhaps surprising that despite these limitations, the attenuation computed using SKIRT profoundly influences colours, improving agreement with data. This can be ascribed to the effects that geometry and scattering have on the optical attenuation of galaxies that cannot be captured by screen models. The localised nature of the dusty ISM around young stars is effective at hiding their blue light, leaving the older populations to contribute relatively more to the

fluxes. Despite invoking similar mean attenuation values (see section 5.4.2, appendix B.4), a screen model yields more apparently blue galaxies because their star forming regions are relatively much less shielded by dust.

Throughout this chapter we focus on using a forward modelling approach to compare simulated and real galaxies in the observable domain. While we discuss many benefits of this approach, we note that forward modelling has the potential to obscure the reasons for discrepancy (or agreement) if the influence of individual physical properties are not well understood. An example where such caution is needed would be in our Hα measurements, influenced by both the ISM structure and star formation rates of EAGLE galaxies. We emphasise that it is therefore important to analyse our forward modelling results in the context of comparison studies in the physical domain (such as Schaye et al., 2015; Furlong et al., 2015, for EAGLE galaxies). We have attempted to provide such context in this work.

We hope that the more realistic observables produced by SKIRT provide a useful resource, opening new avenues of investigation for comparing observations to the simulations. Mock observational data presented in this chapter will be made accessible via the public EAGLE database (McAlpine et al., 2016, for updates register at `http://icc.dur.ac.uk/Eagle/database.php`). Our mock observables are also provided for additional redshifts and EAGLE simulations that are not discussed in this work.

Chapter 6

Estimating Galaxy Stellar Masses from EAGLE Mock Photometry

This chapter represents a study currently in progress, investigating galaxy stellar masses and star formation rates estimated using resolved and unresolved EAGLE photometry, both with and without the dust effects described in chapter 5.

6.1 Introduction

Stellar masses ($M^\star$) are a fundamental property of galaxies, and the accurate determination of $M^\star$ from observations is a subject of great interest. $M^\star$ encodes the history of star formation in galaxies (modulo stellar mass loss), and reproducing the galaxy stellar mass function (GSMF) is a typical touchstone for many theoretical models of galaxy formation (e.g. Vogelsberger et al., 2014; Khandai et al., 2015; Schaye et al., 2015). With stars being so readily observable, quantifying stellar content is often the first step in understanding galaxies in the physical domain, and can be paired with lensing or dynamical measurements to infer the presence of dark matter.

The luminosity of a galaxy is measurable provided an accurate distance is known, so the unknown when determining $M^\star$ becomes the ratio of stellar mass to light, $M^\star/L$. This $M^\star/L$ is typically calculated in terms of a given photometric band, due to the impracticality of measuring bolometric luminosities, and can

be derived for resolved and unresolved photometry. The simplest assumption is a universal $M^\star/L$, often made when using NIR bands, such as K, which are deemed to be less affected by stellar ages or dust (e.g. Rix & Zaritsky, 1995; McGaugh et al., 2000). However, this is often too simplistic when comparing diverse galaxies; from knowledge of stellar populations alone, $M^\star/L$ is predicted to have a strong dependence on galaxy colour (Bell & de Jong, 2001). Colour dependent $M^\star/L$ values have been derived using a variety of approaches, and have been found to mitigate many of the problems of a universal $M^\star/L$ (e.g. Bell et al., 2003; Zibetti et al., 2009; Taylor et al., 2011). Taking the idea of considering multiple photometric bands further, multi-band photometric fitting of the galaxy's SED has become a commonplace approach for estimating $M^\star/L$ (e.g. Sawicki & Yee, 1998; Taylor et al., 2011; Maraston et al., 2013). A wealth of different codes are now available to fit SEDs photometrically and recover $M^\star$ alongside many other salient galaxy parameters (e.g. da Cunha et al., 2008; Kriek et al., 2009; Acquaviva et al., 2011).

Even with advances in photometric fitting, much uncertainty remains in deriving the $M^\star/L$. There are a number of assumptions that imply significant systematic uncertainties for absolute $M^\star/L$ values. Differences between the assumed stellar IMFs and stellar population models can themselves contribute significantly (by $\gtrsim 0.3$ dex in $M^\star$) to the error budget (e.g. Conroy et al., 2009). The application of apertures or extrapolation of galaxy light profiles also contributes, particularly at the bright end (e.g. Bernardi et al., 2013). Even with these properties fixed, considerable uncertainty remains due to the different methods with which $M^\star/L$ is derived. Kannappan & Gawiser (2007) found considerable (~ 0.3 dex) differences between colour-based and SED fitting $M^\star/L$ methods at $z \approx 0$. The uncertainties due to the assumptions within the SED fitting itself, such as assumed priors about star formation histories and dust, have been explored in a number of studies (e.g. Wuyts et al., 2007; Marchesini et al., 2009; Maraston et al., 2010).

Without knowing the true $M^\star$ values, it is a challenge to constrain the appropriate $M^\star/L$ and thus choose an appropriate methodology. Obtaining independent, dynamical masses from observations provide limits on $M^\star/L$ and may

go some way towards constraining them (e.g. Taylor et al., 2010). Insights may also be gained by appealing to model galaxies, where the physical parameters are known. By *forward modelling* mock observations of these galaxies, one can directly assess how robustly $M^\star/L$ and other parameters are recovered using different methods. Mobasher et al. (2015) present a comprehensive investigation in this vein; assessing various combinations of mock photometry and fitting procedures by tasking different working groups to derive $M^\star$ values for provided photometry in a blind test. Of course, the usefulness of such an approach is subject to the realism of the model galaxies. This analysis has been performed for semi-analytic models (e.g. Mitchell et al., 2013), idealised hydrodynamical simulations (e.g. Wuyts et al., 2009a; Hayward & Smith, 2015) and large volume hydrodynamical simulations (e.g. Torrey et al., 2015).

In this chapter I investigate photometric $M^\star$ recovery as an application of the EAGLE galaxy modelling presented in previous chapters. Using the SKIRT photometry provides a novel opportunity to test statistically how well standard procedures cope with the complex star formation histories, enrichment histories, and implied star-dust geometries that emerge in hydrodynamically simulated galaxies. I limit this study to optical photometry ($ugriz$) and focus on the $z = 0.1$ Ref-100 sample ($\sim 30,000$ galaxies). While panchromatic spectra and higher redshift data are generated, their analysis is left to a future work which can build on any insights that are gained here. The chapter is organised as follows: section 6.2 investigates colour-based empirical estimators of $M^\star/L$. Initially, I test the accuracy of $M^\star$ estimates for *integrated* photometry (the net broad-band flux measured for a galaxy) with and without dust. I then analyse how discrepancies build up with *resolved* photometry (i.e. the galaxy surface brightness profile is sampled by multiple pixels), by first looking at SSP properties in an idealised way (section 6.2.2) and then using the realistic SKIRT imaging for archetypal galaxies (section 6.2.3). I then turn to photometric SED fitting using the FAST code (Kriek et al., 2009) to derive $M^\star$ alongside other galaxy properties (e.g. SFR) in section 6.3, initially developing a fiducial set up loosely based on that of Torrey et al. (2015) (section 6.3.1). I then analyse the $z = 0.1$ FAST results by looking at typical mass off-

sets and residual trends, and comparing theoretical plots (particularly the GSMF) constructed using simulated and galaxy properties recovered using FAST. How well the best-fit star formation histories represent those that emerge in EAGLE is assessed in section 6.3.3, and the influence of the SKIRT dust modelling on the mass errors are discussed in section 6.3.4. Finally, the findings are summarised and conclusions are compiled in section 6.4. Additional material supplementing this chapter is provided in appendix C, and referenced when relevant.

6.2 Colour-corrected stellar M/L ratios

Fitting the *spectral energy distributions* (SEDs) of galaxies with model templates is a challenging problem, and the results are contingent on a number of choices and assumptions that are made when setting up the fitting procedure. This complexity renders it difficult to compare fitting procedures.

It has been found that the stellar masses recovered via optical SED fitting are reproduced well on average by a linear combination of an optical broad-band absolute magnitude and an optical broad-band colour (e.g. Taylor et al., 2011). This can be thought of as a constant stellar mass-to-light ratio ($M^\star/L$) with some colour correction, primarily accounting for the effect that hot young stars that give galaxies their blue appearance also contribute disproportionately to other optical bands, such that intrinsically blue galaxies are typically less massive for a given optical luminosity. This empirical relation has been explored for both integrated photometry (e.g. Bell et al., 2004; Taylor et al., 2011; Baldry et al., 2012) and resolved photometry (e.g. Zibetti et al., 2009), with galaxy stellar masses expressible as

$$\log_{10}(M^\star_{\rm col}/{\rm M}_\odot) = -0.4M_X + a(M_Y - M_Z) + b\ , \tag{6.2.1}$$

where M_X is a broad-band optical magnitude, $M_Y - M_Z$ is an optical colour measurement, and $M^\star_{\rm col}$ is the estimated galaxy stellar mass. Here, a and b are empirical factors chosen to minimise the differences between SED template masses ($M^\star_{\rm SED}$) and $M^\star_{\rm col}$. The scatter between $M^\star_{\rm SED}$ and $M^\star_{\rm col}$ is relatively small compared

Table 6.1: Various calibrations of Eq. 6.2.1. Top section tabulates empirical fits to observational data in AB magnitudes, bottom section are fits to the EAGLE data in this work.

Study	a	b	Band (M_X)	Colour ($M_Y - M_Z$)	Resolution
Zibetti et al. (2009, Z09)	1.032	0.856	i	$g-i$	∼100 pc
Taylor et al. (2011, T11)	0.7	1.15	i	$g-i$	unresolved
Baldry et al. (2012, B12)	0.75	1.23	i	$g-i$	unresolved
This work	0.7	1.33	i	$g-i$	unresolved

to systematic uncertainties in mass estimation: Taylor et al. (2011) find that $M^{\star}_{\rm SED}$ is reproduced for GAMA galaxies with a 1σ scatter of only 0.1 dex. A number of these empirical fits are tabulated in Table 6.1[1].

Clearly, there are many fewer parameters in Equation 6.2.1 than can be considered in SED inversion procedures; these $M^{\star}_{\rm col}$ rely on the effect that factors that make galaxies redder (bluer) also tend to make them optically dimmer (brighter), such as increasing (decreasing) stellar ages, metallicities and dust attenuation. The best fit a and b attempt to account for all these nuisance parameters.

The utility of the empirical relationship of equation 6.2.1 is that it enables broad comparison of different SED fitting outputs relatively easily, and provides a simple way to approximate how well SED fitting approaches reproduce the 'true' masses of EAGLE galaxies from the model photometry of previous chapters. A caveat to this approach is that it adds a layer of abstraction to the mass prediction, rendering it difficult to determine why discrepancies arise; disentangling the influence of different fitting methods and input models from differences between data and galaxy properties is not straightforward. By combining insights from

[1]These are converted to AB-magnitudes from $M^{\star}/L_i$ ratios assuming $i_{\odot} = 4.54$ via `http://mips.as.arizona.edu/~cnaw/sun.html`

this method of mass estimation (below) with those obtained via full SED fitting (see section 6.3), one can begin to isolate the source of any discrepancies found.

6.2.1 Integrated Photometry

In order to demonstrate how well these empirical relationships predict masses, I first examine the logarithmic offset (in dex) of $M^{\star}_{\rm col}$, estimated from integrated model EAGLE photometry, from the *'true'* value ($M^{\star}_{\rm true}$, the value taken directly from the simulation). Three empirical calibrations of Eq. 6.2.1 are chosen for comparison; Zibetti et al. (2009), Taylor et al. (2011) and Baldry et al. (2012), detailed in table 6.1. The Taylor et al. (2011) and Baldry et al. (2012) calibrations are chosen to represent differing apertures for the low redshift integrated GAMA photometry. As in previous chapters the GAMA sample is taken to be a useful comparison set for EAGLE, owing to its precise spectroscopic redshifts and high completeness (see chapter 2). Employing two different calibrations for GAMA gives an idea of differences that come about due to different photometric modelling and the choice of subsamples. The Zibetti et al. (2009) calibration is instead designed for resolved photometry of nearby galaxies, using imaging from the SDSS DR7 (Abazajian et al., 2009b). This calibration is used on the integrated EAGLE photometry as for the GAMA calibrations, to compare how the results differ and for reference when resolved photometry is investigated (in section 6.2.3).

Before comparing the results of these estimators, it is worthwhile considering some of the key features and differences between how they are derived and how the underlying SED modelling is performed, for example:

- **IMF:** For all models a Chabrier (2003) stellar IMF is assumed, consistent with what is assumed for EAGLE.

- **SPS model:** The stellar population model choice of Bruzual & Charlot (2003) (BC03) assumed by Baldry et al. (2012) (B12) and Taylor et al. (2011) (T11) is consistent with EAGLE[2], but Zibetti et al. (2009) (Z09) assume the 'CB07'

[2]Except for HII regions in the SKIRT modelling which use the MAPPINGS-III Groves et al. (2008)

update to the BC03 model. CB07 was intended to account for longer lived TP-AGB stars. However, it may overestimate the TP-AGB contribution and BC03 is often preferred (e.g. Zibetti et al., 2013). Z09 find that the primary effect of their CB07 modelling is to assign lower $M^{\star}/L$ ratios for bluer colours relative to BC03 (e.g. to underestimate masses from model galaxy colours generated using BC03).

- **Star formation histories:** The common assumption of smooth, exponentially declining histories is built into both GAMA estimators. Z09 assume the same form of the histories, but allowing for randomly superimposed bursts. All estimators use fixed metallicity histories for the standard BC03 metallicity grid.

- **Dust:** GAMA estimators assume a Calzetti et al. (2000) screen attenuation law, whereas Z09 use the two component Charlot & Fall (2000) model, where the birth cloud and ISM distribution are allowed to vary independently.

- **Galaxy selection:** T11 consider galaxies at $z < 0.2$ and uses Sèrsic magnitudes, B12 consider galaxies at $z < 0.06$ using Petrosian apertures. The EAGLE photometry approximates a Petrosian aperture using a 30 pkpc spherical aperture (see chapter 2.1.2). Z09 consider a small set of nearby ($<$ 26 Mpc) galaxies using pixel-by-pixel ('resolved') photometry.

- **Mass fitting:** The mass fitting employed to derive the GAMA estimators is the same, using a fully Bayesian likelihood-weighted integral over the posterior distribution. In Z09 no fitting is employed; the median $M^{\star}/L$ is computed for their template library in $g-i$ colour bins and fit with a power law.

Fig. 6.1 plots the offset $\log_{10}(M^{\star}_{\rm col}/M^{\star}_{\rm true})$ against $M^{\star}_{\rm true}$ for the different estimators. The median logarithmic offset (in dex) is determined in uniform logarithmic

SEDs

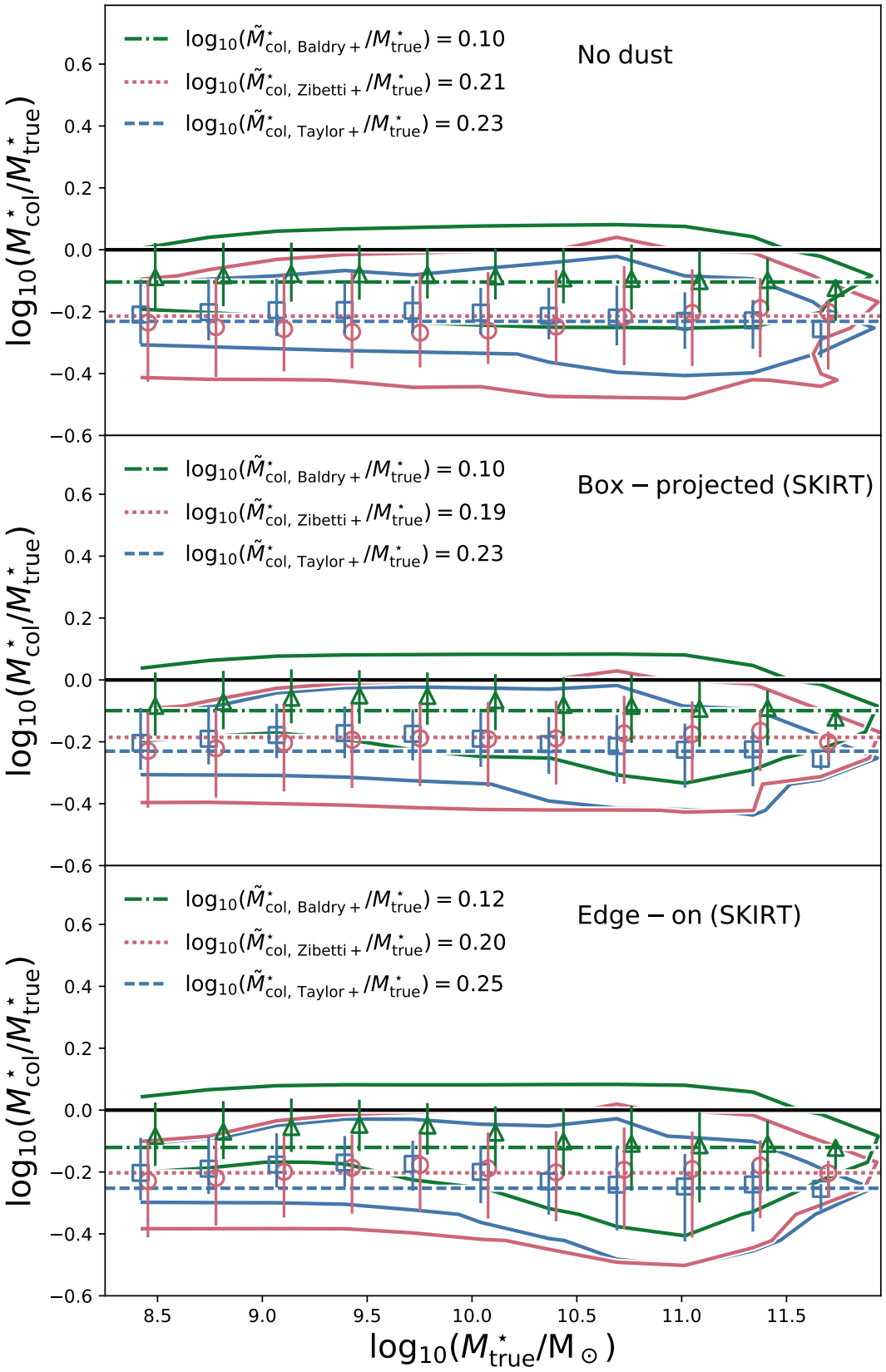

Figure 6.1: {*See following page for caption*}

Figure 6.1: {*See previous page for figure.*} The logarithmic offset (in dex) of EAGLE galaxy stellar mass estimates using the empirical relation of Eq. 6.2.1 from the simulated (or *'true'*) value, plotted as a function of that mass. *Empty symbols* are median offsets in stellar mass bins; *green triangles*, *red circles* and *blue squares* representing the empirical calibrations of Baldry et al. (2012), Zibetti et al. (2009) and Taylor et al. (2011), respectively. *Error bars* signify the 16th-84th percentile range, with *contours* enclosing 99% of galaxies for each calibration, using the same colouring. I also plot horizontal lines to indicate the average offset for each calibration, defined as the mass weighted mean logarithmic offset, again adopting the same colour scheme. Panels from top to bottom show the offsets obtained using different photometry sets; without dust (model ND from chapter 3), with SKIRT photometry in box projection (i.e. randomly oriented galaxies) and edge-on projection (see chapter 5). It can be seen that the empirically calibrated relation underestimates EAGLE masses by a calibration-dependent factor, on average. The offset is largely independent of the true stellar mass and dust effects.

bins of $M^{\star}_{\rm true}$ and plotted as empty symbols, with the overall offsets plotted as horizontal lines, respectively. All the empirical calibrations of Eq. 6.2.1 consistently underestimate the masses of EAGLE galaxies on average. For dust free photometry (top panel, ND in chapter 3) the estimated masses are typically 0.1-0.2 dex below their true values. The error bars indicate the 16-84 percentile range in logarithmic offset. The systematic offset is larger than the scatter at the 1σ level, except for the B12 estimator where the offset is $\sim 1\sigma$.

All the empirical estimators account for dust in their modelling. An arguably fairer comparison is thus shown in the middle panel where the box-projected SKIRT photometry (chapter 5) is used. This does little to improve the mass recovery, however, with only a 0.02 dex (5%) improvement registered for the mass weighted mean offset of the (Zibetti et al., 2009) estimator. This is perhaps unsurprising: the effect of dust on the overall photometry is small for the majority of galaxies, as low mass and passive galaxies have low dust content, as discussed in chapter 5. A more extreme scenario is also plotted in the bottom panel where all

EAGLE galaxies are observed edge-on. This actually makes the mass prediction marginally worse, with the average $M^{\star}_{\rm true}$ underestimated by a further few per-cent. The most dust attenuated galaxies in fact yield the strongest underestimates at high masses, these comprise the extended tail to low values in the contours around $10.5 \lesssim \log_{10}(M^{\star}_{\rm true}/M_{\odot}) \lesssim 11.5$ in the bottom panel.

Despite the simplicity of these estimators, it is apparent from the binned averages that there is very little mass dependence of the offset for each estimator. This is perhaps surprising, as there are many significant correlations between galaxy properties and galaxy stellar mass which could affect how well masses are determined for galaxies of a given mass. A number of EAGLE galaxy properties do appear to show less stellar mass variation than observed, with a flatter than observed metallicity relation (Schaye et al., 2015) and a passive/red fraction that persists to lower masses (Furlong et al. 2015, chapter 3). It is also possible that the contribution of different factors produces a fortuitous constancy in the mass offset with stellar mass. To confirm that this result is convergent between EAGLE resolutions, the same plot is produced for Recal-25 galaxies in appendix C.1 with very similar results. The origin of the mass offset is explored further in the next section.

The existence of a systematic offset in the mass predicted with these estimators was first identified for a small sample of EAGLE galaxies by Camps et al. (2016). In that paper we studied local FIR properties of EAGLE galaxies using the full SKIRT model. Having shown that the discrepancy remains for the complete sample and is remarkably independent of dust effects and stellar mass, we proceed by investigating the origin of the discrepancy.

6.2.2 CSP effects on photometric mass estimators

An EAGLE galaxy represents a *composite stellar population* (CSP); a superposition of SSPs with differing age and metallicity that yield a complex overall star formation and enrichment history. There is no clear physical reason why these should conform to the common parametric models of star formation and enrichment typically assumed in SED fitting (from which colour estimators are derived), and in-

deed EAGLE star formation histories are typically highly stochastic (e.g. McAlpine et al., 2017).

In Fig. 6.2 the offset in the mass estimator and its build up with age is investigated for 1000 randomly selected EAGLE galaxies. In panels *a-c* the estimator offset for Z09 is plotted as a function of integrated physical properties, with each galaxy coloured by their status as members of the intrinsically red, green or blue population, defined via Eq. 4.3.1.

Panel *a* demonstrates the remarkable constancy in mass offset with stellar mass, but shows that the underlying red and blue populations exhibit very different typical offsets. The largest offsets are associated with intrinsically blue galaxies. The relatively constant average offset with $M^{\star}_{\rm true}$ is indicative of a relatively constant intrinsic red and blue fraction over this mass range in EAGLE. The EAGLE colour bimodality persists over a greater mass range than inferred from the data, as described in chapter 3, which may contribute to this effect. The trend between colour and offset foreshadows the relatively tight relation between offset and specific star formation rate (sSFR) that is shown in panel *b*.

The mass underestimate becomes stronger with increasing specific star formation rate, from ≈ -0.1 dex for redder, passive galaxies (sSFR$< 10^{-11.5}$ yr^{-1}) to ≈ -0.4 dex for bluest, most rapidly star forming galaxies ($\sim 10^{-9.5}$ yr^{-1}). This can be understood in terms of the *outshining* effect identified in previous studies of photometric and spectroscopic SED fitting (Gallazzi & Bell, 2009; Maraston et al., 2010; Pforr et al., 2012; Sorba & Sawicki, 2015). Outshining occurs due to the dominance of hot young stars at optical wavelengths in galaxy SEDs, effectively blinding fitting procedures to dim older stellar populations that may comprise a large fraction of the total stellar mass. In theory, this is indicative of significant differences between the fitting forms of star formation histories and those that actually emerge within galaxies. An example of this may be recurrent star formation histories, where the optical SED is dominated by the most recent star formation event, and the mass contained in earlier bursts may be missed[3]. For

[3]In practice even mock observations modelled using exponential histories may not be recovered correctly, as the presence of young stars can yield similar photometry for very different histo-

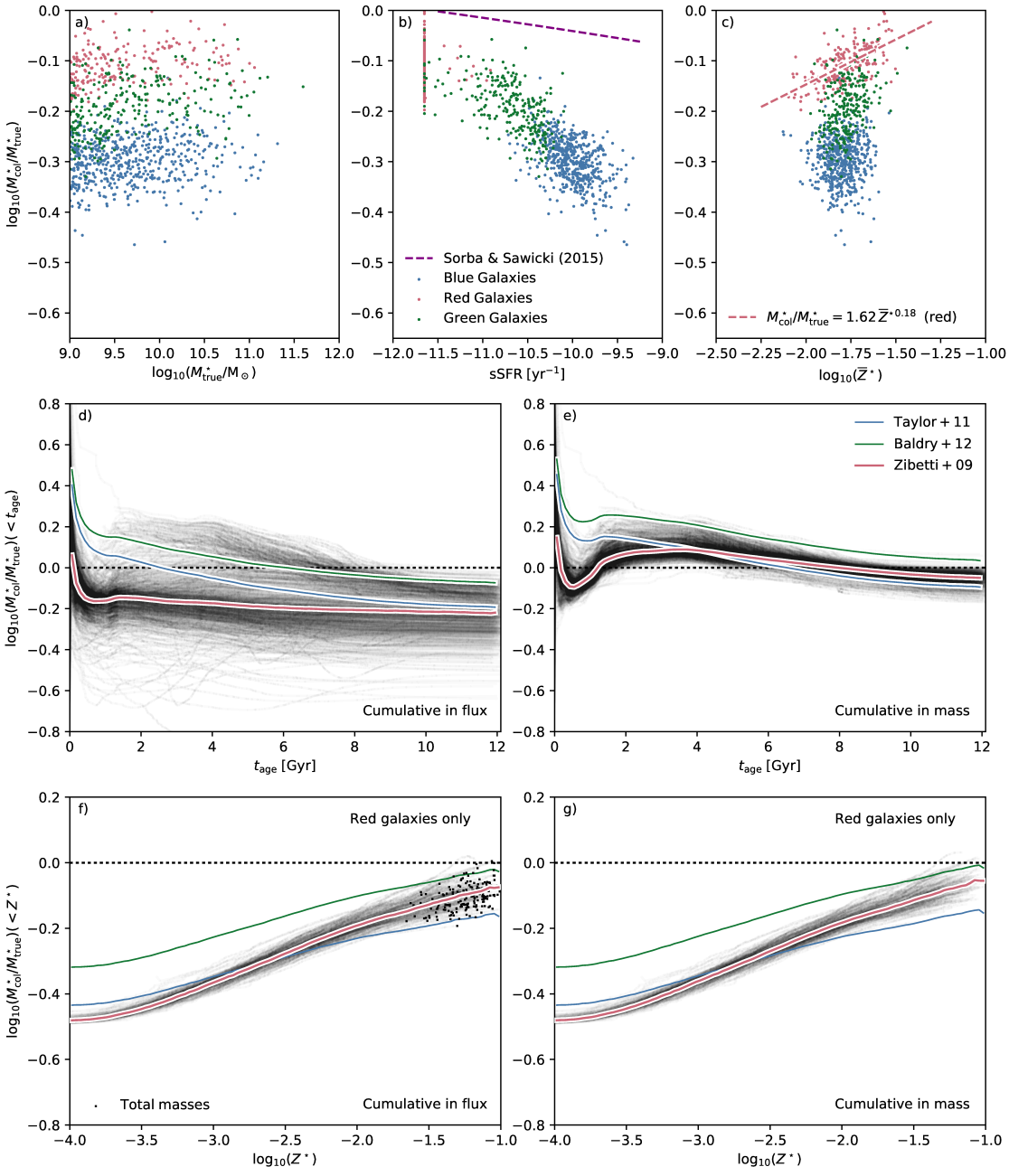

Figure 6.2: Plots illustrating how biases in mass estimation build up for the *composite stellar populations* (CSPs) of 1000 randomly selected EAGLE galaxies, using Eq. 6.2.1 for integrated, dust-free photometry. {*continued on next page...*}

Figure 6.2: {*Continued from previous page...*} The top row shows the mass offset for EAGLE galaxies as a function of physical properties, where galaxies are coloured by their status as *red*, *green* or *blue* (defined as in chapter 4, equation 4.3.1). Panels *a*, *b* and *c* are functions of stellar mass, sSFR and initial mass weighted stellar metallicity, $Z^{\star}$, respectively. Panel *c* also shows a power law fit to highlight the tight relation for red sequence galaxies. The middle row shows the offset in mass estimated cumulatively for stellar populations younger than a given age. Panel *d* shows this offset where the integrated light for all SSPs younger than a given age are used to compute masses, whereas panel *e* shows where the masses for each SSP are estimated individually and summed. *Thin, grey* lines indicate individual galaxies computed using Zibetti et al. (2009) (Z09), with *thick, solid* lines showing medians for different calibrations indicated using the colour schemes of Fig. 6.1. The bottom row is the same as the middle row, but showing the red sequence galaxies only, and are cumulative in stellar metallicity. In panel *f* we also plot the end points for each galaxy as a *black dot* to indicate the maximum stellar metallicity and overall mass offset. We see that resolving SSPs reduces offsets due to age effects, but not due to metallicity effects, see text for further details and discussion.

low sSFR ($\leq 10^{-11.65}$ yr^{-1}) the sSFR dependence of the offset is very small, so galaxies are clipped to $10^{-11.65}$ yr^{-1}.

Panel *c* then plots the offset as a function of the stellar metallicity, computed as the fraction of the stellar initial mass in heavy elements. We see that it is the red galaxies that demonstrate a dependence between metallicity and mass offset, with larger offsets at lower $Z^{\star}$. A power law is fit to the red galaxies to show how the mass underestimate increases for lower metallicity passive galaxies. Notably, the underestimate persists for galaxies at (and above) 'solar metallicity', $Z^{\star} = 0.02$, which is a commonly assumed $Z^{\star}$ value when fitting SED templates.

The build up of mass offset with stellar age is investigated in panels *d* and *e* of Fig. 6.2. In panel *d* the light of all stars younger than a given age is summed cumulatively to evaluate $M^{\star}_{\rm col}(< t_{\rm age})$, and the offset from the true mass of all stars younger than that age is calculated to yield $M^{\star}_{\rm col}$. In panel *e*, $M^{\star}_{\rm col}$ is instead calculated for each SSP individually before being summed cumulatively, and again the offset from $M^{\star}_{\rm true}$ is computed. This elucidates how differently aged SSPs contribute to mass offset in the integrated (panel *d*) and completely resolved (panel *e*, all SSPs are separate) case. The thin lines correspond to individual galaxies. These exhibit much more scatter in offset at all but the very youngest ages for integrated photometry compared to the resolved case. Median lines show that the average total underestimates (rightmost points) are significantly reduced in the resolved case for all estimators, and that the B12 calibration actually slightly overpredicts the average galaxy mass (but is still closer in dex than for the investigated case). It is apparent that the underprediction of mass in young stars (~ 30 Myr) persists to the total underestimate in the integrated case (panel *d*), but is corrected for in the resolved case (panel *e*).

The build up of the mass offset is investigated in panels *f* and *g*, but now cumulative in stellar metallicity and only for red galaxies (selected via equation 4.3.1). It is clear that galaxies display a large spread in metallicity, and that there is a tight relation between mass offset and the metallicity up to which the stellar

ries, and photometric errors can result in the wrong history being recovered (e.g. Sorba & Sawicki, 2015).

mass is truncated. The small spread in this relation is visible for the Z09 calibrations, and all estimators echo this trend. The underestimate is as large as ~ -0.4 dex for $\sim 0.1Z_{\odot}$ ($Z^{\star} \sim 10^{-2.8}$), but the typical overall offset for red galaxies is only ~ -0.1 dex (panel a). This is because red EAGLE galaxies typically have $Z^{\star}$ distributions extending to $\approx 2 - 3Z_{\odot}$, as indicated by the end points (black points) of the cumulative functions plotted in panel f. Metallicities truncated at $Z_{\odot}$ ($Z^{\star} = 10^{-1.8}$) would yield an offset of ~ 0.2 dex. The correlation between $Z^{\star}$ and $\log_{10}(M^{\star}_{\rm col}/M^{\star}_{\rm true})$ exists because while low metallicity stars appear bluer for the same stellar mass, the colour-dependence of $M^{\star}/L$ may not reflect this trend well[4]. This is related to the findings of chapter 4; the SSPs internal to EAGLE galaxies are roughly exponentially distributed in $Z^{\star}$, with a long tail of stars towards high $Z^{\star}$. It was shown that this yields bluer than observed red sequence colours at high mass, despite the fact that the EAGLE mass-weighted $Z^{\star}$ values are similar to the $Z^{\star}$ values obtained from observed galaxy spectra at the bright end. This is because low metallicity stars are bluer, and are more optically luminous than high metallicity stars of the same mass. The internal metallicity distributions of stars in red EAGLE galaxies may therefore explain their typically underestimated masses; red sequence EAGLE galaxies have bluer colours than their observed counterparts, so are predicted to have less mass for the same brightness.

This metallicity effect is *not* equivalent to the *outshining* effect from young stars, as the offset due to metallicity effects is not mitigated by resolution, and the relations and scatter are remarkably similar in panels *f* and *g*. It is common to assume single metallicity templates when modelling SEDs for simplicity, but it seems plausible that the more complex internal metallicity distributions that emerge in EAGLE are more representative of galaxies. If this were true, then real galaxies could have higher than assumed stellar metallicities (in a mass weighted sense) to yield the redder red-sequence colours that are observed. It is difficult

[4]If, for a reduction in metallicity, the stars become bluer more rapidly than they brighten relative to the assumed $M^{\star}/L$ colour dependence, the low metallicity stellar masses are underestimated.

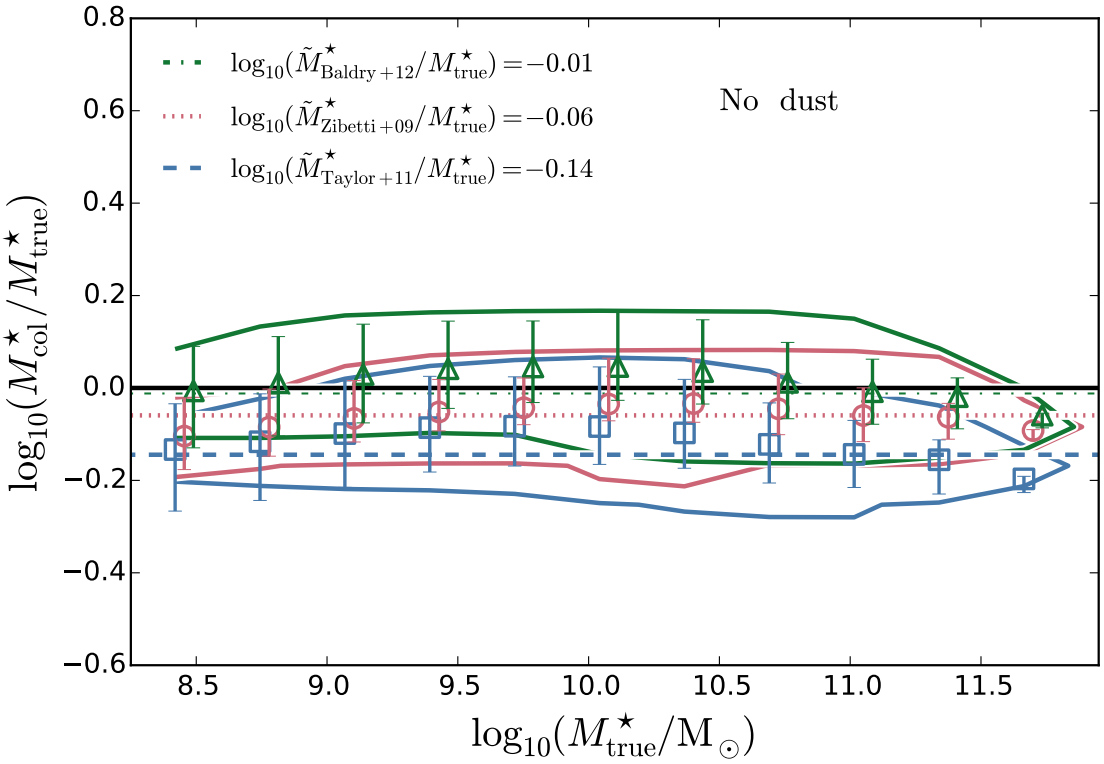

Figure 6.3: As the top panel of Fig. 6.1, but now where SSP masses of individual star particles are estimated separately and summed to yield total masses. While masses remain underestimated on average, median offsets are significantly reduced relative to the integrated photometry plotted in Fig. 6.1. The smallest average offset is found for the Baldry et al. (2012) calibration, only 0.01 dex (∼2%).

to predict how, if at all, this would affect predicted masses when single metallicity templates are assumed for SED fitting, and this issue is further discussed in section 6.3.

It is useful to see how the improved mass estimation for resolved photometry of blue galaxies, seen in the rightmost points of Fig. 6.2e, affects the overall recovery of EAGLE stellar masses and cosmic stellar mass density. For this reason the top panel of Fig. 6.1 is remade in Fig. 6.3, where mass estimates are obtained by instead predicting SSP masses for each star particle individually and summing them. We see that, unsurprisingly, the overall mass underestimate is reduced to $\lesssim 0.1$ dex, and is within ≈ 2 % for the B12 estimator. Of course, this is a highly idealised model of resolved photometry, where SSPs can be observed separately and

there are no dust effects. In resolved observations a pixel still represents a mixed column of stars and dust, and, in addition, may be contaminated with light emanating from outside the column due to PSF smoothing and scattering effects. For passive galaxies this is unlikely to make much difference as they typically have negligible dust masses, and even resolving SSPs perfectly makes an imperceptible change in recovered masses from the integrated case (Fig. 6.2f and g). These effects could, however, be important for star forming galaxies. Indeed, Sorba & Sawicki (2015) find smaller differences between resolved and integrated mass estimators using resolved photometry, and a weaker sSFR dependence plotted in Fig. 6.2b. More representative resolved photometry is tested in the following section, using the SKIRT imaging of chapter 5.

6.2.3 Resolved photometric mass estimators

As discussed in the previous section, resolution can strongly influence how well masses are recovered. In particular, the *outshining* effect can lead to biases in recovered masses, and differences between the true and fitting forms of star formation histories (e.g. Sorba & Sawicki, 2015). It has also been asserted that dust lanes can cause significant differences between resolved and unresolved photometric estimates (e.g. Zibetti et al., 2009).

To investigate these effects, and improve on the simple model of resolved photometry of 6.2, I employ the SKIRT imaging described in chapter 5 and appendix B. This builds the effects of stellar population alignment by projection, smoothing, pixelisation, sampling noise, and the 3D geometric effects of absorption and scattering into the mock resolved photometry. As imaging is only obtained for a small subset of EAGLE galaxies, and dealing with images is much more computationally expensive than integrated photometry values, I focus on just 3 archetypal EAGLE galaxies. These are the same galaxies chosen in Fig. 5.2 (chapter 5) to represent three systems that are resolved with $> 50,000$ star particles, but are morphologically diverse, exemplifying disc (S), elliptical (E) and irregular (Irr) types.

In Fig. 6.4 the dependence of logarithmic $M^{\star}_{\rm col}$ offset on resolution itself is ex-

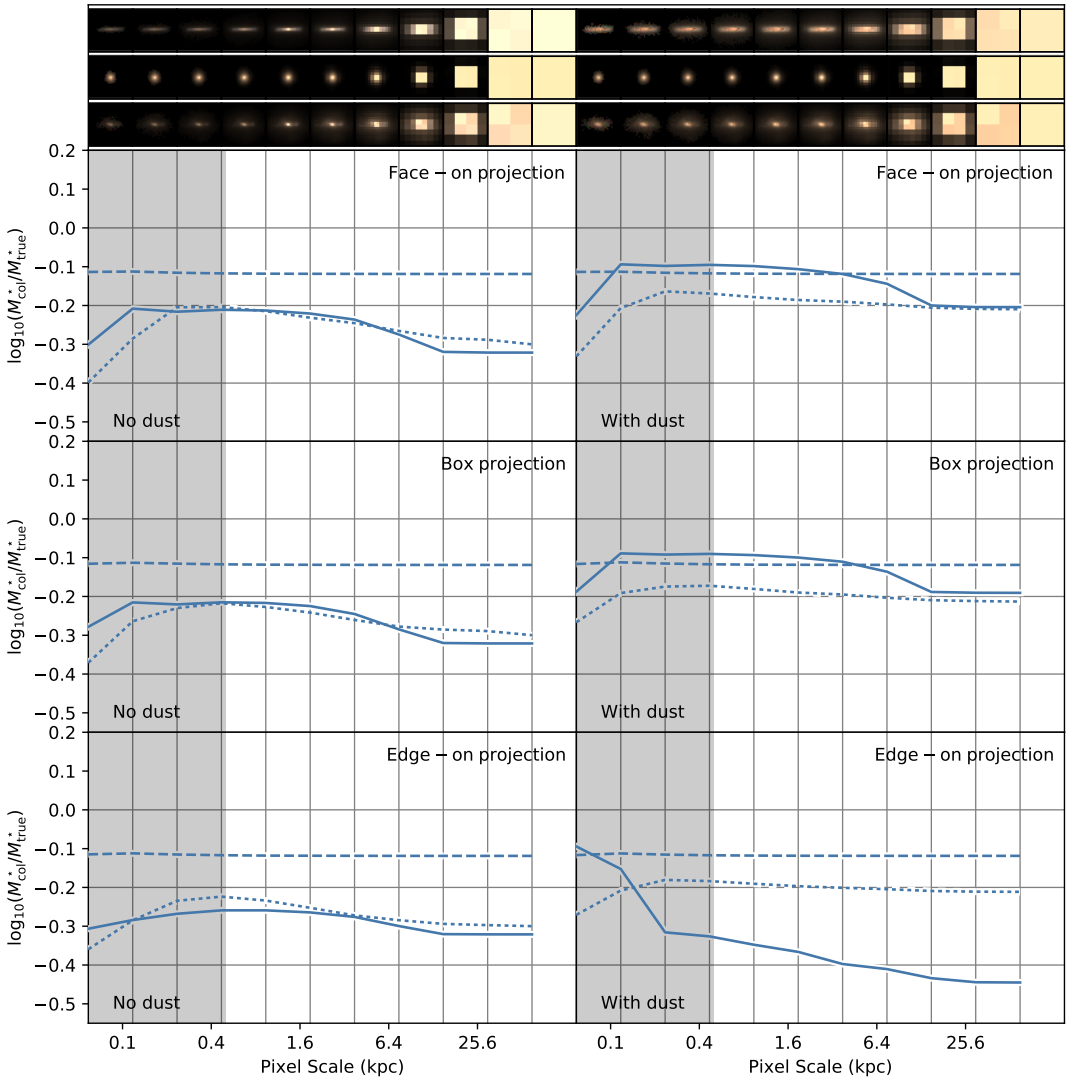

Figure 6.4: The offset in recovered stellar mass using Eq. 6.2.1 for resolved photometry as a function of pixel side length for 3 archetypal galaxies (chosen in chapter 5, table 5.1). The maximal resolution images cover 60 pkpc on a side, with 1024^2 pixels. Images are then degraded sequentially by re-binning light into a factor 2^2 fewer pixels (ie. doubling pixel side lengths), until the field is represented by a single pixel. This yields the integrated result for that galaxy. The panels in the left and right columns are produced for imaging without and with dust respectively, with rows from top to bottom corresponding to face-on, box, and edge-on aspects of the galaxies. Each panel shows mass offset with resolution for the S, E and Irr type galaxies as *solid*, *dashed* and *dotted* lines respectively, using the Z09 calibration. {*continued on next page...*}

Figure 6.4: {*Continued from previous page...*} *Grey shading* indicates pixel scales below the EAGLE intrinsic resolution scale of 0.5 kpc. Three colour grz thumbnail images are also shown above the plots for each galaxy (S, E and Irr types from top to bottom) and corresponding to each resolution in the x-axes. We see that the underestimate grows along with pixel size above the EAGLE resolution limit for types S (solid line) and Irr (dotted line) in all cases, but stays remarkably constant for the E type (dashed line).

plored for SKIRT images. Here, only the Z09 estimator is used in order to simplify the plots, and also because this estimator is intended for resolved photometry. The left column of plots/images uses completely dust-free imaging to isolate stellar effects[5], while the right column uses the full stellar and dust treatment of chapter 5. The intrinsic spatial resolution of EAGLE is ~ 0.5 kpc, and smaller pixel scales are shaded grey to indicate where structure is unresolved. I begin with imaging a 60^2 pkpc^2 field about the galaxy centre with 1024^2 pixels, and degrade resolution as described in the figure caption. This approach is used instead of sequential smoothing, as it preserves the flux within the same field. The overall colours are redder and light is less concentrated when dust is included for the S and Irr types, while neglecting dust makes no difference to the two sets of E images.

Beginning with the dust-free imaging, I first consider the offset-resolution relations for each type projected in the simulation xy-coordinates (box projection, middle row). The E-type galaxy shows an underestimate of 0.1 dex with little to no dependence on resolution. This is consistent with the finding from Fig 6.2g: resolution does very little to improve intrinsic underestimates in masses of red EAGLE galaxies, with metallicity effects dominating the offset. For both the S and Irr types, the galaxy mass underestimate gets progressively larger with poorer resolution above the EAGLE resolution scale[6], with a marginally larger varia-

[5]ie. no ISM dust, replacing the MAPPINGS-III templates with GALAXEV that do not account for nebular absorption and emission.

[6]below this scale, stochastic effects due to limited numbers of photon packets in SKIRT affect

tion and integrated mass underestimate registered for the S type (~ 0.1 dex and ~ 0.3 dex respectively).

Now I look at the differences between offset-resolution relations for differing galaxy projections. In the dust-free case these come about due to the different combinations of SSPs sampled along the line of sight of each pixel. The most extreme comparison conceptually is between the face and edge on projection of the S type at small pixel sizes; for face on discs these pixels bin light from SSPs in close proximity (within $\sim$ the disc thickness), whereas for edge-on cases one pixel could bin light emanating from stars in the bulge and across the entire width of the disc. For pixel side lengths near the intrinsic EAGLE resolution of ~ 0.5 kpc the difference appears maximal, leading to a ~ 0.05 dex lower mass prediction for the edge-on case relative to the face-on case. This is consistent with the idea of *outshining*; in the edge-on case old bulge stars are binned into pixels together with relatively young disc stars and their mass contribution may be missed, whereas in the face-on case the bulge and disc stars typically appear in separate pixels. Apart from this case, it is apparent that differences in the offset-resolution curve are marginal relative to the variation with resolution itself.

Now turning to the imaging with the full SKIRT model dust treatment I again focus on mass offset-resolution relations for the box-projected photometry, which are nearly identical to the face-on projections. We see that the effect of dust for these projections appears to actually increase the mass estimates for the S and Irr, reducing the underestimate at all resolutions. When the pixel scale matches EAGLE resolution the mass estimates are most accurate, underestimated within 0.1 dex for the S type. Interestingly, Z09 identify that the $M^{\star}/L$ for blue colours obtained with their CB07 SEDs is lower than if BC03 is used instead, finding a ~ 0.1 dex typical offset. The choice of BC03 is consistent with EAGLE, which could account for the rest of the offset for the S type galaxy. Again no change is observed for the E type, as it has negligible dust content. Given the Z09 analysis of E type NGC4552, a similar 0.1 dex offset may also be reconciled for the E type

this relation.

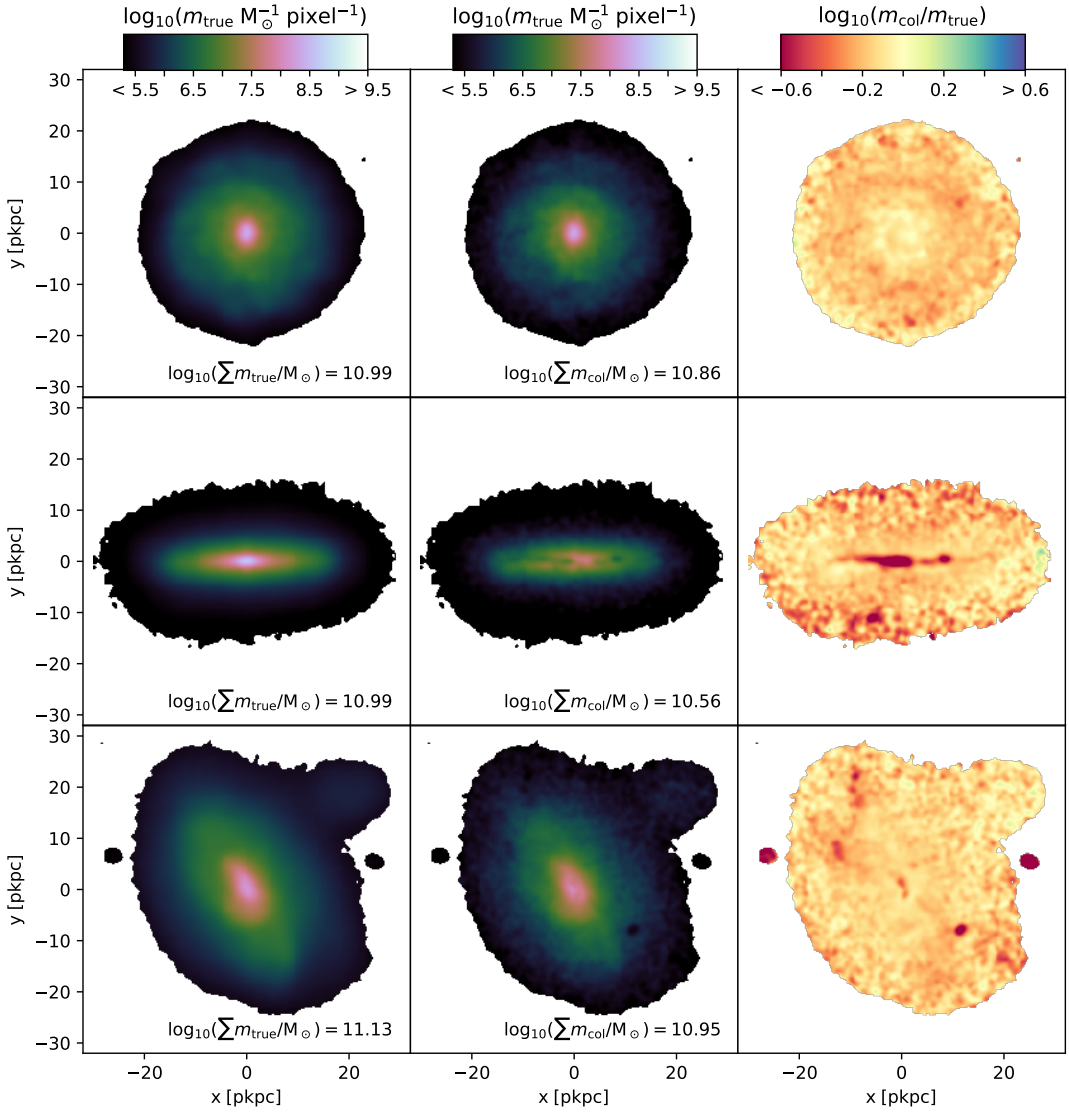

Figure 6.5: Inspecting resolved mass maps recovered for 3 archetypal galaxies (chosen in chapter 5, table 5.1) using the Zibetti et al. (2009) (Z09) calibration of Eq. 6.2.1. Rows from top to bottom show the S type galaxy in face and edge-on projection and the Irr type galaxy in box projection, respectively. The maps from left to right are then the *'true'* mass map of the galaxy, the reconstructed mass map from the dust inclusive imaging and the residual map showing the offset on a pixel-by-pixel basis. Colour bars are shown to quantify shading values. I use the standard SKIRT images of chapter 5, and apply an additional uniform smoothing of ~ 0.5 kpc. We see that masses are recovered within 0.2 dex (~ 25 %) for the face-on S type and box-projected Irr type galaxy, but underestimated by 0.5 dex (a factor 3) for the edge-on S type. It is apparent that heavily dust obscured regions contribute much of this offset.

by the choice of SPS model. However, only one E type galaxy is examined in that study.

The assertion of Sorba & Sawicki (2015) that the difference between resolved and unresolved mass estimates is typically larger for galaxies with higher sSFR also holds true for these three galaxies when dust is included. The degree of variation between resolved and unresolved offset can be compared directly to that found by Sorba & Sawicki (2015); using their relation recovers a ∼-0.03 dex difference for both the S and Irr types, which is accurate for the Irr type but significantly underpredicted for the S type. Differences from Sorba & Sawicki (2015) may be attributable to that study employing full SED fitting at each resolution, rather than a single colour-dependent $M^{\star}/L$ ratio, and fitting different histories than those used to derive the Z09 estimator used here. They also note a considerable jump to lower predicted masses at a resolution of ~ 3 kpc which is not apparent for EAGLE galaxies, however this jump is attributed to the scale of spiral arm features that are not expected to be well resolved in EAGLE galaxies.

The story is the same for the edge-on projected E and Irr, but is significantly different for the S type. Here, the galaxy mass estimate similarly decreases with degraded resolution, but is already ~ 0.3 dex underestimated at the EAGLE resolution pixel scale, growing to a factor of 2-3 underestimate in the integrated photometry. This EAGLE galaxy has strong edge-on attenuation and clear dust lanes, which appear to drive the strong underestimation. This is the largest underestimate and overall difference between resolved-integrated mass estimates. Z09 note that their estimator may be confounded by strong dust lanes, and similarly find that the largest resolved-unresolved variation in estimated mass occurs for galaxies with prominent dust lanes.

True, estimated and residual mass maps are plotted directly in Fig. 6.5 to show the regions that contribute to the overall mass offset in the resolved case. In addition to the underlying stellar smoothing in the SKIRT modelling, I apply a constant smoothing of 500 pc to limit the image resolution to approximately the physical resolution scale of the Ref-100 galaxies. The S type in face and edge-on projection and the Irr type in box projection are chosen as useful examples (the

E type shows negligible spatial variation). From inspecting the residual maps, the face-on S type has stellar masses recovered well in the bulge region, but with systematic underestimates of ~ 0.2 dex in the outer disc that contribute to a net 0.13 dex underestimate. Dust columns are low for the face-on view (overall A_g of 0.5). For the edge-on case, however, dust attenuation is much stronger (overall A_g of 1.3), and masses are underestimated in the dust lane region by > 0.6 dex. This leads to the net underestimate of 0.43 dex. Similar results to the two S type orientations are found for the Irr type; central dust lanes and dense peripheral dust clouds are significantly underestimated, and a less dramatic but more extended underestimate is just visible for the star forming tidal tails, roughly aligned with the $y = -x$ line in this orientation.

As noted for Fig. 6.4, the addition of dust actually improves mass recovery (ie. increases mass estimates) for resolved photometry for low and intermediate ($A_g \lesssim 0.4$ mag) overall attenuation. This suggests that dust attenuation is not simply hiding mass in all cases, but that diffuse and dusty star forming portions of galaxies may lead to relatively subtle large-scale underestimates visible in the face-on and Irr residual map. While the combined effects of differences between the histories and dust model assumed by Z09 and those that emerge in the EAGLE model could contribute to these differences, it is also plausible that these underestimates are again related to the differences between the 'CB07' stellar population model assumed by Z09 and the BC03 model assumed for EAGLE. The CB07 modelling is shown to assign lower $M^\star/L$ ratios for bluer colours relative to BC03 in Z09, with typical total galaxy offsets of ~ 0.1 dex. However for high attenuations ($A_g \gtrsim 1$ mag), stronger underestimates are clearly visible. These cannot be reconciled by SPS model differences alone, and are clearly related to the screen model assumption of Z09 being unable to represent the EAGLE attenuations well when dust becomes optically thick. Z09 acknowledge that dust lane galaxies are particularly uncertain in terms of mass recovery, and that the employed modelling of Charlot & Fall (2000) struggles to represent strong dust features. Qualitatively, the mass underestimation along the dust lane is clearly visible in the resolved mass map for the edge-on S type (middle panel). These dust-aligned deficits do

not appear to be as prominent in the mass maps of galaxies obtained by Z09. This could point to the Charlot & Fall (2000) dust modelling being a better fit to real galaxies than to EAGLE galaxies, even suggesting tension between dust effects in galaxies and those obtained with EAGLE. However, there are no fully edge-on galaxies in the Z09 sample where galaxies have dust lanes of similar optical depth for comparison, and these deficits are only conspicuous for the edge-on S type case. The S type we choose is a particularly dusty and massive spiral in EAGLE, and the underestimate is anomalously high compared to the general population (see Fig. 6.1), suggesting that this virtual galaxy image is an extreme case. Such strong, dust-driven mass underestimates are uncommon in EAGLE at low redshift ($z \lesssim 0.1$). Dust effects are assessed quantitatively below.

Empirically calibrated $M^{\star}/L$ ratios of Eq. 6.2.1 provide insight into how well EAGLE stellar masses can be recovered photometrically, while indicating the associated limiting factors. However, it is difficult to isolate the sources of discrepancy using these measures. In particular, it is not clear how far discrepancies can be ascribed to model EAGLE observables being different from the observational samples, or failures in SED fitting techniques used to derive these relations. As a result, average offsets observed for different estimators are not particularly informative; it is the residual trends that are most interesting. Taking what can be learnt from the above analysis, I now turn to full SED fitting for a more direct analysis of how well assumed histories fit EAGLE, and whether the best fit histories to EAGLE model observations differ from those of observations. Conducting the SED fitting affords more control over modelling assumptions and more insight into the physical origin of any discrepancies, which may allow average stellar mass offsets to be better understood.

6.3 SED fitting

With the popularity of SED fitting techniques, a large number of SED inversion and fitting codes have become publicly available. I use the SED fitting code FAST (Kriek et al., 2009) to derive stellar masses and star formation rates. FAST is a

straightforward code that constructs a grid of template SEDs corresponding to a discrete set of redshifts, stellar metallicities, levels of attenuation and parameters characterising star formation history. FAST then allows the SED normalisation (representative of the present stellar mass) to scale freely, and identifies the parameter set that minimises χ^2 for a set of input fluxes and flux errors as the fitting solution. The default parametric star formation histories are characterised by a star formation timescale (τ) defining the duration of the burst, and an age ($t_{\rm age}$) defining when star formation commences (with $t' = t_{\rm age} - t_{\rm lookback}$). FAST provides exponential ($\dot{M}_\star \propto \exp(-t'/\tau)$ for $t' \geq 0$), 'delayed exponential' ($\dot{M}_\star \propto t' \exp(-t'/\tau)$ for $t' \geq 0$) and constant ($\dot{M}_\star \propto 1$ for $0 < t' \leq \tau$) functional forms.

Here, I focus on the integrated EAGLE spectra, including dust effects and nebular emission as described in chapter 5. I fit broadband fluxes measured in rest-frame $ugriz$, and assume fractional errors consistent with SDSS photometry (taken from Padmanabhan et al. 2008). The initial FAST parameter grid that was constructed to fit the EAGLE SEDs is chosen to be:

- $\log(\tau/{\rm yr}) \in$ [7,10.2] in steps of 0.1 dex
- $\log(t_{\rm age}/{\rm yr}) \in$ [7,10.2] in steps of 0.1 dex
- $Z \in$ [0.004, 0.008,0.02,0.05]
- $A_V \in$ [0,3] in steps of 0.1 mag

where the redshift, z, is held fixed at 10^{-4} to approximate the rest frame[7]. In addition the template SEDs assume the Bruzual & Charlot (2003) SPS model, a Chabrier (2003) IMF, and the attenuation law of Kriek & Conroy (2013).

This set up is similar to that of Torrey et al. (2014), with some significant differences. The time parameter ranges are truncated to $10^{10.2}$ yr as this exceeds the age of the Universe in the Planck cosmology (Planck Collaboration et al., 2014). Most importantly, I use the radiative transfer photometry including dust and allow

[7]The neglected k-correction has negligible effect on the fitting results

FAST to fit for dust attenuation, whereas Torrey et al. (2014) conduct the fitting for intrinsic fluxes (i.e. dust-free, without nebular emission).

6.3.1 Initial SED fitting and the failure population

The first attempt at photometric SED fitting using the parameter grid detailed above provides reasonable stellar mass estimates (within ~ 0.1 dex) for the majority of galaxies, but yields a significant population (≈5%) of galaxies with strongly underestimated stellar masses, as seen in Fig. 6.6.

Fig. 6.6a shows the offset-mass relation, as plotted in Figs. 6.1 and 6.3, for integrated photometry and shaded from dark to light by point density. The median offset found using FAST is significantly reduced compared to that obtained using colour-dependent $M_\star/L$ estimators shown in Fig. 6.1, and will be discussed in the following section. However, the sub-population of galaxies where FAST underestimates masses by ~ 1 dex is not present for the estimators explored in section 6.2. I refer to these galaxies below as *'failures'*, and take them to be galaxies with mass offsets of < -0.7 dex. Failure and non-failure galaxies are shaded using blue and orange colours, respectively.

In panel *b*, it can be seen that these galaxies are distinguishable by a certain parametrisation of the assumed histories. Failure galaxies (blue contours) are almost exclusively fit by very young (~ 10 Myr) histories relative to the overall population (grey shading). They also show a strong preference for similarly short star formation timescales (τ), but with a tail extending to $\tau \lesssim 10$ Gyr. For the delayed exponential histories I assume, timescales longer than the age ($t_{\rm age}$) actually yield rising histories. Such rising (or *'inverted-τ'*) histories have been found to fit model galaxies well at high redshift ($z \sim 2$, Maraston et al., 2010). To characterise these galaxies in terms of model observations, panel *c* then shows where the failure galaxies lie in the ugJ colour-colour plane, utilising the same blue shading as in panel *a*. It is clear that the failures occupy a certain region of the plane, bordering the low (blue) $u-g$ edge of the overall distribution for relatively blue $g-J$ colours ($g-J \lesssim 1.3$). I identify a blue 'wedge' region in ugJ space ($g-J < 1.3 \ \wedge \ 0.45(g-J)-(u-g) < 0.445$) that encloses a majority of

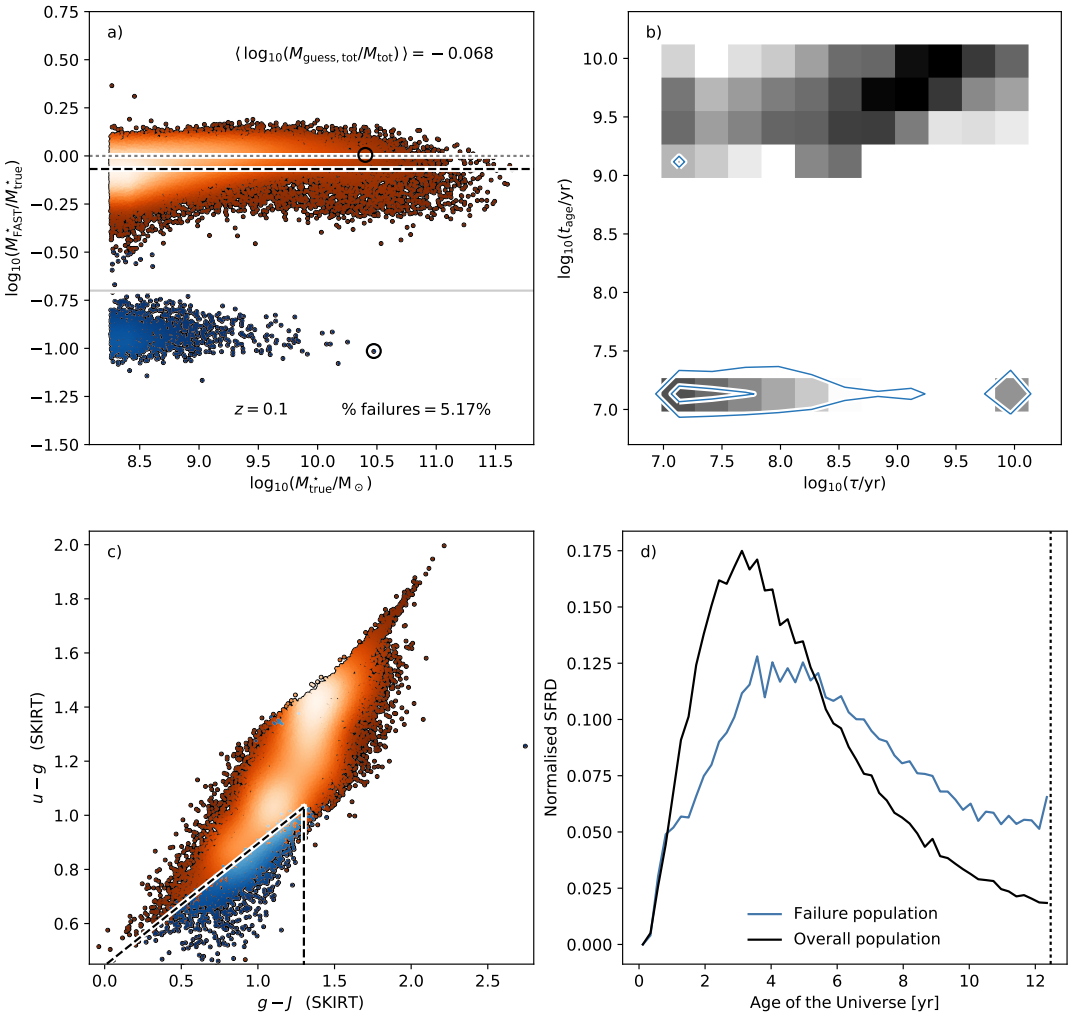

Figure 6.6: Results of the initial SED fitting calibration using FAST (Kriek et al., 2009) for integrated EAGLE photometry, and identifying a failure population where recovered masses are underestimated by a factor of ∼10. Panel *a* shows mass offset as a function of mass for individual galaxies. The failure population is well separated by an offset of more than -0.7 dex (*grey line*). The failure and non-failure populations are coloured blue and orange respectively, and shaded by the logarithmic point density. Panel *b* shows the histories recovered for EAGLE galaxies, in terms of age and timescale. The frequency of recovered parameter combinations for the overall population is indicated by *grey shading*, with *blue contours* denoting the failure population. {*continued on next page...*}

Figure 6.6: {*Continued from previous page...*} Panel *c* shows a ugJ diagram employing the same colouring and shading as panel *a*, revealing that the failure population generally occupy the bluest $u - g$ colours for a given $g - J$ value where $g - J \lesssim 1.3$. This region is demarcated by the dashed line. Panel *d* then shows the stacked SF histories of galaxies in the demarcated region of panel *c* (*blue line*), relative to all galaxies (*black line*), both normalised to unit integral. Overall, we see that FAST recovers anomalously young ages for failure galaxies (by $\gtrsim 2$ dex), and that their actual histories are characterised by more recent star formation than average. In particular, the failure galaxies tend to exhibit a recent burst of star formation.

the failures. Despite being dominated by these failures, the wedge still comprises 42% non-failure galaxies, showing that galaxies with these colours are not always assigned highly underestimated ages. Panel *d* shows normalised histories of blue wedge galaxies (blue) compared to the general population (black). Wedge galaxies typically have younger ages and higher recent star formation rates (double the average over the last ~ 2 Gyr). A small but significant uptick in very recent ($\lesssim 100$ Myr) star formation can also be seen for the wedge population, suggesting that many of these galaxies are actually undergoing bursts at the time of selection.

As bursts cannot be represented in the decaying portion of τ models, and young stars can dominate optical fits due to outshining, it seems that the fitted histories are favouring young bursts or rising histories to fit the light from very young stars at the expense of older stars that may comprise as much as $\sim 90\%$ of the stellar mass. As an example of how such discrepant histories can be found to be the 'best' fits, I compare the SED fitting results of similar failure and non-failure galaxies in Fig. 6.7.

The two galaxies selected for comparison in Fig. 6.7 are highlighted by empty circles in Fig. 6.6. This is the highest mass failure galaxy (left panel), and a similar mass galaxy where the FAST recovered mass is within $\sim 5\%$ of the true value (right panel). The SKIRT photometry fed to FAST (blue circles) and SEDs from which they are derived (blue lines, offset from photometry for clarity) are qual-

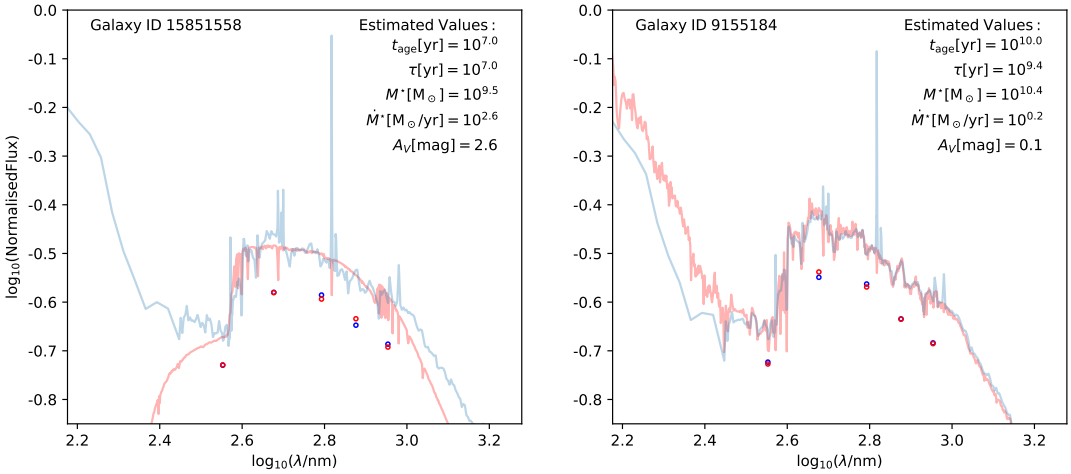

Figure 6.7: Comparing the recovered and SKIRT SEDs of EAGLE galaxies in the cases of a failed (left) and successful (right) mass recovery. *Red* and *blue* lines plot the best fit and SKIRT SED for each galaxy, respectively, with *points* of the same colour indicating the associated $ugriz$ photometry sets. The photometry sets are offset below the SEDs for clarity. The selected galaxies are the highest mass *'failure'* galaxy and a similar mass galaxy where the true mass is recovered within 5 % (highlighted by *black circles* in Fig. 6.6a). The failed and successful recovery instances are shown in the left and right panels respectively. We see that while both galaxies show relatively good agreement between the FAST-fit and SKIRT modelled photometry, the detailed SEDs deviate for the failed fit, particularly at λ longer and shorter than the $ugriz$ photometry set considered by FAST.

itatively very similar for the two example galaxies[8]. However, the best fit SEDs chosen by FAST (red lines) display vastly different shapes for the two galaxies at lower and higher λ. The best-fit SED for the failure case is that of a rising history caught near its peak, with strong optical attenuation of $A_V = 2.6$. Strong attenuation causes the fitted SED to drop towards UV wavelengths, diverging dramatically from the rising SKIRT SED. The SEDs also diverge toward NIR wavelengths, due to the large mass underestimate, with the fit SED dropping more quickly than SKIRT towards longer wavelengths. Looking in detail, SEDs also reveals stark differences; the fit SED is largely smooth with sharp Balmer absorption features, whereas the skirt SED shows complex absorption features indicative of older, metal enriched populations. For the non-failure galaxy, the SEDs are in much better agreement. The NIR continuum levels match very well, and both SEDS display good agreement between detailed absorption features. The NUV fluxes also agree much better, but are slightly (0.1 dex) overpredicted by FAST, which may be attributable to the single screen dust model that lacks dedicated birth cloud absorption. As no nebular emission is built into the FAST templates, there are also large differences between SEDs for both galaxies at certain transition wavelengths, e.g. Hα.

Despite these two galaxies showing very different levels of agreement between their SKIRT and best fit SEDs, the input and recovered photometry agree well in both cases. This is because the SEDs are broadly similar for the wavelengths sampled by $ugriz$ at $z \approx 0$, and any detailed differences between SEDs are averaged out across broad bands. It is clear that the dramatic failure to recover masses comes about due to degeneracy in the model parameters; the extremely young, dusty starburst provides a similar photometry set to this older star forming galaxy with a less dramatic recent burst. With the actual fit to photometric bands being relatively good for the failure case (i.e. having χ^2 similar to that of the non-failure case), it is unclear that incorporating similar histories superimposed with bursts would reliably remove this population (extreme rising

[8] A subtle difference in shape is that the failure galaxy has a slightly boosted NUV ($\lambda \sim 150$ nm) flux and emission line features.

starbursts may still provide the best fit in some cases). Instead, such degeneracy could be broken by including UV (e.g. *GALEX*) or NIR (e.g. *UKIRT*) photometry in the fitting, or even by high signal-to-noise spectroscopic fitting over the $ugriz$ range, given the detailed differences between the optical portions of the SEDs.

The tempermentality of the fit could also be exacerbated by the reduced χ^2 fitting approach employed by FAST; slight variations in photometry can lead to vastly different fitting parameters between models with similar χ^2. To test this, 300 different realisations of the $ugriz$ photometry are re-fit where random Gaussian perturbations (scaled by the uncertainty) are applied to each broad-band flux for both galaxies[9] shown in Fig. 6.7. It is found that the failure galaxy is only a failure in 12% of cases, and that the non-failure galaxy becomes a failure in 2% of the realisations. Not surprisingly, the histogram of recovered masses is multi-modal and dispersed such that the median mass offsets is -0.4 dex. T11 discuss the effect of biases and other problems in the χ^2 fitting, and (along with B12) circumvent this by instead integrating over the posterior distribution of recovered values. Assuming a similar, fully Bayesian approach could help eliminate failures by reducing the viability of extreme templates.

Even though a similar procedure to Torrey et al. (2014) is followed here, the failure population I find is not present in their analysis of the ILLUSTRIS simulation. While it is technically possible that this is caused by the differing properties of the two simulated populations, it seems unlikely that similarly bursty histories do not occur in ILLUSTRIS. Otherwise, the key difference must be in the fitting procedure; either the chosen histories or inclusion of dust. Repeating the fitting using pure exponential histories (as in Torrey et al. 2014) yields a similarly offset population of failure galaxies, albeit halved in number density. Using dust free photometry and forcing $A_V = 0$ in FAST eliminates these failures completely. These offset-mass plots are shown appendix C. This result confirms that the dust fitting is the key factor causing these failures; strong dust attenuation is needed to make extremely young bursts look similar to older EAGLE galaxies photomet-

[9]This is similar to the approach of Sorba & Sawicki (2015).

rically.

As it is SED fitting with integrated $ugriz$ SKIRT photometry that I am investigating, I continue fitting for dust attenuation, but attempt to mitigate the failure population by limiting the ages of histories to $t_{\rm age} > 10^{8.5}$ yr (reasonable at $z \sim 0.1$). This reduces the failure population to $\approx 0.4\%$. The following section looks at the recovered properties of EAGLE galaxies on adopting this modified fitting procedure and compares them to observationally derived scaling relations obtained through inverse modelling. The modified set-up is hereafter referred to as the *'fiducial'* FAST model

6.3.2 SED fitting results at $z = 0.1$

With a fiducial set-up for FAST established, the fitting results and recovered parameters may now be explored. Residual trends between the true and FAST masses are first described and discussed by returning to the familiar offset-mass relation in Fig. 6.8. In general, it is apparent that the full FAST fitting provides better mass recovery than the simpler empirical estimators of Fig. 6.1; masses are still underestimated on average, but only by ~ 0.07 dex ($\sim 20\%$) on average rather than the 0.1-0.2 dex obtained using different calibrations of Eq. 6.2.1. This suggests that some part of the systematic underprediction originally found for Fig. 6.1 may be attributable to intrinsic shortcomings of broad-band optical SED fitting across the $ugriz$ range, but that it may also arise from fundamental differences in the photometric properties of EAGLE galaxies or disparate fitting approaches in independent studies. Interestingly, the stellar mass range where masses are best recovered is around the 'knee' of the mass function; these galaxies contribute most strongly to the cosmic stellar mass density. Larger underestimates are found for the highest mass EAGLE galaxies.

First looking at the $u - r$ plot of Fig. 6.8 (top left), it is apparent that underestimated galaxies are typically red in $u - r$ for $M^{\star}_{\rm true} > 10^{9}{\rm M}_{\odot}$. As seen in chapter 5, galaxies appearing red in the SKIRT photometry are either passive or exhibit strong dust attenuation. The fraction of dusty and passive galaxies on the red sequence only become comparable at high mass with SKIRT ($\sim M^{\star}_{\rm true} > 10^{11}{\rm M}_{\odot}$,

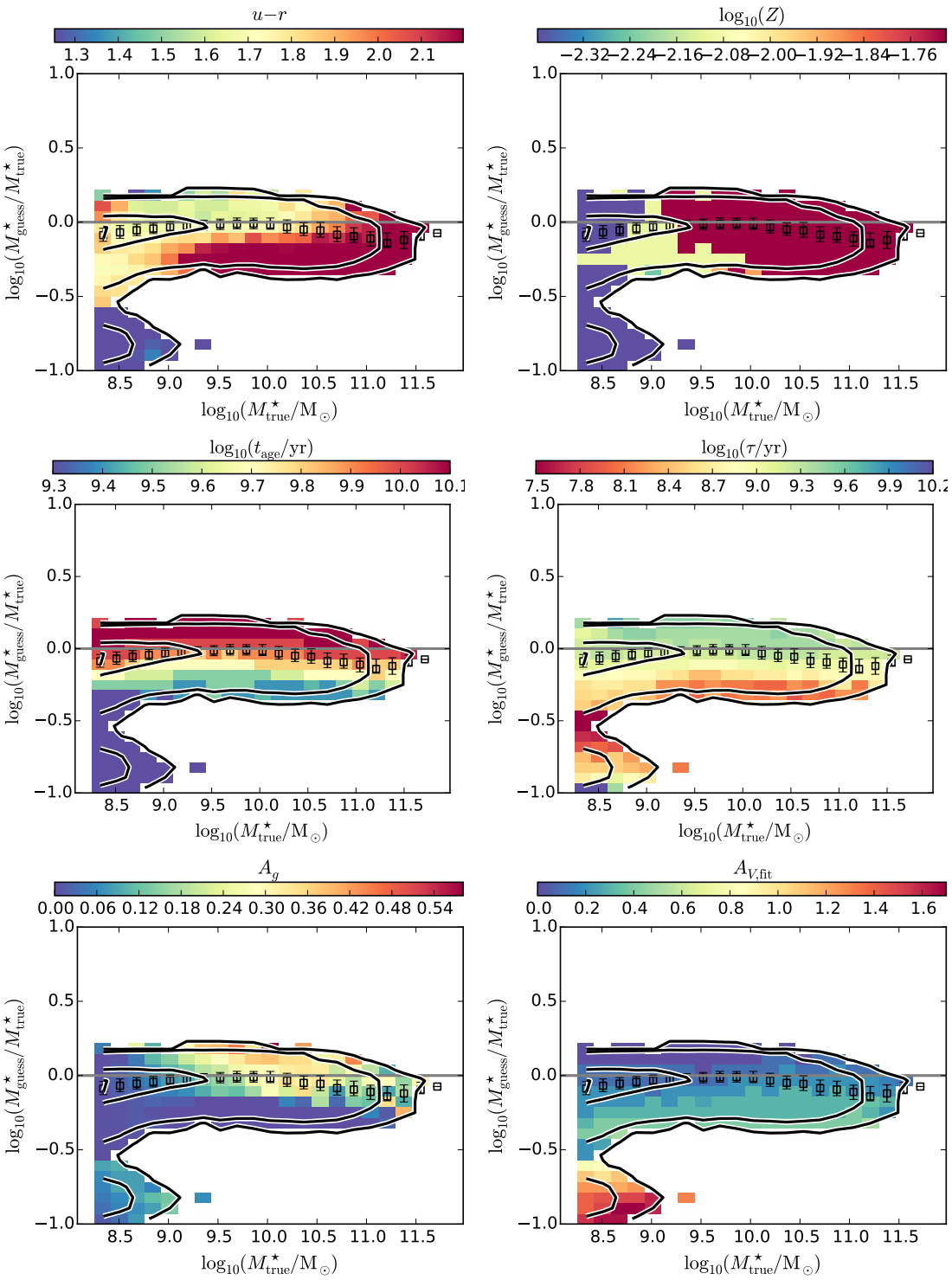

Figure 6.8: Mass offset as a function of the true stellar mass obtained for SKIRT photometry using our fiducial FAST set-up. Residual trends between the true and estimated masses are explored by binning galaxies in uniform, logarithmic offset-mass bins and colouring them by median parameter or property values for bins containing > 10 galaxies. {*Continued on the next page...*}

Figure 6.8: {*Continued from previous page.*} Colour maps are provided above each panel to signify which trends are being shown, and quantify their values. A number of significant trends are displayed, which are discussed further in the text. *Black squares* again indicate the median offset in stellar mass bins. The average offset is found to be 0.07 dex

Fig. 5.7), so these red galaxies are predominately passive over the majority of this mass range. This may be related to metallicity effects previously described in chapter 4.2 and section 6.2; EAGLE galaxies have exponentially distributed internal metallicity distributions, yielding slightly bluer colours than the observed red sequence, and driving a disparity between the mass and light weighted metallicities. The commonly assumed single metallicity templates used by FAST may not be able to represent these more complex enrichment histories, leading to compensation by other parameters and resulting in mass underestimation. This situation is likely not helped by the coarse metallicity coverage of many SPS models, including BC03 assumed here. The metallicity panel (top right) shows that, while a general trend of increasing metallicity with stellar mass is recovered by FAST, the majority of galaxies with $M^{\star}_{\rm true} > 10^{9}{\rm M}_{\odot}$ are fit by 'solar metallicity' ($Z^{\star} = 0.02$) template. The underestimate in red galaxy masses at ~ 0.1 dex is at a similar level to that found using the Z09 estimator in Fig. 6.2, suggesting they are impervious to both resolution and a full SED fitting treatment. It is plausible that composite metallicity SED templates would be able to reproduce masses for passive galaxies in EAGLE better, and also may be a more reasonable physical model in any case. Even simply interpolating between the coarse BC03 metallicities to yield a finer metallicity grid may help (implemented by e.g. T11 and Mitchell et al. 2013). It is interesting to note that apparently blue galaxy masses are well recovered, or even marginally overpredicted (discussed further below).

The middle row of Fig. 6.8 shows the time parameters of fitted histories, with age ($t_{\rm age}$, left) and star formation timescale (τ, right). A remarkable trend is recovered between the offset and the age, with the most underestimated galaxies assigned the youngest ages. This is perhaps counter-intuitive to what we saw in

the $u - r$ panel; that red galaxies are preferentially underestimated. Turning to the τ plot, however, shows that underestimated galaxies are also assigned much shorter timescales, such that $t_{\rm age}/\tau$ is generally larger for underestimated galaxies and therefore have lower fitted sSFR relative to their true value. This is then consistent with the $u - r$ colour trend.

The bottom row of Fig. 6.8 focuses on dust. The left panel is the true, ISM g-band dust attenuation, whereas the right panel gives the Calzetti et al. (2000) A_V value fit by FAST. Blue star-forming galaxies will generally have more dust attenuation than red passive galaxies, so it is perhaps unsurprising that the attenuation is generally higher for overpredicted than underpredicted galaxies given the trends identified above. What is more surprising is that this trend is then reversed for the best fit A_V value. Comparing the recovered and true attenuation values suggests that attenuation is overpredicted for galaxies with underestimated mass. This may appear strange considered in isolation; overestimating the amount of light being blocked by dust would intuitively lead to an overestimate in the amount of stars in a galaxy. However this effect happens in concert with the other strong correlations between offset and the properties discussed above, such as stellar ages and sSFR, where the dust is often sub-dominant. The apparent discrepancy could also be related to the different attenuation curves observed for SKIRT relative to the Calzetti et al. (2000) law (as was shown in Fig. 5.6). The role of dust in the mass error is explored further in section 6.3.4.

Overall, it seems that red galaxies are typically assigned short timescale, intermediate age bursts by FAST and are assumed to have dust attenuation. Conversely, blue galaxies are assigned older but more slowly decaying histories. The typical theoretical expectation is that galaxies form earlier in massive halos, an effect termed 'cosmic downsizing'. Given that the truncated star formation histories of red galaxies imply higher halo mass for a given stellar mass, the recovered younger ages of red galaxies seem to go against expectation. The true star formation histories of red galaxies in EAGLE do exhibit shorter formation times than their blue counterparts, but tend to begin forming stars earlier than estimated by FAST, the stellar age distribution appearing peaking at ≈ 9 Gyr for both red

and blue galaxies. This is demonstrated in appendix C.4, better in line with the theoretical picture. Typical star formation histories implied by FAST are further compared to those that emerge in EAGLE in section 6.3.3.

We now explore how the EAGLE galaxy stellar mass function (GSMF) is modified if $M^{\star}_{\rm FAST}$ values are used instead of $M^{\star}_{\rm true}$, which is of particular interest. The $z = 0.1$ mass function is the primary calibrator of subgrid parameters for the EAGLE simulations (Schaye et al. 2015, Crain et al. 2015), but this calibration is between the actual masses formed in the simulations and masses estimated from observations. It is arguably more appropriate to instead compare the derived $M^{\star}_{\rm FAST}$[10] GSMF to the GSMF similarly derived for real galaxies. The $M^{\star}_{\rm true}$, $M^{\star}_{\rm FAST}$, and GAMA Baldry et al. (2012) mass functions are compared in Fig. 6.9.

As noted in Schaye et al. (2015), the $M^{\star}_{\rm true}$ mass function (blue line) is generally consistent with that of GAMA (Baldry et al. 2012, black line) with a significant underestimate (~ 0.1 dex) around the knee. In Fig. 6.9 I first compare the derived $M^{\star}_{\rm FAST}$ mass function (red solid line) to the $M^{\star}_{\rm true}$ and GAMA mass functions. At $M_{\star} \sim 10^{10}{\rm M}_{\odot}$ the $M^{\star}_{\rm FAST}$ and $M^{\star}_{\rm true}$ functions are indistinguishable, as expected from the very small offset at this mass noted in Fig. 6.8. Turning to the lower masses ($M_{\star} \lesssim 10^{10}{\rm M}_{\odot}$), the level of agreement with GAMA remains very similar for the $M^{\star}_{\rm FAST}$ and $M^{\star}_{\rm true}$ GSMF. Even though the average FAST mass underestimate grows to ~ 0.1 dex for stellar masses lower than $10^{10}{\rm M}_{\odot}$, the shallow nature of the GSMF slope below the knee means adjacent bins have similar values, such that small shifts in $M_{\star}$ make little difference to the mass function. For the massive end ($M_{\star} \gtrsim 10^{10.5}{\rm M}_{\odot}$), the $M^{\star}_{\rm FAST}$ GSMF underpredicts that of $M^{\star}_{\rm true}$ increasingly towards higher masses (up to 0.2-0.3 dex). Although FAST underestimates EAGLE masses for high mass galaxies to a similar level as the lowest mass galaxies on average (~ 0.1 dex), the steep form of the GSMF at the high mass end means that small shifts can lead to large differences in high mass galaxy number counts. The observationally derived $M^{\star}_{\rm FAST}$ GSMF exacerbates disagreement with the GAMA mass function around and above the knee region, $10^{10.5} \lesssim M_{\star} \lesssim 10^{11.5}{\rm M}_{\odot}$, as

[10]Derived from the representative SKIRT photometry of chapter 5

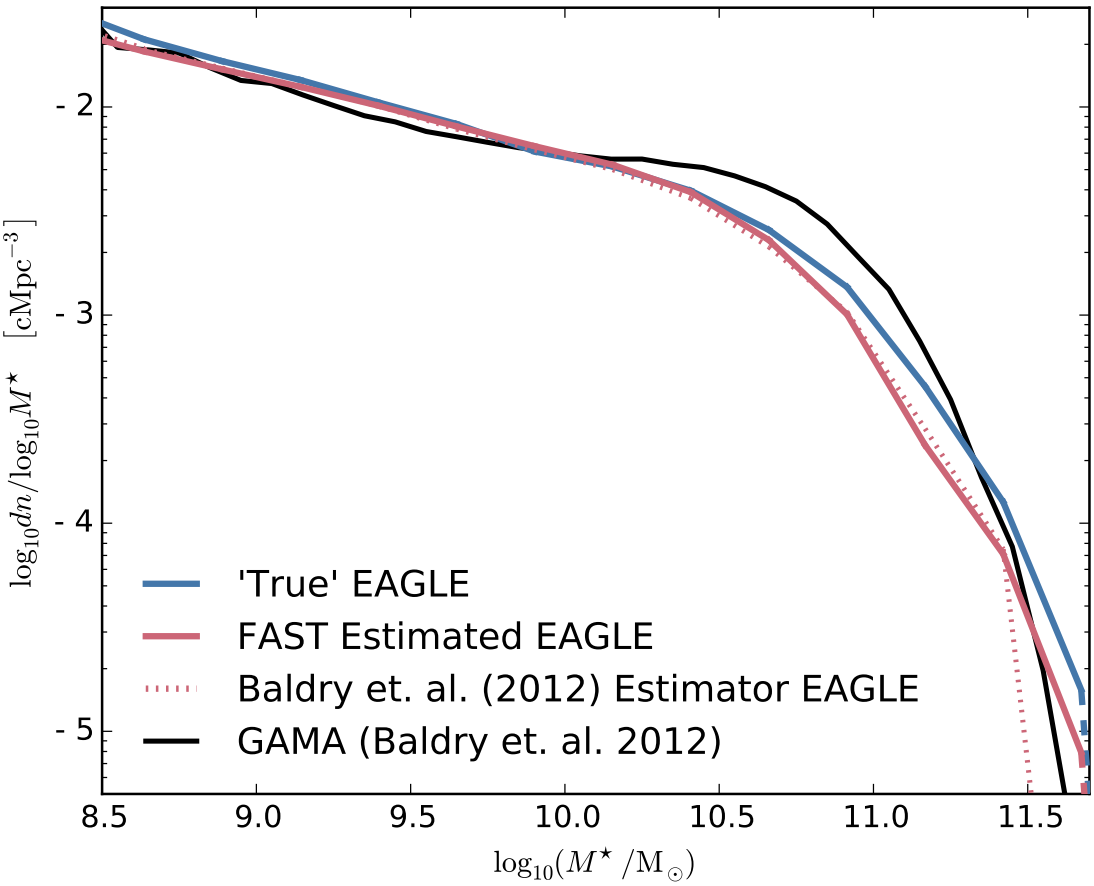

Figure 6.9: Galaxy stellar mass functions (GSMF) constructed for a variety of $M_\star$ measurements of EAGLE galaxies, and compared to the GAMA mass function of Baldry et al. (2012). *Solid blue* line shows the *'true'* EAGLE GSMF, using 30 pkpc aperture stellar masses taken directly from the simulation output ($M^\star_{\rm true}$). *Solid red* line instead uses masses derived using the fiducial FAST SED fitting model ($M^\star_{\rm FAST}$). The *dotted red* line instead uses $M^\star_{\rm col}$ (Eq. 6.2.1), using the Baldry et al. (2012) (B12) calibration. For comparison, the GAMA survey GSMF of Baldry et al. (2012) is plotted in black. We see that while the EAGLE GSMFs agree well for $M_\star \lesssim 10^{10}\mathrm{M}_\odot$, estimated stellar masses underpredict the true EAGLE GSMF at the bright end and degrade agreement with GAMA.

much as doubling the deficit in number counts. I also plot the GSMF constructed using B12 calibrated $M^{\star}_{\rm col}$ values (dotted red line). This is the best performing estimator in Fig. 6.1, and is arguably the most appropriate for EAGLE, being calibrated for integrated Petrosian photometry at $z \sim 0$. The $M^{\star}_{\rm col}$ underestimate (green points in middle panel Fig. 6.1) is similar to that of $M^{\star}_{\rm FAST}$ for massive galaxies, and as a result the two mass functions appear very similar.

The result that emulating a photometric SED fitting approach actually degrades agreement between the model and observed GSMF has been found before in the comprehensive Mitchell et al. (2013) study of photometric SED fitting for the GALFORM semi-analytic models. The degradation they find is worse for the same redshift, as analysed below. They attribute the degradation to highly attenuated, compact galaxies around the knee of the mass function. Mitchell et al. (2013) also find a ~ 0.1 dex overprediction of galaxy masses on average, but this can be ascribed to the Kroupa et al. (1993) and Salpeter (1955) IMFs assumed in the model photometry and SED fitting templates, respectively. It is known that the SKIRT photometry does not reproduce the most attenuated, highly-inclined disc galaxies that are observed at low redshift due to the pressure floor that is imposed in EAGLE yielding 'puffed-up' disc thicknesses (e.g. Fig. 5.3). Whether higher edge-on attenuations in EAGLE would provide a similar underestimated population is discussed further in section 6.3.4. The influence of such mass fitting discrepancies is just one of host of uncertainties affecting the massive end of the observational GSMF, from stellar population effects to how galaxy luminosities are determined (e.g. Bernardi et al., 2017).

An advantage that the full SED fitting results have over colour based estimators is that they simultaneously recover the full star formation history, and thus present day SFR, of a galaxy. In Fig. 6.10 I plot stellar mass functions as in Fig. 6.9, now weighted by stellar mass (top panel) and instantaneous star formation rates (bottom panel). For the *'true'* functions this is computed from the stellar masses and SFRs output by the simulation, while for FAST these are the masses and SFRs derived from SED fitting. The integral of these plots provide the cosmic density of the weighted property, and as such they are useful to visualise how differ-

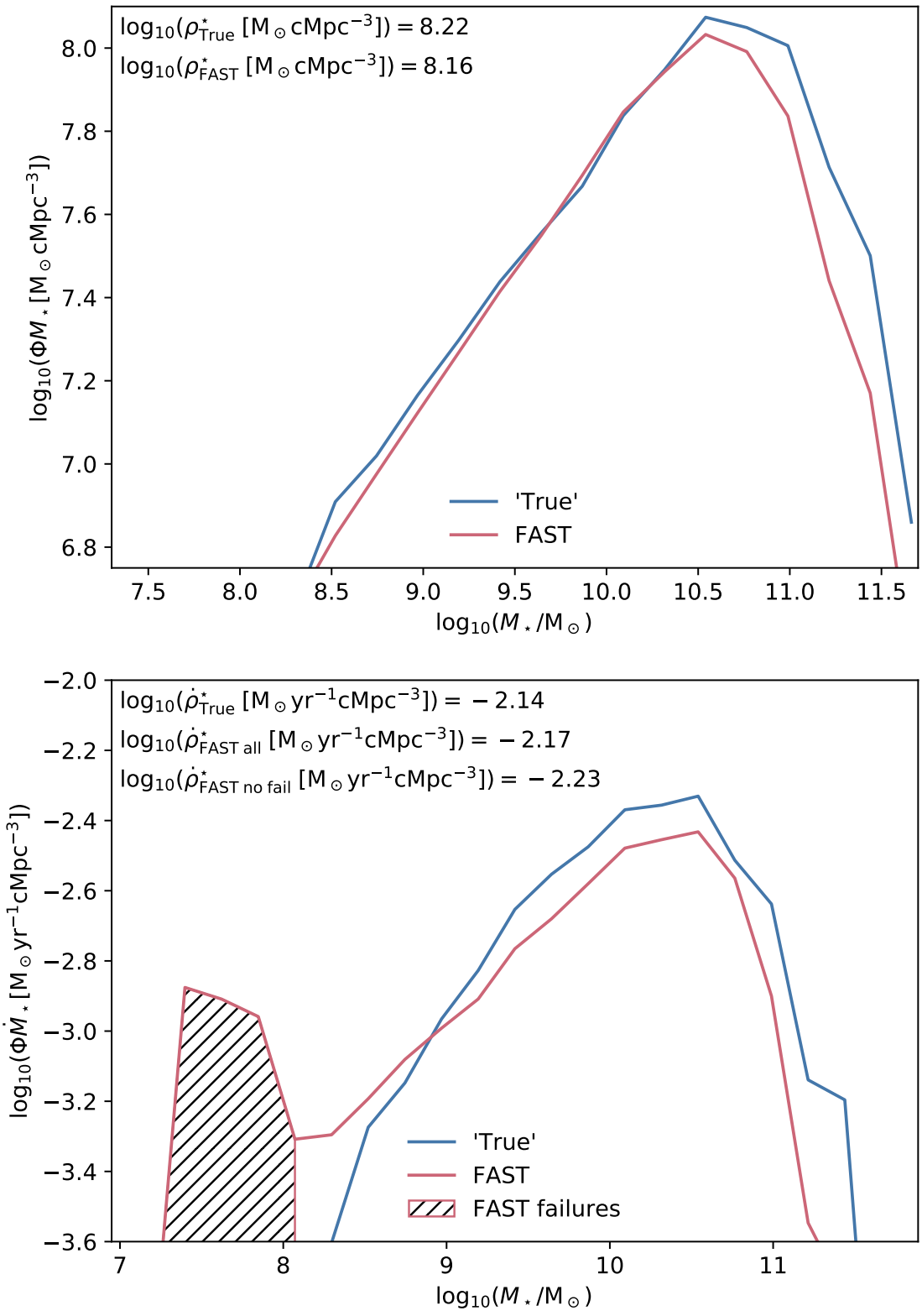

Figure 6.10: EAGLE mass functions weighted by $M_{\star}$ and SFR at $z = 0.1$, the integrals of which yield cosmic stellar and star formation rate densities, respectively (these values annotate the plot). {*Continued on the following page...*}

Figure 6.10: {*Continued from the previous page...*} Top and bottom panels are $M_\star$ and SFR weighted, respectively. *Red lines* are plotted using galaxy properties (SFR, $M_\star$) derived by fitting SEDs to SKIRT $ugriz$ photometry using FAST (Kriek et al., 2009), *Blue lines* are plotted using the galaxy properties that are directly output by the simulation. For the FAST SFR weighted plot, the heavily $M_\star$-underestimated ('*failure*') galaxies are simultaneously assigned highly overestimated SFRs, and are highlighted as a hatched region. It is apparent that the $M_\star$ weighted function is underestimated increasingly for $M^\star_{\rm true} > 10^{10.5}{\rm M}_\odot$, whereas the SFR weighted is systematically low for $M^\star_{\rm true} > 10^{9}{\rm M}_\odot$, but higher at the lowest masses.

ent mass ranges contribute to differences in the cosmic density of stellar mass ($\rho_\star$) and star formation rate ($\dot{\rho}_\star$) calculated using the true and FAST recovered properties. It can be seen that the $M^\star$ weighted functions agree very well until $M^\star_{\rm true} \sim 10^{10.5}{\rm M}_\odot$ where the FAST values are progressively underestimated, while the SFR weighted FAST function is systematically low for $M^\star_{\rm true} > 10^{9}{\rm M}_\odot$ but higher at the lowest mass. This low mass boost can be attributed to the small population of failure galaxies that persist in the fiducial fitting model being assigned erroneously high SFRs, and those can be removed from the integral. The calculated ρ values are inset in each plot, and were first calculated using the true properties in Furlong et al. (2015). When calculating these, I add a correction factor to account for the fraction of the total EAGLE stellar mass found outside of the 30 pkpc apertures or within galaxies of $M^\star_{\rm true} < 1.2 \times 10^{8}{\rm M}_\odot$ at $z = 0.1$, ie. the fraction of the EAGLE cosmic stellar mass missed in my simulated galaxy sample, which is only ~ 0.06 dex. We see that the cosmic mass density is 0.06 dex underpredicted using FAST, which again increases the discrepancy from the very good agreement found by Furlong et al. (2015). The star formation rates have a similar underestimate when the whole population is considered (~ 0.07 dex), but neglecting the small percentage of failure galaxies that persist in the fiducial model increases the underestimate to ~ 0.09 dex.

For completeness, I show the SFR-$M_\star$ plot for star-forming galaxies in Fig. 6.11,

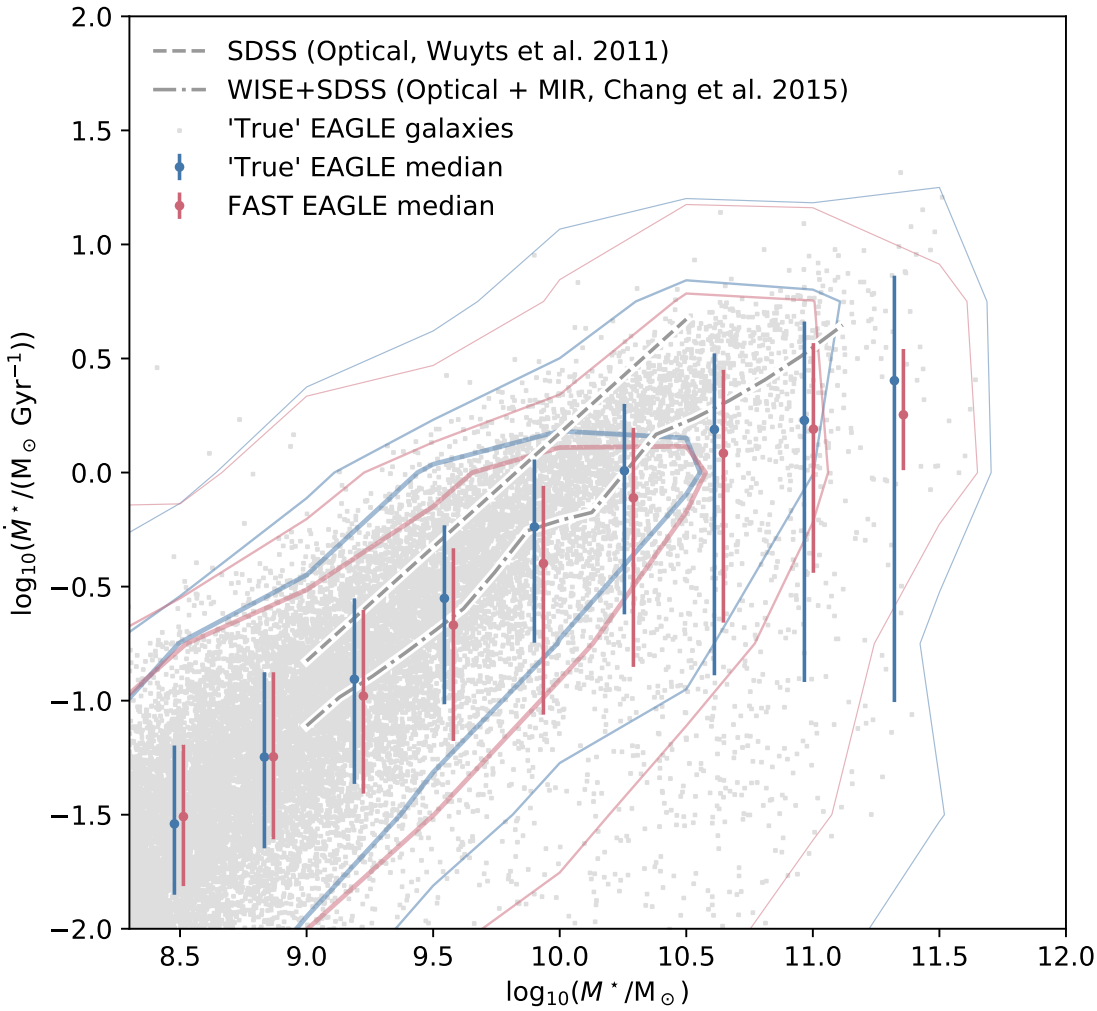

Figure 6.11: The SFR-$M_\star$ relation for EAGLE galaxies at $z = 0.1$, visualising the *'main sequence'* (MS) of star forming galaxies. *Red* and *blue colour* elements are indicative of FAST recovered and simulation output galaxy properties respectively. *Points with error bars* indicate the median SFR of galaxies in bins of $M_\star$, not including passive galaxies (SFR$< 10^{-4}\mathrm{M}_\odot\ \mathrm{yr}^{-1}$), with errors showing the 16-84 percentile range. *Contours* are plotted to show the underlying distribution, enclosing bins of 10, $10^{2.2}$ and $10^{2.8}$ galaxies or more. Light grey points also indicate the *'true'* values for individual galaxies. For comparison, the linear MS fit of Wuyts et al. (2011) is shown as a *grey dashed* line, and the median MS values of Chang et al. (2015) are plotted as *grey dot-dashed* lines. The FAST and true value plots appear to agree well within the scatter, although the median MS SFRs estimated by FAST appear low at a given mass.

revealing a *'main sequence'* (MS) of star forming galaxies (SFR$< 10^{-4}\mathrm{M}_{\odot}\ \mathrm{yr}^{-1}$). The median SFR value of the MS calculated by FAST (red points) appear to agree well with the true values at low masses, but deviate by up to $0.1 - 0.2$ dex at $M^{\star}_{\mathrm{true}} \sim 10^{10}\mathrm{M}_{\odot}$, incidentally where mass estimates are most accurate (Fig. 6.8). Any deviations are small compared to the scatter. The MS scatter is similar for $M^{\star}_{\mathrm{true}} < 10^{10.25}\mathrm{M}_{\odot}$ but appears larger for true EAGLE SFRs at the high-mass end, which scatters to lower values than inferred by FAST. This is likely related to low sSFRs being poorly constrained by optical photometry, and therefore not recovered by the fitting. Furlong et al. (2015) found that EAGLE MS star formation rates were $\sim 0.2 - 0.4$ dex lower than the observed normalisation, as represented by the Wuyts et al. (2011) linear MS fit plotted over the applicable range ($M^{\star}_{\mathrm{true}} \lesssim 10^{10.5}\mathrm{M}_{\odot}$). As discussed in chapter 5, the study of Chang et al. (2015) found a lower MS normalisation by including MIR WISE bands in their fitting, also plotted in Fig. 6.11. This is in better agreement with both the FAST and true EAGLE MS (within $0.1 - 0.2$ dex over the same range). Whether the Chang et al. (2015) result is an anomaly in the literature remains inconclusive.

Overall, I find similar underestimates in both $M_{\star}$ and SFR values using FAST. As a result, the ratio between the FAST-recovered $z \approx 0.1$ cosmic star formation rate density ($\dot{\rho}_{\star}$) and cosmic stellar density ($\rho_{\star}$) is the same as is found using the simulated values. This then maintains an apparent tension between simulations and observation; that the $\dot{\rho}_{\star}$ values are ~ 0.2 dex lower than observed while $\rho_{\star}$ is < 0.1 dex lower than observed, possibly indicative of inconsistencies between stellar mass and SFR measurements (Furlong et al., 2015). The star formation histories and $M_{\star}$ values of EAGLE galaxies are of course self consistent by construction, for both sets of data measured from the simulation and sets inferred from the templates fit by FAST. However, it is not common practice to use photometric optical SED fitting to obtain SFRs; observers commonly turn to more direct tracers of recent star formation such as UV continuum, emission line and FIR measurements to estimate global star formation rates (Walcher et al., 2011). Therefore, the evolution of the total star formation rate and stellar mass formed are not necessarily self consistent for observations (e.g. Salim et al., 2007). Emu-

lating observational techniques that are used to obtain masses and star formation rates at differing epochs with mock EAGLE observers could provide further insight into this apparent tension, and is planned for future work. In order to illustrate to what extent FAST star formation rate histories agree with those obtained by FAST, I now turn to comparing the histories.

6.3.3 Recovered histories at $z = 0.1$

To gain further insight into the FAST SED fitting results, I now investigate the star formation histories implied by the best fit FAST SEDs[11]. While FAST $M_\star$ and SFR estimates are found to recover their simulated values to a reasonable level, this does not ensure that these idealised histories are a good representation of those in EAGLE. In Fig. 6.12 the cosmic star formation history (*'Madau'*) plot is shown, and compared to observational data. This figure is very similar to that of Furlong et al. (2015), with the same comparison data sets and symbol choices, but plotted linearly in cosmic time. As in Furlong et al. (2015), the simulated EAGLE $\dot{\rho}_\star$ evolution and a 0.2 dex boosted curve show that EAGLE uniformly underestimates the cosmic SFRD inferred from the data at different epochs.

The composite $\dot{\rho}_\star$ evolution inferred using FAST (red line) is averaged in coarse ~ 500 Myr bins to mitigate the artificial effects of coherence in the best-fit FAST histories. This coherence is caused by the fact that the ages and star formation timescales of EAGLE galaxies are discretised in logarithmically spaced bins, which leads to sharp peak features in the instantaneous $\dot{\rho}_\star$ corresponding to the aligned star formation peaks of a large number of galaxies. The FAST curve is quite different to both that of the actual EAGLE evolution, and the observationally derived $\dot{\rho}_\star$ evolution. The FAST Madau plot predicts much younger stellar ages on average, peaking at ~ 7 Gyr ($z \sim 0.6$) instead of the ~ 3 Gyr ($z \sim 2$) peak found in both the true EAGLE data inferred by multiple observational data sets. While the contemporary $z = 0.1$ FAST star formation rates agree with the true EAGLE by better than

[11] A slight modification is made to the FAST code to output the total initial stellar mass to scale histories by, instead of the final mass which includes stellar mass loss.

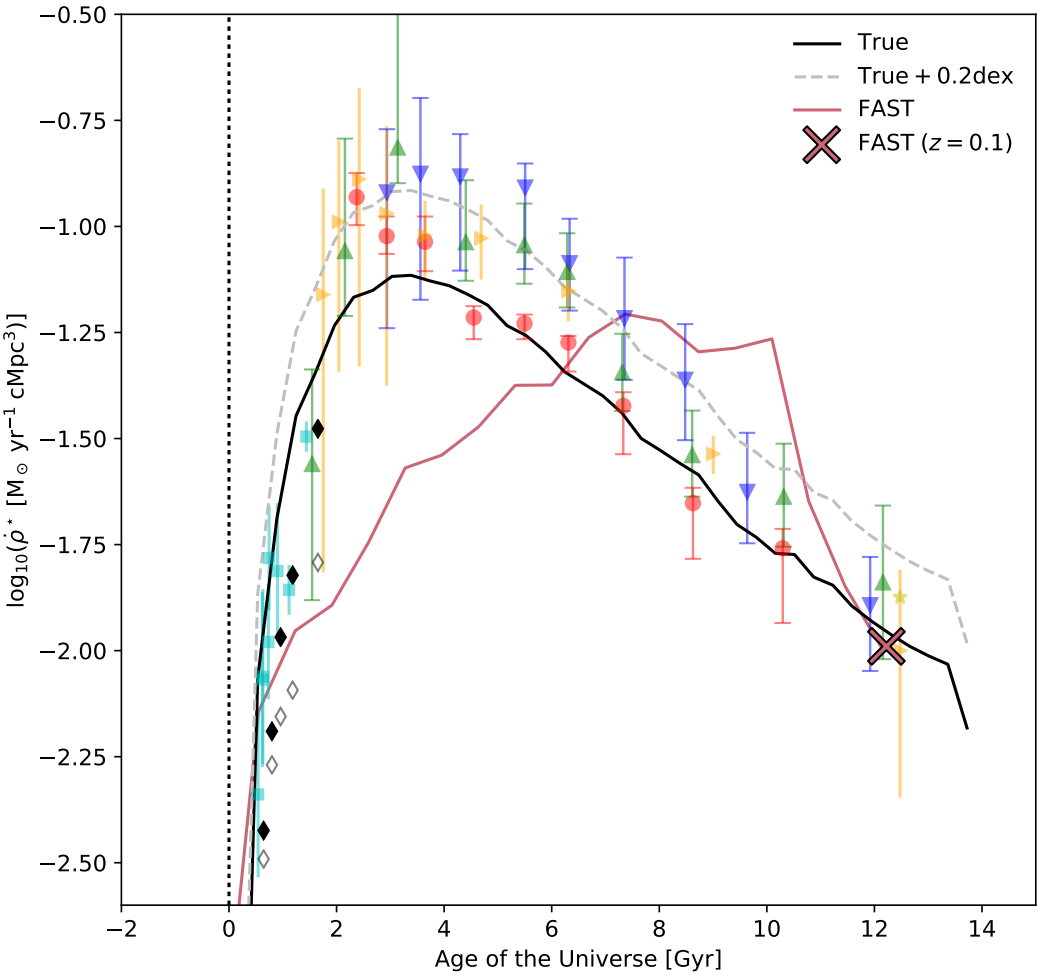

Figure 6.12: The evolution of $\dot{\rho}_{\star}$ with cosmic time, or *'Madau'* plot, for true and FAST derived EAGLE values and observational data. *Black line* shows the true EAGLE $\dot{\rho}_{\star}$ evolution, derived for a random subset of the EAGLE star particles. Observational data are plotted as in Furlong et al. (2015), using the same symbol choices. In addition, the *red line* $\dot{\rho}_{\star}$ derived by summing the histories fit by FAST to EAGLE galaxies with $M^{\star}_{\rm true} > 1.2 \times 10^{8} \mathrm{M}_{\odot}$ at $z = 0.1$. To mitigate the coherent histories in FAST introducing artificial features in this plot, the history is plotted in broad ~ 500 Myr averaged bins (see text). As for the Fig. 6.10 integrals, I add a correction factor of 0.06 dex to account for the fraction of the total EAGLE stellar mass found outside of 30 pkpc apertures and within $M^{\star}_{\rm true} < 1.2 \times 10^{8} \mathrm{M}_{\odot}$ galaxies at this redshift (see text for details). The 30 Myr averaged star formation rates at $z = 0.1$ are also plotted with the *red cross marker*. We see that the $\dot{\rho}_{\star}$ evolution inferred using FAST is quite different from the true evolution as well as the data, peaking at ~ 7 Gyr ($z \sim 0.6$) as opposed to ~ 3 Gyr ($z \sim 2$).

0.1 dex, the discrepancy grows rapidly with look-back time, such that the star formation rates 2 Gyr prior to the $z = 0.1$ snapshot are over predicted by ~ 0.5 dex. In short, photometric $ugriz$ SED fitting does a poor job of predicting the true stellar mass build up in EAGLE galaxies. UV-NIR photometry of observed galaxies were used by Walcher et al. (2008) to compare the stellar mass build up inferred using best-fit SFHs to those using instantaneously measured star formation rates, in order to compare the derived GSMF evolution at higher redshift. This fitting is more sophisticated than is presented in this study, and includes detailed priors on galaxy parameters, but there are still difficulties reconciling fitted star formation histories with instantaneously measured masses at higher z (Walcher et al. 2008[12]), as well as discrepancies between SFRs measured from emission lines and SED fitting in some galaxies (Salim et al., 2007).

It is interesting to investigate how this discrepancy in the global star formation histories comes about for the FAST fitting, by examining how well histories are recovered for differing EAGLE galaxies. In Fig 6.13, the real star formation histories of EAGLE galaxies with $M^{\star}_{\rm true} > 10^{9}{\rm M}_{\odot}$ galaxies are calculated and re-binned in stretched and scaled time units, such that the best-fit history is represented by the black line. The idea of this is to represent the *'typical'* (or perhaps expected) star formation histories of EAGLE galaxies, in a way that can be compared to the fitting form. Given the knowledge that FAST yields different mass offsets for different EAGLE galaxies, separating galaxies into offset bins reveals mismatches and trends in the histories that may drive the incorrect mass recovery. In general, it is clear that the expected EAGLE histories are more dispersed than the FAST histories; in each case star formation begins before the fitting history assumes it does, and a low-level residual probability of star formation continues after FAST star formation rates essentially decay to zero. Part of this dispersion may be driven by the fact that fitting ages and timescales are discrete in nature, i.e. represent 'nearest' values, and may be reduced if histories were allowed to be continuous. However, it seems plausible that this is predominately a real effect, due to a more

[12]Discrepancy between instantaneous galaxy SFRs and those inferred from histories of succeeding populations is taken to be indicative of the role of mergers

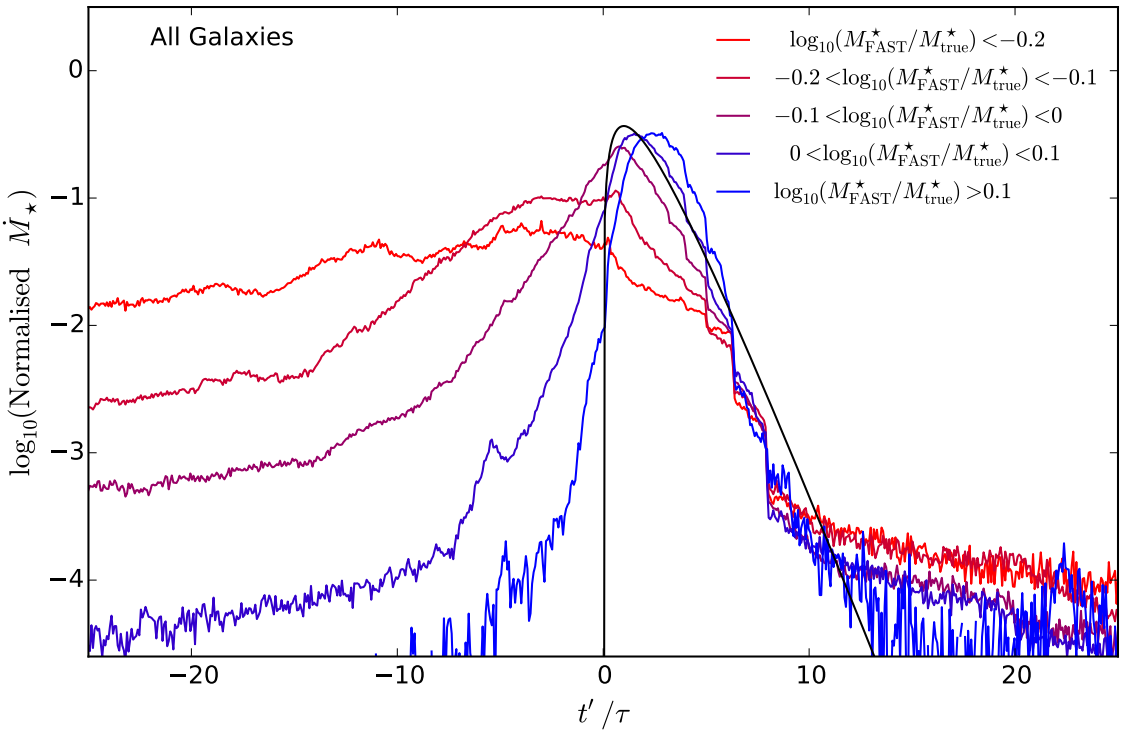

Figure 6.13: Comparison between the real form of EAGLE star formation histories (normalised to unit integral) and their fitted form in bins of logarithmic offset of the $M^\star_{\rm FAST}$ values from the $M^\star_{\rm true}$. Galaxy histories are binned for each galaxy individually in time units shifted and stretched by the best fitting age and timescale values ($t'/\tau = (t_{\rm age} - t_{\rm lookback})/\tau$). In these units, the best fit delayed exponential history ($\dot{M}_\star \propto t' \exp(-t'/\tau)$ for $t' \geq 0$) is always represented by the *solid black* line. Galaxy histories are binned by their FAST mass offset, as indicated by the legend, and summed together to yield composite histories that can be compared to the fitted form. In general EAGLE histories are more dispersed in time, and more underpredicted galaxies (redder curves) consistently show more star formation prior to when the FAST galaxies estimate SF to commence, at $t' = 0$.

gradual initial build-up of star formation, and the possibility of star formation events at late times. The star formation probability of EAGLE galaxies appear to drop more rapidly than FAST assumes in the range $7 \lessapprox t'/\tau \lessapprox 10$, but is overtaken and remains higher than assumed for $t'/\tau \gtrapprox 10$. Comparing the function representing different bins in offset, a clear trend can be seen in star formation prior to $t' = 0$; more underestimated galaxies have more of their stellar mass formed before the fitted history assumes it to start. This can be considered an example of *'outshining'* (Gallazzi & Bell, 2009; Maraston et al., 2010; Pforr et al., 2012; Sorba & Sawicki, 2015); residual star formation at late times that can dominate the optical SEDs and the inability of the delayed exponential to represent the non-idealised EAGLE histories, may lead to a considerable fraction of the mass in old stars being missed at early times. The star formation probability in galaxies that have their masses overestimated appears to peak at a later time than FAST assumes them to. The older stellar populations assumed by FAST would generally need more mass for the same brightness, hence the underestimation.

Given the correlation between colour and offset found in Fig. 6.8, and the very different properties of red and blue galaxies in general, in Fig 6.14 I remake Fig. 6.13 for red and blue galaxies separately. For blue galaxies (top panel), the histories show very similar behaviour to that of Fig. 6.13, if slightly less dispersed and with a more steady, exponential increase in star formation for $t' < 0$. The star formation histories for $t' > 0$ are fit reasonably well by the delayed exponential, but the EAGLE SFRs appear to decay over a shorter period. The overpredicted stellar mass contribution at $t' > 0$ somewhat mitigates the underpredicted stellar mass contribution at $t' < 0$.

For red galaxies, however, the histories look very different. Red galaxies show a much more significant offset in when the star formation rate probability peaks from the assumed history, with underestimated galaxies (the majority of red galaxies), showing peaks occurring ~ 10 timescales before the FAST history assumes it to. Red composite galaxy histories also seem generally much more dispersed than the short bursts that are fit by FAST. Note that this does not reflect the true red EAGLE galaxy histories being particularly broad relative to the gen-

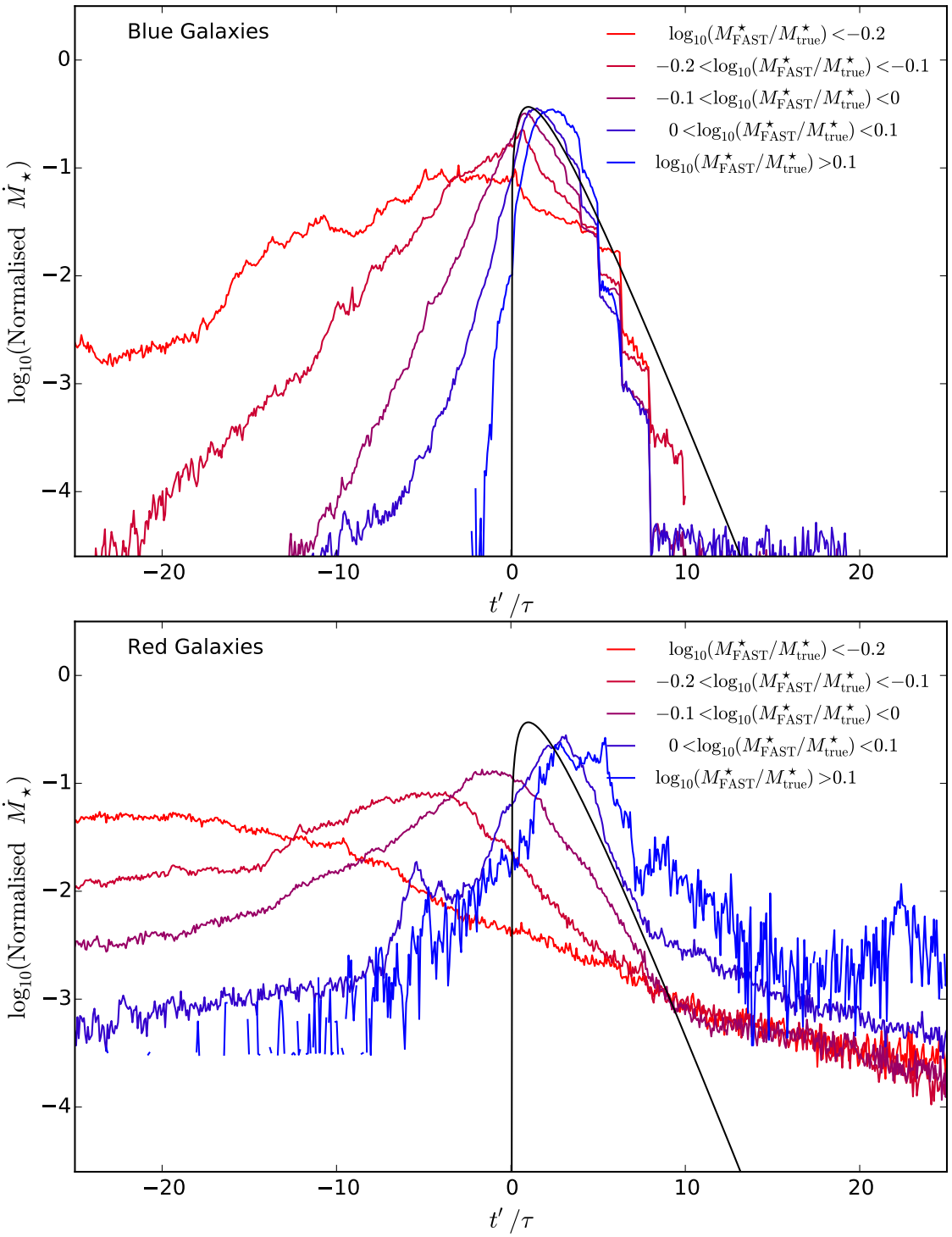

Figure 6.14: As Fig. 6.13, but with galaxies now split into red and blue populations (at $z = 0.1$) using the intrinsic $u - g$ vs. $M^\star_{\rm true}$ cut of Eq. 4.3.1. We see that the red and blue galaxies in the same offset bins relate differently to the FAST best-fit star formation history.

eral population: as shown in appendix plot Fig. C.4, they in fact form the majority of their mass over shorter periods than blue galaxies on average. This dispersion may instead be attributed to the τ values recovered by FAST for red galaxies being even shorter than those that emerge in EAGLE (recovering $\tau \sim 100$ Myr in Fig. 6.8), combined with uncertainty in $t_{\rm age}$ caused by age-metallicity degeneracy, and discretisation of possible ages fit by FAST[13].

Overall, the vast underprediction of star formation rates at the true peak ($z \sim 2$) by FAST can be ascribed to more slowly rising histories contributing more old stars in the overall galaxy population, and that red galaxies form much earlier than predicted by the best-fit histories. A potential cure for this problem would be to build a more gradual onset of star formation into the fitting histories and, as discussed before, allow composite metallicity SEDs that give a better fit to the ages of red galaxies with extended internal stellar metallicity distributions. Although it is informative to compare histories in this way, it does not tell us about the role of dust; a novel element to this study of SED fitting with a large volume cosmological simulation. In the next section the influence of dust on recovered masses is explored.

6.3.4 Influence of dust on SED fits

Another key uncertainty in fitting SEDs is the effects of dust. As was shown in section 6.3.1, dust is an important source of degeneracy, which can lead to catastrophic errors in the broad band optical fitting. With the SKIRT photometric model for EAGLE galaxies developed in chapter 5, the effect of assuming a much simpler single-screen dust prescription can be tested.

In Fig. 6.15 the logarithmic FAST mass offset is plotted as a function of the SKIRT g-band ISM dust attenuation, A_g, for EAGLE galaxies. A clear median trend is observed here: unattenuated galaxies typically show systematic underestimates of ~ 0.15 dex. The accuracy of the FAST mass estimation improves with A_g, peaking at $A_g \approx 0.4$. The underestimate then begins to increase again, such

[13]There is typically ~ 300 Myr between $t_{\rm age}$ grid points at the recovered red galaxy ages.

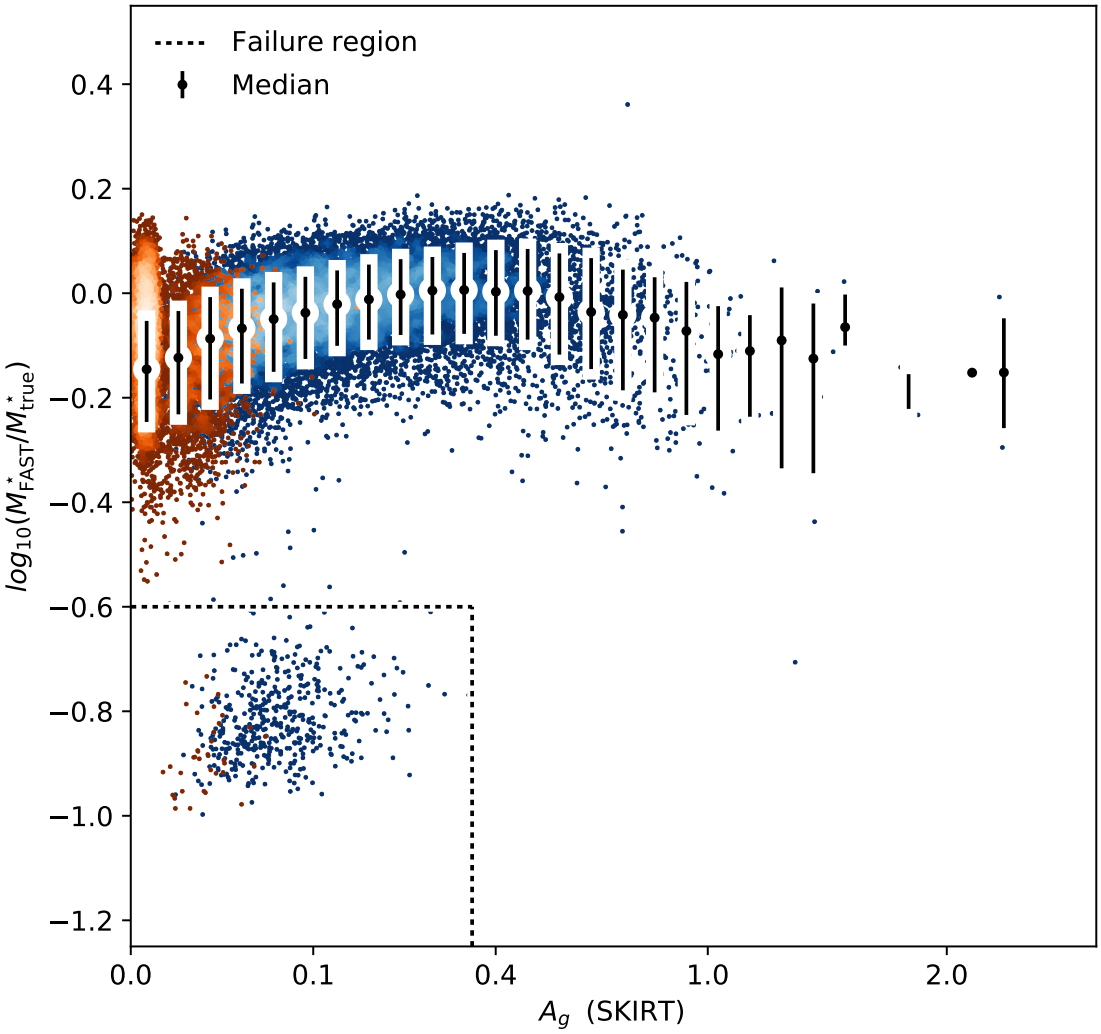

Figure 6.15: The logarithmic mass offset of $M^\star_{\rm FAST}$ from $M^\star_{\rm true}$ as a function of the *'true'* g-band ISM dust attenuation arising in the SKIRT model photometry, A_g. *Shaded points* show individual EAGLE galaxies for redshifts $z \lessapprox 0.2$, shaded from dark to light by point density. *Orange shading* indicates intrinsically red galaxies (via the Eq. 4.3.1 definition), whereas *blue shading* indicates bluer intrinsic colours. the median values in A_g bins are shown using *black points*, with error-bars indicating the 14-86 percentiles. *Dotted lines* are used to roughly demarcate the region where the 'failure' population (Fig. 6.6) resides. A clear median dependence is found with ~ 0.2 dex scatter; the accuracy of the FAST mass estimate peaks at $A_g \sim 0.4$, decreasing towards both lower and higher levels of attenuation.

that by $A_g \approx 1$ galaxies are again underestimated by ~ 0.15 dex. The numbers of galaxies with higher attenuations in EAGLE is low at $z = 0.1$, so it is hard to constrain whether this trend would continue from this plot. From initial examination of the SKIRT photometry generated at different epochs, this trend appears to be largely redshift independent. The Fig. 6.15 plot for all EAGLE galaxies with $z \lessapprox 2$ can be found in appendix C.3 (Fig. C.3), probing A_g to higher values and improving number counts at high values. This reveals that the mass discrepancy continues increasing to higher A_g, along with the overall mass offset scatter.

The result that accuracy actually improves with A_g for low attenuation values is related to the perhaps counter-intuitive finding that the fitted attenuation in less underestimated or even overestimated mass galaxies is lower than the true attenuation, as seen in the bottom row of Fig. 6.8. This effect can be attributed to the more selective attenuation and redder attenuation curves found for the SKIRT modelling, relative to screen models such as the Calzetti et al. (2000) attenuation law assumed by FAST. As discussed at length in chapter 5, selective absorption due to geometry, particularly in relatively face-on or lower inclination galaxies, can effectively hide young stars and make galaxies appear redder and more passive in colour-colour space. By assuming a single Calzetti et al. (2000) screen model, FAST cannot reconcile this selective absorption, and instead finds the galaxies to be less star forming and hence more massive than they really are. This is also evidenced by the reduced SFRs recovered with FAST. Overall, in the low attenuation ($A_g \lessapprox 0.4$) regime that dominates at $z = 0.1$, selective dust effects counteract those of *'outshining'* in integrated photometry by reducing the dominance of young stars in the integrated SED.

In the higher attenuation regime ($A_g \gtrapprox 0.4$) the increasing accuracy with A_g trend is reversed. As was shown in Fig. 5.6, more edge-on galaxies, which represent the highest attenuations (Fig. 5.3), have integrated attenuation profiles that are significantly greyer and hence are closer to the Calzetti et al. (2000) law assumed by FAST. This may explain why these galaxy underestimates are closer to the unattenuated galaxies on average. The continuation of this trend at higher attenuations is seen in the appendix plot Fig. C.3, suggesting that the attenua-

tion profile may become greyer still as attenuation increases, leading to much larger mass underestimates. Individual sight-lines through dust lanes demonstrate higher attenuation than the overall integrated values, and have their masses strongly underestimated in the resolved mass maps of Fig. 6.5. This could again be down to behaviour not captured by single screen models, and the break down of the screen approximation for the optically thick regime. To test this hypothesis, further investigation of the attenuation properties of high-redshift EAGLE galaxies is needed.

In the dust-inclusive (via a Calzetti et al. 2000 screen) SED fitting of Mitchell et al. (2013), a significant population of galaxies with underestimated masses are found at $z = 0$, and these are found to correspond to highly attenuated, particularly compact discs. Such a population of galaxies is not found for EAGLE. This appears to be due to the fact that with the SKIRT dust modelling, and in the low attenuation regime that dominates at low redshift, dust improves the fit. The idealised dust disc model used in GALFORM reaches higher observed attenuations that the 'puffed-up' geometries of EAGLE galaxies do not allow. If the EAGLE galaxies were thinner, perhaps a significant population of highly inclined EAGLE galaxies would appear with large mass underestimates, following the higher attenuation trend of Fig. 6.15.

The effect of geometry on attenuation profile and mass recovery was also investigated in the detailed study of Wuyts et al. (2009a), which utilises idealised hydrodynamical simulations of major mergers at higher redshift ($z \sim 2$). This is achieved through a more sophisticated analytic model than a single screen that accounts for geometry; each star particle uses enriched gas to compute the dust column computed towards an observer. This dust column is used to scale a foreground Calzetti et al. (2000) screen. Intriguingly, Wuyts et al. (2009a) find *greyer* than Calzetti et al. (2000) integrated attenuation profiles. This may also be true of EAGLE in the high attenuation regime and at similarly high redshifts, pending investigation as discussed above. However it could also come about in Wuyts et al. (2009a) from the initially uncorrelated nature of stars and dust. Mixing stars that see extincting screens of different strength yields an attenuation curve greyer

than that of the extincting screen, which is effectively built in to the Calzetti et al. (2000) attenuation profile itself to model starburst galaxies (e.g. Fischera et al., 2003). The geometric effect of mixing stars and dust is therefore arguably 'double-counted' in the modelling to some extent if the Calzetti et al. (2000) screen is used. Wuyts et al. (2009a) begin to recover the effect of preferential reddening of young stars as the simulations evolve and star particles form in enriched gas. They find that this indeed makes their integrated attenuation curves steeper, approaching Calzetti et al. (2000), and this improves mass recovery. It could be argued that attenuation profiles of EAGLE galaxies should be greyer than they are to account for small scale fluctuations in column density that cannot be resolved at EAGLE resolution, as currently dust and stellar distributions are treated as perfectly smooth below the resolution scale with the exception of birth clouds in the MAPPINGS-III SEDs. Investigating this effect is left to future work.

6.4 Summary and Conclusions

I have examined the recovery of galaxy properties from optical photometry of EAGLE galaxies, with a focus on galaxy stellar mass. I compare empirical $M^\star/L$ ratios using different calibrations of Eq. 6.2.1 by assessing how well they recover the true stellar masses of EAGLE galaxies from different sets of integrated EAGLE photometry[14] (Fig. 6.1). The effects of resolution on the accuracy of the mass estimates are constrained without dust for an idealised comparison of integrated photometry and completely separable SSPs. Such a comparison allows the contribution of SSP properties to integrated and resolved mass offsets to be directly characterised. Full SKIRT images of 3 archetypal galaxies are then used to explore the influence of SSP alignment and dust on recovered masses at differing resolutions.

Some of the key findings when investigating the colour-dependent $M^\star/L$ estimators are:

[14]The ND prescription of chapter 3 and the full SKIRT model of chapter 5 are used.

- Eq. 6.2.1 $M^\star/L$ estimators are shown in Fig. 6.1 to yield a remarkably mass independent and convergent (Fig. C.1 in appendix) underestimate of $\sim 0.1-0.2$ dex on average. The Baldry et al. (2012) (B12) calibration is arguably the most appropriate for integrated EAGLE photometry, and indeed proves the most accurate (~ 0.1 dex underestimated).

- Comparing idealised resolved and integrated photometric mass estimates in Fig. 6.2 suggests that EAGLE mass underestimates are driven by star formation in blue galaxies and the internal distribution of SSP $Z^\star$ values in red galaxies when dust is neglected. While *outshining* (Gallazzi & Bell, 2009; Maraston et al., 2010; Pforr et al., 2012; Sorba & Sawicki, 2015) due to young stellar populations can be mitigated by improving resolution, the effects of the underlying metallicity distribution prove impervious to the benefits of resolution.

- The accuracy of the Zibetti et al. (2009) (Z09) mass estimator applied to realistic dust-inclusive SKIRT images is revealed to vary for 3 archetypal EAGLE galaxies (of type S, Irr and E) at differing resolutions and viewing angles (Fig. 6.4). The accuracy of the estimator is found to generally improve with resolution above the intrinsic EAGLE resolution of ~ 500 pc. While differences between the CB07 stellar population model assumed by Z09 and the BC03 model assumed by EAGLE may account for the typical offsets at EAGLE resolution, the highly attenuated edge-on S type cannot be reconciled by this effect and is underestimated by ~ 0.3 dex even when resolved. Dust lanes are seen to contribute large mass underestimates in the Z09 estimated mass maps (Fig. 6.5).

- The difference between resolved and unresolved mass estimates in Fig. 6.4 is reproduced well using the sSFR-dependent relation of Sorba & Sawicki (2015) for the E and Irr type (0 and ~ 0.03 respectively), but this still underestimates the difference found for the S type galaxy (~ 0.1 dex).

Building on the insights attainable from simple empirical estimators of mass, I employ the FAST code (Kriek et al., 2009) to perform full SED fitting on integrated

$ugriz$ SKIRT photometry at $z = 0.1$. Initial testing shows that adopting a similar FAST set-up to Torrey et al. (2014) leads to a small population of galaxies with catastrophically underestimated masses (termed *failures*) when dust is included in the fitting. This is mitigated by employing a higher minimum age of $10^{8.5}$ yr for $z = 0.1$ galaxies, limiting failures to $\lesssim 1\%$ of the population, in the fiducial FAST set-up. The offsets in fiducial FAST-predicted masses from their true values are characterised, and residual trends between offset and galaxy properties are explored. I compare the simulated and FAST-derived forms of theoretical plots to assess the systematic effects of SED fitting and modelling photometry in EAGLE. Finally, I explore how FAST mass offsets are influenced by fitting complex EAGLE star formation histories and SKIRT dust attenuation with simpler parametric models.

Key results from investigating the optical photometric SED fitting with FAST include:

- The *failure* population arises due to the similarity between the rest-frame $ugriz$ photometry of regular SF galaxies and extremely young, vigorous and dusty starbursts (Fig. 6.7).

- The fitting of blue galaxies can be highly temperamental in the reduced χ^2 approach of FAST, which could be mitigated by instead integrating over a posterior distribution of fitting probabilities, as advocated by e.g. Taylor et al. (2011).

- The FAST recovered mass estimates are generally superior to those obtained from Eq. 6.2.1 $M^\star/L$ estimators of Fig. 6.1, with an average underestimate of ~ 0.07 dex (marginally better than the B12 estimator).

- The SED fitting leads to an underestimate in high mass number counts for the GSMF. This may contribute to the bright-end systematic error alongside uncertainties associated with SPS models and galaxy definition (e.g. Bernardi et al. 2017), and bias due to random errors (demonstrated for EAGLE by Furlong et al. 2015).

- The 'main-sequence' in the SFR-$M^\star$ relation recovered by FAST is very similar to the true EAGLE relation; both stellar mass and SFR are underestimated to a similar degree by FAST, and the main sequence is close to linear

- Red galaxy masses are typically underestimated with FAST (top right panel, Fig. 6.8). This appears to be related to a systematic underestimate in their ages. The fitting bias is attributed to skewed internal metallicity distributions that yield bluer red sequence colours than observed, and composite metallicity templates are suggested as a possible solution.

- Masses of blue galaxies tend to be more accurate or even overestimated, despite having underestimated ~ 500 nm attenuations (Fig. 6.8). This is ascribed to the assumed Calzetti et al. (2000) law having a 'greyer' attenuation profile than exhibited by the SKIRT modelling of EAGLE for galaxies at the typically low effective attenuations found in the $z = 0.1$ sample (section 6.3.4). Fig. 6.15 shows that for higher than typical attenuations ($A_g \gtrapprox 0.4$) galaxy masses again become more underestimated, consistent with what is seen for the edge-on S type of Fig. 6.4.

- The star formation histories inferred by FAST are highly discrepant with those of EAGLE galaxies (section 6.3.3); more so than the quality of mass and SFR estimates might suggest. The FAST cosmic star formation history plot of Fig. 6.12 peaks at $z \sim 0.6$ rather than the $z \sim 2$ peak found for the true EAGLE histories. This difference can be ascribed to SED fitting underestimating the ages of red galaxies (mentioned above), and missing the gradual initial mass build up in the general galaxy population (Fig. 6.14). In addition to composite metallicity templates, parametric histories with a slower build up in their early stellar mass are offered as a solution.

Overall, it is reassuring to see how well SED fitting with very simple assumptions can recover stellar masses of the EAGLE $z = 0.1$ galaxy population on average, despite the relative complexity of the simulated galaxy star formation histories. Still, the EAGLE analysis does suggest a number of potential systematic effects and trends that may also appear in the data. It is already known that

a plethora of degeneracies make it difficult to constrain star formation histories photometrically (e.g. Maraston et al., 2010; Mitchell et al., 2013). Where more data is available, UV-FIR broad-band or spectral fitting have been found to break degeneracies between effects of dust, star formation rate and metallicities, yielding improved parameter recovery (e.g. Hayward & Smith, 2015). Panchromatic SED fitting is something that could be explored using the SKIRT model for EAGLE in a future work; appealing to FIR properties of galaxies that we detail in Camps et al. (2016).

Having tested this analysis at low redshift ($z = 0.1$) where data is generally better constrained, these insights can be carried over to study EAGLE galaxies at higher redshifts, particularly around the cosmic noon, $z \sim 1.5 - 3$. Here, more extreme properties of galaxies (e.g. in terms of SFR, dust attenuation) and higher uncertainties in the observations and modelling may manifest larger systematics in the recovered properties of galaxies (e.g. Wuyts et al., 2009a,b; Maraston et al., 2010). It is also important to note that SFRs are not typically derived simultaneously with stellar masses, as they are here; it is more common to appeal to a variety of observable SFR indicators that give a more direct measure of star formation. Another potential EAGLE investigation could look at deriving these indicators for their appropriate epochs, and investigating how this may affect the shape and normalisation of the derived evolution of the cosmic star formation rate. Planned improvements in the simulations (e.g. higher resolutions and more realistic ISM properties) and in observational data sets are poised to further strengthen the relationship between observation and theory, opening many exciting new avenues of study.

Chapter 7

Conclusions

In this chapter conclusions are drawn about the results found in this thesis, the potential limitations of the adopted approach and the future studies that may be accessible by building upon this work. I first summarise my findings in section 7.1. Section 7.2 then critically assesses the forward modelling approach I have adopted and suggests potential future improvements. Finally, potential future studies are outlined and discussed in section 7.3

7.1 Summary of findings

In this thesis I have applied a forward modelling approach to the simulated galaxies of the EAGLE suite of cosmological simulations, in order to produce mock observables that may be compared more directly to data. Through this comparison I have examined how well the simulations reproduce the data, and attempted to understand the physical properties that cause agreements and discrepancies. Exploiting the traceable evolution of simulated galaxies, I also predicted how galaxy colours and colour bimodality evolve. Mock observations are produced as a useful resource for future studies, and initial attempts are made to re-derive physical properties and assess inverse modelling procedures by following observational techniques.

Such forward modelling analysis of simulations and semi-analytic galaxy formation models is by no means a new approach, and was inspired by a procession

of important works in the literature (e.g. Kauffmann & Charlot, 1998a; Font et al., 2008; Wuyts et al., 2009a,b; Jonsson et al., 2010; Mitchell et al., 2013; Torrey et al., 2014; Hayward & Smith, 2015). Some novel aspects of the work presented here derive from the use of EAGLE (described in chapter 2), which has been shown to reproduce a number of important characteristics of the observed population well (e.g. Schaye et al., 2015; Furlong et al., 2015; Lagos et al., 2015c; Bahé et al., 2016; Artale et al., 2016), and the application of radiative transfer to a large sample of hydrodynamically simulated galaxies.

I first provided a general review on the topic of galaxy observations and formation theory in chapter 1, and then a more specific grounding on the EAGLE simulations and datasets that I use in chapter 2. Chapters 3-6 then detailed the original research of this thesis. Individual summaries of these chapters are detailed below.

Chapter 3 summary: In chapter 3, I presented a first look at the predicted colours and luminosities of $z = 0.1$ EAGLE galaxies produced using the Bruzual & Charlot (2003) SEDs alongside different analytic dust models, primarily comparing to data from the GAMA survey (Taylor et al., 2015). A simple fiducial model (termed GD+O) to account for dust effects was developed: a two-component Charlot & Fall (2000) screen model accounting for attenuation by the ISM (applied to all stars) and birth clouds around young stars (applied to stars younger than 30 Myr), with optical depths scaled by the estimated dust mass in galaxies and a factor to account for the effects of random orientation. The $g - r$ colour vs. mass distribution for galaxies (Fig. 3.1) and broad-band luminosity functions (Fig. 3.3) were found to agree with GAMA at a level of consistency that had not been seen for cosmological simulations, and are competitive with contemporary semi-analytic models.

Despite this, there are clear discrepancies between EAGLE and the data. The red sequence is 0.1 mag bluer than observed at high mass ($M_\star \gtrsim 10^{11.2}\mathrm{M}_\odot$) with a flatter slope towards lower masses, which I attributed to discrepancy between the EAGLE and observationally-derived stellar mass-metallicity relation (Schaye

et al., 2015). The red sequence also persists to lower mass ($M_\star \lesssim 10^{9.75}\mathrm{M}_\odot$) than is seen in the data; this appears to be at least partially due to poor resolution of star formation and feedback in low mass galaxies, but is difficult to test as many of the faint red galaxies are in large halos missed by the small volume high resolution simulations. A blue cloud population was also recovered, and found to peak at $g-r \approx 0.4$ in good agreement with GAMA at intermediate masses ($M_\star \sim 10^{10}\mathrm{M}_\odot$). This conversely extends to higher masses than are seen in the data. It was speculated that the high mass blue galaxies could reflect low levels of star formation not sufficiently quenched by the black hole implementation, but also that it could be an artefact of our photometric modelling; particularly the treatment of dust in galaxies with geometries atypical of most star forming systems. Overall, the mass-dependent colour distribution generally agrees with observations, transitioning from being blue to red dominated at around the observed mass, despite the bimodality continuing over a broader mass range than is observed.

A similar level of agreement was found for luminosity functions in bands from near UV to NIR. The discrepant low galaxy number counts at the knee of the redder luminosity functions are reflective of a general underprediction registered for the galaxy stellar mass function (GSMF) itself (Schaye et al., 2015). It was found that while the GD+O dust model improves agreement with data, the majority of these results are also recovered if dust is neglected completely (the ND model).

Chapter 4 summary: Dust free modelling was then used in chapter 4 to investigate how intrinsic galaxy colours evolve to yield the bimodal distribution observed at low redshift ($z \sim 0.1$), with a particular focus on 'green' galaxies transitioning from one population to the other. It is found that EAGLE galaxies turn intrinsically red either due to interactions as they become satellites or due to the influence of AGN feedback processes, that dominate at low and high mass, respectively. The red sequence builds up from high and low mass ends as a result, with a 'hole' in the red sequence seen most clearly at $M_\star \sim 10^{10}\mathrm{M}_\odot$ for $z \approx 1$. The typical transition time for galaxies to turn from blue to red was found to be

~ 2 Gyr, consistent with passive evolution. This suggests a rapid shut down of star formation, consistent with instantaneous quenching. Even without star formation being explicitly disrupted, star forming EAGLE galaxies become redder over cosmic time as the sSFRs, $\dot{M}^{\star}/M^{\star}$, decrease.

Around 40% of galaxies with $M_{\star} \gtrsim 10^{10}\mathrm{M}_{\odot}$ exhibit rapid colour transitions ($\Delta(u^{\star}\text{-}r^{\star}) > 0.8$ mag over any 2 Gyr interval), with the remaining galaxies exhibiting a more gradual transition. Most galaxies remain on the red sequence, with those that exhibit similarly rapid transitions from red to blue comprising only 1.6% of the $M_{\star} \gtrsim 10^{10}\mathrm{M}_{\odot}$ sample. However, a larger fraction of EAGLE galaxies evolve to become measurably bluer than they were in the past ($\Delta(u^{\star}\text{-}r^{\star}) < -0.05$ mag), with a 17% chance that a random EAGLE galaxy observed in the interval $0 < z < 2$ is becoming bluer. While these results provide insight into the evolution of galaxies and the main mechanisms driving colour transition, the lack of dust could lead to significant differences in the trends and distributions that are measured, particularly at high redshift. The choice to neglect dust was due to uncertainty about how the empirically calibrated screen prescription used at $z = 0.1$ should evolve with redshift.

Chapter 5 summary: A more representative dust model was pursued in chapter 5; full dust radiative transfer is performed on each EAGLE galaxy using the simulated 3D distributions of stars and enriched gas that emerge for each system. In addition, sub-resolution scale attenuation in HII regions is accounted for using the MAPPINGS-III SEDs for young stars (Groves et al., 2008). As in chapter 3, this analysis took place at $z = 0.1$, but data products were generated at all redshifts. While an increase in attenuation naturally emerges for high inclination EAGLE galaxies with this approach, edge-on galaxies were found to be less attenuated than observed, ascribed to EAGLE discs being too thick. This is a clear limitation of the modelling, but only manifests major differences in the optical properties of edge-on discs and has little bearing on the overall results presented. Despite the problems with disc thickness, the typical attenuation profile is examined at differing inclinations and the result that edge-on galaxies have less frequency de-

pendent (greyer) attenuation profiles is recovered.

Direct comparison of optical colours were conducted against the GAMA data and that of chapter 3, with some key differences found; SKIRT photometry boosts the green valley and red sequence populations relative to that of GD+O and brings colour distributions into better agreement with the GAMA data. ugJ plots showed explicitly that the SKIRT modelling was more effective at hiding young stellar populations such that some active galaxies appear passive, similarly reflected in the D4000 spectral index measurements. Hα measurements are used as a direct proxy of SFR, and the dust effects were investigated. The Hα luminosity function was found to be discrepant, as expected from Furlong et al. (2015), though this may be reconciled by revised SFR calibrations (e.g. Chang et al., 2015). The bright end was also found to be intrinsically shallower than a constant dust correction suggests, similar to the findings of Gunawardhana et al. (2013).

Chapter 6 summary: Testing the inference of physical properties from synthetic optical observations was continued in chapter 6, with a particular focus on galaxy stellar masses, $M^{\star}$. As a colour-dependent mass to light ratio (M/L) is often taken to be a good approximation of empirical $M^{\star}$ estimates, I investigated how well they can reproduce simulated $M^{\star}$ values from the EAGLE photometry of chapters 3 and 5. Empirical estimators applied to integrated photometry were found to generally underpredict EAGLE masses by a uniform 0.1-0.2 dex over the modelled mass range, depending on the calibration used. It was found that appealing to resolved photometry may help this situation for blue galaxies dominated by age effects, but does not improve the prediction for red galaxies dominated by metallicity effects. Generally, including dust was found to improve mass estimation at $z = 0.1$, except for the highest attenuations and densest dust columns, where it leads to strong underestimates.

For more physical insight than the abstract colour-M/L relations provide, photometric SED fitting is investigated using the FAST code (Kriek et al., 2009). A similar set-up to Torrey et al. (2014) was used, but including dust. The dust inclusion is found to induce degeneracies, with some star forming galaxies being

fit as extreme starbursts. These recover much lower $M^\star$ and much higher SFR values than simulated (both by a factor $\sim$5-10). Extreme fitting failures were mitigated by increasing the minimum age of template starbursts (leading to a $< 1\%$ incidence of failures). Plots in the physical domain (i.e. $M^\star$ and SFR) were constructed using both simulated values and those re-derived from SED fitting the EAGLE photometry, then compared alongside those derived from observations. It is found that using FAST-derived $M^\star$ values reduces number counts at the bright end of the GSMF relative to the simulated values, which then increases the discrepancy with Baldry et al. (2012). This was recognised as but one of many potential systematic effects on the bright end that are not investigated in this thesis. The $M^\star$-SFR plot changes little due to both SFR and $M^\star$ being underestimated.

On comparing star formation histories in EAGLE to those fit by FAST, it was suggested that more gradually rising star formation histories with composite metallicities could provide better fits to EAGLE. A clear relationship was also found between mass offset and dust, where mass estimation is optimal for $A_g \approx 0.4$, indicating that varying the attenuation profile with obscuration may help mass recovery for the SKIRT photometry. Systematic effects due to stellar population models, IMF, etc are neglected in this investigation, as these are fixed for the EAGLE photometry that has been modelled. This study is a first step towards investigating how well properties are recovered with more sophisticated spectral fitting, larger wavelength ranges and higher redshift samples in EAGLE.

Overall, it is found that model observables generated for the EAGLE simulations generally reproduce data well at low redshifts ($z \approx 0.1$), and may provide insight into both the evolution between galaxy populations observed at different epochs, and the influence of common observational techniques and assumptions. Despite this it is important to critically assess the inherent problems of this approach, and, more fundamentally, how informative applying a forward modelling approach to simulations actually is.

7.2 Assessment of the methods used in this thesis

The feedback parameters used in the EAGLE simulations are calibrated to reproduce certain relations derived from observational data. These relations include the galaxy stellar mass function at $z = 0.1$, the black hole mass ($M_{\rm BH}$) vs. $M^\star$ relation and the size vs. $M^\star$ relation for galaxies (Schaye et al., 2015; Crain et al., 2015). Clearly, these relations cannot then be considered *predictions* of the simulations as they emerge by construction, thus limiting the physical insight they can provide. Complex relationships exist between galaxy properties in EAGLE, and the influence of calibration on all results should be considered. Luminosities are often driven by stellar mass content, particularly in redder optical and NIR bands. As a result, it is hardly surprising that the luminosity functions show a similar level of agreement with the observed galaxy luminosity functions as is found for the GSMF. However, agreement at shorter wavelength bands (e.g. u-band) relies more on dust effects and the mass in young stars. In a similar vein, optical colours are less directly dependent on calibrated properties, and predominately influenced by the ratio of young to old stars, stellar metallicities and dust effects. However, the relationship between black hole growth and stellar mass that manifests the $M_{\rm BH}$-$M^\star$ relation and the break in the GSMF also ensures that star formation is disrupted in massive galaxies to a large extent. Furthermore, ensuring realistic galaxy sizes profoundly influences the stellar and gas geometries of galaxies, and thus the results obtained for dust modelling. It remains difficult to gauge how far we might be validating our prejudices by focusing on simulation results that are shaped by our calibration and assumptions. Still, calibration far from guarantees that features such as the observed red/blue galaxy fraction are reproduced as well as is found.

Another limitation is simulation resolution. The standard physical resolution of EAGLE is ~ 0.5 kpc, meaning that structure on smaller scales is missing. The resolution limitations also necessitate the pressure floor that limits cooling to $\sim 10^4$ K in the EAGLE ISM. One effect of this missing structure may be on dust attenuation, where neglected small scale 'clumpiness' of the ISM may potentially

lead to systematic effects not accounted for in our modelling. Indeed, this effect has been suggested as a potential contributor to the discrepancy between the observed and modelled UVJ (or ugJ) distributions at high redshifts ($1.5 \lesssim z \lesssim 3$, e.g. Wuyts et al. 2009b). It also affects macroscopic scales; as has been shown, the gas discs in EAGLE are artificially 'puffed-up' leading to particularly underestimated edge-on attenuations in discs. In addition, features such as tidal arms that affect the age-dependent configurations of stars and dust may also be diminished. Aside from spatial resolution, mass resolution also plays a role. At $\sim 10^6 \mathrm{M}_\odot$, star particles are more massive than typical bound stellar clusters and GMCs (e.g. Relaño & Kennicutt, 2009). This results in artificial stochasticity in the stellar component, which may affect colours systematically unless this is mitigated using something like our resampling approach, and which may influence feedback and enrichment, carried out on a coarse particle-by-particle basis. While appealing to galaxies resolved by more particles may mitigate many of these problems, observations blue-ward of optical wavelengths may be dominated by a few very young particles, even at higher $M^\star$. The EAGLE team is currently developing a successor simulation with better spatial and mass resolution, that allows gas to cool to $\sim$ molecular phase temperatures. This aims to provide a significant improvement in the resolution of small scale and macroscopic scale features of galaxies. Repeating the analysis of this thesis using such improved simulations could provide more realistic mock observables and evolution.

Along with the lack of a molecular gas phase, there is no explicit dust component or model for dust grain creation or destruction in EAGLE. Dust is entirely *post-hoc* in the modelling, using the enrichment properties of cool gas and a constant metal-to-dust ratio to imply its distribution in the ISM. While a constant metal-dust ratio is thought to be reasonable in many cases, it clearly is not applicable in all environments, and currently redshift evolution is not considered. Another motivation for an explicit dust component is that radiation pressure on dust has been posed as a potentially important mechanism to drive outflows (e.g. Veilleux et al., 2013). This may in turn influence dust attenuation in self-consistent modelling; Wuyts et al. (2009b) suggest that dusty outflows could act as fore-

ground screens, and help reproduce the reddest observed galaxies in the $z \sim 2$ ugJ (or UVJ) diagram. Building the lifecycle of dust and its role in driving outflows into simulations has been attempted by others (e.g. Bekki, 2015; Aoyama et al., 2016; McKinnon et al., 2016), and could provide a more physical model for the ISM dust distributions in future EAGLE-like simulations.

It may also be possible to improve the self consistency and realism of the SKIRT modelling without modifying the simulations themselves. To account for subresolution dust effects, the SKIRT model currently relies on the MAPPINGS-III HII region SEDs of Groves et al. (2008). While these build in modelling for HII dust and gas radiative transfer, the dust attenuation is averaged both spherically and over the age of the HII region. Properly accounting for dust represented in the HII region models from the overall budget (a constant fraction of the metal mass in enriched ISM gas) is therefore somewhat ambiguous. They are also built on the Leitherer et al. (1999) population models, which could lead to some inconsistencies for the small fraction of stars in HII regions. Perhaps a more consistent approach would be to model HII regions internally within SKIRT using a single stellar population library, and allowing it to model an anisotropic dust screen around young stellar populations that gradually disperses with the population age. This could be paired with a resampling approach that also accounts for realistic stochastic sampling of the IMF and cluster mass function (CMF) of stellar populations on those mass scales, as built in to some modern stellar population codes such as SLUG (da Silva et al., 2012). Such variations could lead to a more self-consistent model, where the influence of stochasticity and sub resolution dust are more tractable.

Various other assumptions in the modelling are not investigated directly in this thesis. As detailed in chapter 2, the modelling in chapters 3-5 consistently uses a Chabrier (2003) IMF and the Bruzual & Charlot (2003) population synthesis model for the majority of stars, considering all self-bound material within a 30 pkpc spherical aperture. In the $M^\star$ derivation of chapter 6, the fitting and indicators use the same Bruzual & Charlot (2003) population synthesis model

with a Chabrier (2003) IMF[1], and any aperture effects are marginalised over by comparing the masses derived using 30 pkpc spherical aperture photometry to the true 30 pkpc spherical aperture $M^\star$ values. This was originally chosen for simplicity and consistency, assuming that population model differences are relatively small for the optical wavelengths and low redshift focused on here ($z \approx 0.1$, e.g. Gonzalez-Perez et al. 2014a). However, to get a better idea of how large the uncertainties and discrepancies that we identify are in the context of these unexamined systematic uncertainties, especially at higher redshifts, future work could test IMF variations and stellar population variations using models such as Conroy et al. (2009) which allow these assumptions to be changed. It is important to test these effects in concert with the dust, as demonstrated by Wuyts et al. (2009b). A separate analysis of aperture modelling effects would be similarly useful, and could be tested using SKIRT imaging of bright-end galaxies to replicate observational techniques.

7.3 Future work

As well as various modifications that could be made to the approach taken in this thesis, there are also a host of applications of this work going forward. The broadband SKIRT imaging developed in chapter 5 itself provides a number of possible applications, particularly for investigating the morphologies and morphological evolution of EAGLE galaxies. Using this mock data, observational image analysis techniques could be emulated to measure morphologies, and compared to kinematic metrics (e.g. Abadi et al., 2003; Sales et al., 2010). The influence of dust on morphological measures could also be characterised. To this end, a pipeline to reduce the mock images and to emulate instrumental noise and seeing is in development. This analysis will be used to characterise when discs and bulges emerge in the simulations, and study progenitors of present-day early and late types. Image analysis of EAGLE galaxies could also prove very informative for

[1] with the exception of Zibetti et al. 2009 who use the 2007 update to Bruzual & Charlot 2003

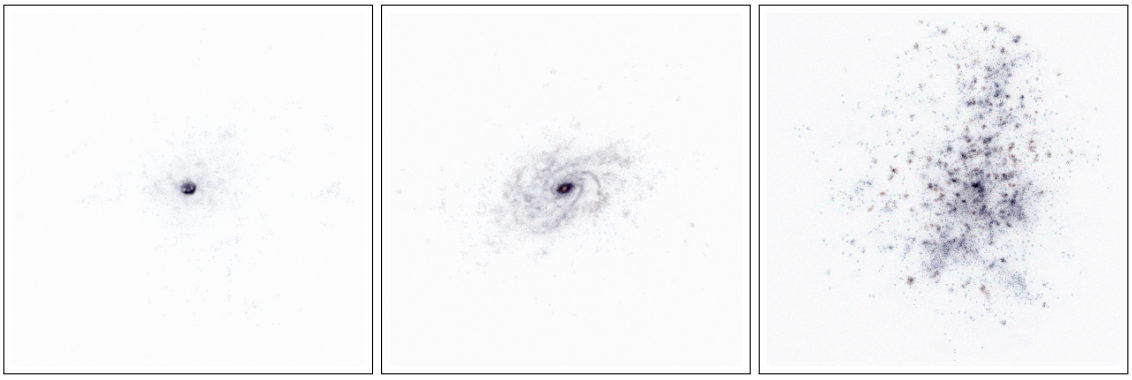

Figure 7.1: Inverted three colour *Herschel* PACS-like images of EAGLE galaxies of 60 pkpc on a side, produced using the SKIRT modelling described in chapter 5 and Camps et al. (2016). From left to right, a central starbursting galaxy, a spiral galaxy and a clumpy galaxy are selected from redshifts $z \approx 2-4$. The diversity of modelled EAGLE dust morphologies can be seen.

weak lensing studies, in preparation for upcoming missions such as *Euclid*. These studies primarily aim to decouple the influence of cosmic shear in galaxy images from their intrinsic morphologies and alignments. The EAGLE imaging data then provides a unique resource for such analysis, comprising a large sample of hydrodynamically simulated galaxies with non-idealised morphologies imaged using dust radiative transfer. For instance, a cosmic shear signal could be applied to each EAGLE galaxy image, and its recovery could be tested for accuracy and precision.

Extending this analysis to new wavelengths and redshift ranges may also provide a number of new opportunities. A potential study, mentioned in chapter 6.4, would be to model and measure a variety of proxies for galactic star formation rate that are accessible observationally at different redshifts. Reconstructing the star formation rate density evolution plot from this would enable an assessment of systematic effects, and a consideration of how different methods of inferring SFR with redshift can modify the perceived star formation history of the universe. In addition, reproducing the observed UVJ diagram at $1.5 < z < 3$ could prove a challenging test for the radiative transfer dust modelling, so far analysed at $z \approx 0$ (Wuyts et al., 2009b). This may provide insight into any modifications to

the SKIRT procedure that might be appropriate at higher redshift.

Another study, following initial tests of high redshift dust modelling, would be to characterise sub-millimetre properties of galaxies in EAGLE and EAGLE-like simulations. Sub-millimetre observations reveal a population of enigmatic, ultra-luminous galaxies at high redshift (SMGs). The broad consensus is that these are dusty, star-forming systems, but their nature and origin remain poorly understood. Using the radiative transfer modelling of SKIRT at longer wavelengths, as explored by Camps et al. (2016), emergent SMG analogues can be selected from the simulation on their FIR flux. Initial investigation reveals a population of candidates. Resolved FIR images reveal these galaxies to have diverse morphologies, with concentrated nuclear emitters, extended discs and clumpy asymmetric structures. This is demonstrated in Fig. 7.1. It would be informative to classify this heterogeneous population and quantify the fraction of galaxies of each type, comparing their various statistics. The processes that drive the SMG analogues could then be considered (e.g. whether they are predominately late-stage mergers) and identify the properties of their low-redshift descendants. Such a theoretical study of SMGs would complement the growing data from facilities such as ALMA.

In addition, the instrument modelling could be extended to produce and analyse mock data for the new generation of surveys. IFU observations are of particular interest with instruments such as SAMI, MaNGA, SAURON, MUSE or KMOS all now probing the kinematic properties of galaxies. Mock IFU data produced using the non-idealised virtual galaxies of EAGLE are particularly sought-after to test IFU reduction pipelines. Functionality to include Doppler shift has already been built into SKIRT, and initial IFU-like cubes have been constructed for EAGLE galaxies[2]. We can also match our observations to detectors across the UV-FIR range, for example making predictions for the MIRI instrument of the upcoming JWST mission. Ultimately, the goal is to develop an interface that allows users to generate customised mock data easily by applying the modelling of this thesis to

[2]An example animated figure of an SKIRT IFU cube of an EAGLE galaxy can be found at `http://icc.dur.ac.uk/~wmfw23/img/figures/dustscroll.gif`

EAGLE and other simulations.

New components could also be included in the radiative transfer, to open new potential avenues for investigation. The EAGLE simulations model accretion and feedback by AGN, and their growth and relationship to their host galaxies have been investigated in the physical domain (Bower et al., 2017; McAlpine et al., 2017). Including AGN as a source component in the SKIRT modelling would allow AGN contamination effects to be studied, and AGN observations to be emulated. In particular, the stark effects of galaxy selection on the SFR vs. black hole accretion rate relation inferred for observations, and identified in EAGLE by McAlpine et al. (2017), could be reappraised using mock observations. The FIR contribution of AGN would also be an important consideration for the SMG study mentioned above. In addition to AGN, a longer term goal would be to include gas as both an absorbing and emitting component in the radiative transfer, alongside the calculations performed for dust. This would provide emission lines and line diagnostics for EAGLE galaxies, and potentially enable the study of Lyman-α emitters and their properties. The problem of 3D line transfer is difficult due to the complexity of photoionisation, the importance of scattering and the need to account for relative motions of emitting and attenuating media.

A final application is for the development of simulations themselves. As mentioned above, the successor to the EAGLE simulation is in development as of writing, and aims to provide an explicit cold gas phase alongside a step change in resolution. EAGLE and contemporary simulations such as ILLUSTRIS (Vogelsberger et al., 2014) already produce GSMFs calibrated to agree with observation at a level comparable to semi-analytic models. However, as seen in chapter 6, this level of agreement is similar to the systematic uncertainties in mass derivation from observations. By instead emulating observational techniques such as SED fitting as closely as possible (i.e. using the same underlying assumptions and modelling), many of the same systematic effects and offsets that may be present in the observational analysis could be built into the simulation data. As a result, it is perhaps more appropriate to calibrate directly to an observable target (such as the NIR luminosity function) or via masses re-derived from mock observations. This idea

can be extended to other calibrators, such as galaxy sizes and black hole scaling relations. There is thus potential for forward modelled galaxy properties to inform and even calibrate the next generation of cosmological simulations, as we strive to gain a deeper understanding of the physics of galaxies and their evolution.

Bibliography

Abadi M. G., Navarro J. F., Steinmetz M., Eke V. R., 2003, ApJ, 597, 21

Abazajian K. N., et al., 2009a, ApJs, 182, 543

Abazajian K. N., et al., 2009b, ApJs, 182, 543

Acquaviva V., Gawiser E., Guaita L., 2011, ApJ, 737, 47

Allen J. T., et al., 2015, MNRAS, 446, 1567

Allende Prieto C., Lambert D. L., Asplund M., 2001, ApJl, 556, L63

Alpaslan M., et al., 2015, MNRAS, 451, 3249

Altay G., Theuns T., 2013, MNRAS, 434, 748

Aoyama S., Hou K.-C., Shimizu I., Hirashita H., Todoroki K., Choi J.-H., Nagamine K., 2016, preprint, (arXiv:1609.07547)

Artale M. C., et al., 2016, preprint, (arXiv:1611.05064)

Asplund M., Grevesse N., Sauval A. J., Allende Prieto C., Kiselman D., 2004, A&A, 417, 751

Baes M., Camps P., 2015, Astronomy and Computing, 12, 33

Baes M., Dejonghe H., 2001, MNRAS, 326, 733

Baes M., et al., 2003, MNRAS, 343, 1081

Baes M., Dejonghe H., Davies J. I., 2005, in Popescu C. C., Tuffs R. J., eds, American Institute of Physics Conference Series Vol. 761, The Spectral Energy Distributions of Gas-Rich Galaxies: Confronting Models with Data. pp 27–38 (arXiv:astro-ph/0503483), doi:10.1063/1.1913913

Baes M., et al., 2010, A&A, 518, L39

Baes M., Verstappen J., De Looze I., Fritz J., Saftly W., Vidal Pérez E., Stalevski M., Valcke S., 2011, ApJs, 196, 22

Bahé Y. M., McCarthy I. G., Balogh M. L., Font A. S., 2013, MNRAS, 430, 3017

Bahé Y. M., et al., 2016, MNRAS, 456, 1115

Baldry I. K., Glazebrook K., Brinkmann J., Ivezić Ž., Lupton R. H., Nichol R. C., Szalay A. S., 2004, ApJ, 600, 681

Baldry I. K., et al., 2010, MNRAS, 404, 86

Baldry I. K., et al., 2012, MNRAS, 421, 621

Baldry I. K., et al., 2014, MNRAS, 441, 2440

Baldwin J. A., Phillips M. M., Terlevich R., 1981, PASP, 93, 5

Ball N. M., Loveday J., Brunner R. J., 2008, MNRAS, 383, 907

Balogh M. L., Morris S. L., Yee H. K. C., Carlberg R. G., Ellingson E., 1999, ApJ, 527, 54

Balogh M. L., Navarro J. F., Morris S. L., 2000, ApJ, 540, 113

Balogh M. L., Baldry I. K., Nichol R., Miller C., Bower R., Glazebrook K., 2004, ApJl, 615, L101

Barnes J., Efstathiou G., 1987, ApJ, 319, 575

Bastian N., Covey K. R., Meyer M. R., 2010, ARA&A, 48, 339

Beckwith S. V. W., et al., 2006, AJ, 132, 1729

Bekki K., 2015, ApJ, 799, 166

Bell R., Rodgers A., 1969, Monthly Notices of the Royal Astronomical Society, 142, 161

Bell E. F., de Jong R. S., 2001, ApJ, 550, 212

Bell E. F., McIntosh D. H., Katz N., Weinberg M. D., 2003, ApJs, 149, 289

Bell E. F., et al., 2004, ApJ, 608, 752

Bell E. F., et al., 2012, ApJ, 753, 167

Benson A. J., Lacey C. G., Baugh C. M., Cole S., Frenk C. S., 2002, MNRAS, 333, 156

Benson A. J., Bower R. G., Frenk C. S., Lacey C. G., Baugh C. M., Cole S., 2003, ApJ, 599, 38

Bernardi M., Meert A., Sheth R. K., Vikram V., Huertas-Company M., Mei S., Shankar F., 2013, MNRAS, 436, 697

Bernardi M., Meert A., Sheth R. K., Fischer J.-L., Huertas-Company M., Maraston C., Shankar F., Vikram V., 2017, MNRAS, 467, 2217

Best P., et al., 2013, Astrophysics and Space Science Proceedings, 37, 235

Bigiel F., et al., 2011, ApJl, 730, L13

Blanton M. R., Moustakas J., 2009, ARA&A, 47, 159

Blanton M. R., Roweis S., 2007, AJ, 133, 734

Blanton M. R., et al., 2001, AJ, 121, 2358

Bolzonella M., Miralles J.-M., Pelló R., 2000, A&A, 363, 476

Bond J. R., Cole S., Efstathiou G., Kaiser N., 1991, ApJ, 379, 440

Booth C. M., Schaye J., 2009, MNRAS, 398, 53

Boquien M., et al., 2013, A&A, 554, A14

Boselli A., Cortese L., Boquien M., Boissier S., Catinella B., Gavazzi G., Lagos C., Saintonge A., 2014, A&A, 564, A67

Bourne N., et al., 2013, MNRAS, 436, 479

Bouwens R. J., et al., 2015, ApJ, 803, 34

Bower R. G., Lucey J. R., Ellis R. S., 1992, MNRAS, 254, 601

Bower R. G., Benson A. J., Malbon R., Helly J. C., Frenk C. S., Baugh C. M., Cole S., Lacey C. G., 2006, MNRAS, 370, 645

Bower R. G., Schaye J., Frenk C. S., Theuns T., Schaller M., Crain R. A., McAlpine S., 2017, MNRAS, 465, 32

Brainerd T. G., Blandford R. D., Smail I., 1996, ApJ, 466, 623

Brammer G. B., van Dokkum P. G., Coppi P., 2008, ApJ, 686, 1503

Bressan A., Fagotto F., Bertelli G., Chiosi C., 1993, A&AS, 100, 647

Brinchmann J., Charlot S., White S. D. M., Tremonti C., Kauffmann G., Heckman T., Brinkmann J., 2004, MNRAS, 351, 1151

Brinks E., Burton W. B., 1984, A&A, 141, 195

Bruzual A. G., 1983, ApJ, 273, 105

Bruzual G., Charlot S., 2003, MNRAS, 344, 1000

Bundy K., et al., 2015, ApJ, 798, 7

Byun Y. I., Freeman K. C., Kylafis N. D., 1994, ApJ, 432, 114

Calzetti D., 2001, New A Rev., 45, 601

Calzetti D., Armus L., Bohlin R. C., Kinney A. L., Koornneef J., Storchi-Bergmann T., 2000, ApJ, 533, 682

Camps P., Baes M., 2015, Astronomy and Computing, 9, 20

Camps P., Trayford J. W., Baes M., Theuns T., Schaller M., Schaye J., 2016, MNRAS, 462, 1057

Cen R., 2014, ApJ, 781, 38

Chabrier G., 2003, PASP, 115, 763

Chang Y.-Y., van der Wel A., da Cunha E., Rix H.-W., 2015, ApJs, 219, 8

Charlot S., Fall S. M., 2000, ApJ, 539, 718

Chung A., van Gorkom J. H., Kenney J. D. P., Vollmer B., 2007, ApJ, 659, L115

Coil A. L., et al., 2008, ApJ, 672, 153

Cole S., Lacey C. G., Baugh C. M., Frenk C. S., 2000, MNRAS, 319, 168

Cole S., et al., 2005, MNRAS, 362, 505

Colless M., et al., 2003, ArXiv Astrophysics e-prints,

Conroy C., Gunn J. E., White M., 2009, ApJ, 699, 486

Conselice C. J., 2003, ApJs, 147, 1

Conselice C. J., 2014, ARA&A, 52, 291

Conselice C. J., Blackburne J. A., Papovich C., 2005, ApJ, 620, 564

Cortese L., 2012, A&A, 543, A132

Cortese L., Hughes T. M., 2009, MNRAS, 400, 1225

Cortese L., Catinella B., Boissier S., Boselli A., Heinis S., 2011, MNRAS, 415, 1797

Cowley W. I., Lacey C. G., Baugh C. M., Cole S., 2015, MNRAS, 446, 1784

Crain R. A., et al., 2009, MNRAS, 399, 1773

Crain R. A., et al., 2015, MNRAS, 450, 1937

Creasey P., Theuns T., Bower R. G., 2013, MNRAS, 429, 1922

Creasey P., Theuns T., Bower R. G., 2015, MNRAS, 446, 2125

Croton D. J., et al., 2006, MNRAS, 365, 11

Dalla Vecchia C., Schaye J., 2012, MNRAS, 426, 140

Davé R., Thompson R., Hopkins P. F., 2016, MNRAS, 462, 3265

Davé R., Rafieferantsoa M. H., Thompson R. J., 2017, preprint, (arXiv:1704.01135)

Davis M., Efstathiou G., Frenk C. S., White S. D. M., 1985, ApJ, 292, 371

De Cia A., Ledoux C., Savaglio S., Schady P., Vreeswijk P. M., 2013, A&A, 560, A88

De Geyter G., Baes M., Camps P., Fritz J., De Looze I., Hughes T. M., Viaene S., Gentile G., 2014, MNRAS, 441, 869

De Looze I., et al., 2014, A&A, 571, A69

Dehnen W., Aly H., 2012, MNRAS, 425, 1068

Dekel A., Silk J., 1986, ApJ, 303, 39

Delvecchio I., et al., 2015, MNRAS, 449, 373

Disney M., Davies J., Phillipps S., 1989, MNRAS, 239, 939

Doi M., et al., 2010, AJ, 139, 1628

Dolag K., Borgani S., Murante G., Springel V., 2009, MNRAS, 399, 497

Draine B. T., 2003, ARA&A, 41, 241

Draine B. T., Li A., 2007, ApJ, 657, 810

Draine B. T., et al., 2007, ApJ, 663, 866

Dressler A., 1980, ApJ, 236, 351

Driver S. P. *et al..*, 2012, MNRAS, 427, 3244

Driver S. P., et al., 2006, MNRAS, 368, 414

Driver S. P., Popescu C. C., Tuffs R. J., Liske J., Graham A. W., Allen P. D., de Propris R., 2007, MNRAS, 379, 1022

Driver S. P., et al., 2009, Astronomy and Geophysics, 50, 12

Driver S. P., et al., 2011, MNRAS, 413, 971

Durier F., Dalla Vecchia C., 2012, MNRAS, 419, 465

Dwek E., 1998, ApJ, 501, 643

Efstathiou G., 1992, MNRAS, 256, 43P

Efstathiou G., Eastwood J. W., 1981, MNRAS, 194, 503

Faber S. M., et al., 2007, ApJ, 665, 265

Fall S. M., Efstathiou G., 1980, MNRAS, 193, 189

Feldmann R., 2015, MNRAS, 449, 3274

Feldmann R., Quataert E., Hopkins P. F., Faucher-Giguère C.-A., Kereš D., 2016, preprint, (arXiv:1610.02411)

Ferland G. J., Korista K. T., Verner D. A., Ferguson J. W., Kingdon J. B., Verner E. M., 1998, PASP, 110, 761

Finke J. D., Razzaque S., Dermer C. D., 2010, ApJ, 712, 238

Fischera J., Dopita M. A., Sutherland R. S., 2003, ApJl, 599, L21

Font A. S., et al., 2008, MNRAS, 389, 1619

Franx M., et al., 2003, ApJl, 587, L79

Frenk C. S., White S. D. M., Davis M., Efstathiou G., 1988, ApJ, 327, 507

Fukugita M., Hogan C. J., Peebles P. J. E., 1998, ApJ, 503, 518

Fumagalli M., Fossati M., Hau G. K. T., Gavazzi G., Bower R., Sun M., Boselli A., 2014, MNRAS, 445, 4335

Furlong M., et al., 2015, MNRAS, 450, 4486

Furlong M., et al., 2017, MNRAS, 465, 722

Gabor J. M., Davé R., 2012, MNRAS, 427, 1816

Gadotti D. A., Baes M., Falony S., 2010, MNRAS, 403, 2053

Gallazzi A., Bell E. F., 2009, ApJs, 185, 253

Gallazzi A., Charlot S., Brinchmann J., White S. D. M., Tremonti C. A., 2005, MNRAS, 362, 41

Gebhardt K., et al., 2000, The Astrophysical Journal Letters, 539, L13

Genel S., et al., 2014, MNRAS, 445, 175

Gilbank D. G., Baldry I. K., Balogh M. L., Glazebrook K., Bower R. G., 2010, MNRAS, 405, 2594

Gonzalez-Perez V., Lacey C. G., Baugh C. M., Lagos C. D. P., Helly J., Campbell D. J. R., Mitchell P. D., 2014a, MNRAS, 439, 264

Gonzalez-Perez V., Lacey C., Baugh C., Lagos C., Helly J., Campbell D., Mitchell P., 2014b, Monthly Notices of the Royal Astronomical Society, 439, 264

González J. E., Lacey C. G., Baugh C. M., Frenk C. S., Benson A. J., 2009, MNRAS, 397, 1254

Grootes M. W., et al., 2013, ApJ, 766, 59

Groves B., Dopita M. A., Sutherland R. S., Kewley L. J., Fischera J., Leitherer C., Brandl B., van Breugel W., 2008, ApJs, 176, 438

Guidi G., Scannapieco C., Walcher C. J., 2015, MNRAS, 454, 2381

Gunawardhana M. L. P., et al., 2013, MNRAS, 433, 2764

Gunawardhana M. L. P., et al., 2015, MNRAS, 447, 875

Gunn J. E., Gott III J. R., 1972, ApJ, 176, 1

Haardt F., Madau P., 2001, in Neumann D. M., Tran J. T. V., eds, Clusters of Galaxies and the High Redshift Universe Observed in X-rays. (arXiv:astro-ph/0106018)

Haines C. P., et al., 2013, ApJ, 775, 126

Häring N., Rix H.-W., 2004, ApJ, 604, L89

Harrison C. M., et al., 2012, ApJl, 760, L15

Häußler B., et al., 2013, MNRAS, 430, 330

Hayward C. C., Smith D. J. B., 2015, MNRAS, 446, 1512

Hearin A. P., Zentner A. R., Berlind A. A., Newman J. A., 2013, MNRAS, 433, 659

Heavens A., Panter B., Jimenez R., Dunlop J., 2004, Nature, 428, 625

Heckman T. M., Lehnert M. D., Strickland D. K., Armus L., 2000, ApJs, 129, 493

Henriques B., White S., Thomas P., Angulo R., Guo Q., Lemson G., Springel V., Overzier R., 2014, preprint, (arXiv:1410.0365)

Henriques B. M. B., White S. D. M., Thomas P. A., Angulo R., Guo Q., Lemson G., Springel V., Overzier R., 2015, MNRAS, 451, 2663

Hernández-Pérez F., Bruzual G., 2013, MNRAS, 431, 2612

Hewett P. C., Warren S. J., Leggett S. K., Hodgkin S. T., 2006, MNRAS, 367, 454

Heyer M. H., Carpenter J. M., Snell R. L., 2001, ApJ, 551, 852

Hickox R. C., Mullaney J. R., Alexander D. M., Chen C.-T. J., Civano F. M., Goulding A. D., Hainline K. N., 2014, ApJ, 782, 9

Hill D. T., et al., 2011, MNRAS, 412, 765

Hogg D. W., 1999, ArXiv Astrophysics e-prints,

Hopkins P. F., 2013, MNRAS, 428, 2840

Hopkins P. F., 2015, MNRAS, 450, 53

Hopkins A. M., et al., 2003, ApJ, 599, 971

Hopkins P. F., Richards G. T., Hernquist L., 2007, ApJ, 654, 731

Hopkins P. F., Quataert E., Murray N., 2011, MNRAS, 417, 950

Horiuchi S., Beacom J. F., Bothwell M. S., Thompson T. A., 2013, ApJ, 769, 113

Hu W., Dodelson S., 2002, ARA&A, 40, 171

Hubble E. P., 1926, ApJ, 64

Hughes T. M., et al., 2015, A&A, 575, A17

Hunt L. K., Hirashita H., 2009, A&A, 507, 1327

Inoue A. K., 2012, preprint, (arXiv:1202.2932)

Jackson N., Bryan S. E., Mao S., Li C., 2010, MNRAS, 403, 826

James P. A., et al., 2004, A&A, 414, 23

Jenkins A., Booth S., 2013, preprint, (arXiv:1306.5771)

Jing Y. P., Mo H. J., Börner G., 1998, ApJ, 494, 1

Johnston R., 2011, Astronomy and Astrophysics Review, 19, 41

Jones D. H., Peterson B. A., Colless M., Saunders W., 2006, MNRAS, 369, 25

Jonsson P., 2006, MNRAS, 372, 2

Jonsson P., Groves B., Cox T. J., 2009, preprint, (arXiv:0906.2156)

Jonsson P., Groves B. A., Cox T. J., 2010, MNRAS, 403, 17

Kannappan S. J., Gawiser E., 2007, ApJl, 657, L5

Kant I., 1755, Universal Natural History and Theory of the Heavens. Ann Arbor paperbacks, University of Michigan Press

Katz N., Weinberg D. H., Hernquist L., 1996, ApJs, 105, 19

Kauffmann G., Charlot S., 1998a, MNRAS, 294, 705

Kauffmann G., Charlot S., 1998b, MNRAS, 297, L23

Kauffmann G., et al., 2003a, MNRAS, 341, 33

Kauffmann G., et al., 2003b, MNRAS, 341, 54

Kelvin L. S., et al., 2014, MNRAS, 439, 1245

Kennicutt Jr. R. C., 1992, ApJ, 388, 310

Kennicutt Jr. R. C., 1998a, ARA&A, 36, 189

Kennicutt Jr. R. C., 1998b, ApJ, 498, 541

Kewley L. J., Ellison S. L., 2008, ApJ, 681, 1183

Khandai N., Di Matteo T., Croft R., Wilkins S., Feng Y., Tucker E., DeGraf C., Liu M.-S., 2015, MNRAS, 450, 1349

King A. R., Pounds K. A., 2003, MNRAS, 345, 657

Knobel C., et al., 2013, ApJ, 769, 24

Komatsu E., et al., 2011, ApJs, 192, 18

Kormendy J., Richstone D., 1995, ARA&A, 33, 581

Kornei K. A., Shapley A. E., Martin C. L., Coil A. L., Lotz J. M., Schiminovich D., Bundy K., Noeske K. G., 2012, ApJ, 758, 135

Koyama K., 2016, Reports on Progress in Physics, 79, 046902

Kriek M., Conroy C., 2013, ApJl, 775, L16

Kriek M., van Dokkum P. G., Labbé I., Franx M., Illingworth G. D., Marchesini D., Quadri R. F., 2009, ApJ, 700, 221

Kroupa P., 2001, MNRAS, 322, 231

Kroupa P., Tout C. A., Gilmore G., 1993, MNRAS, 262, 545

Lacey C., Cole S., 1994, MNRAS, 271, 676

Lacey C. G., et al., 2015, preprint, (arXiv:1509.08473)

Lacey C. G., et al., 2016, MNRAS, 462, 3854

Lagos C. d. P., et al., 2015a, preprint (arXiv:1510.08067)

Lagos C. d. P., et al., 2015b, MNRAS, 452, 3815

Lagos C. d. P., et al., 2015c, MNRAS, 452, 3815

Larson R. B., 1974, MNRAS, 169, 229

Larson R. B., Tinsley B. M., Caldwell C. N., 1980, ApJ, 237, 692

Lawrence A. *et al.*., 2007, MNRAS, 379, 1599

Leitherer C., et al., 1999, ApJs, 123, 3

Li C., White S. D. M., 2009, MNRAS, 398, 2177

Lintott C., et al., 2011, MNRAS, 410, 166

Lotz J. M., Primack J., Madau P., 2004, AJ, 128, 163

Loveday J., 1998, ArXiv Astrophysics e-prints,

Loveday J., et al., 2012, MNRAS, 420, 1239

Lovell M. R., Frenk C. S., Eke V. R., Jenkins A., Gao L., Theuns T., 2014, MNRAS, 439, 300

Lupton R., Blanton M. R., Fekete G., Hogg D. W., O'Mullane W., Szalay A., Wherry N., 2004, PASP, 116, 133

Ly C., Malkan M. A., Kashikawa N., Ota K., Shimasaku K., Iye M., Currie T., 2012, ApJl, 747, L16

Magorrian J., et al., 1998, AJ, 115, 2285

Maneewongvatana S., Mount D. M., 2001, On the efficiency of nearest neighbor searching with data clustered in lower dimensions. Springer

Maraston C., 2005, MNRAS, 362, 799

Maraston C., Pforr J., Renzini A., Daddi E., Dickinson M., Cimatti A., Tonini C., 2010, MNRAS, 407, 830

Maraston C., et al., 2013, MNRAS, 435, 2764

Marchesini D., van Dokkum P. G., Förster Schreiber N. M., Franx M., Labbé I., Wuyts S., 2009, ApJ, 701, 1765

Martin C. L., 1999, ApJ, 513, 156

Martin D. C., et al., 2007, ApJs, 173, 342

Martizzi D., Faucher-Giguère C.-A., Quataert E., 2014, preprint, (arXiv:1409.4425)

Mattsson L., De Cia A., Andersen A. C., Zafar T., 2014, MNRAS, 440, 1562

McAlpine S., et al., 2016, Astronomy and Computing, 15, 72

McAlpine S., Bower R. G., Harrison C. M., Crain R. A., Schaller M., Schaye J., Theuns T., 2017, MNRAS, 468, 3395

McCarthy I. G., Frenk C. S., Font A. S., Lacey C. G., Bower R. G., Mitchell N. L., Balogh M. L., Theuns T., 2008, MNRAS, 383, 593

McConnell N. J., Ma C.-P., 2013, ApJ, 764, 184

McGaugh S. S., Schombert J. M., Bothun G. D., de Blok W. J. G., 2000, ApJl, 533, L99

McGee S. L., Bower R. G., Balogh M. L., 2014, MNRAS, 442, L105

McKinnon R., Torrey P., Vogelsberger M., Hayward C. C., Marinacci F., 2016, preprint, (arXiv:1606.02714)

McMillan P. J., 2011, MNRAS, 414, 2446

McNamara B. R., Nulsen P. E. J., 2012, New Journal of Physics, 14, 055023

Mitchell P. D., Lacey C. G., Baugh C. M., Cole S., 2013, MNRAS, 435, 87

Mo H., van den Bosch F., White S., 2010, Galaxy Formation and Evolution. Galaxy Formation and Evolution, Cambridge University Press, http://books.google.co.uk/books?id=Zj7fDU3Z4wsC

Mobasher B., et al., 2015, ApJ, 808, 101

Murante G., Monaco P., Borgani S., Tornatore L., Dolag K., Goz D., 2015, MNRAS, 447, 178

Murphy E. J., et al., 2011, ApJ, 737, 67

Muzzin A., et al., 2014, ApJ, 796, 65

Naab T., Ostriker J. P., 2016, preprint, (arXiv:1612.06891)

Natale G., Popescu C. C., Tuffs R. J., Debattista V. P., Fischera J., Grootes M. W., 2015, MNRAS, 449, 243

Navarro J. F., Frenk C. S., White S. D. M., 1997, ApJ, 490, 493

Netzer H., 2015, ARA&A, 53, 365

Norberg P., et al., 2002, MNRAS, 336, 907

Okamoto T., Gao L., Theuns T., 2008, MNRAS, 390, 920

Oke J. B., 1974, ApJs, 27, 21

Padmanabhan N., et al., 2008, ApJ, 674, 1217

Peebles P. J. E., 1982, ApJl, 263, L1

Peng C. Y., Ho L. C., Impey C. D., Rix H.-W., 2010, AJ, 139, 2097

Penzias A. A., Wilson R. W., 1965, ApJ, 142, 419

Pforr J., Maraston C., Tonini C., 2012, MNRAS, 422, 3285

Planck Collaboration et al., 2014, A&A, 571, A16

Popescu C. C., Tuffs R. J., 2002, MNRAS, 335, L41

Press W. H., Schechter P., 1974, ApJ, 187, 425

Price D. J., 2008, Journal of Computational Physics, 227, 10040

Qu Y., et al., 2017, MNRAS, 464, 1659

Quilis V., Moore B., Bower R., 2000, Science, 288, 1617

Rafferty D. A., McNamara B. R., Nulsen P. E. J., Wise M. W., 2006, ApJ, 652, 216

Rahmati A., Schaye J., Bower R. G., Crain R. A., Furlong M., Schaller M., Theuns T., 2015, preprint, (arXiv:1503.05553)

Rees M. J., 1986, MNRAS, 218, 25P

Relaño M., Kennicutt Jr. R. C., 2009, ApJ, 699, 1125

Rix H.-W., Zaritsky D., 1995, ApJ, 447, 82

Robotham A., et al., 2010, PASA, 27, 76

Roediger E., Brüggen M., 2007, MNRAS, 380, 1399

Roediger E., Brüggen M., 2008, MNRAS, 388, 465

Rosario D. J., et al., 2012, A&A, 545, A45

Rosas-Guevara Y. M., et al., 2015, MNRAS, 454, 1038

Rosdahl J., Schaye J., Teyssier R., Agertz O., 2015, preprint, (arXiv:1501.04632)

Rosdahl J., Schaye J., Dubois Y., Kimm T., Teyssier R., 2017, MNRAS, 466, 11

Rubin V. C., Ford Jr. W. K., Thonnard N., 1980, ApJ, 238, 471

Saftly W., Camps P., Baes M., Gordon K. D., Vandewoude S., Rahimi A., Stalevski M., 2013, A&A, 554, A10

Saftly W., Baes M., De Geyter G., Camps P., Renaud F., Guedes J., De Looze I., 2015, A&A, 576, A31

Sales L. V., Navarro J. F., Schaye J., Dalla Vecchia C., Springel V., Booth C. M., 2010, MNRAS, 409, 1541

Sales L. V., et al., 2015, MNRAS, 447, L6

Salim S., et al., 2007, ApJs, 173, 267

Salpeter E. E., 1955, ApJ, 121, 161

Sandage A., Visvanathan N., 1978, ApJ, 225, 742

Saunders W., Rowan-Robinson M., Lawrence A., Efstathiou G., Kaiser N., Ellis R. S., Frenk C. S., 1990, MNRAS, 242, 318

Sawala T., et al., 2014, preprint, (arXiv:1406.6362)

Sawicki M., Yee H. K. C., 1998, AJ, 115, 1329

Scannapieco C., Gadotti D. A., Jonsson P., White S. D. M., 2010, MNRAS, 407, L41

Scannapieco C., et al., 2012, MNRAS, 423, 1726

Schaller M., et al., 2014, preprint, (arXiv:1409.8617)

Schaller M., Dalla Vecchia C., Schaye J., Bower R. G., Theuns T., Crain R. A., Furlong M., McCarthy I. G., 2015a, MNRAS

Schaller M., et al., 2015b, MNRAS, 452, 343

Schawinski K., et al., 2014, MNRAS, 440, 889

Schaye J., 2004, ApJ, 609, 667

Schaye J., Dalla Vecchia C., 2008, MNRAS, 383, 1210

Schaye J., et al., 2010, MNRAS, 402, 1536

Schaye J., et al., 2015, MNRAS, 446, 521

Schechter P., 1976, ApJ, 203, 297

Shapley H., Curtis H. D., 1921, The scale of the universe. Vol. 2, National research council of the National academy of sciences

Sharp R., et al., 2006, in Society of Photo-Optical Instrumentation Engineers (SPIE) Conference Series. p. 62690G (arXiv:astro-ph/0606137), doi:10.1117/12.671022

Shen S., Mo H. J., White S. D. M., Blanton M. R., Kauffmann G., Voges W., Brinkmann J., Csabai I., 2003, MNRAS, 343, 978

Sijacki D., Springel V., Di Matteo T., Hernquist L., 2007, MNRAS, 380, 877

Simard L., Mendel J. T., Patton D. R., Ellison S. L., McConnachie A. W., 2011, ApJs, 196, 11

Sivanandam S., Graham J. R., Abraham R., Tekatch A., Steinbring E., Ngan W., Welch D. L., Law N. M., 2012, in Society of Photo-Optical Instrumentation Engineers (SPIE) Conference Series. p. 43 (arXiv:1206.6901), doi:10.1117/12.926251

Smethurst R. J., et al., 2015, MNRAS, 450, 435

Smoot G. F., et al., 1992, ApJl, 396, L1

Sobral D., Smail I., Best P. N., Geach J. E., Matsuda Y., Stott J. P., Cirasuolo M., Kurk J., 2013, MNRAS, 428, 1128

Sodre L., Ribeiro da Silva A., Santos W. A., 2013, MNRAS, 434, 2503

Somerville R. S., Davé R., 2015, ARA&A, 53, 51

Sorba R., Sawicki M., 2015, MNRAS, 452, 235

Springel V., 2005, MNRAS, 364, 1105

Springel V., 2010, MNRAS, 401, 791

Springel V., White S. D. M., Tormen G., Kauffmann G., 2001, MNRAS, 328, 726

Springel V., Di Matteo T., Hernquist L., 2005a, MNRAS, 361, 776

Springel V., et al., 2005b, Nature, 435, 629

Springel V., Frenk C. S., White S. D., 2006, Nature, 440, 1137

Stalevski M., Fritz J., Baes M., Nakos T., Popović L. Č., 2012, MNRAS, 420, 2756

Stalevski M., Ricci C., Ueda Y., Lira P., Fritz J., Baes M., 2016, MNRAS, 458, 2288

Stancliffe R. J., Jeffery C. S., 2007, MNRAS, 375, 1280

Stanley F., Harrison C. M., Alexander D. M., Swinbank A. M., Aird J. A., Del Moro A., Hickox R. C., Mullaney J. R., 2015, MNRAS, 453, 591

Steinacker J., Baes M., Gordon K. D., 2013, ARA&A, 51, 63

Stoughton C., et al., 2002, AJ, 123, 485

Strateva I., et al., 2001, AJ, 122, 1861

Strauss M. A., et al., 2002, AJ, 124, 1810

Taylor E. N., Franx M., Brinchmann J., van der Wel A., van Dokkum P. G., 2010, ApJ, 722, 1

Taylor E. N., et al., 2011, MNRAS, 418, 1587

Taylor E. N., et al., 2015, MNRAS, 446, 2144

Tempel E., Saar E., Liivamägi L. J., Tamm A., Einasto J., Einasto M., Müller V., 2011, A&A, 529, A53

Thoul A. A., Weinberg D. H., 1995, ApJ, 442, 480

Tokunaga A. T., Vacca W. D., 2005, PASP, 117, 1459

Torrey P., et al., 2014, preprint, (arXiv:1411.3717)

Torrey P., et al., 2015, MNRAS, 447, 2753

Trayford J. W., et al., 2015, MNRAS, 452, 2879

Trayford J. W., Theuns T., Bower R. G., Crain R. A., Lagos C. d. P., Schaller M., Schaye J., 2016, MNRAS, 460, 3925

Trayford J. W., et al., 2017, preprint, (arXiv:1705.02331)

Tremonti C. A., et al., 2004, ApJ, 613, 898

Tuffs R. J., Popescu C. C., Völk H. J., Kylafis N. D., Dopita M. A., 2004, A&A, 419, 821

Tully R. B., Fisher J. R., 1977, A&A, 54, 661

Veilleux S., Cecil G., Bland-Hawthorn J., 2005, ARA&A, 43, 769

Veilleux S., et al., 2013, ApJ, 776, 27

Viaene S., et al., 2016a, preprint, (arXiv:1609.08643)

Viaene S., et al., 2016b, A&A, 586, A13

Vogelsberger M., et al., 2014, MNRAS, 444, 1518

Volonteri M., Capelo P. R., Netzer H., Bellovary J., Dotti M., Governato F., 2015, MNRAS, 452, L6

Vulcani B., Poggianti B. M., Finn R. A., Rudnick G., Desai V., Bamford S., 2010, ApJ, 710, L1

Walcher C. J., et al., 2008, A&A, 491, 713

Walcher J., Groves B., Budavári T., Dale D., 2011, Ap&SS, 331, 1

Weiner B. J., et al., 2009, ApJ, 692, 187

Wendland H., 1995, Advances Comput. Math., 4, 389

Wetzel A. R., Tinker J. L., Conroy C., van den Bosch F. C., 2013, MNRAS, 432, 336

Whitaker K. E., et al., 2011, ApJ, 735, 86

White S. D. M., Frenk C. S., 1991, ApJ, 379, 52

White S. D. M., Rees M. J., 1978, MNRAS, 183, 341

Whitney B. A., 2011, Bulletin of the Astronomical Society of India, 39, 101

Wiersma R. P. C., Schaye J., Smith B. D., 2009a, MNRAS, 393, 99

Wiersma R. P. C., Schaye J., Theuns T., Dalla Vecchia C., Tornatore L., 2009b, MNRAS, 399, 574

Wild V., Kauffmann G., Heckman T., Charlot S., Lemson G., Brinchmann J., Reichard T., Pasquali A., 2007, MNRAS, 381, 543

Wild V., Charlot S., Brinchmann J., Heckman T., Vince O., Pacifici C., Chevallard J., 2011, MNRAS, 417, 1760

Wild V., et al., 2014, MNRAS, 440, 1880

Willett K. W., et al., 2013, MNRAS, 435, 2835

Williams R. J., Quadri R. F., Franx M., van Dokkum P., Labbé I., 2009, ApJ, 691, 1879

Wisnioski E., et al., 2015, ApJ, 799, 209

Witt A. N., Thronson Jr. H. A., Capuano Jr. J. M., 1992, ApJ, 393, 611

Worthey G., 1994, ApJs, 95, 107

Wright T., 1750, An Original Theory Or New Hypothesis of the Universo, Founded Upon the Laws of Nature, and Solving by Mathematical Principles the General Phaenomena of the Visible Creation and Particularly the Via Lactea. Chapelle

Wuyts S., et al., 2007, ApJ, 655, 51

Wuyts S., Franx M., Cox T. J., Hernquist L., Hopkins P. F., Robertson B. E., van Dokkum P. G., 2009a, ApJ, 696, 348

Wuyts S., et al., 2009b, ApJ, 700, 799

Wuyts S., et al., 2011, ApJ, 742, 96

Wyder T. K., et al., 2007, ApJs, 173, 293

Xilouris E. M., Byun Y. I., Kylafis N. D., Paleologou E. V., Papamastorakis J., 1999, A&A, 344, 868

York D. G., et al., 2000, AJ, 120, 1579

Zafar T., Watson D., 2013, A&A, 560, A26

Zahid H. J., Yates R. M., Kewley L. J., Kudritzki R. P., 2013, ApJ, 763, 92

Zahid H. J., Dima G. I., Kudritzki R.-P., Kewley L. J., Geller M. J., Hwang H. S., Silverman J. D., Kashino D., 2014, ApJ, 791, 130

Zaragoza-Cardiel J., Font J., Beckman J. E., García-Lorenzo B., Erroz-Ferrer S., Gutiérrez L., 2014, MNRAS, 445, 1412

Zehavi I., et al., 2005, ApJ, 630, 1

Zehavi I., et al., 2011, ApJ, 736, 59

Zibetti S., Charlot S., Rix H.-W., 2009, MNRAS, 400, 1181

Zibetti S., Gallazzi A., Charlot S., Pierini D., Pasquali A., 2013, MNRAS, 428, 1479

Zubko V., Dwek E., Arendt R. G., 2004, ApJs, 152, 211

Zucca E., et al., 2009, A&A, 508, 1217

Zurita A., Rozas M., Beckman J. E., 2000, A&A, 363, 9

Zwicky F., 2009, General Relativity and Gravitation, 41, 207

da Cunha E., Charlot S., Elbaz D., 2008, MNRAS, 388, 1595

da Silva R. L., Fumagalli M., Krumholz M., 2012, ApJ, 745, 145

von der Linden A., Wild V., Kauffmann G., White S. D. M., Weinmann S., 2010, MNRAS, 404, 1231

Appendix A

EAGLE photometry

A.1 Re-sampling

Young stellar populations are optically much brighter and bluer than older populations, due to the presence of O, B and A type stars. As such, the convergence of optical magnitudes and colours depend on wavelength and star formation in a complex way. Coarse sampling of young star particles is expected to introduce Poisson scatter in the colour distribution of low-mass galaxies. The standard resolution particle mass of $m_g = 2 \times 10^6 \mathrm{M}_\odot$ is $\sim$2 orders of magnitude larger than individual HII regions (Zaragoza-Cardiel et al., 2014; Relaño & Kennicutt, 2009), so this scatter may be artificially high in the simulations compared to observed galaxies.

To mitigate this effect, we re-sample recent star formation in the simulation outputs at finer mass resolution than the simulation gas particle mass. The re-sampling procedure assumes that the galactic star formation rate is constant over the previous 100 Myr of galaxy evolution. The general procedure is outlined below.

Gas particles with non-zero star formation rates and star particles that formed within the past 100 Myr are first identified. Star formation rates of progenitor gas particles are then obtained for the selected star particles. We calculate the star formation rates for star particles using the stored gas density at birth and initial particle masses (see Schaye, 2004), and assume that the progenitor particles lie on

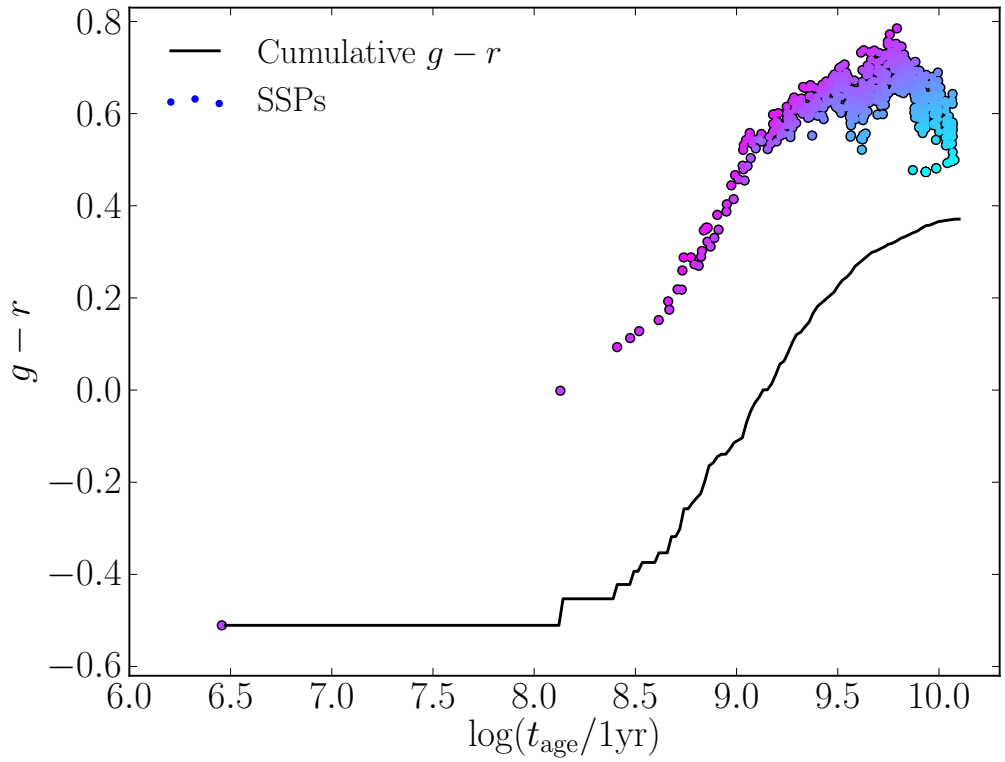

Figure A.1: Demonstration of the re-sampling technique for the stellar component of an example EAGLE galaxy from the 50^3 Mpc^3 box at redshift $z = 0.1$. This panel shows particle SSP $g - r$ colours as a function of starburst age for an individual EAGLE galaxy as points coloured from blue to magenta indicating low to high metallicity. The black line indicates the cumulative galaxy colour when including particles with increasing age (from left to right) so that the far right point of the line gives the total galaxy colour. {*continued on next page...*}

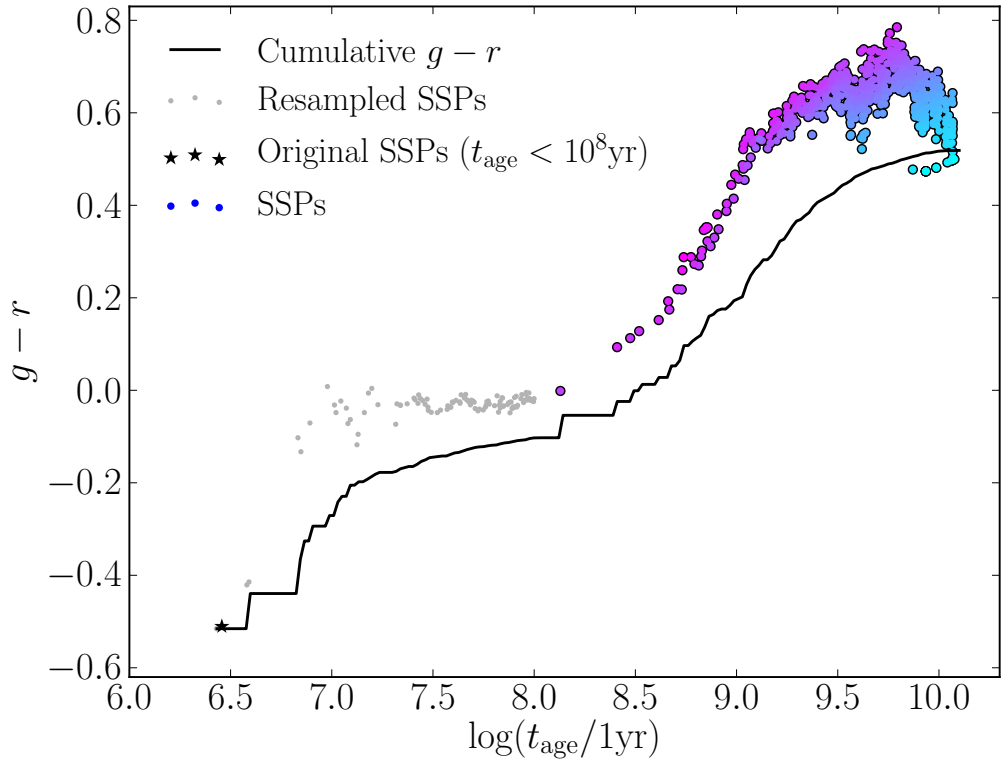

Figure A.1: {*Continued from previous page*} This panel shows the same galaxy after star particles of age < 100 Myr have been re-sampled. These particles (black stars; only one in this example) are removed from the photometry calculation and the re-sampled stars (grey points) are included. This changes the cumulative $g-r$ indicated by the black line, and yields a different overall colour.

the equation of state (see S15). We then take the sum of the star formation rates found for the gas and young stars to be the galactic star formation rate.

We then use some discretisation mass, $m_{\rm dis}$, to represent the mass of re-sampled star particles. Each selected star or gas particle is split into the integer number of equal-mass subparticles yielding a subparticle mass closest to $m_{\rm dis}$. We also obtain the ratio of subparticle mass over progenitor particle star formation rate and interpret this as a conversion timescale for each subparticle to become a star particle. We then randomly sample individual conversion times t for subparticles using an exponential distribution of the appropriate timescale. If $t < 100$ Myr, a subparticle is deemed to be converted into a star particle with $t_{\rm age} = t_i$, a mass equal to the subparticle mass and the $Z_\star$ value inherited from the parent particle.

For our analysis we use $m_{\rm dis} = 10^4$ M$_\odot$ as our target re-sampling mass resolution. This represents a more reasonable HII region mass, to better reproduce the discretisation in observed galaxies. To illustrate the effect of re-sampling, the first panel of Figure A.1 shows the $g - r$ colour and age of individual star particles in an actively star-forming EAGLE galaxy. We also plot the cumulative colour of the galaxy by star particle age as a black line. This shows the influence that the few youngest star particles can have on the colour of the entire galaxy. The first and second panels show the result with and without re-sampling respectively, yielding different overall colours for the galaxy (seen as the rightmost point of the black line). The presence of a single very young star particle in the simulation output causes this galaxy to appear ~ 0.2 mag bluer than with re-sampling. Though re-sampling can have a significant effect on individual galaxy colours, the colour distributions for the entire EAGLE population are only marginally affected. At the low-mass end, the re-sampling generally serves to tighten the $g-r$ colour distribution, move the blue peak to slightly bluer colours (~ 0.05 mag) and to suppress extremely blue outliers.

A.2 Colour Convergence

As simulation Recal-25 has a factor of 8 finer mass resolution than the fiducial model Ref-100, the stellar mass threshold above which galaxies are considered well resolved is pushed to lower masses. By comparing colour distributions of the Ref-100, Ref-25 and Recal-25 simulations (Table 2.1, S15) for galaxies within a certain mass range, we attempt to decouple the effects of simulation volume and resolution on the colours of low-mass galaxies in EAGLE. In Figure A.2 we compare colour distributions for galaxies of mass $9.45 < \log(\mathrm{M}_*/\mathrm{M}_\odot) \leq 10.05$ and $8.7 < \log(\mathrm{M}_*/\mathrm{M}_\odot) \leq 9.3$ in the first and second panels respectively. The histograms for differing simulation volumes have different y axis ranges, with the 25 Mpc simulation axis range a factor of 64 smaller to account for the differing simulation volumes.

In the $9.45 < \log(\mathrm{M}_*/\mathrm{M}_\odot) \leq 10.05$ mass range, the position of the red and blue peaks appear roughly the same in the different simulations. However, the relative strengths of the red and blue populations differ, with the red sequence being significantly weaker than the blue cloud in the high-resolution Recal-25 model compared to Ref-100 and Recal-25. This is consistent with the lower passive fractions in the high resolution simulation at $z = 0.1$ shown in S15.

The $8.7 < \log(\mathrm{M}_*/\mathrm{M}_\odot) \leq 9.3$ range shows less consistency, with the red sequence becoming practically absent in the Recal-25 model while remaining in the Ref-100 and Ref-25 models. The redder colour and larger scatter of the blue population in the reference model is attributable to poor sampling of star forming gas in these galaxies. The lower star formation rates in the fiducial volume may also account for the different colours. However, we also see a larger difference between Ref-25 and Ref-100 here, particularly in the relative contributions of the red and blue populations. We attribute the higher contribution of the red sequence in the Ref-100 model to the presence of large cluster environments in the Ref-100 simulations, and thus quenched satellite galaxies, that are not sampled by the Ref-25 box. This suggests that volume effects also contribute to the weaker red sequence seen in the Recal-25 box. In both plots the greater area un-

der the Recal-25 histogram is indicative of the systematic shift in galaxy number densities between the simulations, also seen in Figure 3.3.

A.3 SSP Parameter Influence

As intrinsic galaxy colours are sensitive to star formation histories and elemental abundance patterns, comparing EAGLE model colours directly to observed galaxy colours is a difficult way to disentangle the influence of different SSP parameters and to identify the source of any discrepancies.

To go some way towards assessing how the EAGLE stellar metallicities and star formation histories influence our mock photometry, we use the simple photometric model without dust (N). Two sets of photometric data are first generated for the simulated galaxy sample using simulation output for one parameter while using empirical relations for the other. The galaxy metallicities and light-weighted ages (LWAs) as functions of stellar mass presented by Gallazzi et al. (2005) are used to provide the empirical input. For the LWA values, we include a Gaussian scatter about the median values of the published width, which is assumed to be uncorrelated with metallicities. Clearly the assumption that galaxies may be treated as a single starburst and that the metallicity and age parameters are uncorrelated are poor, so the amount of information that can be drawn from this type of analysis is limited. Rather, this comparison serves as a basic qualitative illustration of the influence of different SSP parameters on galaxy colours.

The colour distributions in four M_* bins are plotted for the simulation-empirical hybrid photometry models, and are compared to the EAGLE photometry in Figure A.3. The black lines indicate distributions of Ref-100 simulation galaxies. The distributions using the raw emission model with EAGLE ages and metallicities are plotted as solid histograms. The photometry models using observed LWA and Z_* values are plotted as the dashed and dotted lines, respectively. The observational data of Taylor et al. (2015) are also plotted in blue for comparison.

We see that the age parameter has the biggest influence on the colour distribution, with the empirical ages introducing a generally larger spread than metal-

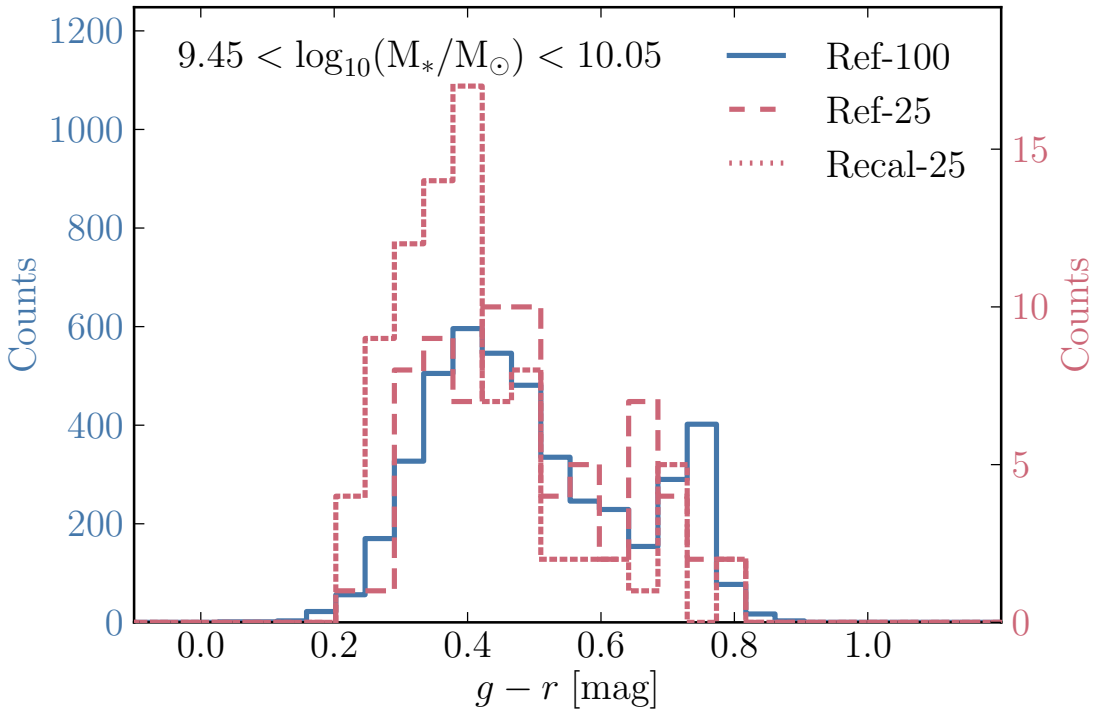

Figure A.2: Comparison of $g - r$ colour distributions of the Ref-100, Ref-25 and Recal-25 simulations (see table 2.1) to assess the weak convergence and volume effects on model colours. Ref-100 and Ref-25 have the same resolution, while Recal-25 has a resolution 8 times finer. This panel panel shows the galaxy stellar mass range of $9.45 < \log(M_*/M_\odot) \leq 10.05$, respectively. Blue and red histograms represent the counts per colour bin in the 100 Mpc and 25 Mpc simulations respectively. The Ref-100, Recal-25 and Ref-25 simulations, are plotted as solid, dotted and dashed lines respectively. Separate y-axes are labelled and coloured to correspond to the 100 Mpc (left) and 25 Mpc (right), with their ranges scaled by a factor of 64 to account for the differing box volume. {*continued on next page...*}

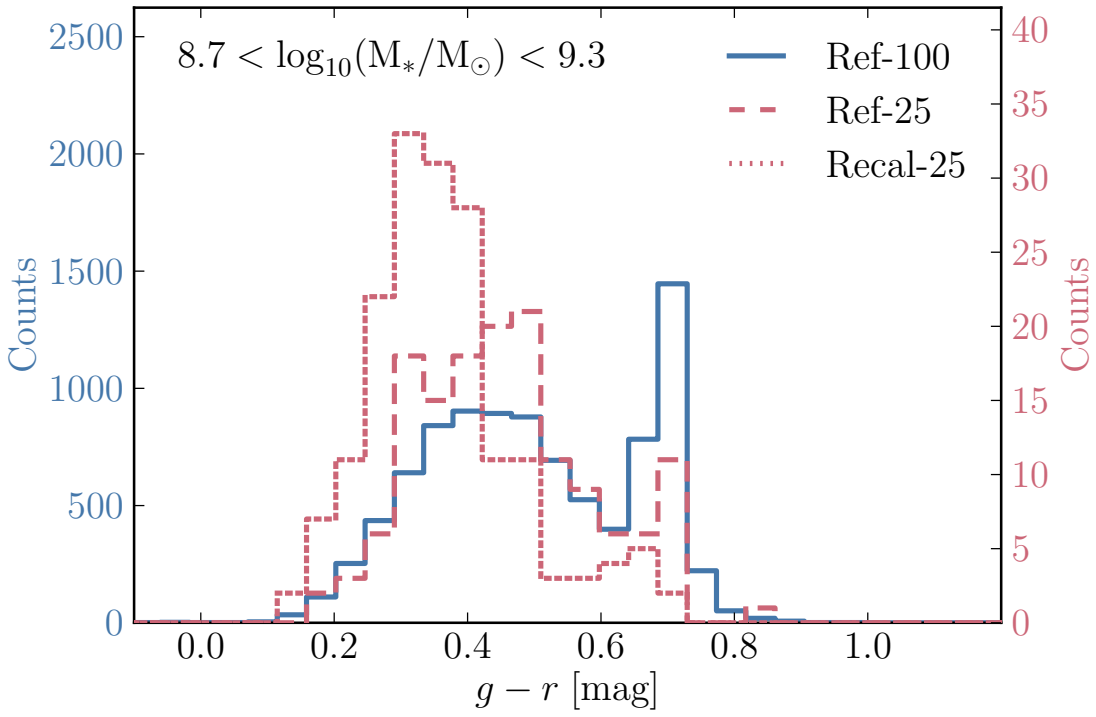

Figure A.2: {*Continued from previous page*} As previous panel, now for lower galaxy stellar masses in the range $8.7 < \log(M_*/M_\odot) \leq 9.3$. Both resolution and box size appear to significantly effect the colour distributions of low-mass EAGLE galaxies.

licities, when compared to the pure EAGLE photometry. We have verified that this is still the case when we include the scatter on observed metallicity values. Figure A.3 shows that giving galaxies a single age stellar population using the observational LWA data of Gallazzi et al. (2005) (dashed line) works reasonably well in the two most massive bins where stellar populations are old. However in the lower-mass bins where galaxies are generally younger they provide a poor fit to the observed colours, inferior to our model photometry using the complex star formation histories of EAGLE (solid line).

The bimodality seen for the full EAGLE photometry in the two most massive bins, but not for the observational LWA model, shows that the EAGLE populations are intrinsically bimodal in age. This supports the assertion that there is an excess of star forming galaxies in this regime relative to the observed population. The bluer than observed high-$M_\star$ red sequence in the observational LWA model could be a result of the lower metallicities of high-$M_\star$ galaxies. The inferior agreement of the observational LWA model relative to the full EAGLE model in the lower-mass bins suggests that the complex star formation histories of EAGLE reproduce the data better than an empirical model assuming a single age population.

The observational Z model reveals a poor fit to observation for the two highest-mass bins. The red sequence is also much less prominent than seen in the observations and the other models across the M_* range.

The systematic effect of assuming uncorrelated scatter between the age parameter may also account for the fact that the colour distributions are broader and flatter than observed for this model, especially in the low-mass bins.

The resolution effects that drive much improved agreement between observed low-mass colours and Recal-25 relative to Ref-100 are noted in section 3.3 and appendix A.2. In the lowest-mass bin of Figure A.3, we see that using observed metallicities has less impact on EAGLE colours than using observed LWAs. This indicates that star formation rate resolution is the primary resolution effect on colours, with metallicity resolution secondary to this. The presence of a faint red sequence is due to lower star formation rates and higher stellar ages than found in low-mass Ref-100 galaxies, whereas the position of the red sequence is redder

Band	ϕ_* [h^3 cMpc^{-3} mag^{-1}]	α	$-2.5\log_{10}(L_\star/h^2)$ [mag]	Range [mag]
u	$13.7^{+1.8}_{-1.5} \times 10^{-3}$	$-1.11^{+0.04}_{-0.03}$	$-18.8^{+0.1}_{-0.2}$	[-14.0, -21.0]
g	$11.1^{+1.4}_{-1.3} \times 10^{-3}$	$-1.17^{+0.03}_{-0.03}$	$-20.1^{+0.2}_{-0.2}$	[-14.0, -22.5]
r	$9.5^{+1.5}_{-1.3} \times 10^{-3}$	$-1.21^{+0.04}_{-0.03}$	$-20.7^{+0.2}_{-0.2}$	[-14.2, -23.2]
i	$7.6^{+0.8}_{-0.8} \times 10^{-3}$	$-1.26^{+0.02}_{-0.02}$	$-21.2^{+0.1}_{-0.2}$	[-16.0, -24.0]
z	$6.7^{+0.8}_{-0.6} \times 10^{-3}$	$-1.28^{+0.02}_{-0.02}$	$-21.6^{+0.1}_{-0.2}$	[-16.0, -24.0]
Y	$6.2^{+0.7}_{-0.7} \times 10^{-3}$	$-1.29^{+0.02}_{-0.02}$	$-21.9^{+0.1}_{-0.2}$	[-16.0, -24.5]
J	$5.9^{+0.6}_{-0.6} \times 10^{-3}$	$-1.29^{+0.02}_{-0.02}$	$-22.0^{+0.1}_{-0.2}$	[-16.0, -24.5]
H	$5.5^{+0.6}_{-0.6} \times 10^{-3}$	$-1.30^{+0.02}_{-0.02}$	$-22.3^{+0.1}_{-0.2}$	[-16.0, -24.5]
K	$5.6^{+0.6}_{-0.5} \times 10^{-3}$	$-1.29^{+0.02}_{-0.01}$	$-22.0^{+0.1}_{-0.2}$	[-16.0, -24.5]

Table C1: Best-fitting Schechter function (Eq. 3.3.7) parameters for EAGLE AB-magnitude luminosity functions in $ugrizYJHK$ using the GD+O photometry for simulation Ref-100 at redshift $z = 0.1$. The EAGLE luminosity functions are fit over the magnitude range indicated in the final column. Errors on the best-fit parameters were computed using jackknife sampling.

by ~ 0.1 due to the higher than observed metallicities at these masses. The star formation rate resolution is also the main contributor to the redder than observed blue cloud position in Ref-100.

A.4 Schechter fits

Table C1 provides best-fit Schechter function parameters for the GD+O $ugrizYJHK$ EAGLE luminosity functions. Each luminosity function is fit over a range indicated in the final column using χ^2 minimisation. In the fitting, Poisson errors are assumed for the ϕ values of each bin and additionally weighted by the median bin luminosity. This weighting causes bins close to $L_\star$ to most strongly constrain the fit, similar to observed luminosity functions.

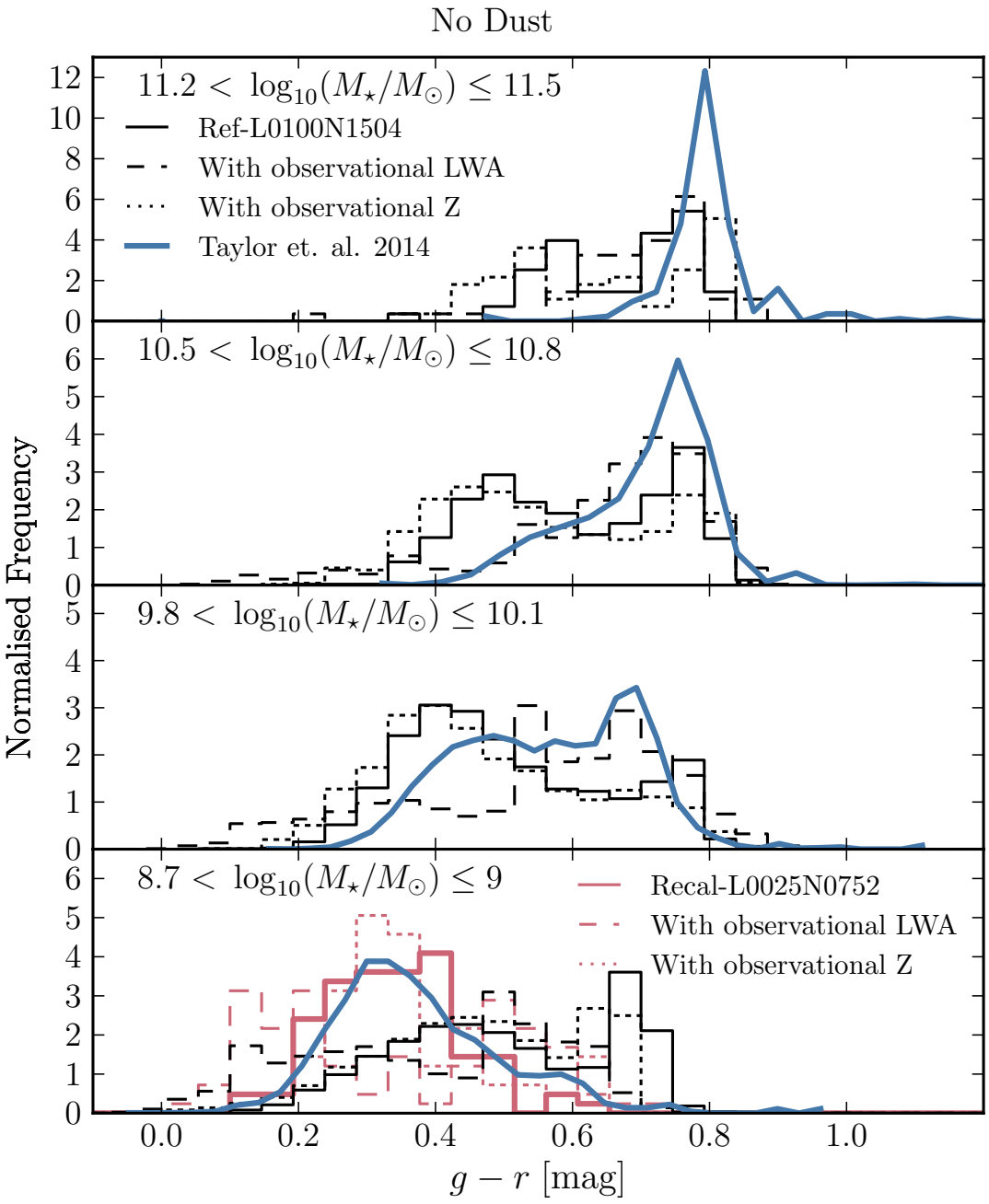

Figure A.3: $g - r$ colour distributions for EAGLE galaxies for the dust-free model. The 4 panels show colour distributions for 4 bins of stellar mass, as indicated by the legend. The solid, dotted and dashed lines show the EAGLE SSP values and the EAGLE SSP values with Gallazzi et al. (2005) metallicities and ages respectively. {*continued on following page...*}

Figure A.3: {*Continued from previous page*} Gallazzi metallicities and ages are assigned to each galaxy, based on the median parameter values at the galactic stellar mass. Z values are simply taken as the observed median value. The LWA values are sampled from a normal distribution with standard deviation taken from Gallazzi et. al. (2005), assuming that the scatter in age and metallicity is uncorrelated. We see that the complex star formation histories of EAGLE provide a better match to the observed colour distributions than a single SSP model using empirical values for age and metallicity.

Appendix B

Radiative Transfer

B.1 Smoothing Lengths

Star and gas particles in EAGLE function as tracers of the baryonic mass. Because particles are the smallest resolution elements in the simulations, the distribution of the material represented by a single particle is unresolved. However, some 3D form for the traced material needs to be assumed to facilitate radiative transfer with SKIRT. A kernel distribution is thus used to set the density profile of the stars and gas. A truncated Gaussian distribution is used to approximate the cubic spline kernel used by the EAGLE simulations in SKIRT (Altay & Theuns, 2013; Baes & Camps, 2015). As this is isotropic, it is parametrised solely by a position and a smoothing length.

Smoothing lengths are tracked by EAGLE for baryonic particles on the fly (see S15, appendix A). These values are derived using the distance to the weighted Nth nearest neighbouring gas particle, to facilitate SPH interaction between gas and chemical enrichment of gas by stars. As such this kernel size represents the spatial smoothing of gaseous material well, but implies that for star particles the smoothing is entirely dependent on their proximity to gas.

For resolved disc galaxies in EAGLE this stellar smoothing is reasonable as the galaxies have high gas fractions, with star and gas particles being well mixed. However for a minority of gas-poor elliptical galaxies, the smoothing values may become extremely large (up to $\sim$ 70 kpc). This distorts the surface brightness

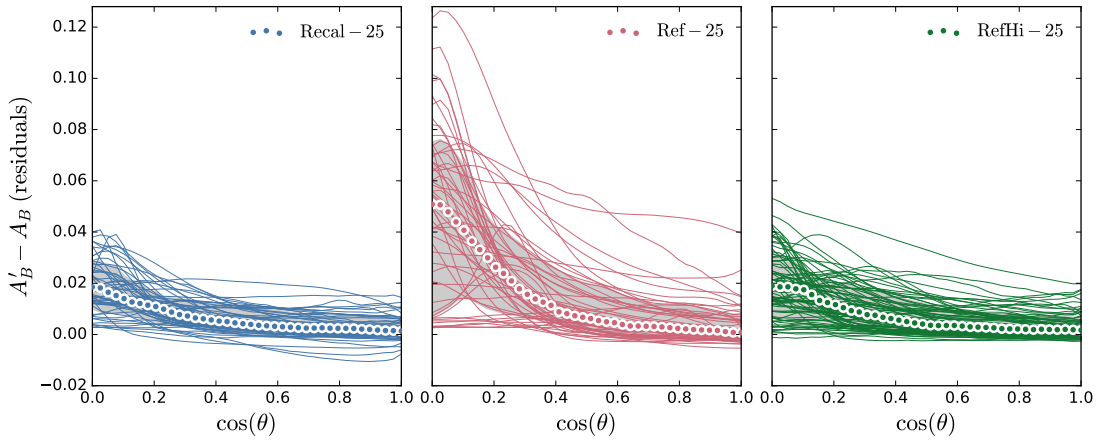

Figure B.1: The difference between r-band attenuation in EAGLE galaxies when using no smoothing (A'_B) and employing the standard nearest neighbours smoothing used in this work (A_B) plotted as a function of inclination, $\cos(\theta)$. The panels from left to right represent simulations Recal-25, Ref-25 and RefHi-25, and are also coloured blue, red and green respectively. *Thin Lines* represent $A'_B - A_B$ values of individual galaxies taken from their respective simulations at 40 inclinations evenly spaced in $\cos(\theta)$. *Shaded circles* represent the median $A'_B - A_B$ value of galaxies at each $\cos(\theta)$ value, with *grey shading* illustrating the 16th-84th percentile range. We see that not using stellar smoothing leads to a slightly stronger inclination dependence for orientation, with increased attenuation for edge-on galaxies. The maximal difference is seen for edge-on galaxies in the Ref-25 simulation, $\Delta A_B \approx 0.1$, with typical values for edge-on galaxies of $\Delta A_B \approx 0.05$.

profiles to become kernel-shaped, and renders them much more extended than the actual stellar surface density.

To alleviate this problem, we re-compute more appropriate smoothing lengths for EAGLE star particles within each galaxy. There is no unique smoothing scale for star particles that can be defined, as they do not interact with each other using an SPH kernel. Using the same smoothing length calculation between star particles as between gas particles also results in significantly smaller smoothing lengths, due to a higher fraction of galaxy mass being in stars than gas, and such small smoothing lengths yields unrealistic granularity in galaxy images. For this reason we use a somewhat *ad-hoc* method of 'morphological convergence', observing galaxy images smoothed on a variety of scales, in a similar vein to Torrey et al. (2014).

We use a kd-tree algorithm (Maneewongvatana & Mount, 2001) to identify nearby star particles. This is performed for each galaxy as it is extracted from the simulation data. We find that using as a smoothing length the distance to the 64th nearest neighbouring star particle works well, in the sense that this yields reasonable galaxy images, avoiding both unrealistic granularity and over-smoothing. Using the re-computed or simulation smoothing lengths make only marginal difference to the scientific results presented in this work. Intrinsic properties (i.e. without dust effects) are of course unaffected, as all light emitted by material within the 30 pkpc aperture is measured for consistency with previous chapters. The effect on dust attenuated properties is small because the smoothing lengths differ most in large galaxies where there is minimal gas and thus minimal attenuation.

To constrain the effect of stellar smoothing on the attenuation measured for EAGLE galaxies, we compare attenuation measured for EAGLE galaxies without any smoothing of sources (i.e. treating star particles as point sources) to those measured using the re-computed smoothing lengths. Fig. B.1 is set out in a similar way to Fig. 5.4, except we plot the *difference* between the r-band attenuation without smoothing (A'_B) and with smoothing (A_B) on the y-axis. The thin coloured lines show the residuals for individual galaxies at different orientations, and the

data points show the median residuals. Again, all galaxies of mass $M_\star > 10^{10}\mathrm{M}_\odot$ are included for each of the Ref-25, Recal-25 and RefHi-25 simulations.

We see that, in general, treating stellar particles as point sources leads to a stronger dependence of attenuation on inclination, with more attenuation for edge on inclinations. This can be understood as a higher fraction of the stellar emission emanating from near the disc plane when no smoothing is applied, as the smoothing effectively thickens the emissivity distribution of the stellar disc. Although this effect is measurable, the difference is $\lessapprox 10\%$ for the galaxies in this sample, suggesting that even an extreme choice in stellar smoothing has only a marginal effect on the integrated dust reddening for these galaxies. The difference is most pronounced for the low resolution Ref-25 galaxies, because this has lower stellar particle resolution and larger smoothing lengths for the same mass range of $M_\star > 10^{10}\mathrm{M}_\odot$.

B.2 Resolution and Convergence

B.2.1 Radiative Transfer

Here we test the convergence of photometry results with respect to the sampling of photon packages. We look at both the spectral resolution used to represent SEDs, and the number of photon packets sampled at each wavelength. In order to test this efficiently for our fiducial model, we randomly select a test sample of galaxies in 9 contiguous and logarithmically spaced mass bins, over the range $9 < \log_{10}(M_\star/\mathrm{M}_\odot) \leq 11.6$. 200 galaxies are randomly selected from each mass bin, except in the two highest mass bins where all the galaxies are sampled due to insufficient counts. The highest and second highest bins contain 23 and 64 galaxies respectively.

B.2.1.1 Sampling Noise

SKIRT tracks an equal number, N_γ, of photon packets per wavelength bin. The stochastic emission and absorption of these photon packets introduces Poisson

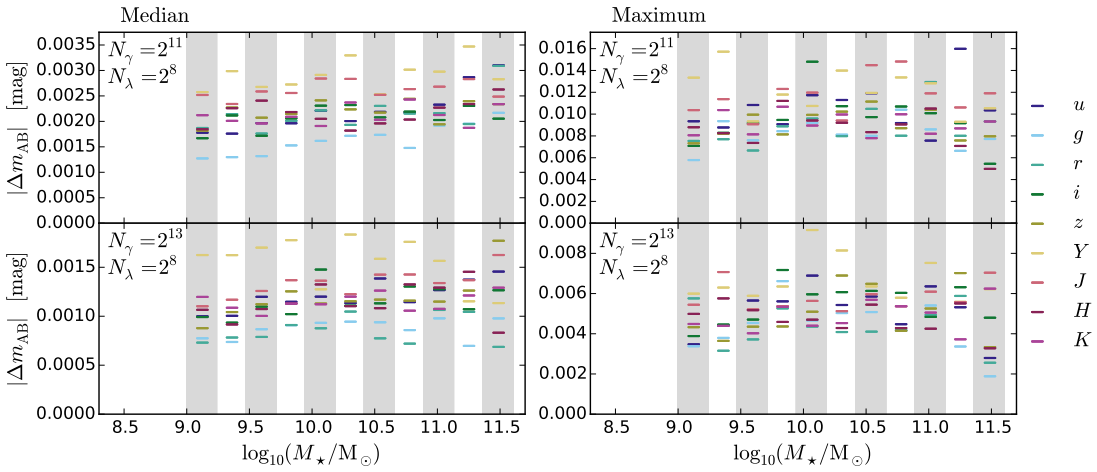

Figure B.2: SDSS $ugriz$ and UKIRT $YJHK$ absolute magnitude convergence properties for sample EAGLE galaxies (section B.2) varying the number of photon packets launched per wavelength bin, N_γ, at a constant spectral resolution. SKIRT simulations with low, medium and high N_γ values of 2^{11}, 2^{13} and 2^{15} respectively are run for each galaxy. The top and bottom panels of each column then show the comparison of the low and medium N_γ simulations with the high value respectively. The left panel shows the median absolute magnitude difference in each bin for the 9 photometric bands, the right panel shows the maximum difference.

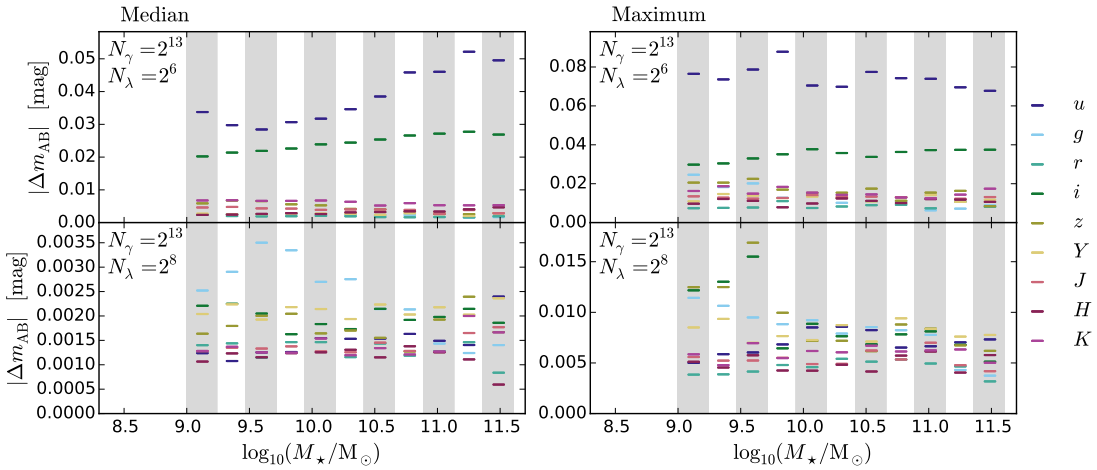

Figure B.3: As Figure B.2, but now exploring convergence as a function of continuum spectral resolution, N_λ, at fixed N_γ. SKIRT simulations with low, medium and high N_λ values of 2^7, 2^8 and 2^9 respectively are run for each galaxy. Again, the low and medium resolutions are compared to the high resolution in the top and bottom panels of each column respectively.

noise into the photometric measurements. The degree of this variation depends not only on N_λ, but also on the emissivity at each wavelength, and the complex distribution of sources and dust in the galaxy. A natural target level of convergence is variation comparable to photometric errors in SDSS observations, on the order of ~ 0.01 mag for $griz$ and ~ 0.02 mag for the u-band, dominated by uncertainty in the un-modelled atmospheric effects at Apache Point (Padmanabhan et al., 2008).

We test photometric convergence by running separate SKIRT simulations launching $N_\lambda = 2^{11}$ 2^{13} and 2^{15} photon packets per wavelength bin on each of our test sample galaxies. We then compare the variation in $ugrizYJHK$ photometry between the $N_\lambda = 2^{15}$ run and the lower N_λ runs. Figure B.2 shows this level of variation. Both the median and maximum variations are below the threshold 0.01 mag uncertainty for $ugriz$ with $N_\gamma = 2^{13}$, the number we used in chapter 5.

B.2.1.2 Spectral Resolution

To sample SEDs, SKIRT performs radiative transfer for a grid of wavelengths. The number of wavelengths we choose is a trade-off between spectral resolution and computational expense. For our purposes we want to resolve the continuum well enough to capture the overall shape of the SED and produce accurate photometry in arbitrary optical broad-bands, as well as focusing on certain spectral indices of interest. After some initial experimentation, we begin with a superposed grid of wavelengths:

1. 2^8 (256) logarithmically spaced wavelengths to sample the continuum between 280 nm and 2500 nm
2. 33 wavelengths to sample the peak and continuum either side of 11 prominent spectral lines in emission line galaxies (Stoughton et al., 2002)
3. 22 evenly spaced wavelengths to better sample the Hα and OII line profiles
4. 10 logarithmically spaced wavelengths from 150 nm to 280 nm to sample the UV slope
5. 12 additional wavelengths about the 4000Å break.

We test numerical convergence by measuring the variation between individual galaxies when different spectral resolutions are used. We vary the continuum wavelength grid resolution, (i), using the standard value of 2^8 as medium resolution and 2^7 and 2^9 as low and high resolution respectively and comparing the standard and low resolutions to the high resolution in each plot. Figure B.3 shows this level of variation.

We find that the median variation is < 0.01 mag for all bands at standard resolution, $N_\lambda = 2^8$. When looking at the most extreme outliers in each bin we see that the most extreme differences are ~ 0.015 mag in the lowest mass bin. We decide this to be sufficient resolution for our purposes.

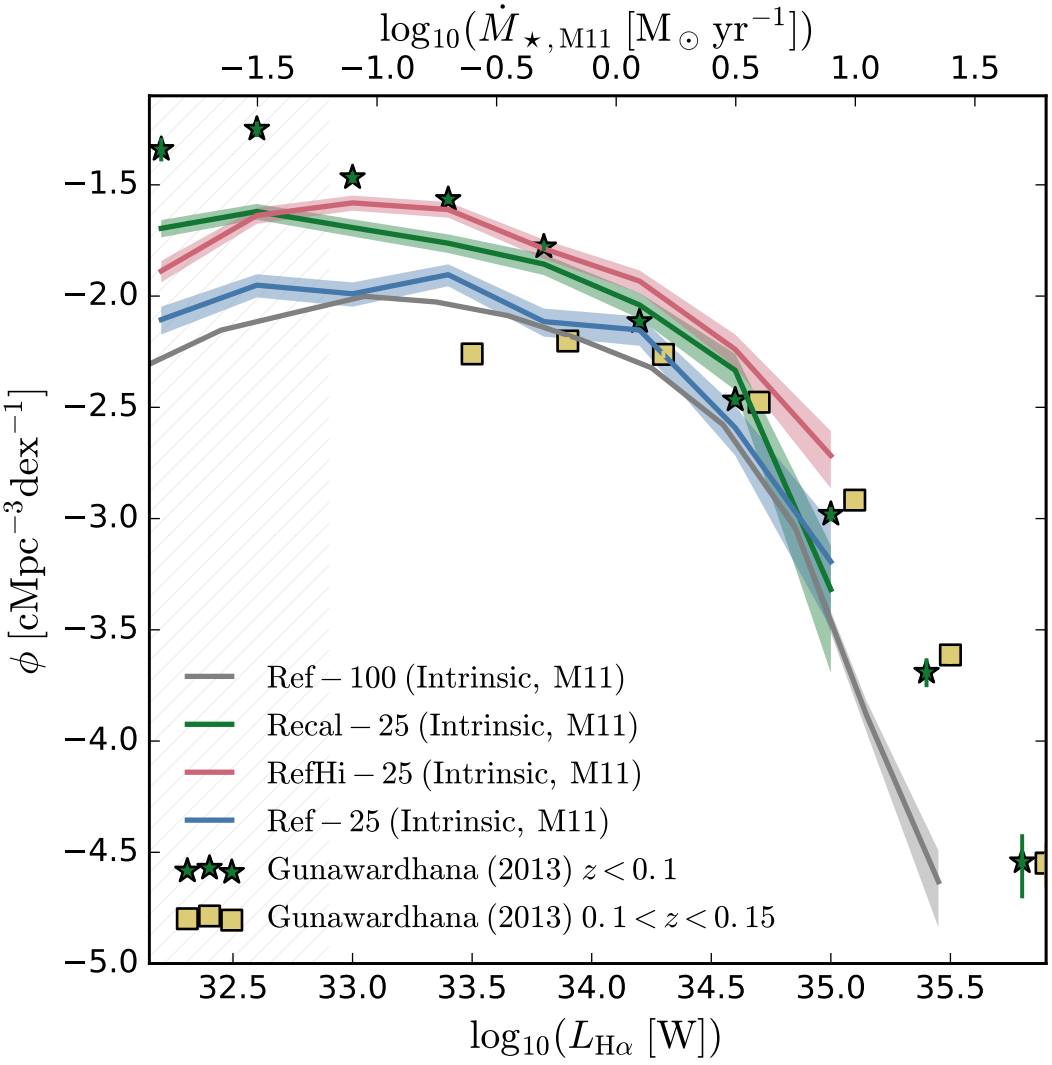

Figure B.4: As Fig. 5.12, but excluding C15 recalibrated lines and including the Ref-25 and RefHi-25 Hα luminosity functions. The Ref-100, Recal-25, RefHi-25 and Ref-25 luminosity functions are represented as *grey*, *green*, *red* and *blue* lines respectively, with Poisson error indicated by the shaded regions of the same colour.

B.2.2 Convergence of H_α Luminosity and Flux

Here we investigate the convergence properties of the Hα line fluxes, by comparing between all the simulations listed in Table 2.1 in Fig. B.4. Comparing Ref-100 and Ref-25 simulations, plotted as grey and blue lines respectively, isolates the effects of volume because the sub-grid calibration and resolution are the same. We see that the Ref-25 LF agrees better with Ref-100 than any of the other 25^3 Mpc^3 boxes. However the Ref-25 LF is still between 0 and 0.3 dex higher at all luminosities sampled. The higher number density of Hα-emitting galaxies is likely due to a 25^3 Mpc^3 being too small to represent large scale modes in the density distribution, and thus does not sample massive halos. As was shown in chapter 4, star formation is significantly suppressed within these environments in the EAGLE simulation. This could lead to the lower normalisation of the LF in the Ref-100.

Comparing the Ref-25 and Recal-25 LFs instead tests 'weak' convergence (defined by S15) with resolution. The Recal-25 LF is in general higher still, typically by ~ 0.2 dex. The higher normalisation of the Recal-25 LF is attributable to the effect of resolution on passive fractions of galaxies. As was discussed in chapter 3, coarse sampling of feedback events paired with the resolution of the star forming component of galaxies contributes to the surplus of passive galaxies seen at $(M_\star/\mathrm{M}_\odot) \lesssim 10$ in the lower resolution simulations. Because these resolution effects become significant at a factor of ~ 8 lower mass at higher resolution, the proportion of star forming galaxies at relatively low mass is more realistic. This contributes to boosting the Recal-25 LF closer to observations.

We also investigate the attenuation of the Hα line by the diffuse dust component, $A(\mathrm{H}\alpha,\ \mathrm{ISM})$, using the simulations listed in Table 2.1 in Fig. B.5. We look specifically at the ISM attenuation here, as this is controlled by the ISM structure that may vary with resolution. Taking

$$A(\mathrm{H}\alpha,\ \mathrm{ISM}) = 2.5 \log_{10}(L_{\mathrm{H}\alpha,\ \mathrm{SKIRT}}/L_{\mathrm{H}\alpha,\ \mathrm{intrinsic}}) \tag{B.2.1}$$

we plot $A(\mathrm{H}\alpha,\ \mathrm{ISM})$ as a function of star formation rate for individual galaxies with $\log_{10}(M_\star/\mathrm{M}_\odot) > 8.5$ from each simulation as grey points, over-plotting the

average attenuation in bins of star formation rate for each simulation in different colours, and indicating the scatter using the 16th-84th percentile ranges. We see that attenuation generally increases with star formation rate but exhibits a large scatter, skewed to high values. This is consistent with general observational trends. (e.g. Gunawardhana et al., 2015). We notice that the typical attenuation values are similar for all the simulations, and consistent with each other within the scatter, suggesting $A(\mathrm{H}\alpha)$ converges with resolution. This is consistent with what we find for Fig. 5.4, that attenuation is limited by the artificial pressurisation of the EAGLE ISM rather than resolution, and attenuation would likely increase if gas were able to cool to lower temperatures.

B.3 fitting SKIRT results using the GD+O model

To make a detailed comparison between the radiative transfer photometry presented in this work and the GD+O photometry of chapter 3, we calibrate the dust-screen parameters used in chapter 3 to the results obtained with SKIRT. Comparing these parameters to the fiducial GD+O values helps us understand how the models differ. This can be achieved by finding the ML parameter values using an MCMC approach.

The flux density for an EAGLE galaxy measured in a certain band using the GD+O model, $F_{\mathrm{GD+O}}$, can be expressed as

$$F_{\mathrm{GD+O}} = \left(F_{\mathrm{o}} + F_{\mathrm{y}} e^{-\hat{\tau}_{\mathrm{BC}}}\right) e^{-\hat{\tau}_{ISM} O(\theta|q)}$$

where

$$\hat{\tau}_{\mathrm{ISM}} = \tau_{\mathrm{ISM}} f_{\mathrm{M}} f_{\mathrm{Z}} \left(\tfrac{\lambda_{\mathrm{eff}}}{550\mathrm{nm}}\right)^{-0.7}, \tag{B.3.2}$$

$$\hat{\tau}_{\mathrm{BC}} = \tau_{\mathrm{BC}} f_{\mathrm{M}} f_{\mathrm{Z}} \left(\tfrac{\lambda_{\mathrm{eff}}}{550\mathrm{nm}}\right)^{-0.7}, \tag{B.3.3}$$

Here, f_{M} and f_{Z} are the star forming gas mass and metallicity in units of the Milky Way value, respectively, λ_{eff} is the effective wavelength of the filter, and F_{o} and F_{y} are the intrinsic flux densities for star particles older and younger than 10 Myr, respectively. The $O(\theta|q)$ term accounts for galaxy orientation, as detailed

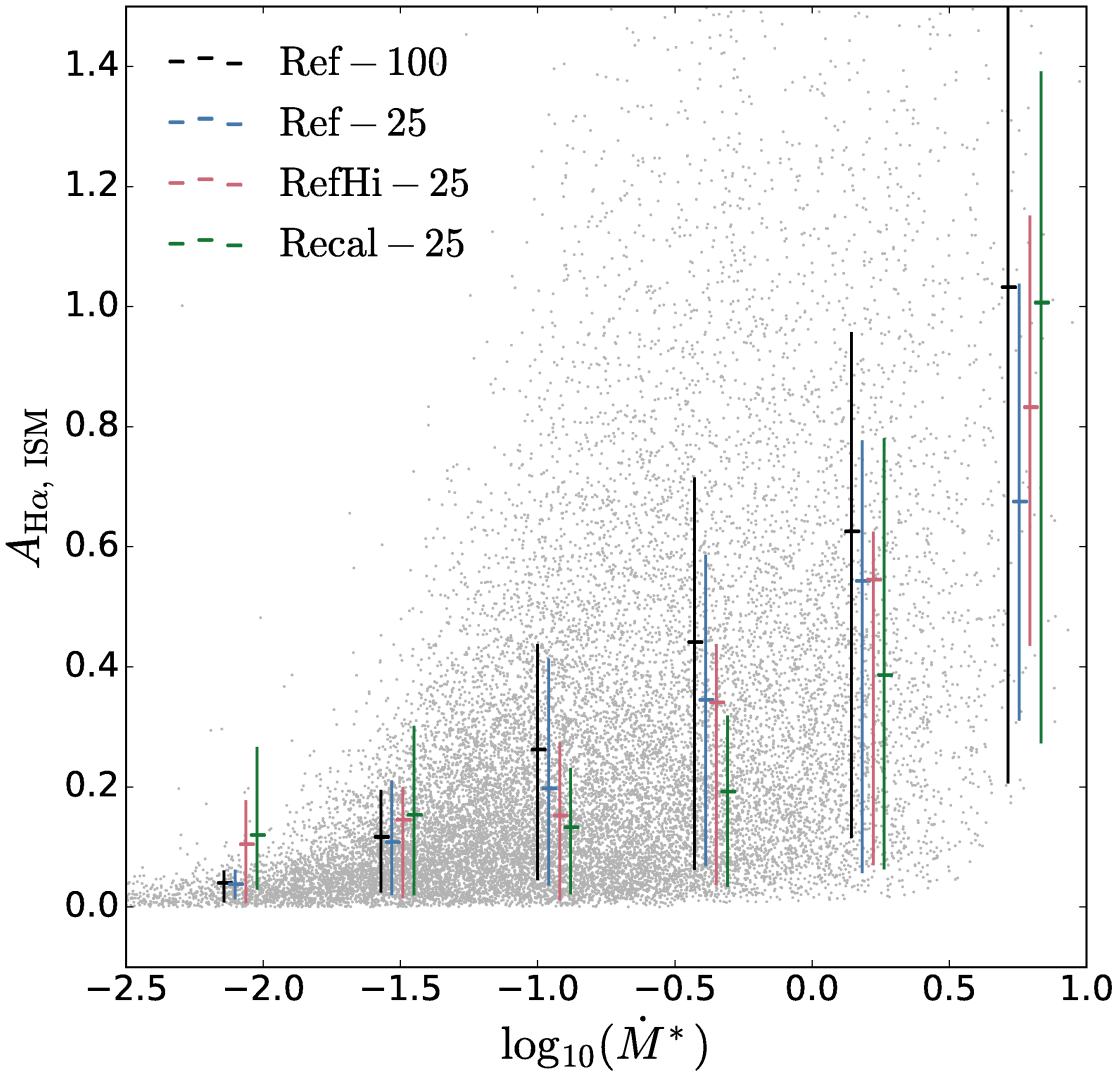

Figure B.5: Plot of $A(\mathrm{H}\alpha,\ \mathrm{ISM})$ (Eq. B.2.1) as a function of star formation. Individual galaxies with $\log_{10}(M_\star/\mathrm{M}_\odot) > 8.5$ from each simulation of Table 2.1 are plotted as *grey points*. Average values for each simulation are over-plotted as coloured points, with error bars indicating the 16th-84th percentile ranges. We see that the attenuation generally increases as a function of star formation rate, exhibiting large scatter skewed towards high values. The average relations agree between simulations within errors, suggesting that $A(\mathrm{H}\alpha,\ \mathrm{ISM})$ is well converged in our modelling.

in section 3.2.3 of chapter 3. The free parameters of the GD+O model which we fit for, are $\tau_{\rm ISM}$, $\tau_{\rm BC}$ and q, representing the typical ISM optical depth, birth cloud optical depth and dust disc axial ratio.

The attenuation applied for GD+O is deterministic, apart from the randomised orientation term, $O(\theta|q)$, where the disc inclination angle is sampled uniformly in $\cos(\theta)$. However, as we store the inclination angle of each SKIRT image, the expected $F_{\rm GD+O}$ value corresponding to a particular SKIRT galaxy observation, F_S, is fully deterministic.

Clearly, no parametrisation of the simple GD+O model can provide perfect agreement with the SKIRT photometry. The inclination also has an associated uncertainty. So that any possible F_S has a finite likelihood of being observed with a particular GD+O parametrisation, we build in a Gaussian observational tolerance. This contributes to the log-likelihood as:

$$\ln \mathcal{L}(F \mid F_{\rm GD+O}, \sigma) = C - \frac{1}{2\sigma^2} \sum_{i=1}^{n} (F_i - F_{{\rm GD+O},i})^2 \,, \tag{B.3.4}$$

where C is a constant, σ is a fixed uncertainty, and we sum over each randomly oriented $ugrizYJHK$ observation of an EAGLE galaxy sample. The constant σ value means that better resolved galaxies generally provide stronger constraints on the model, so the likelihood is effectively luminosity weighted. The exact value of σ we use is unimportant as we aim to maximise l, but should be comparable to the observations to avoid numerical errors. We use the $5^{\rm th}$ percentile of all F_S values as σ. For simplicity, we do not explicitly incorporate an additional uncertainty on our input inclination angles.

With an imperfect model, the galaxies we use to constrain our fit will affect the recovered ML parameters. However, using all galaxies may not provide the best parametrisation for those where dust is effective. For insufficiently resolved galaxies, the SKIRT dust modelling is itself unreliable, and dust effects are anyway minimal. For the most luminous galaxies the simple geometric assumptions of GD+O are inappropriate and do not help constrain the parameters. For this reason we select a sample in stellar mass . To capture sufficiently resolved galaxies over which the disc geometry assumption is appropriate, we select galaxies in

the range $10^{9.75} < M_\star/\mathrm{M}_\odot < 10^{11}$.

Initially we assume uniform prior distributions for each parameter and fit simultaneously, with the conservative ranges $q \in [0, 1)$, $\tau_{\mathrm{BC}} \in [0, 10)$ and $\tau_{\mathrm{ISM}} \in [0, 10)$. However, we found that the τ_{BC} parameter tends to ~ 10. Indeed, relaxing the prior to $\tau_{\mathrm{BC}} \in [0, 1000)$ yields a median ~ 800, such that F_{y} contributes effectively nothing to $F_{\mathrm{GD+O}}$. The reason for this may be that the spectra representing stellar populations younger than 10 Myr are intrinsically different in the models, and the clearing timescale for birth clouds is longer in Charlot & Fall (2000) (30 Myr). While GD+O uses the GALAXEV spectra (Bruzual & Charlot, 2003), the SKIRT model uses the MAPPINGS-III spectra (Groves et al., 2008). While both models account for birth-cloud reddening, the MAPPINGS-III spectra include emission lines and a different ionising spectrum (from Leitherer et al., 1999) than GALAXEV.

As a second approach, we try fixing $\tau_{\mathrm{BC}} = 2\tau_{\mathrm{ISM}}$, as suggested in the fiducial Charlot & Fall (2000) model and GD+O, while assuming the same priors for τ_{ISM} and q. The τ_{BC} parameter has only marginal influence on the photometry, as it only affects a small fraction of stars, and the fiducial GD+O value of ~ 0.67 already significantly reduces their contribution. We therefore expect that fixing $\tau_{\mathrm{BC}} = 2\tau_{\mathrm{ISM}}$ rather than allowing it to freely vary over the range $[0, 1000)$ has minimal influence on the other parameters, such that all parameter values remain physically plausible. We find that including this constraint yields ML q and τ_{ISM} values only $\sim 8\%$ and $\sim 11\%$ higher respectively. We therefore use this second approach as our default procedure.

With this set-up we recover ML values for the three parameters, which are encouragingly very close to the values assumed in chapter 3, as discussed in sections 5.4.2 and 5.6. Figure B.6 shows the posterior distribution constructed for the GD+O model parameters given the SKIRT data, with the ML listed in table 5.2. We use 1×10^5 samples, employing a burn-in of 1×10^4 samples and a thinning factor of 5. The results of this are presented in Table 5.2, and discussed in section 5.4.2. The first panel of Fig. B.6 shows the constructed posterior distribution.

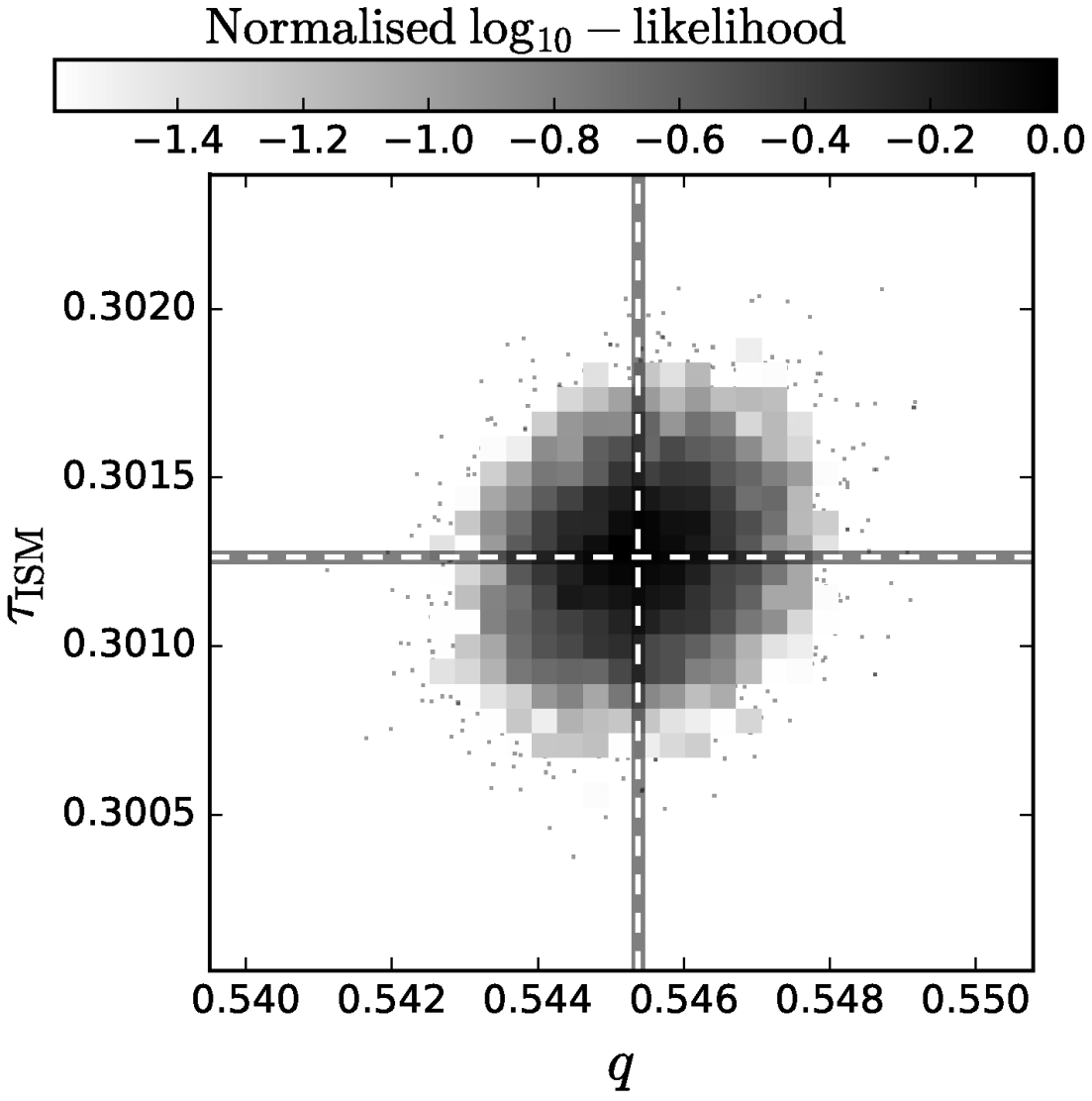

Figure B.6: Shaded maps of likelihood for GD+O $\tau_{\rm ISM}$ and q values fitting the SKIRT photometry of galaxies from the Ref-100 simulation. The $\tau_{\rm BC}$ parameter is fixed to be $2\tau_{\rm ISM}$. Where the normalised $\log_{10}$-likelihood falls below -1.5, the individual Markov-chain samplings are plotted. This panel represents the fiducial SKIRT model. The white dotted lines indicate the median value for each parameter. {*continued on following page*}

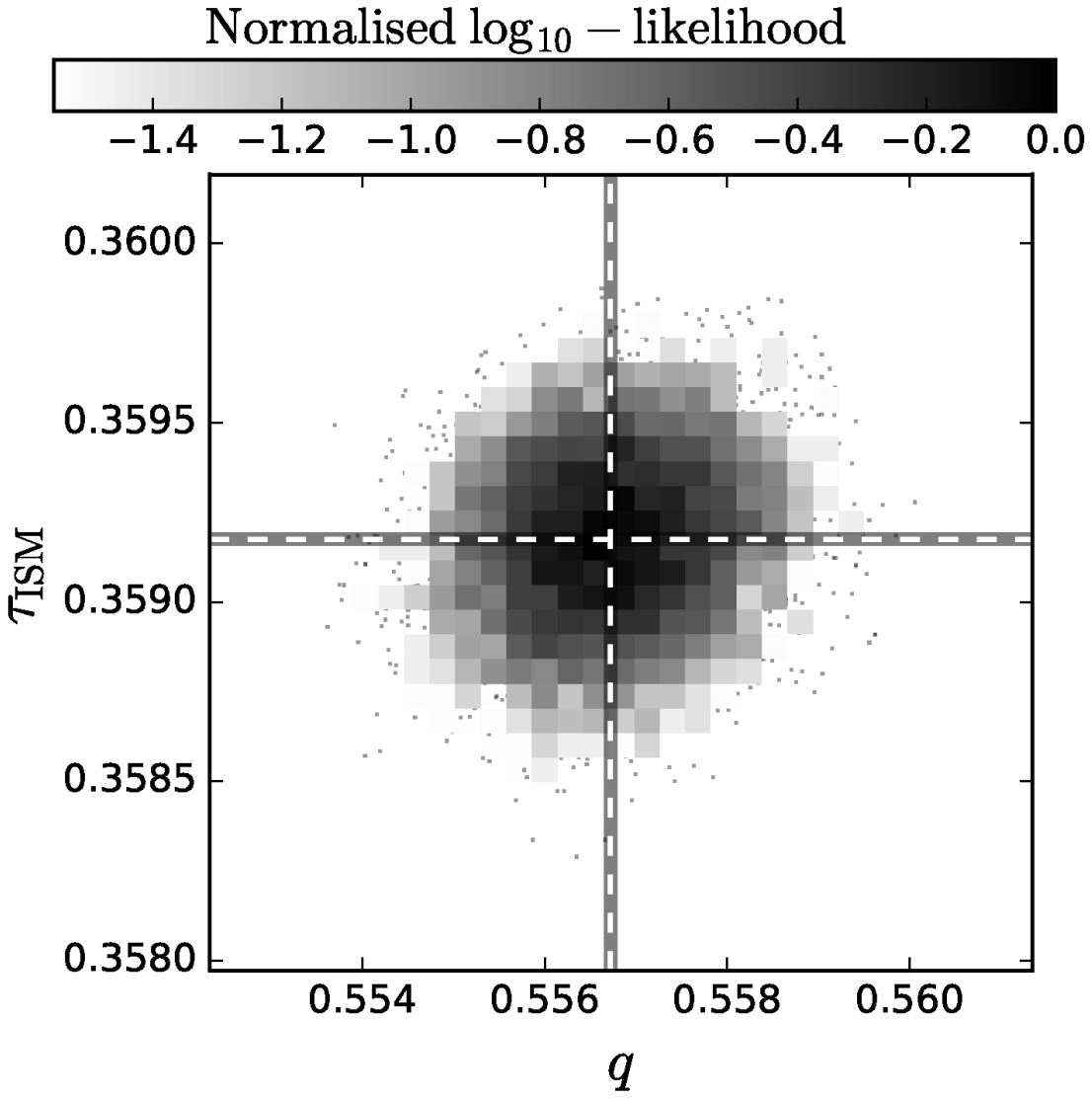

Figure B.6: {*Continued from previous page*} This panel represents the 'uncalibrated'SKIRT model discussed in Appendix B.4. These are generated by constructing the posterior distribution using an MCMC method, as described in section 5.4.2. The ML parameter values for both panels are taken from the three dimensional distribution in parameter space, and listed in table 5.2.

B.4 Comparing fiducial and uncalibrated SKIRT models

The $f_{\rm dust}$ and $f_{\rm PDR}$ parameters are the two values in our dust model that are not assigned using the simulation output. These effectively scale the optical depths in the diffuse and birth cloud components respectively. The parameters of our fiducial SKIRT model were calibrated using local dust scaling relations, indicative of dust mass and temperature, presented in the companion study of Camps et al. (2016) (C16). This is desirable as it allows the same model to be consistent with observations over a large spectral range, from optical to FIR wavelengths. FIR measurements also provide a more direct measurement of dust mass than optical attenuation, which depends strongly on star formation histories and the geometries of stellar and ISM distributions. The C16 calibrated values used in our fiducial model are $f_{\rm dust} = 0.3$ and $f_{\rm PDR} = 0.1$. Without FIR constraints, we would default to the best literature values for our assumed dust parameters.

In order to test the effect our choice of dust parameters has on our results, we also generated results using literature values for the parameters of $f_{\rm dust} = 0.4$ (Draine & Li, 2007) and $f_{\rm PDR} = 0.2$ (Groves et al., 2008), hereby referred to as the 'uncalibrated' SKIRT model. For comparison we apply the ML fitting procedure presented in Appendix B.3 to the uncalibrated model and plot the posterior distribution as the second panel in Fig. B.6.

Comparing the posterior distributions of the fiducial and uncalibrated SKIRT models reveals that the ML values for $\tau_{\rm ISM}$ are $\sim 10\%$ below and above their chapter 3 values respectively. The q values for both models are ~ 0.4 dex higher than in chapter 3, with the uncalibrated model giving a q value $\sim 10\%$ higher than fiducial[1]. Overall, a similar level of agreement with the fiducial GD+O parame-

[1]This comparison also highlights incompatibility between the screen and SKIRT models; the q parameter that independently describes geometry in GD+O has different ML values for two SKIRT models with identical geometries but re-scaled dust optical depths. However the dependence of q on optical depth is relatively weak. The change in $\tau_{\rm ISM}$ is ~ 10 times larger in terms of the marginalised parameter uncertainty.

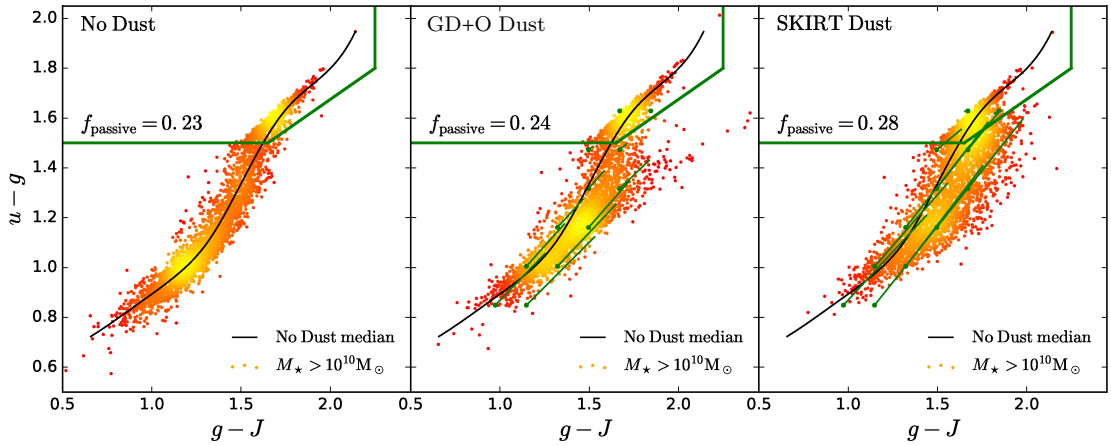

Figure B.7: As Fig. 5.9, except using the uncalibrated SKIRT model with values of $f_{\rm dust} = 0.4$ and $f_{\rm PDR} = 0.2$. We see that this model marginally improves agreement with the observed blue and red fractions for masses $M_\star > 10^{10} M_\odot$.

ters is achieved for both the uncalibrated and fiducial SKIRT models.

To exhibit the effects of the calibration on the overall photometry, we also plot ugJ colour-colour distributions in Fig. B.7. This is the same plot as Fig. 5.9, except using the uncalibrated rather than fiducial SKIRT model. We see that the higher optical depth normalisation has a small effect on the colours, shifting galaxies to marginally redder colour in both indices. It seems that the effects on passive fractions are relatively minor, with only a $\sim 7\%$ change in the passive fractions compared to 5.9.

B.5 Differential Attenuation

A way to directly show the preferential ISM attenuation of young stars discussed throughout chapter 5 is to compare representative attenuation curves for certain stellar populations to the overall attenuation. A natural population to choose for this purpose, given the data produced in our modelling, is the HII region particles represented by MAPPINGS-III SEDs. Fig. B.8 is similar to Fig. 5.6, comparing the total galaxy attenuation to that seen by the MAPPINGS-III particles alone (ie. stars <10 Myr old). Here the birth cloud absorption built into MAPPINGS-III SEDs are not included in the plots, so we are seeing purely the difference due to differential

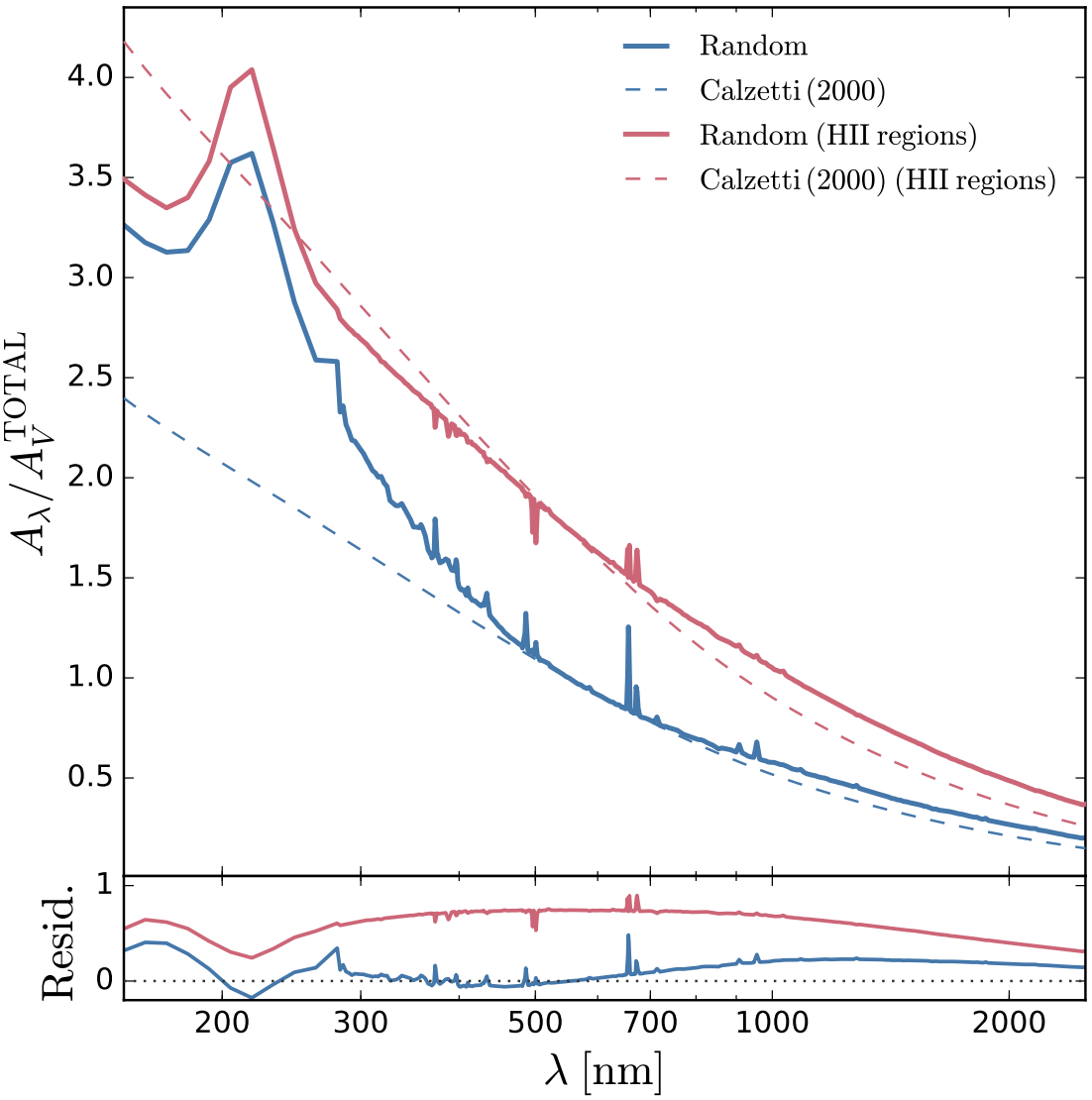

Figure B.8: Composite *ISM* attenuation curves for randomly projected EAGLE galaxies, normalised to 1 for the V-band attenuation of all stars. The blue line indicates the effective attenuation curve of all stars from the overall galaxy SEDs, as in Fig. 5.6, whereas the red line is the effective attenuation experienced by HII regions alone. We see that due to preferential ISM attenuation, the MAPPINGS-III attenuation is boosted, and appears greyer, closer to a Calzetti-like attenuation curve. We see features in the blue attenuation curve due to the preferential reddening of HII regions in general. We attribute features in the red curve to the environmental (ISM pressure) dependence of line strengths in the MAPPINGS-III SED templates, which also scales with ISM attenuation.

ISM absorption. Both curves are normalised to the integrated galaxy attenuation at 5500 Å to show any boost in ISM attenuation that might be seen by the young stars relative to the overall population at a given wavelength

We see that these young stars indeed have boosted ISM attenuation (vertical offset). They also exhibit a different attenuation curve shape, that appears to be more consistent with Calzetti (greyer profile). This is perhaps unsurprising, as the Calzetti law assumes that the dust and sources are well mixed, which is likely the case for the MAPPINGS-III particles as they are largely co-spatial. We attribute features in this attenuation curve to the MAPPINGS-III SEDs having different line strengths in gas of differing density and metallicity.

B.6 Investigating a 'negatively reddened' galaxy

A population of galaxies with negative reddening (i.e. dust effects making galaxies appear bluer in a given colour index) are identified in the SKIRT photometry, as discussed in section 5.3.2. For the low redshift sample discussed here, this effect is very small and can be attributed solely to random photometric errors (appendix B.2). However in the data produced for all epochs, rare instances of significant negative reddening are observed. The two explanations for this effect are either attenuation that predominately obscures the redder stars, perhaps due to high centralised attenuation, or the effects of scattering into the line of sight making galaxies appear bluer in some scenarios (e.g. Baes & Dejonghe, 2001).

In Figure B.9 we analyse an example object displaying this behaviour at $z = 0.9$. This galaxy has an intrinsic $g - r$ colour of 0.4, but with dust effects is measured to have a $g - r$ colour of 0.3. We use the capabilities of SKIRT to identify the fraction of the emitted light at each wavelength that is directly transmitted (medium grey) and that is scattered into the line of sight (light grey), compared to the overall received flux (black line). It is apparent that the bluer colours are contributed predominately by the directly measured starlight, with a secondary contribution from scattered light. The broad band attenuations (also plotted) support this, indicating strong overall attenuation with the strongest absorption in

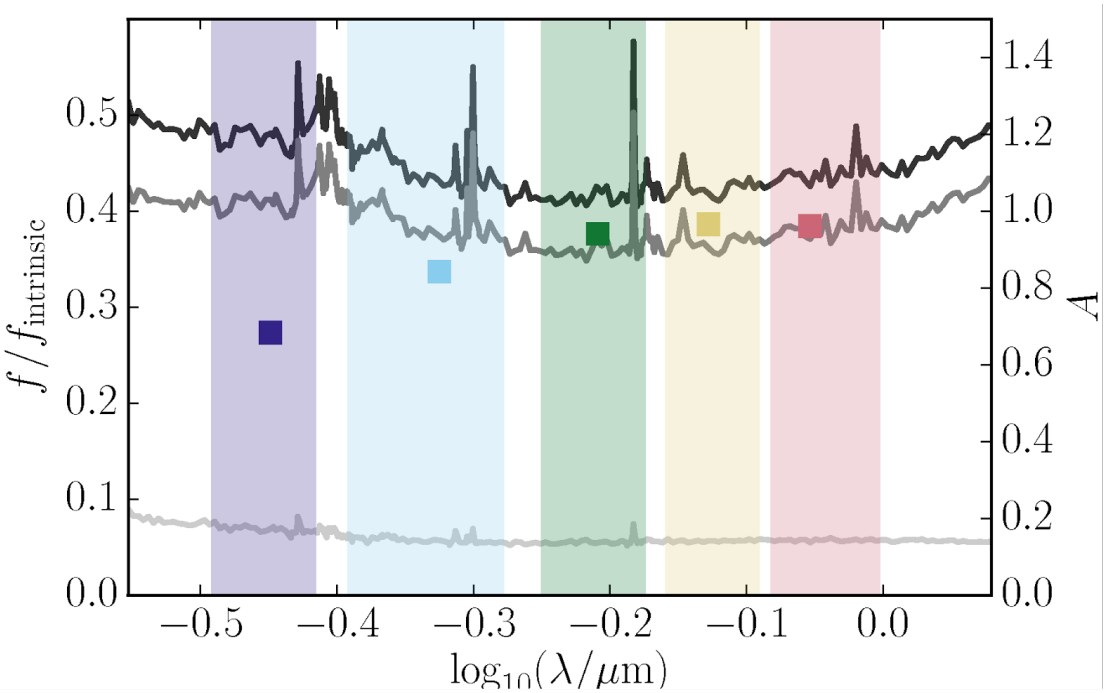

Figure B.9: Plot of the ratio of total intrinsic flux contributions (left hand y-axis) by different components for a negatively reddened EAGLE galaxy at z=0.9 as a function of redshift. Black line shows total transmitted light fraction, medium grey line shows contribution of transmitted light that comes directly from sources, light grey line shows the contribution by light scattered into the line of sight. Coloured bands indicate the 5-95 percentiles of ugriz bands from left to right. Coloured squares indicate the attenuation in each band via the right hand y-axis scale. We see that the attenuation is actually lower in the bluer bands, which appears to be contributed by direct light, suggesting more blue light is escaping the galaxy. This appears to be due to heavy dust obscuration in the central regions, such that blue stars in the outskirts dominate the transmitted light. Scattered light also contributes to this effect, but this contribution is marginal.

redder bands. This is suggestive that, at least for this example, negative reddening is caused by dense dust clouds strongly obscuring the older central bulge, such that less obscured light from star forming regions in the outer regions dominates the measured flux. Inspecting the galaxy image supports this conclusion. Whether this is a physically plausible scenario, or is indicative of a breakdown of the dust modelling in this case, is as yet unclear.

Appendix C

SED Fitting

C.1 Mass estimators at higher resolution

To indicate convergence with resolution, the Fig. 6.1 plot is remade for galaxies taken from the Recal-25 simulations in Fig. C.1. The typical Recal-25 offsets appear remarkably similar to that of Ref-100; suggesting convergent, mass-independent offsets for each estimator.

C.2 The Failure Population

It is important to understand why the SED fitting of section 6.3.1 recovers vastly underestimated masses for a sub-population of galaxies that are not found by Torrey et al. (2014), despite similar fitting approaches. To test how procedural differences influence this result, the offset-mass relation of Fig. 6.6a is reproduced for slightly different FAST set-ups. In the left panel, it can be seen that fitting pure exponential histories (as in Torrey et al. 2014) approximately halves the number of failure galaxies. Unlike delayed exponential histories, the pure exponentials have no rising portion, and thus cannot approximate young *'inverted-τ'* histories (Maraston et al., 2010). The reduction in failures may be related to this; when fitting bursting galaxies there are no rising histories to compete with more realistic older histories in the fitting. Still, it seems that very young exponential histories can still provide the best fits for some EAGLE galaxies.

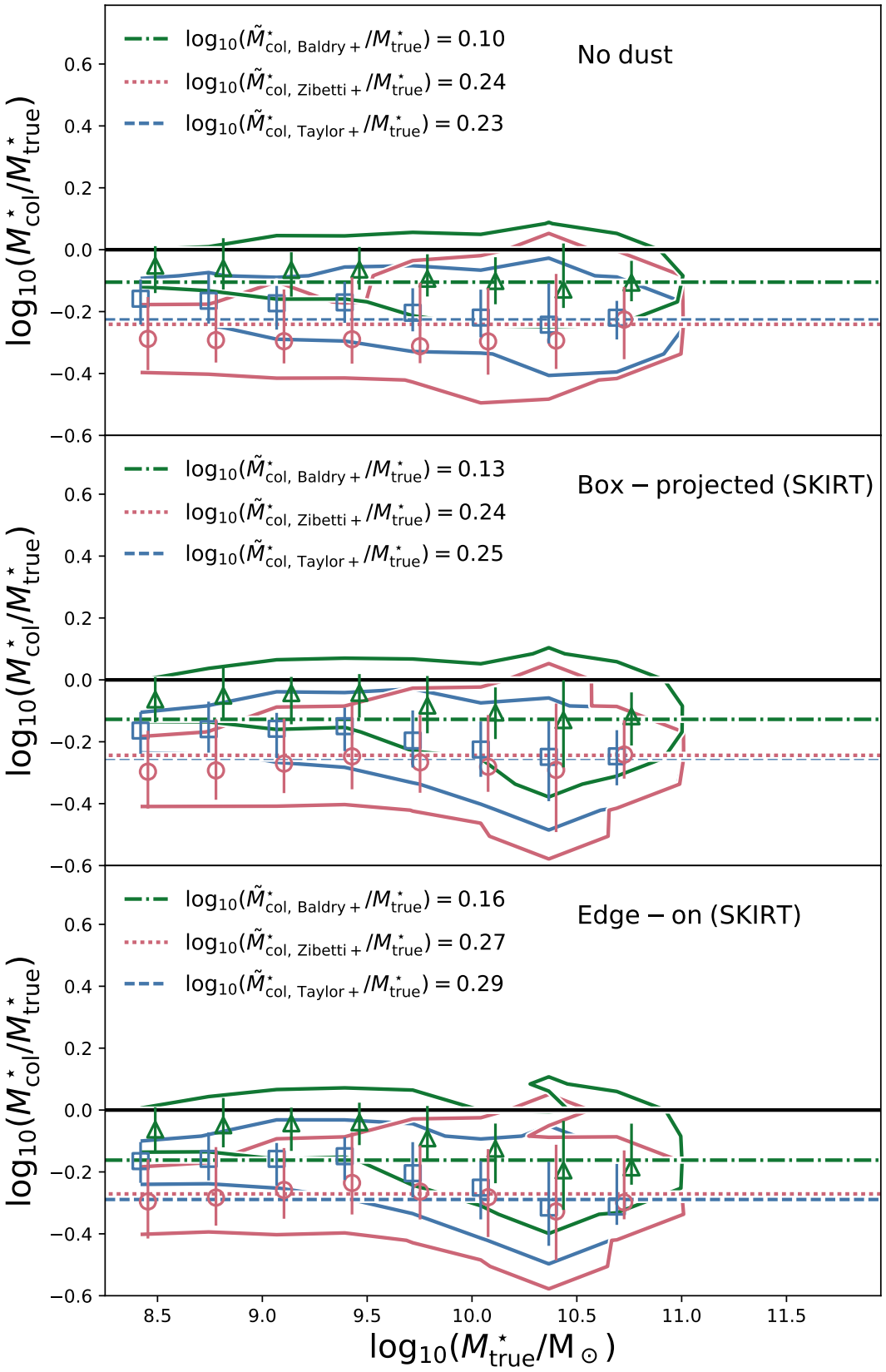

Figure C.1: As Fig. 6.1, but for galaxies taken from the Recal-25 simulation. The finding of a nearly mass independent mass underestimation appears convergent.

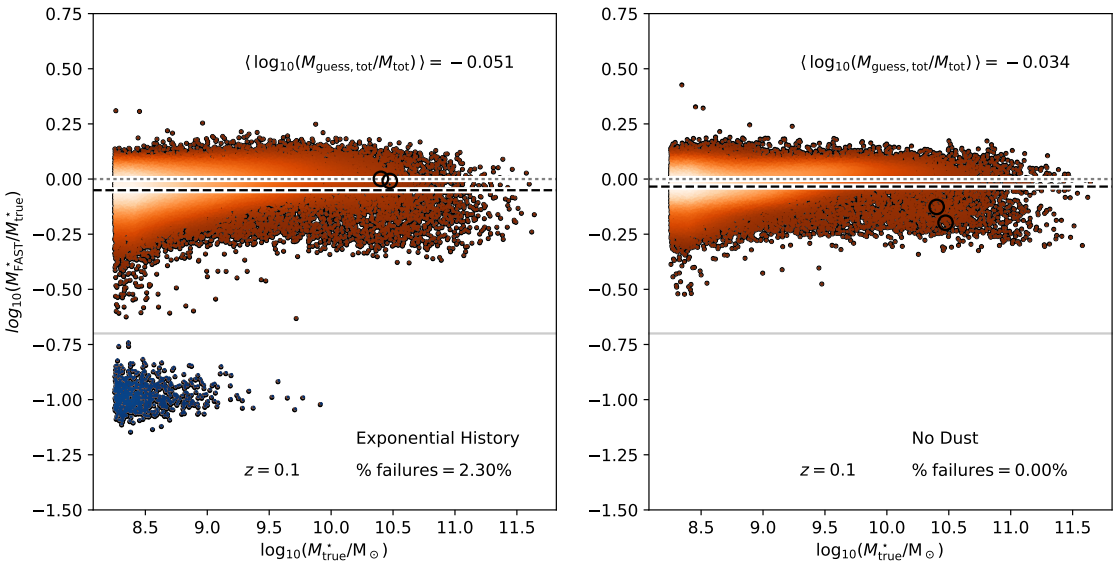

Figure C.2: As Fig. 6.6a, but for modified SED fitting procedures from the initial approach plotted there (see section 6.3). In the left panel, the initial approach is modified to fit pure exponential ($\psi \propto e^{-t/\tau}$) rather than delayed exponential ($\psi \propto te^{-t/\tau}$) histories. In the right panel, the initial approach is changed to fit intrinsic (ie. $A_V = 0$) SEDs to the dust-free (ND, chapter 3) EAGLE photometry. It shows that using exponential histories halves the number of failures, whereas fitting to dust free SEDs eliminates them completely.

In the right panel, we instead fit dust-free photometry with intrinsic ($A_V = 0$) SEDs. This completely eliminates the failures, showing that significant dust attenuation is needed to make these very young starbursts look similar to EAGLE galaxies photometrically. The offset-mass distribution seen here also appears very similar to that of Fig. 9 in Torrey et al. (2014), with a similar subpopulation of underestimated galaxies at offsets of ~ -0.2 dex.

C.3 The effect of dust on predicted masses

As discussed in chapter 6.3.4, a characteristic median relation in the offset between $M^{\star}_{\rm FAST}$ from $M^{\star}_{\rm true}$ is observed with A_g, but is limited by the small number counts of galaxies, particularly at high attenuations. In C.3 this is extended to $z \lessapprox 2$ EAGLE galaxies, using the same rest frame $ugriz$ photometric fitting (i.e. no

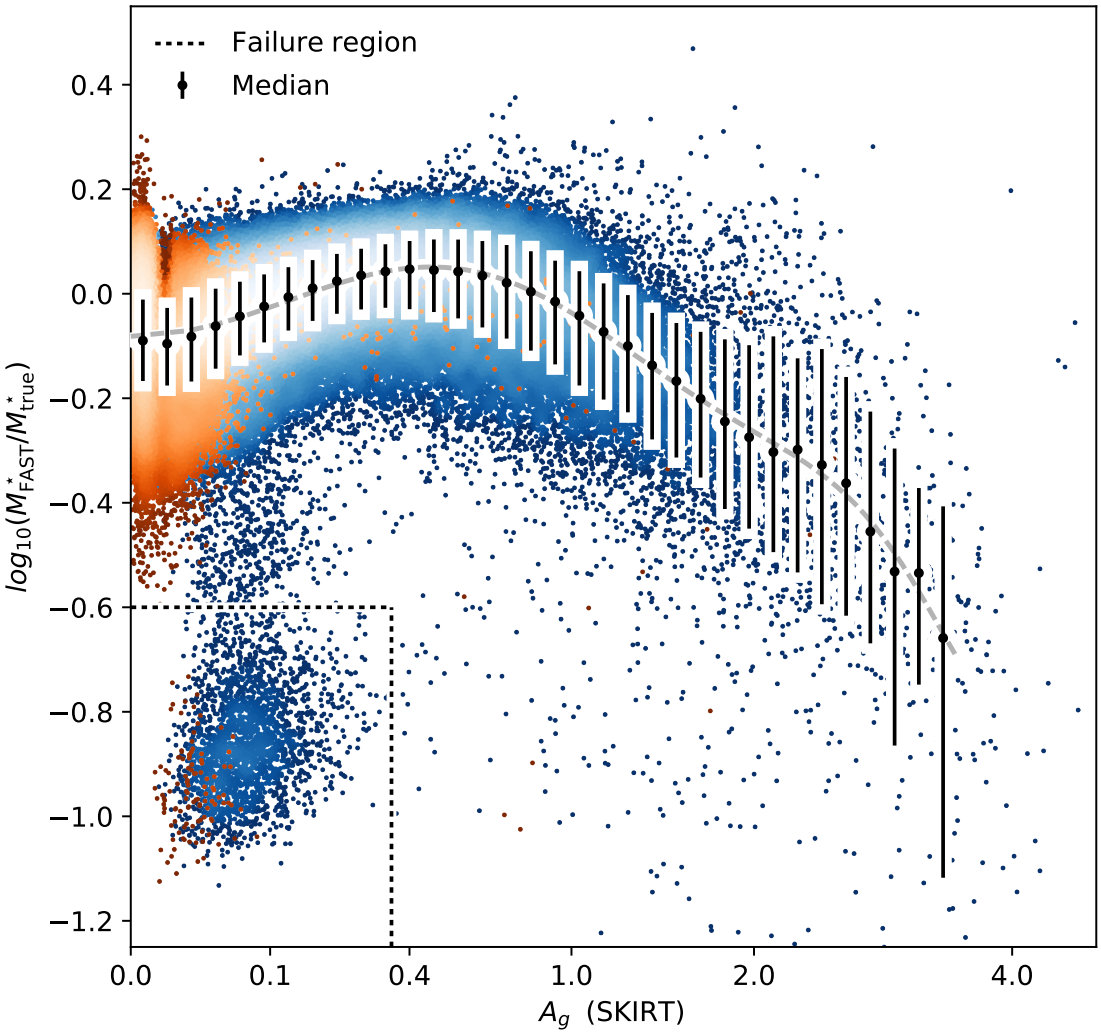

Figure C.3: As Fig. 6.15, now for EAGLE galaxies with $M^\star_{\rm true} > 1.2 \times 10^8 {\rm M}_\odot$ at $z \lessapprox 2$ ($\sim 420,000$ galaxies). Probing higher attenuations and with higher number counts than at $z = 0.1$, the decreasing accuracy of FAST mass estimates with A_g for high attenuations ($A_g \gtrapprox 0.4$) is seen to continue for $A_g > 1$ while exhibiting increasing scatter.

redshifting or IGM absorption effects are included in the SEDs). A very similar trend to Fig. 6.15 is observed at attenuations of $A_g \lesssim 1$, but is seen to continue with increasing scatter to higher A_g values.

C.4 True histories of red and blue galaxies

As seen in chapter 6.3, the FAST code fits red galaxies to have short burst star formation histories, typically found to commence after their blue counterparts. To show how this picture compares with the true formation histories of red and blue EAGLE galaxies, Fig C.4 compares properties of the red and blue population.

The upper panel of Fig C.4 shows the composite distributions of SSP ages for red and blue galaxies selected at $z = 0.1$ using Eq. 4.3.1 with $M^{\star}_{\rm true} > 10^{9.5}{\rm M}_{\odot}$. It is clear that the true star formation histories of red EAGLE galaxies do not commence after the blue galaxies, and contain a higher fraction of star particles at the oldest ages than found in the blue galaxies. The lower panel of Fig C.4 then compares the true duration of the star formation history for red and blue galaxies selected in the same way, by comparing histograms of the time interval between when a galaxy has formed 5% and 95% of its stellar mass for both populations. It is clear that the true star formation histories of red galaxies are typically shorter in duration than those of blue galaxies.

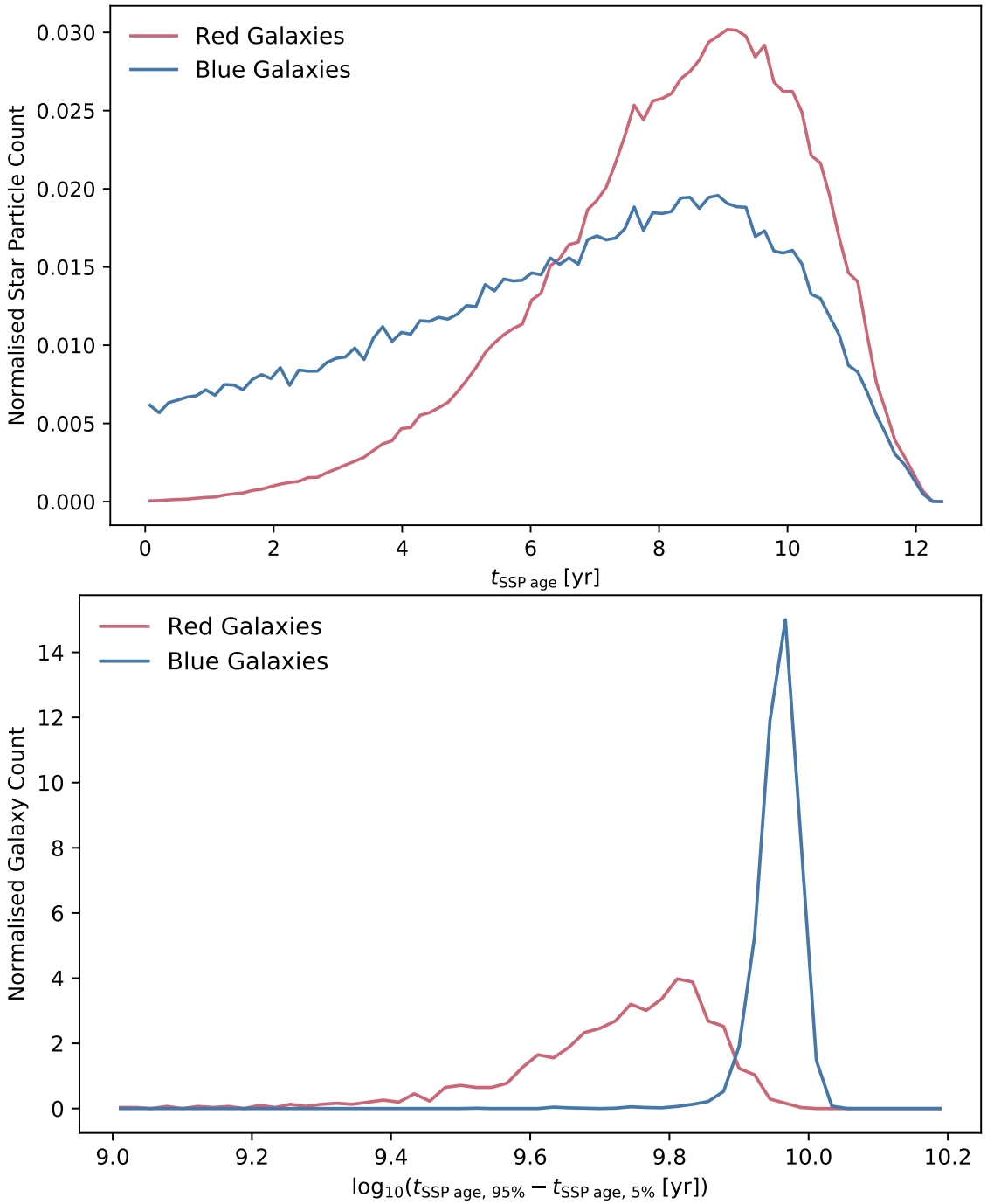

Figure C.4: Comparing stellar mass assembly properties of red and blue EAGLE galaxies selected at $z = 0.1$ with Eq. 4.3.1, and having $M^{\star}_{\mathrm{true}} > 10^{9.5}\mathrm{M}_{\odot}$. Top panel compares the distributions of star particle ages in red and blue galaxies, coloured red and blue respectively. Bottom panel compares the distribution of the star formation timescales in red and blue galaxies, represented by the logarithm of the period over which a galaxy forms between 5% and 95% of its stellar mass. Red galaxies begin forming at a similar time to blue galaxies, both peaking at $z \sim 9$ Gyr, but form stars over a shorter period.